Measurement of Neutral Current Drell-Yan production using ATLAS data collected at $\sqrt{s} = 8$ TeV

Dissertation

zur Erlangung des Doktorgrades
an der Fakultät für Mathematik, Informatik
und Naturwissenschaften
Fachbereich Physik
der Universität Hamburg

vorgelegt von
ELENA YATSENKO

Hamburg, 2015

Gutachter/in der Dissertation:	PD Dr. Alexandre Glazov Prof. Dr. Johannes Haller
Gutachter/in der Disputation:	Prof. Dr. Sven-Olaf Moch Prof. Dr. Michael Rübhausen PD Dr. Hannes Jung
Tag der Disputation:	6. January 2015
Vorsitzender des Prüfungsausschusses:	Prof. Dr. Michael Rübhausen
Vorsitzender des Promotionsausschusses:	Prof. Dr. Daniela Pfannkuche
Dekan des MIN-Fakultät:	Prof. Dr. Heinrich Graener

Abstract

This dissertation presents measurements of the $pp \to Z/\gamma^* \to e^+e^- + X$ production cross-section and of the Forward-Backward asymmetry, A_{FB}, of dielectron pairs with the ATLAS experiment at the Large Hadron Collider. Both measurements use the dataset collected in 2012 at a center-of-mass energy of $\sqrt{s} = 8$ TeV corresponding to an integrated luminosity of 20.1 fb^{-1}. The cross-section is measured single- and triple-differentially as a function of the rapidity, invariant mass and scattering angle of the dielectron pairs. The Forward-Backward asymmetry is measured double-differentially in bins of the dielectron invariant mass and rapidity. The study is performed with one of the final-state electrons detected in the forward calorimeter which allows large rapidities and scattering angles to be probed.

The $pp \to Z/\gamma^* \to e^+e^- + X$ process is a rich source of information on electroweak and QCD effects. The wide range of dilepton invariant masses accessible to this measurement probes different scales of the interaction and provides access to both photon and Z boson dominated regions. The rapidity dependence provides information on the fraction of the initial proton's momentum carried by the interacting partons, which makes the measurement sensitive to the proton parton density functions. The angular distribution allows testing of fundamental properties of the electroweak interactions, giving access to the weak mixing angle via the A_{FB} measurements.

The measurements are compared to theoretical predictions calculated at next-to-leading order QCD. The measured cross-sections agree with the theoretical calculation within the uncertainty in the bulk of the measured phase space. The deviation observed in certain phase space regions warrants the study of higher order electroweak and QCD corrections. The measured cross-sections can be used for PDF fits and for the determination of the electroweak parameters.

Zusammenfassung

Diese Dissertation stellt Messungen des $pp \to Z/\gamma^* \to e^+e^- + X$ Produktionsquerschnitts und der Vorwärts-Rückwärts-Asymmetrie A_{FB} von Dielektron-Paaren mit dem ATLAS-Experiment am Large Hadron Collider vor. Dafür wurden Daten von 2012 bei einer Schwerpunktsenergie von $\sqrt{s} = 8$ TeV analysiert. Das entspricht einer integrierten Luminosität von 20.1 fb^{-1}. Der Produktionsquerschnitt wurde ein- und dreifach differentiell gemessen als Funktion der Rapidität, der invarianten Masse und des Streuwinkels der Dielektron-Paare. Die Vorwärts-Rückwärts-Asymmetrie wurde doppelt differentiell gemessen als Funktion der invarianten Dielektronenmasse und Rapidität. Ereignisse wurden analysiert, wobei ein Elektron mit dem Vorwärts-Kalorimeter gemessen wurde. Das ermöglicht, große Rapiditäten und Streuwinkel zu messen.

Der Prozess $pp \to Z/\gamma^* \to e^+e^- + X$ liefert reichhaltige Informationen über elektroschwache und QCD-Effekte. Der breite Massenbereich umfasst unterschiedliche Skalen der Wechselwirkung und ermöglicht, sowohl Photonen als auch Z-Boson-dominierte Bereiche zu untersuchen. Die Rapidität ermöglicht Rückschlüsse auf der Anteil des Impulses des ursprünglichen Protons, der von den wechselwirkenden Parton getragen wird, was die Messung sensitiv auf die Parton-Dichtefunktion (PDF) macht. Die Winkelverteilung ermöglicht, die fundamentalen Eigenschaften der elektroschwachen Wechselwirkung zu untersuchen, wie den schwachen Mischungswinkel, der mit Hilfe der Messungen von A_{FB} bestimmt werden kann.

Die Messungen wurden mit theoretischen Vorhersagen von NLO-QCD-Berechnungen verglichen. Die gemessenen Wirkungsquerschnitte stimmen im Allgemeinen innerhalb der Unsicherheit mit den theoretischen Vorhersagen überein. Die Abweichung von den Vorhersagen, die in einigen Klassen gefunden wurde, rechtfertigt die Untersuchung von elektroschwachen Prozessen höherer Ordnung. Der Wirkungsquerschnitt kann in PDF-Fits und für die Bestimmung der elektroschwachen Parameter verwendet werden.

Hiermit erkäre ich an Eides statt, dass ich die vorliegende Dissertationsschrift selbst verfasst und keine anderen als die angegebenen Quellen und Holfsmittel benutzt habe.

I hereby declare, on oath, that I have written the present dissertation by my own and have not used other than the acknowledged resources and aids.

Hamburg, 26/11/2014

CONTENTS

CHAPTER 1

Thesis organization

The thesis is organized in three parts. The theoretical and experimental input are described in parts 1 and 2. The cross-section and Forward-Backward asymmetry measurements performed by the author are described in part 3.

The work presented in this thesis was performed within the ATLAS collaboration. All the plots in this thesis were produced by the author, unless referenced otherwise. A significant part of the author's work is presented in Appendices A-F.

The theoretical input is described in the following chapters.

Chapter 2, Theoretical introduction, contains a brief introduction to the Standard Model and the theory of electroweak interactions. The chapter includes a description of the proton structure.

Chapter 3, Neutral-current Drell Yan process in proton-proton collisions, discusses the Drell-Yan process and the motivation for measuring the differential cross-section and Forward-Backward asymmetry with central-forward electrons.

The experimental input is described in the following chapters.

Chapter 4, The LHC and the ATLAS experiment, contains a description of the LHC accelerator complex and the ATLAS detector.

Chapter 5, Data and Monte-Carlo samples, provides information on the data sample used in this analysis as well as a description of the Monte-Carlo simulation.

Chapter 6, Electrons in ATLAS, contains a detailed description of the electron identification and reconstruction in ATLAS. The electron energy and efficiency corrections, derived by the performance group, are presented here, including the resolution smearing correction which was derived by the author.

The following chapters present a series of studies, which unless otherwise specified, were performed by the author. More specifically,

Chapter 7, Selection, describes a set of selection criteria used to derive a sample of $pp \to Z/\gamma^* \to e^+e^- + X$ candidate events.

Chapter 8, Event weights, describes the corrections applied to generated Monte-Carlo events in

order to improve the agreement with data. These corrections were derived by the ATLAS performance groups.

Chapter 9, Binning definition and bin-to-bin migration effects, introduces the binning used in the presented measurements and discusses the motivations behind this particular binning choice.

Chapter 10, Background estimation, describes the processes that constitute the background to the Drell-Yan process and presents the methods used to estimate their contribution to the signal sample.

Chapter 11, Control distributions, provides various observables that illustrate the level of agreement between the selected data sample and the Monte-Carlo simulation including the contribution of the background processes.

Chapter 12, Unfolding, contains a description of the two most widely used unfolding techniques. The input used for the unfolding of the cross-section to the fiducial volume is also presented here.

Chapter 13, Uncertainties of the measurement, describes the sources of experimental and theoretical uncertainties that affect the cross-section and Forward-Backward asymmetry measurements, together with the error propagation techniques used in the analysis.

Chapter 14, Theoretical predictions, contains NLO QCD predictions for the presented measurements.

Chapter 15, Cross-section results, contains the results for the single- and triple-differential cross-section measurements as well as a comparison to the theoretical predictions.

Chapter 16, Forward-Backward asymmetry measurement, presents the results for the double-differential measurement of the Forward-Backward asymmetry

Theoretical introduction

CHAPTER 2

Theoretical introduction

2.1 The Standard Model

The Standard Model summarizes our current understanding of High Energy Physics, describing collectively the electromagnetic, weak and strong interactions between fermions, the fundamental constituents of matter. The Standard Model accommodates twelve fundamental fermions of spin $1/2$ that form two categories - leptons and quarks. The fermions come in three generations as shown in table 2.1. Interactions between fermions are mediated by the gauge bosons γ, Z, $W^{\pm}$ and eight gluons of different 'color' charge, as shown in table 2.2. The charged leptons interact via electromagnetic and weak forces, while the neutral leptons interact only via weak interactions. Quarks interact with strong, weak and electromagnetic interactions.

Within each generation left-handed quarks and leptons can be arranged into doublets, containing two particles differing by their third isospin component, one particle having $T_3 = 1/2$ and the other having $T_3 = -1/2$. Each generation contains a quark with charge $+\frac{2}{3}$ together with a quark with charge $-\frac{1}{3}$ (in units of electron charge). To each of these particles one associates an antiparticle by charge conjugation. Each of the quarks come in three 'color' charges - conventionally denoted red, green and blue.

In mathematical terms, the Standard Model is a non-Abelian gauge theory with the symmetry group $SU(3) \times SU(2)_L \times U(1)_Y$. The construction of the Standard Model started with the works of Glashow, Weinberg and Salam [1–3]. In the model that they proposed the electromagnetic and weak interactions are unified under the $SU(2)_L \times U(1)_Y$ gauge group, where $Y = 2(\mathrm{Q} - T_3)$ is the hypercharge and Q is the charge. In this unified description the $SU(2)_L$ symmetry describes the interaction mediated by three massless gauge bosons W^0, W^1 and W^2, while the $U(1)_Y$ symmetry corresponds to a massless gauge boson B. The $W^{\pm}$, Z and γ bosons are produced by spontaneous symmetry breaking described by the Higgs mechanism when the $SU(2)_L \times U(1)_Y$ symmetry is broken down to $U(1)_{\mathrm{Q}}$, which is the gauge symmetry of electromagnetism. The Higgs mechanism was developed in the works of Higgs, Englert, Brout, Guralnik, Hagen and Kibble [4–8]. The Higgs field, predicted by the electroweak theory, has a non-zero vacuum expectation value, which is not invariant under a gauge transformation.

The observation of neutral current interactions in the Gargamelle bubble chamber and the discovery of the W and Z bosons by the UA1 and UA2 experiments [9–12] provided the experimental confirmation of the electroweak theory. The Higgs mechanism of the symmetry breaking has been confirmed with the discovery of the Higgs boson at the Large Hadron Collider (LHC) [13] by the

Fermions			U(1) charge	T_3
Leptons				
$\begin{pmatrix} e^- \\ \nu_e \end{pmatrix}$	$\begin{pmatrix} \mu^- \\ \nu_\mu \end{pmatrix}$	$\begin{pmatrix} \tau^- \\ \nu_\tau \end{pmatrix}$	-1 0	$-1/2$ $1/2$
Quarks				
$\begin{pmatrix} u \\ d \end{pmatrix}$	$\begin{pmatrix} c \\ s \end{pmatrix}$	$\begin{pmatrix} t \\ b \end{pmatrix}$	$2/3$ $-1/3$	$1/2$ $-1/2$
I	II	III	Generation	

Table 2.1: The Standard Model fermion families and corresponding properties of the particles: charge in units of electron charge Q and third component of the isospin T_3.

Interaction	Gauge Boson	Charge
Electromagnetic	γ	electric charge Q
Weak	$W^{\pm}, Z$	weak isospin I
Strong	$g_1, ..., g_8$	color C

Table 2.2: The Standard Model gauge bosons that mediate electromagnetic, weak and strong interactions.

ATLAS and CMS collaborations [14, 15]. The electroweak interaction is of particular interest for this thesis and is described in more detail in section 2.2.

The strong interactions are described by Quantum Chromodynamics (QCD), a non-Abelian gauge theory with symmetry group $SU(3)$. QCD originates from the quark model, which was a phenomenological attempt to describe the hadron resonances [16,17]. The observation of the Δ^{++} particle, which consists of three up-type quarks with the same spin, required the introduction of a new degree of freedom, which was dubbed 'color', in order to be consistent with the Pauli exclusion principle [18].

The measurement of the cross-section ratio $\sigma(e^-e^+ \to \text{hadrons})/\sigma(e^-e^+ \to \mu^-\mu^+)$ at SLAC [19] provided evidence for the existence of three colors and the observation of gluons in three-jet events at PETRA, DESY gave the first direct evidence about the validity of QCD as the correct theory of strong interactions.

The strength of the electromagnetic, weak and strong interactions are described by the coupling constants α, α_w and α_s respectively. Experimental determinations of the coupling constants found their dependence on the energy scale Q^2[1]. This phenomenon is known as running coupling constant. The approximate dependence of the three coupling constants on Q^2 is shown in figure 2.1.

[1] Q^2 denotes the square of the four-momentum exchanged in an interaction.

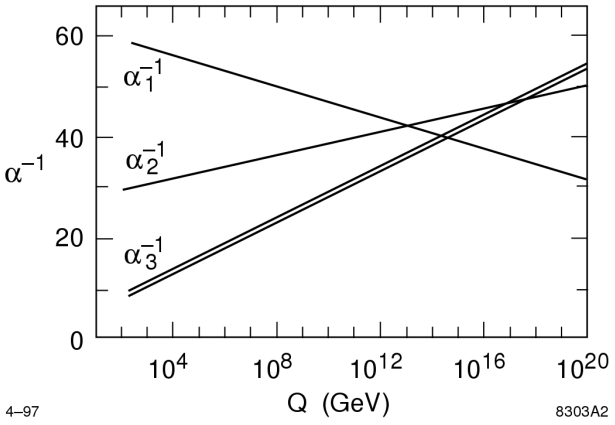

Figure 2.1: Evolution of the SU(3)×SU(2)×U(1) gauge couplings to high energy scales, the double line for α_3 indicates the experimental error on this quantity, the errors in α_1 and α_2 are too small to be visualised, [20].

2.2 Electroweak interactions

The weak bosons acquire masses via the Higgs mechanism and appear to be non-invariant under the gauge transformations. The physical massive weak bosons W^+ and W^- are described as a superposition of the W^1 and W^2 bosons:

$$W_\mu^\pm = \frac{1}{\sqrt{2}}\left(W_\mu^1 \mp iW_\mu^2\right). \tag{2.1}$$

Symmetry breaking can be described as a rotation of the $W^0 - B$ plane onto the physical Z and γ gauge bosons as shown in equation 2.2. The rotation angle θ_W is called weak mixing angle or Weinberg angle.

$$\begin{pmatrix} A_\mu \\ Z_\mu \end{pmatrix} = \begin{pmatrix} \cos\theta_W & \sin\theta_W \\ -\sin\theta_W & \cos\theta_W \end{pmatrix} \begin{pmatrix} B_\mu \\ W_\mu^0 \end{pmatrix}. \tag{2.2}$$

The masses of the weak bosons arise from the interactions of the gauge fields with the Higgs field and at tree level satisfy the relation

$$\frac{M_W}{M_Z} = \cos\theta_W. \tag{2.3}$$

The electromagnetic and weak interactions between fermions can be described by the following Lagrangians:

$$\mathscr{L}_{\text{int}}^{\text{em}} = -e\bar{\psi}\gamma^\mu Q\psi A_\mu, \tag{2.4}$$

$$\mathscr{L}_{\text{int}}^{\text{NC}} = \frac{g}{\cos\theta_W}[\bar{\psi}_L\gamma^\mu\frac{\tau_3}{2}\psi_L - \sin^2\theta_W Q\bar{\psi}\gamma^\mu\psi]Z_\mu, \tag{2.5}$$

$$\mathscr{L}_{\text{int}}^{\text{CC}} = \frac{g}{\sqrt{2}}(j_\mu^+ W_\mu^- + j_\mu^- W_\mu^+), \tag{2.6}$$

where ψ is a spinor wave function describing the fermion fields, $j_\mu^+ = \bar{\psi}_L\gamma_\mu\psi_L'$, $j_\mu^- = \bar{\psi}_L'\gamma_\mu\psi_L$, $\gamma^\mu = (\gamma^0,\gamma^i) = (\beta,\beta\alpha^i)$ are Dirac matrices defined in the Dirac-Pauli representation by

$$\gamma^0 = \beta = \begin{pmatrix} I & 0 \\ 0 & -I \end{pmatrix}, \gamma^j = \beta\alpha^i \text{ and } \alpha^i = \begin{pmatrix} 0 & \sigma^i \\ \sigma^i & 0 \end{pmatrix}, \tag{2.7}$$

where σ^i are the Pauli matrices

$$\sigma^1 = \begin{pmatrix} 0 & 1 \\ 1 & 0 \end{pmatrix}, \ \sigma^2 = \begin{pmatrix} 0 & -i \\ i & 0 \end{pmatrix}, \ \sigma^3 = \begin{pmatrix} 1 & 0 \\ 0 & -1 \end{pmatrix}. \ \tau_3 = \begin{pmatrix} 1 & 0 \\ 0 & -1 \end{pmatrix}. \tag{2.8}$$

Under the parity transformation the electromagnetic current, being a vector, changes its sign: $\hat{P}[\bar{\psi}\gamma^\mu\psi] = -\bar{\psi}\gamma^\mu\psi$ which leads to parity conservation $\hat{P}[\mathscr{L}^\gamma_{\text{int}}] = \mathscr{L}^\gamma_{\text{int}}$.

Since

$$\bar{\psi}_L\gamma^\mu\psi_L = \underbrace{\frac{1}{2}\bar{\psi}\gamma^\mu\psi}_{\text{Vector}} - \underbrace{\frac{1}{2}\bar{\psi}\gamma^\mu\gamma_5\psi}_{\text{Axial Vector}}, \tag{2.9}$$

the weak current contains a mixture of vector (V) and axial vector (A) terms, giving rise to the V-A form of weak interactions. Applying a parity transformation, the weak current becomes $\hat{P}[\bar{\psi}_L\gamma^\mu\psi_L] = -\frac{1}{2}\bar{\psi}\gamma^\mu\psi - \frac{1}{2}\bar{\psi}\gamma^\mu\gamma_5\psi = \bar{\psi}\gamma^\mu\frac{1+\gamma_5}{2}\psi = \bar{\psi}_R\gamma^\mu\psi_R$. Terms containing right-handed components of the matter fields are not present in the weak Lagrangian, therefore the weak interactions are not invariant under parity.

The vertex factors for the electroweak interactions are encoded in the Feynman rules. The couplings of the EW bosons to fermions are listed in table 2.3. The coupling of the Z boson to fermions has vector and axial vector components, which are determined in the Standard Model by the following relations:

$$\begin{aligned} \mathrm{v}_f &= g_L + g_R = T_f^3 - 2\sin^2\theta_W \mathrm{Q}_f, \\ a_f &= g_L - g_R = T_f^3, \end{aligned} \tag{2.10}$$

where $g_L = T_3 - \mathrm{Q}_f \sin^2\theta_W$ and $g_R = -\mathrm{Q}_f \sin^2\theta_W$, Q_f is the charge of fermion. The values of v_f and a_f are listed in 2.4.

Vertex	Vertex factor
$\gamma f\bar{f}$	$-ieQ_f\gamma^\mu$
$Zf\bar{f}$	$-i\frac{g}{\cos\theta_W}\gamma^\mu\frac{1}{2}(\mathrm{v}_f - a_f\gamma^5)$
$Wf\bar{f}$	$-i\frac{g}{\sqrt{2}}\gamma^\mu\frac{1}{2}(1-\gamma^5)$

Table 2.3: Vertex factors for electroweak interactions, [21].

Fermion	a_f	v_f
u, c, t	$\frac{1}{2}$	0.25
d, s, b	$-\frac{1}{2}$	-0.33
e, μ, τ	$-\frac{1}{2}$	-0.038
ν_e, ν_μ, ν_τ	$\frac{1}{2}$	$\frac{1}{2}$

Table 2.4: The $Zf\bar{f}$ vertex factors, [22].

2.3 Proton structure

The main knowledge about the proton structure comes from lepton-proton scattering experiments. A lepton probes a target proton via the exchange of an electroweak boson. While elastic lepton-proton scattering allows to investigate the electric and magnetic form factors associated with charge and the magnetic distributions of the proton, the inner proton structure is studied by deep inelastic scattering (DIS) experiments.

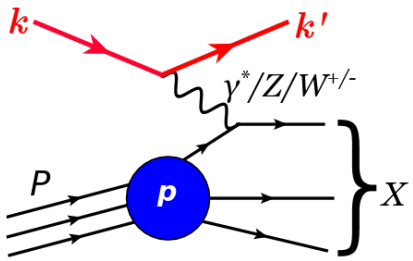

Figure 2.2: Schematic diagram of a lepton-proton DIS process mediated by γ^*, Z or $W^\pm$ exchange.

In DIS experiments a lepton of energy E scatters on a nucleon of mass M and four-momentum P. Neutral-current (NC) DIS is mediated by γ^* and Z exchanges ($\ell N \to \ell X$) and charged-current (CC) DIS is mediated by $W^\pm$ exchanges ($\ell N \to \nu X$ or $\nu N \to \ell X$). The lepton-proton scattering is schematically shown in figure 2.2. The lepton breaks the proton apart and hadrons with a total invariant mass X are produced in the collision. The energy transfer Q in the reaction is determined from the initial and final lepton four momenta $k = (E, \mathrm{k})$ and $k' = (E', \mathrm{k}')$:

$$Q^2 = -q^2 = -(k-k')^2. \tag{2.11}$$

The lepton energy loss in the proton rest-frame can be defined as $\nu = \frac{q\cdot P}{M} = E - E'$. DIS is an inelastic process with the energy transfer much larger than the mass of the proton $Q^2 \gg M^2$. The inelasticity of the scattering is characterized by the fractional energy transfer $y = \frac{\nu}{E}$.

The neutral-current DIS cross-section for unpolarized electron-proton scattering can be written in terms of the inelasticity parameter $Y_\pm = 1 \pm (1-y)^2$:

$$\frac{d^2\sigma^{NC}_{e^\pm p}}{dxdQ^2} = \frac{2\pi\alpha^2}{xQ^4}\left[Y_+\tilde{F}_2 - y^2\tilde{F}_L \mp Y_- x\tilde{F}_3\right], \tag{2.12}$$

where the generalized structure functions $\tilde{F}_2$, $\tilde{F}_3$ and $\tilde{F}_L$ can be decomposed according to the contributions from pure photon exchange, pure Z boson exchange and from γZ interference:

$$\begin{aligned} \tilde{F}_2 &= F_2^\gamma - k_z v_e F_2^{\gamma Z} + k_z^2(v_e^2 + a_e^2)F_2^Z, \\ \tilde{F}_L &= F_L^\gamma - k_z v_e F_L^{\gamma Z} + k_z^2(v_e^2 + a_e^2)F_L^Z, \\ x\tilde{F}_3 &= k_z e_e x F_3^{\gamma Z} - k_Z^2 2 v_e a_e x F_3^Z, \end{aligned} \tag{2.13}$$

with

$$k_z = \frac{1}{4\sin^2\theta_W \cos^2\theta_W}\frac{Q^2}{Q^2 + M_Z^2}. \tag{2.14}$$

DIS is described by the quark-parton model. In this model the proton is considered not as a point-like particle, but as a composite object made of partons. The interaction is described as an elastic scattering of the lepton with a parton carrying a fraction x of the proton's momentum ($0 \leq x \leq 1$). The contribution of partons to the structure functions can be expressed in terms of the parton distribution functions (PDF) $f(x,Q^2)$, which express the probability of finding a parton that carries a momentum fraction between x and $x+dx$. The PDFs are not predicted by the parton model and must be determined experimentally. The main source of information about the proton structure comes from the F_2 electromagnetic structure function, which is proportional to a singlet quark density [23]:

$$\begin{aligned} F_2^{\gamma} &= x \sum_{i=q,\bar{q}} \mathrm{Q}_i^2 [f_i(x,Q^2)], \\ F_2^{\gamma Z} &= x \sum_{i=q,\bar{q}} 2\mathrm{Q}_i v_i [f_i(x,Q^2)], \\ F_2^{Z} &= x \sum_{i=q,\bar{q}} (v_i^2 + a_i^2) [f_i(x,Q^2)]. \end{aligned} \tag{2.15}$$

The structure function xF_3 arises from γZ interference. At leading order in QCD xF_3 is determined by the difference between the momentum distributions of the quarks and the anti-quarks and is therefore sensitive to the valence quark distributions:

$$\begin{aligned} F_3^{\gamma Z} &= \sum_q 2\mathrm{Q}_q \mathrm{v}_q [f_q(x,Q^2) - f_{\bar{q}}(x,Q^2)], \\ F_3^{Z} &= \sum_q 2a_q^2 \mathrm{v}_q^2 [f_q(x,Q^2) - f_{\bar{q}}(x,Q^2)]. \end{aligned} \tag{2.16}$$

In the naïve quark-parton model the longitudinal structure function F_L vanishes at leading order in QCD for spin 1/2 quarks.

One of the predictions of the parton model is that the structure functions $F_i(x,Q^2)$ scale, i. e. they become independent of Q^2 in the limit $Q^2 \to \infty$, with $\frac{\nu}{Q^2}$ fixed. This property, known as Bjorken scaling, is based on the assumption that the transverse momentum of the partons inside the proton is negligible. The development of QCD led to the prediction of a small deviation from scaling due to the radiation of hard gluons from quarks. According to this theory the lepton is not only scattered by the three valence quarks u_v, u_v, d_v, but also by gluons and the so-called sea of quark-antiquark pairs produced from a radiated gluon via $g \to q\bar{q}$. The radiation of gluons produces the evolution of the structure functions. At very high energies ($\lambda \ll r_p$) more and more gluons are radiated, which in turn split into $q\bar{q}$ pairs. This process leads to the growth of the gluon and the $q/\bar{q}$ sea density at small x. Due to gluon and (anti) quark emissions the longitudinal structure function in QCD differs from zero unlike the quark-parton model.

2.3.1 Factorization theorem and PDF evolution

The DIS cross-section, as well as other observables, can be calculated with the help of perturbation theory. Perturbative calculations rely on partons, whereas experimentally only hadrons are observed. Therefore a link is needed to connect the hadronic observables, which one measures, with perturbative calculations done at parton level. This link is provided by the factorization theorem, which states that the hadronic cross-section σ can be expressed as a convolution of the perturbatively calculable

partonic cross-section $\hat{\sigma}$ with the parton densities f_i:

$$\sigma = \sum \int dx f_i(x, \mu_f) \hat{\sigma}. \tag{2.17}$$

The factorization theorem expresses the fact that in certain kinematic regimes, the non-perturbative dynamics can be separated from the perturbative dynamics. The perturbative dynamics is associated with high energy scales (or short distances) while the non-perturbative dynamics is associated with low energy scales (or long distances). In those regimes one encounters ultraviolet (UV) divergences in the limit $Q \to \infty$ and infrared (IR) divergences in the limit $Q \to 0$. The UV divergences are absorbed by the renormalization procedure in the definition of the strong coupling, which acquires a dependence on the renormalization scale μ_R. Similarly, the IR divergences are absorbed in the definition of the parton densities which thus acquire a dependence on the factorization scale μ_F. Both the renormalization and factorization scales are not physical quantities so observable quantities such as the cross-section should be independent of μ_R and μ_F. This requirement leads to the so-called renormalization group equations [2]

$$\mu_{R,F} \frac{d\sigma}{d\mu_{R,F}} = 0. \tag{2.18}$$

Calculations that retain only a finite number of terms in the perturbative expansion display a residual dependence on μ_R and μ_F. Therefore in order to perform perturbative calculations, one has to determine these scales. To avoid large logarithms in the perturbation series, μ_R and μ_F are typically taken to be close to the hard scale of the interaction.

The long-distance part of the cross-section, encoded in the PDFs, is not calculable by perturbation theory and needs to be determined on an experimental basis. Perturbation theory can nonetheless predict the energy dependence of the PDFs, which is governed by the Dokshitzer-Gribov-Lipatov-Altarelli-Parisi (DGLAP) evolution equations [24–27]

$$\frac{\partial f_i(x, \mu_F^2)}{\partial \log \mu_F^2} = \frac{\alpha_s}{2\pi} \sum_j \int_x^1 \frac{dz}{z} P^{(1)}_{i \leftarrow j}(z) f_i\left(\frac{x}{z}, \mu_F^2\right). \tag{2.19}$$

An example of PDFs determined from DIS experiments at HERA is shown in figure 2.3. The valence quark distributions peak at around $x = 1/3$ as the naïve parton model predicts, however due to the interaction of the valence quarks with gluons, the distribution is smeared. One can also observe the rise of the gluon and sea-quark densities at low x.

The QCD factorization theorem states that the quark densities can be used universally for other proton scattering processes, such as Drell-Yan pair production. The PDFs determined by the DIS experiments do not cover the kinematic region (x, Q^2) of parton dynamics accessible at the LHC. This could potentially give rise to a large source of uncertainty, and limit the discovery potential for new physics. The data measured at the LHC can be included in addition to the DIS data in QCD fits to better constrain PDFs. Table 2.5 shows some LHC processes and their primary sensitivity to PDFs.

[2] From these equations one obtains in turn the expression for the running coupling and the DGLAP equations.

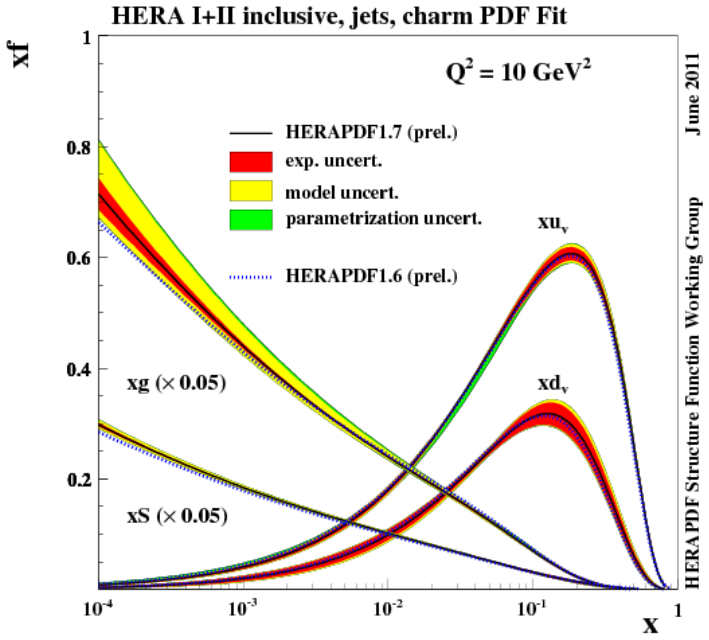

Figure 2.3: Parton distribution functions measured by the HERA experiments at $Q^2 = 10$ GeV^2, [28].

Process	Subprocess	Partons
$pp \to (Z \to \ell^+\ell^-)X$	$u\bar{u}, d\bar{d}, \ldots \to Z$	$u, d, \ldots$
$pp \to (\gamma^* \to \ell^+\ell^-)X$	$u\bar{u}, d\bar{d}, \ldots \to \gamma^*$	$\bar{q}$
$pp \to jet + X$	$gg, qg, qq \to 2j$	g, q
$pp \to (W^\pm \to l^\pm\nu)X$	$u\bar{d} \to W^+, d\bar{u} \to W^-$	$u, d, \bar{u}, \bar{d}$
$pp \to bbX$	$gg \to b\bar{b}$	g
$pp \to \gamma X$	$gq \to \gamma q, g\bar{q} \to \bar{q}$	g

Table 2.5: The LHC processes relevant to PDF determination, [22].

CHAPTER 3

Neutral-current Drell-Yan process in proton-proton collisions

The neutral-current Drell-Yan process [29] is the dominant way of Z boson production at the LHC. In leading order QCD (α_s^0), the process is defined as the annihilation of a quark-antiquark pair through an s-channel exchange of a gauge boson, which subsequently decays into a fermion pair. The interaction proceeds via the exchange of a virtual photon, a virtual Z boson, or the interference of these two processes. At leading order the Z boson can be produced either from the annihilation of a valence quark with a sea-quark or from the annihilation of two sea quarks. An illustration of the Drell-Yan process is shown in figure 3.1.

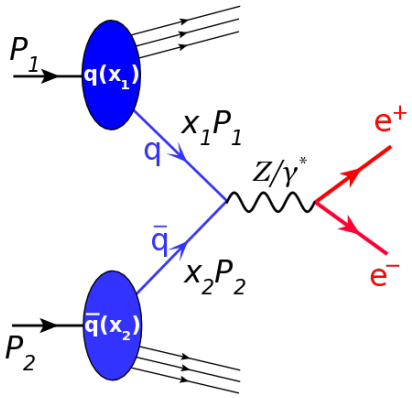

Figure 3.1: The Drell-Yan process.

The Drell-Yan process has been extensively studied at the LHC, the major measurements include the cross-section results from ATLAS and CMS experiments [30, 31]. The total cross-section of the neutral current Drell-Yan process has been measured at $\sqrt{s} = 7$ by the ATLAS experiment and found to be 27.94 nb [32]. The result of the measurement agrees well with the Standard Model predictions and is shown in figure 3.2 together with several other processes in pp collisions. The precision electroweak measurements on the Z resonance using data of electron-positron colliders LEP and SLC are summarized in [33]. At hadron colliders the Drell-Yan process has been explored in $p\bar{p}$ collisions at the CERN $Sp\bar{p}S$ and at the Tevatron.

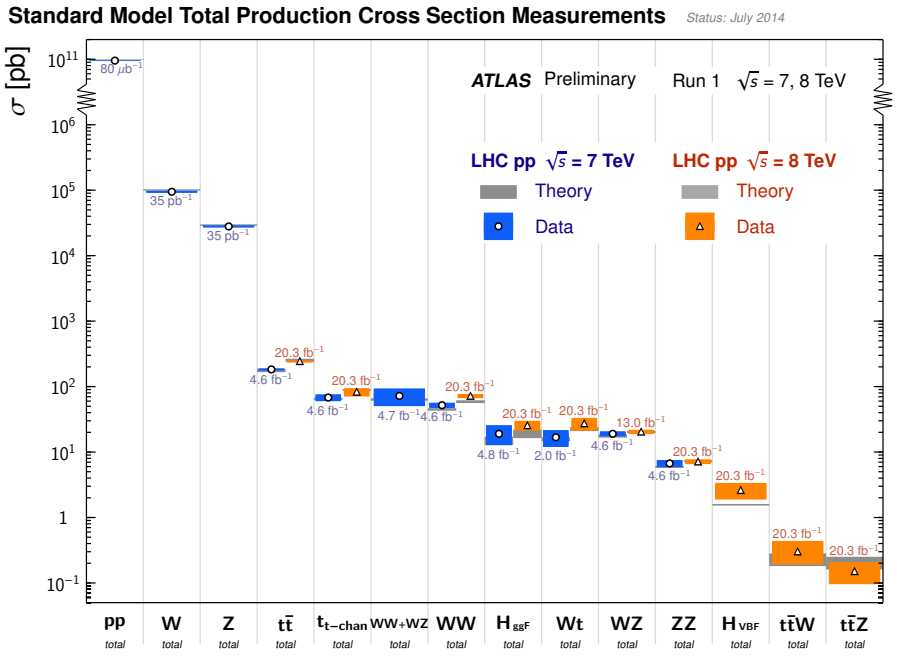

Figure 3.2: The Drell-Yan production cross-section measured by the ATLAS experiment at the LHC together with total proton-proton cross-section and measurement of number of hard processes, [34].

3.1 Kinematics of the Drell-Yan process in pp collisions

The center-of-mass energy of a proton-proton collision can be written in terms of the four-momenta of the colliding protons p_1 and p_2:

$$\sqrt{s} = \sqrt{(p_1 + p_2)^2}. \tag{3.1}$$

The quark and anti-quark carry fractions x_1 and x_2 of the colliding protons' momenta. The momentum transfer can be written as $Q^2 = (x_1 p_1 + x_2 p_2)^2$. If we neglect the parton masses, the momentum transfer is given by

$$Q^2 \approx x_1 x_2 s = \hat{s}. \tag{3.2}$$

The rapidity of a particle with a total energy E is given by

$$y = \frac{1}{2} \ln \frac{E + p_z}{E - p_z}, \tag{3.3}$$

where p_z is the component of momentum along the beam axis. The accessible rapidity range for the production of a Z boson is determined by the available center-of-mass energy and the Z mass:

$$|y_Z^{\max}| = \ln \frac{\sqrt{s}}{M_Z}. \tag{3.4}$$

Thus, for a center-of-mass energy of $\sqrt{s} = 8$ the Z boson can be produced in the rapidity range $|y_Z| \leq 4.47$. The rapidity of the boson is related to the momentum fraction carried by the initial

partons, and at LO can be written as:

$$x_{1,2} = \frac{M_Z e^{\pm y_Z}}{\sqrt{s}}. \tag{3.5}$$

This relation for the Z boson production at different center-of-mass energies is shown in figure 3.3. The invariant mass $M_{\ell\ell}$ of the final-state lepton pair with four-momenta p_1^ℓ and p_2^ℓ can be written as

$$M_{\ell\ell} = \sqrt{(p_1^\ell + p_2^\ell)^2}. \tag{3.6}$$

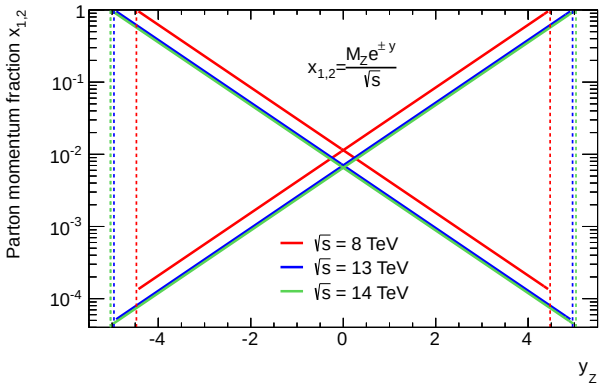

Figure 3.3: The relation between momentum fraction $x_{1,2}$ carried by annihilating partons and rapidity of the Z boson. Three center-of-mass energies of the proton collision are considred: $\sqrt{s}$ = 8 TeV, $\sqrt{s}$ = 13 TeV and $\sqrt{s}$ = 14 TeV. The vertical dashed lines denote accessible rapidity range for each of the three case.

When the difference between the momentum fractions carried by the interacting partons is large, the boson is produced with a large longitudinal momentum and high rapidity. The longitudinal momentum is transferred to the leptons. One can distinguish three topologies of the final state leptons with respect to their directions.

- The "central-central" topology is schematically shown in figure 3.4a. Two final-state leptons, produced by a boson with a relatively small rapidity, go to a region, which in termes of a detector structure is called "central".
- The "central-forward" topology of the final state lepton pair corresponds to higher rapidities of the Z/γ^* boson. While one of the leptons go to the "central" region another one is boosted more forward. This case is illustrated in figure 3.4b.
- The last option is the "forward-forward" topology, which correspond to large rapidities of the Z/γ^* boson. Both final-state leptons acquire large longitudinal momentum and directed to a "forward" region as shown in figure 3.4c.

The definition of the "central" and "forward" regions is driven by the ATLAS detector design described in section 4.2. The "central" region corresponds to a part of the detector covered by the tracking system, and the "forward" region is defined being beyond the tracking system, covered however by electromagnetic and hadronic calorimeters.

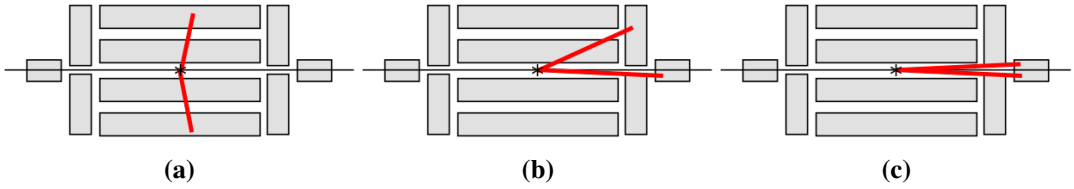

Figure 3.4: Configurations of the final-state dielectron pair in the neutral-current Drell-Yan process.

The subject of this thesis is the measurement of the central-forward configuration with dielectron final state. The experimentally accessible rapidity range of the exchanged gauge boson in this configuration is up to $|y_{Z/\gamma^*}| < 3.6$, while with the central-central topology the accessible rapidity range is limited to $|y_{Z/\gamma^*}| < 2.4$. The forward-forward topology is not measured with ATLAS due to experimental constrains.

Measuring the Drell-Yan cross-section in the forward rapidity region extends the kinematic (Q^2, x) plane towards lower and higher x as shown in figure 3.5, compare to a measurement at central rapidities which at $\sqrt{s} = 8$ TeV and a scale of the Z boson mass, $Q = M_Z$, covers x range of $1.03 \cdot 10^{-3} - 1.26 \cdot 10^{-1}$. The extended rapidity range $|y_{Z/\gamma^*}| < 3.6$ makes it possible to access lower and higher x values, which extend down to $x = 3.11 \cdot 10^{-4}$ and up to $x = 4.17 \cdot 10^{-1}$.

The directions of the outgoing leptons can be described with respect to the directions of the incoming quarks. Schematically it is shown in figure 3.6a with θ^* angle between the momenta of a lepton and a quark. The angle θ^* allows to classify events into two categories: forward and backward. Events where the lepton goes in the same direction as the incoming quark are classified as forward, while events where the lepton is going opposite to the quark direction are classified as backward. In the presented measurements the angular variable is defined with respect to the Collins-Soper frame [35], schematically shown in figure 3.6b. In this frame the $\cos\theta^*_{CS}$ is an angle between electron momenta and $\hat{z}$-axis, which bisects the angle between momentum of one of the partons and negative momentum of the other. In the Collins-Soper frame the angular variable is defined by

$$\cos\theta^*_{CS} = \frac{p_z^{\ell\ell}}{|p_z^{\ell\ell}|} \frac{2(p_1^+ p_2^- - p_1^- p_2^+)}{M_{\ell\ell}\sqrt{M_{\ell\ell}^2 + (p_T^{\ell\ell})^2}}, \tag{3.7}$$

with $p_i^{\pm} = \frac{1}{\sqrt{2}}(E_i \pm p_{Z,i})$

In a pp collision it is unknown from which of the two protons the quark (antiquark) originates. Moreover when the transverse momentum of the dilepton pair is non-zero the longitudinal direction of the center-of-mass of the $q\bar{q}$ system is also unknown. Experimentally the quark direction in a $q\bar{q}$ annihilation process is determined on a statistical basis. While the annihilating antiquark is from the quark sea, the quark is typically a valence quark. The assumption is that the dilepton system is boosted in the direction of the incoming valence quark, which on average carries a higher momentum fraction than the sea quark [36, 37]. The sign of the longitudinal momentum of the dielectron pair reflects this assumption in the $\cos\theta^*_{CS}$ definition (equation 3.7).

3.2 The differential cross-section

The Drell-Yan cross-section can be studied in multiple dimensions. Information on electroweak and QCD effects can be extracted by studying the cross-section as a function of the dilepton invariant

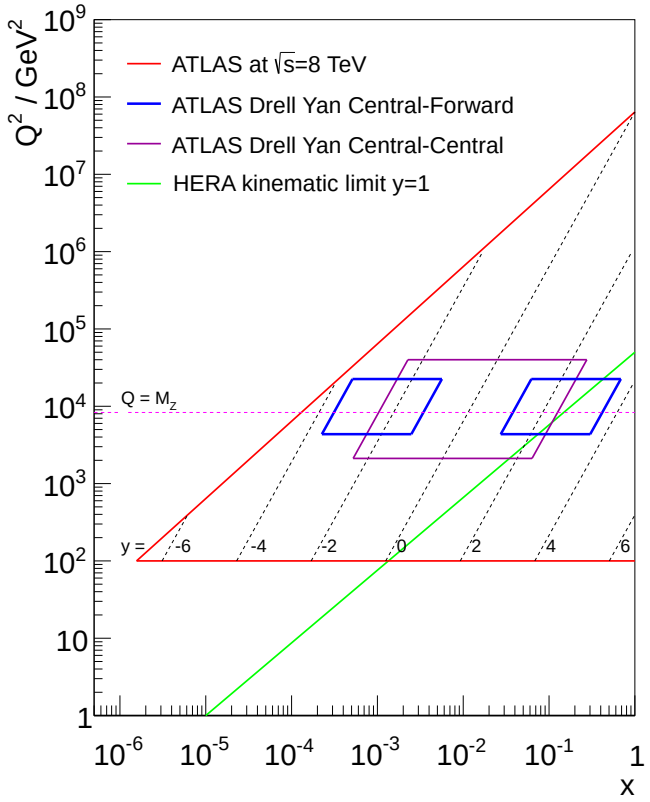

Figure 3.5: Kinematic plane in Q^2, x bins. The ATLAS kinematic limit is shown at $\sqrt{s} = 8$ TeV, according to formulas 3.4, 3.5. The Drell-Yan kinematic coverage is shown for the case of the central boson rapidity ($|y_Z| < 2.4$), with dilepton invariant mass $46 < M_{\ell\ell} < 200$ GeV. The forward rapidity Drell-Yan kinematic is defined for the measurement with $1.2 < |y_Z| < 3.6$ and $66 < M_{\ell\ell} < 150$ GeV. Small values of x with negative rapidities corresponds to high values of x with positive y. That splits the kinematic region of the forward Drell-Yan measurement into two parts. The kinematic region of HERA experiments is below the inelasticity limit of $y = 1$.

mass, Z/γ^* boson rapidity and $\cos\theta^*$, which at leading order, can be written as

$$\frac{d^3\sigma}{\mathrm{d}M\ \mathrm{d}y_{Z/\gamma^*}\ \mathrm{d}\cos\theta^*} = \frac{\pi\alpha^2}{3Ms}\sum_q \left(P_q^\gamma + P_q^{\gamma Z}\frac{2M^2(M^2-M_Z^2)}{(M^2-M_Z^2)^2+\Gamma_Z^2M_Z^2} + P_q^Z\frac{M^4}{(M^2-M_Z^2)^2+\Gamma_Z^2M_Z^2}\right)\cdot \cdot \left[F_q\left(x_1,Q^2\right)F_{\bar{q}}\left(x_2,Q^2\right)+(q\leftrightarrow\bar{q})\right], \tag{3.8}$$

where

$$P_q^\gamma = Q_l^2Q_q^2\left(1+\cos^2\theta^*\right), \tag{3.9}$$

$$P_q^{\gamma Z} = \frac{Q_lQ_q}{\sin^2\theta_W\cos^2\theta_W}\left[\mathrm{v}_l\mathrm{v}_q(1+\cos^2\theta^*)+2a_la_q\cos\theta^*\right], \tag{3.10}$$

$$P_q^Z = \frac{1}{\sin^4\theta_W\cos^4\theta_W}\left[(\mathrm{v}_l^2+a_l^2)(\mathrm{v}_q^2+a_q^2)+8\mathrm{v}_la_l\mathrm{v}_qa_q\cos\theta^*\right]. \tag{3.11}$$

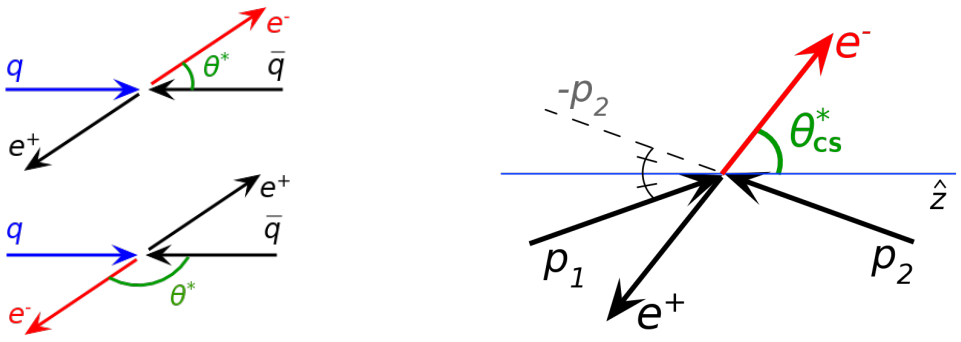

(a) **(b)**

Figure 3.6: Angle θ^* between the incoming anti-quark and lepton (a), the top configuration is denoted as "forward" and bottom as "backward". θ^*_{CS} angle in the Collins-Soper frame (b).

The measurement of the Drell-Yan production cross-section as a function of the dilepton invariant mass $M_{\ell\ell}$ and boson rapidity is important for constraining the PDF distributions, as is explained in the following.

Photon and Z boson exchanges dominate in different regions of the $M_{\ell\ell}$ spectrum as shown in figure 3.7. At low and high mass regions (below and above the Z mass peak) the cross-section is dominated by virtual photon exchanges. The Z boson exchange forms a peak near the Z boson mass. The contribution due to γZ interference is small over the entire mass range and vanishes at the Z pole.

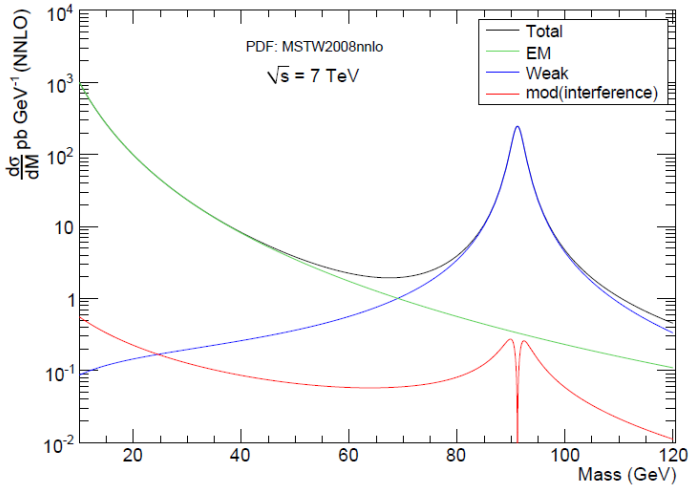

Figure 3.7: The DY cross-section at $\sqrt{s} = 7$ TeV with the contributions from the pure Z and γ production and interference of those two processes. [38]

The contribution of quark-antiquark annihilation is different for photon and Z boson production due to the different coupling constants of the photon and Z boson to quarks. The direct relation of the boson rapidity to the momentum fraction carried by the partons, given by equation 3.5, allows to ob-

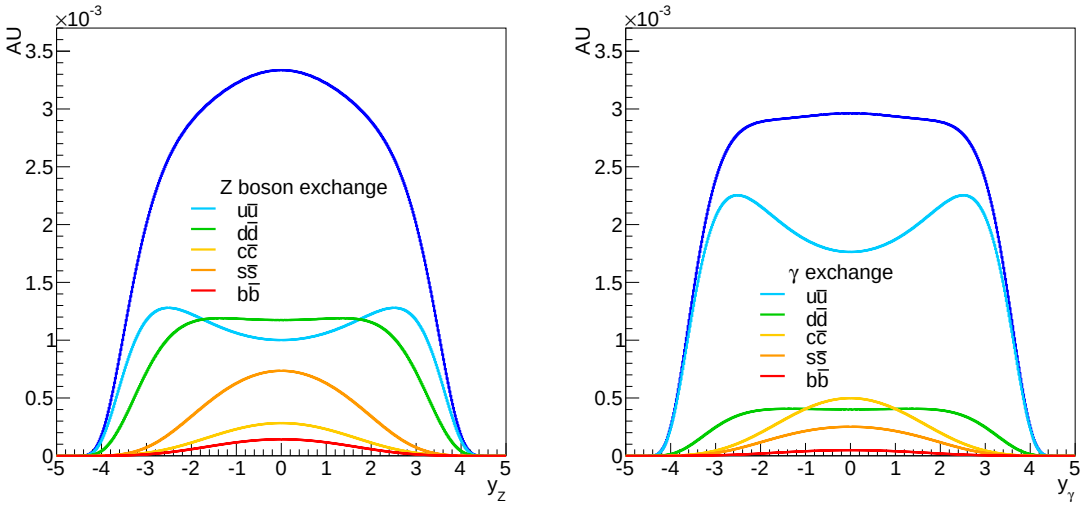

Figure 3.8: Flavor decomposition of the Neutral Current Drell-Yan production as a function of boson rapidity at $\sqrt{s} = 8$ TeV via Z boson (left) and photon (right) exchange.

tain the flavor decomposition for the two processes as a function of the rapidity of the produced boson (figure 3.8). The process mediated by the photon exchange arises dominantly from the annihilation of $u\bar{u}$ quarks, where u can be either a valence or a sea-quark. The contribution from $d\bar{d}$ annihilation is smaller since the coupling of the photon to quarks is proportional to the electric charge (table 2.3, equation 3.9). Measuring the Drell-Yan cross-section in the low and high invariant mass regions allows to improve the knowledge of the $\bar{u}$ distribution obtained from DIS experiments. The region under the Z-peak provides information about the valence quarks, $\bar{u}$, $\bar{d}$ and the fraction of strange-to-down quarks. An example of an analysis using Drell-Yan data to obtain constraints on proton PDFs can be found in Appendix A.

Measuring the cross-section as a function of $\cos\theta^*$ is important for extracting of the Forward-Backward asymmetry and weak mixing angle as is explained in the next section. The cross-section calculated in different $\cos\theta^*$ bins, shown in figure 3.9, depends on the sub-processes contributions.

3.3 Forward-Backward asymmetry

Due to the V-A nature of the electroweak interactions the Drell-Yan production cross-section is not symmetric with respect to the angular distribution θ^*. Namely, due to the different couplings of left and right-handed fermions to the weak currents, the directions of the final state leptons are asymmetric with respect to the initial quark directions.

The asymmetry can be quantified using the relative change of the integrated cross-sections for forward and backward events:

$$A_{FB} = \frac{\sigma_F - \sigma_B}{\sigma_F + \sigma_B}, \tag{3.12}$$

where $\sigma_F = \int_0^1 \frac{d\sigma}{d\cos\theta^*} d\cos\theta^*$ and $\sigma_B = \int_{-1}^0 \frac{d\sigma}{d\cos\theta^*} d\cos\theta^*$. In terms of the vector and axial vector

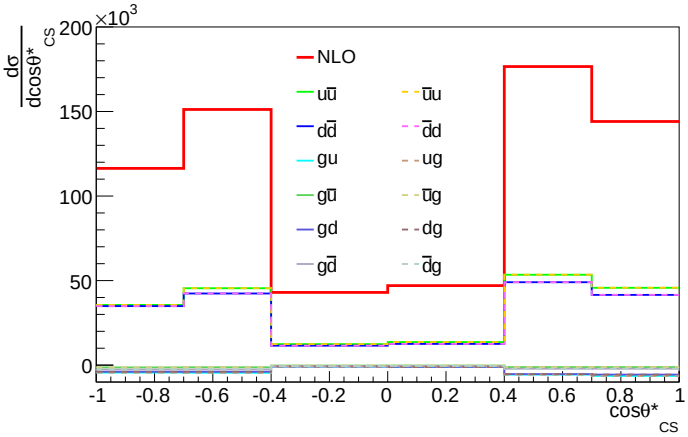

Figure 3.9: Flavor decomposition of the Neutral Current Drell-Yan production as a function of $\cos\theta^*_{CS}$ at $\sqrt{s} = 8$ TeV for the central-forward configuration, calculated with the MCFM and APPLGRID programs.

fermion couplings the A_{FB} asymmetry can be expressed as

$$A_{FB} = \frac{3A_1}{8A_0}, \tag{3.13}$$

with

$$\begin{aligned} A_0 &= Q_q^2 Q_\ell^2 + 2\mathrm{Re}[\chi] Q_q Q_l v_q v_\ell + |\chi|^2 (v_q^2 + a_q^2)(v_\ell^2 + a_\ell^2), \\ A_1 &= 4\mathrm{Re}[\chi] Q_q Q_\ell a_q a_\ell + 8|\chi|^2 v_q a_q v_\ell a_\ell, \end{aligned} \tag{3.14}$$

where χ is the ratio of the coefficients of the Z and photon amplitudes, Q represents the charge of a quark q or a lepton ℓ, and v and a the corresponding vector and axial vector couplings.

The asymmetry in (3.8) arises from the terms proportional to $\cos\theta^*$. Pure photon exchanges do not lead to an asymmetry. Above and below the Z mass peak the main contribution to the asymmetry arises from γ/Z interference. At the Z pole the interference term vanishes and the asymmetry is only due to pure Z exchange. The asymmetry here is small due the small value of the vector coupling of charged leptons to the Z boson (table 2.4).

The A_{FB} dependence on y_{Z/γ^*} arises from the assumptions involved in the determination of $\cos\theta^*_{CS}$ (see section 3.1). At low rapidities ($|y_{Z/\gamma^*}| \sim 0$) the difference between the quark momentum fractions x_1 and x_2 is small, as illustrated in figure 3.3. This increases the probability that in valence-sea quarks interaction the sea quark carries bigger momentum fraction than the valence quark. In this regime the Z/γ^* boson is boosted in the direction of the sea, and not valence quark, thus the sign of $\cos\theta^*_{CS}$ will not be determined correctly. This in turn reduces the measured asymmetry (dilution effect). A similar effect appears when a sea-sea quarks pair annihilate into the Z/γ^* boson, and a judgment of the initial quark directions is not possible. At higher rapidities, the difference between x_1 and x_2 grows, and the probability that the Z/γ^* boson originates from a valence-sea pair increases (see figures 3.8). That ensures that the directions of the quarks are defined correctly. The dependence of A_{FB} on the dilepton invariant mass and the reduction of A_{FB} at low rapidities is illustrated in figure 3.10.

The Forward-Backward asymmetry has been intensively studied in hadron and electron-positron collider experiments. The measurement of the asymmetry is traditionally domain of e^+e^- colliders,

where high precision of the measurement can be archived in study of $e^+e^- \to f^+f^-$ processes. At the LHC the asymmetry has been measured double-differentially as a function of mass and rapidity up to $|y_{Z/\gamma^*}| = 2.4$ by the CMS experiment [39], and single-differentially as a function of mass including the forward regions with $|y_{Z/\gamma^*}|$ up to 3.6 by the ATLAS experiment [40].

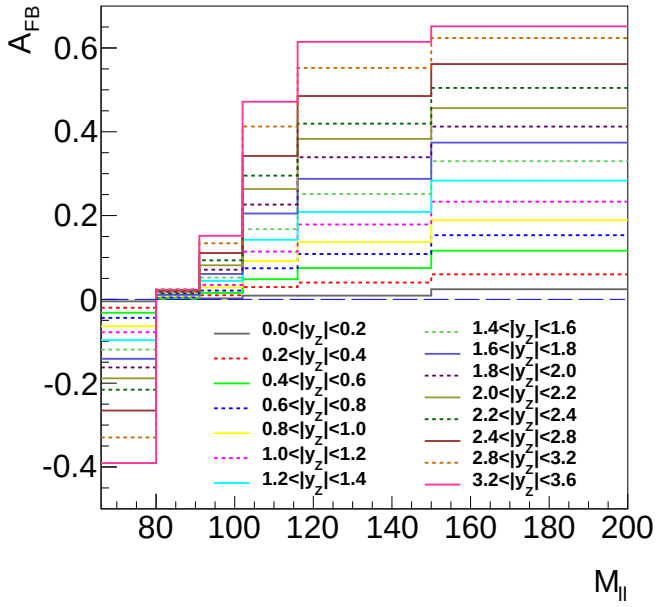

Figure 3.10: The Forward-Backward asymmetry simulated with MCFM and APPLGRID as a function of $M_{\ell\ell}$ and $|y_{Z/\gamma^*}|$.

The dependence of the A_{FB} distribution on the vector and axial-vector couplings makes it sensitive to the Weinberg angle. At tree level the relation between the Weinberg angle and the vector and axial vector couplings takes the form

$$\frac{v_f}{a_f} = 1 - \frac{2Q_f}{T_3^f} \sin^2\theta_W = 1 - 4|Q_f| \sin^2\theta_W. \tag{3.15}$$

When weak radiative corrections are taken into account this expression is modified to give an effective weak mixing angle $\sin^2\theta_W^{\text{eff}}$. Experimentally $\sin^2\theta_W^{\text{eff}}$ can be determined from the Forward-Backward asymmetry. This is accomplished either by fitting the measured A_{FB} distribution to templates derived from simulation with different values of θ_W, or by including θ_W in the PDF fit as a free parameter. The measurement of the Weinberg angle is an important test of the Standard Model, as a deviation from the predicted value can be a sign of new physics [36]. The comparison of the experimentally measured values of $\sin^2\theta_W^{\text{eff}}$ is shown in figure 3.11, including the two most accurate measurements from LEP and SLC [33]. Preliminary results from the ATLAS measurement at $\sqrt{s} = 7$ TeV indicate that the central-forward configuration has a higher sensitivity to the weak mixing angle value compared to the central-central measurement (figure 3.12).

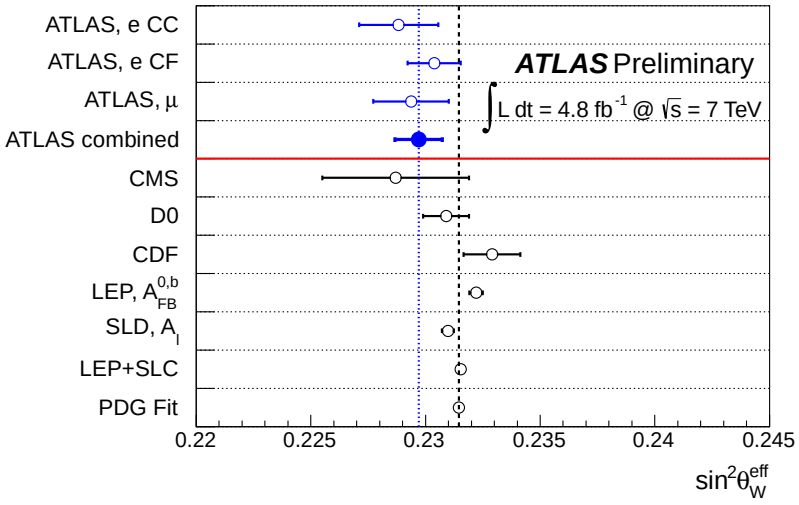

Figure 3.11: Comparison of the $\sin^2\theta_W^{\text{eff}}$ measurements from LEP, SLC, Tevatron and LHC, including the PDG global fit, [40].

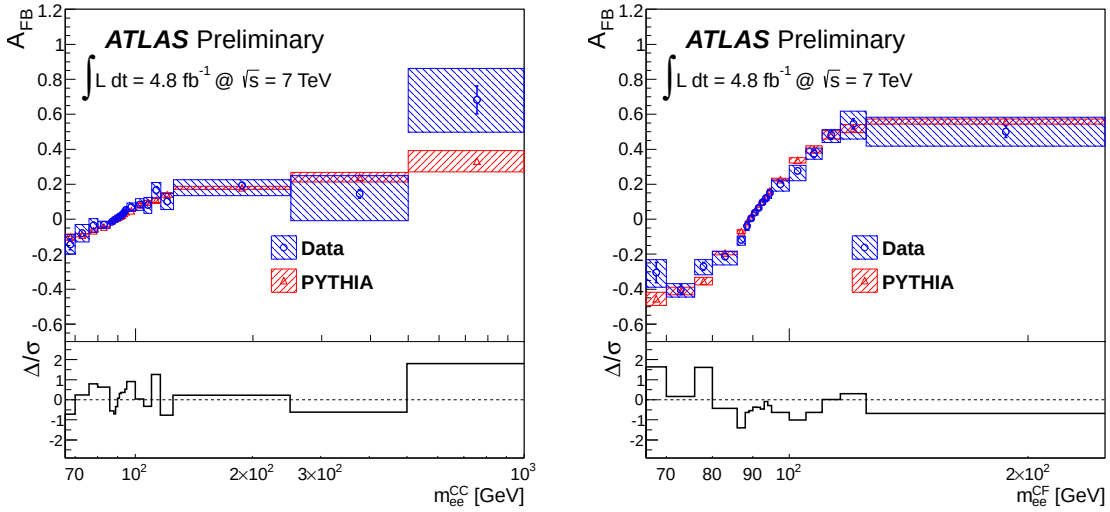

(a) **(b)**

Figure 3.12: A_{FB} distributions before correction for dilution effects, measured in the central-central (a) and central-forward (b) electron channels. [40].

Experimental setup

CHAPTER 4

The Large Hadron Collider (LHC) and the ATLAS experiment

4.1 The LHC and accelerator complex

The Large Hadron Collider is a synchrotron accelerator designed to accelerate protons and lead ions (Pb^{82+}). The LHC is designed to study a number of modern theories and hypotheses in high energy physics. Among them are the Higgs mechanism, supersymmetry, dark matter, matter-antimatter asymmetry, the quark-gluon plasma properties in heavy-ion collisions and exotic theories beyond the Standard Model.

To achieve the center-of-mass energy of 8(14) TeV the protons go through a chain of accelerators as shown in figure 4.1a. Protons are obtained from the ionization of hydrogen gas. The Linac2 is the starting point of the proton acceleration, here the protons reach an energy of 50 MeV. Then they enter the Proton Synchrotron Booster (PSB) and are accelerated to 1.4 GeV. After circulating in the Proton Synchrotron (PS) the protons reach an energy of 25 GeV. The last step before the injection to the LHC is the beam acceleration to the energy of 450 GeV by the Super Proton Synchrotron (SPS).

Particles circulate in the LHC in bunches. Under nominal operating conditions each proton beam has 2808 bunches, consisting of about 10^{11} protons each, with a bunch spacing of 25 ns.

Lead ions go through a similar chain of accelerators, although there are specifics related to the heating, atomization and ionization of lead atoms.

The LHC consists of a 27-kilometer ring made of 8 arcs and 8 insertions as shown in figure 4.1b. The beams circulate in two vacuum pipes in opposite directions. Electromagnetic devices are used to form the trajectory and bunch size. Dipole magnets keep the particles in circular orbits. Quadrupole magnets focus the beam. The accelerating cavities are electromagnetic resonators that accelerate particles and then keep them at a constant energy by compensating for energy losses.

There are seven experiments installed at the LHC:

- ALICE - A Large Ion Collider Experiment [41],
- ATLAS - A Toroidal LHC ApparatuS [30],
- CMS - the Compact Muon Solenoid [31],
- LHCb - the Large Hadron Collider beauty [42],
- LHCf - the Large Hadron Collider forward [43],

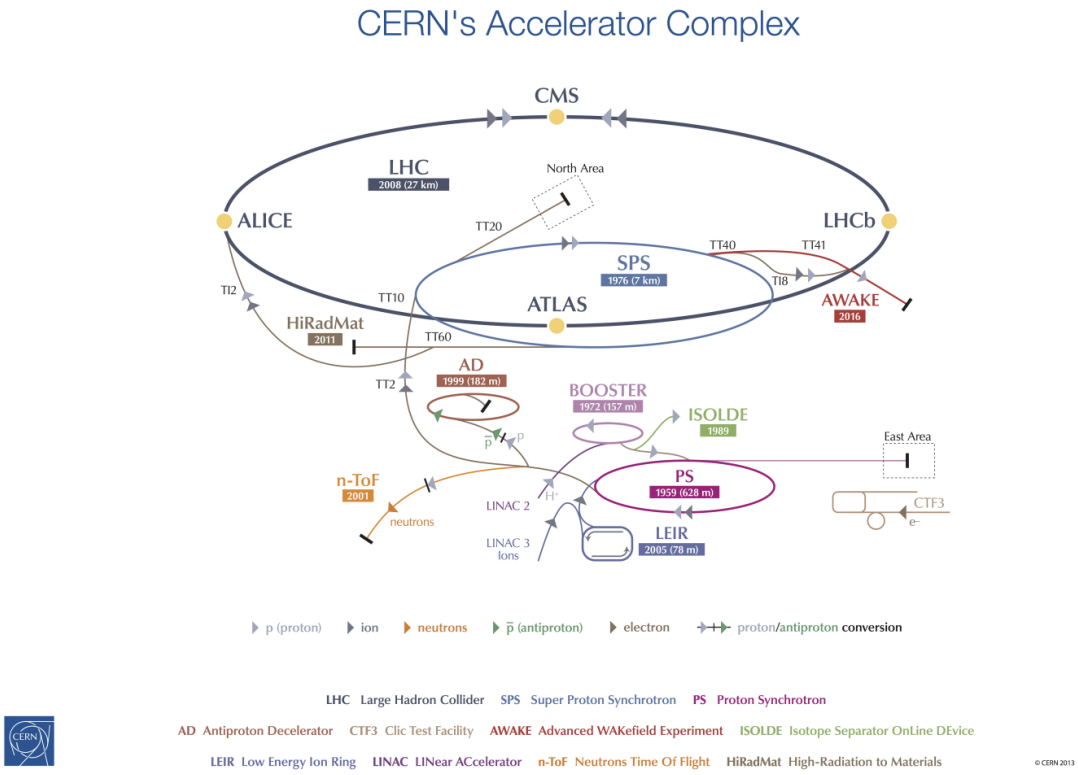

(a)

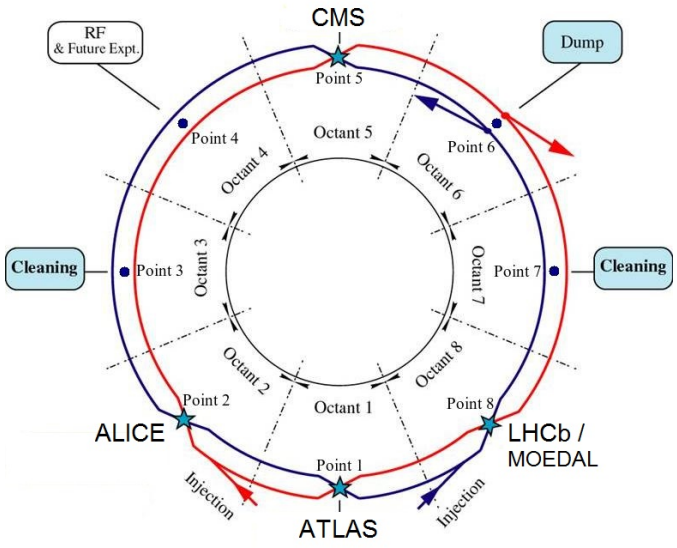

(b)

Figure 4.1: The CERN's accelerator complex (a) [44] and the LHC ring (b), adapted from [45].

- TOTEM - the TOTal Elastic and diffractive cross-section Measurement [46],
- MoEDAL - the Monopole and Exotics Detector at the LHC [47].

CMS and ATLAS are general purpose detectors designed to study a wide range of physical phenomena. ALICE is a detector specialized in analyzing ion collisions. It is designed to study the physics of the quark-gluon plasma formation. The LHCb experiment specializes in the study of the asymmetry between matter and antimatter present in the interactions of B hadrons. The LHCf experiment uses forward particles to study cosmic rays. The TOTEM experiment focuses on the proton effective cross-section measurements and the monitoring of the LHC luminosity using forward particles. The prime motivation of MoEDAL is to search directly for magnetic monopoles - hypothetical particles with a magnetic charge.

ALICE, ATLAS, CMS and LHCb are installed at four collision points of the LHC beam. TOTEM is installed close to the CMS interaction point and LHCf is installed near ATLAS. MoEDAL shares the cavern at Point 8 with LHCb.

4.2 The ATLAS experiment

ATLAS is a general purpose detector designed to measure a wide range of signals from the production and decay of particles, rather than focusing on a specific physical process. This ensures that, regardless of the specific form of a new physical process or particle, ATLAS will be able to detect and measure its properties.

The physics goals and the signatures of the particles produced in the collision put specific requirements on the detector design. Charged particles leave ionization tracks and their trajectory changes when they pass through a magnetic field. Neutral particles leave no tracks, but interact with the calorimeter material creating showers of secondary particles. Muons penetrate behind the calorimeter system and their path can be determined by additional tracking information coming from the outer detector systems. Neutrinos escape the detector without interactions; their signature is the missing energy in the collision. Short-lived particles decay fast, and can be studied only by their decay products. B hadrons travel a distance of the order of 1 mm, after which they decay producing secondary vertices. Thus vertex detectors close to the interaction region are required in order to observe secondary vertices. The momentum of charged particles needs to be measured with good resolution and with a high reconstruction efficiency. Very good identification and energy measurement of electrons, photons and hadrons is expected from the calorimetry. Muon detection and momentum measurements should be provided by muon spectrometer. The LHC operation conditions require fast, radiation-hard electronics and sensor elements.

The ATLAS detector layout is shown in figure 4.2. Three subdetector systems are used for particle detection. The innermost part of the detector is the tracking system. It is comprised of the Pixel detector, silicon microstrip (SCT) and transition radiation (TRT) trackers. All of the system, called inner detector, is immersed in a 2 T solenoidal magnetic field. Here the charge and momentum of charged particles are measured. The calorimetric system is comprised of electromagnetic and hadronic calorimeters. Electron, photon and hadron energies are measured here. The outermost part of the detector is the muon system, designed to detect muons and measure their momenta. Identifying interesting evens and transferring those events from the detector read-out to the mass storage is the responsibility of the trigger and data acquisition system, collectively called TDAQ.

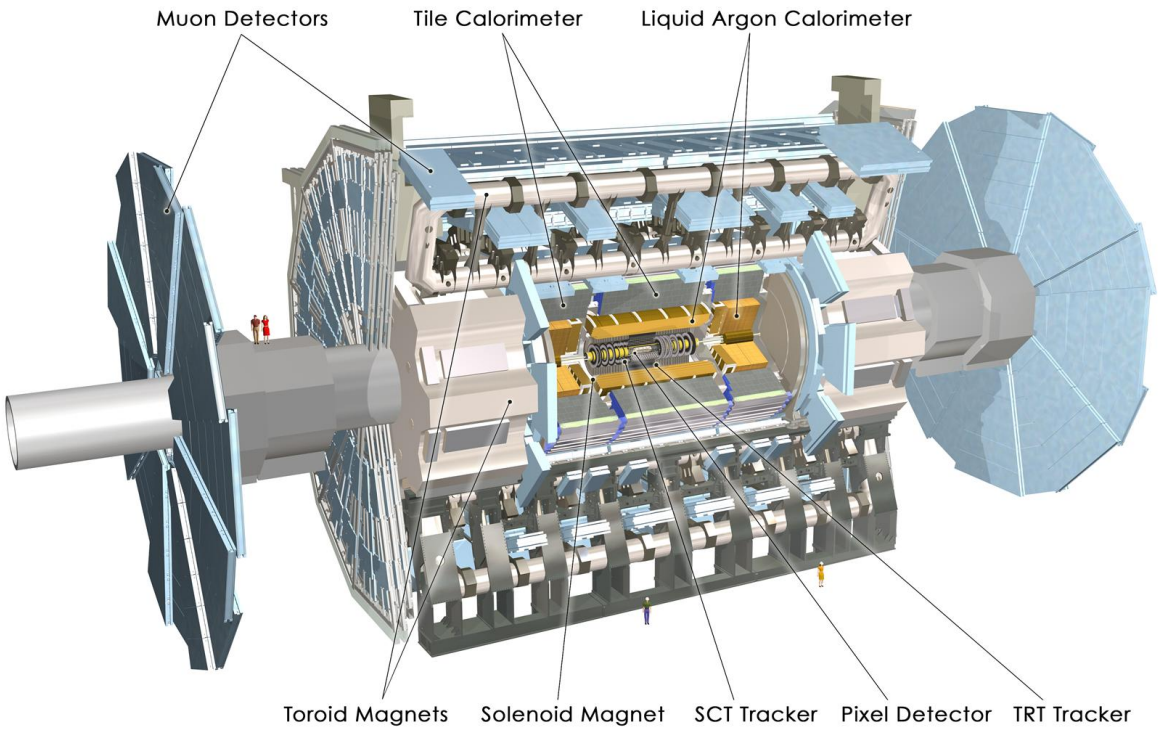

Figure 4.2: A computer generated image of the ATLAS detector, [48].

In the forward detector region three smaller systems are installed. Two systems which determine the luminosity delivered to ATLAS, LUCID (LUminosity measurement using Cerenkov Integrating Detector) and ALFA (Absolute Luminosity For ATLAS). The third system is the Zero-Degree Calorimeter (ZDC) which determines the centrality of heavy-ion collisions.

ATLAS uses a right-handed coordinate system with the origin at the interaction point. The beam direction defines the z-axis, the x-axis points to the center of the LHC ring and the positive y-axis is defined as pointing upwards. Cylindrical coordinates (r, ϕ) are used in the transverse plane, ϕ being the azimuthal angle. The pseudorapidity is defined in terms of the polar angle θ as $\eta = -\ln(\tan(\theta/2))$. The transverse momentum p_T, transverse energy E_T, and the missing transverse energy E_T^{miss} are defined on the $x-y$ plane. ATLAS is forward-backward symmetric with respect to the interaction point.

4.2.1 Inner detector

The ATLAS Inner Detector provides charged-particle tracking with high efficiency over the pseudorapidity range $\eta < 2.5$. A particle crosses three layers of pixel detectors, then eight layers of silicon strips comprising the SCT. The TRT detector provides a large number of hits (in average 36). The passage of the particle through the inner detector is shown in figure 4.3. The position and momentum is required to be measured with minimum energy losses to allow for a precise energy measurement by the calorimeter system.

The highest granularity is achieved around the vertex region using a silicon pixel detector. Ap-

proximately 80 million pixels, each with individual readout chips, are used. Each pixel module consists of a top silicon layer and a lower layer of electronics. The chips include buffering to store the data while awaiting the level-1 trigger decision. In the barrel region the Pixel detector is arranged in concentric cylinders around the beam axis while in the end-cap regions, the pixels form disks perpendicular to the beam axis. When a charged particle traverse the silicon layer it ionizes the silicon molecules. The movement of electron-hole pairs cause elecrical current detected by readout electronics.

The pixel detector is surrounded by the SCT. The SCT is composed of four layers of silicon strips. The SCT modules are double sided, thus providing two hits in each layer. In the end-cap regions nine forward discs are located on each side. The SCT works in a similar way to the pixel detector, using the ionization of the silicon for particle detection. The SCT has 6.3 million readout channels. The SCT detector contributes to the measurement of momentum, impact parameter and vertex position.

The outer part of the inner detector is the TRT, which consists of many layers of straw tube elements interleaved with transition radiation material. Each straw is 4 mm in diameter, more than one meter long and filled with a gas mixture (xenon, carbon dioxide, oxygen). Inside each straw, thin gold plated tungsten wires are located, which work as anodes. The inner part of the straws is covered with conducting material, and works as a cathode. The voltage difference between the anode and the cathode is a few kV. The space between the straws is filled with a material with widely varying indices of refraction, which cause charged particles to produce transition radiation. Thus, when a charged particle passes through the material between the tubes photons are produced. When the particle enters the tube it is accompanied by radiated photons. The particle and the produced photons interact with the molecules in the gas, freeing electrons, which move towards the anode, where the current is measured. The amount of the transition radiation depends on the mass of particle. An electron, for example, radiates far more photons than a pion, so more gas electrons are liberated and measured by the electronics. The precision per point of the straw hits is lower compared to the silicon detectors. However, due to the large number of measurements, the TRT detector contributes significantly to the determination of a particle's momentum. The TRT straws in the barrel region are parallel to the beam axis and straws in the end-caps region are arranged radially in wheels.

4.2.2 Calorimeters

The ATLAS calorimetry system consists of electromagnetic (EM) and hadronic sub-detectors. The electromagnetic calorimetry is comprised of the Liquid Argon (LAr) EM calorimeter and the first module of FCal (Forward calorimeter). The energies of hadrons are measured by the hadronic calorimeter which is divided into two parts: the Tile and the end cap (HEC). In the forward region, the energies of hadrons are measured by two FCal modules. The general structure of the ATLAS calorimeters is shown in figure 4.4.

The ATLAS Level-1 calorimeter trigger uses reduced-granularity information from all the ATLAS calorimeters. The calorimeter trigger electronics has a fixed latency of about 1 ms, using programmable custom-built digital electronics.

Electromagnetic calorimeter

The EM calorimeter consists of a barrel part (EMB) and two symmetric end-caps (EMEC). The EMB is made of two half-barrels centered around the z-axis and covers the pseudorapidity region $|\eta| < 1.475$. The EM end-caps are mechanically divided into two coaxial wheels. The outer wheel covers the region $1.375 < |\eta| < 2.5$ and the inner wheel covers the region $2.5 < |\eta| < 3.2$.

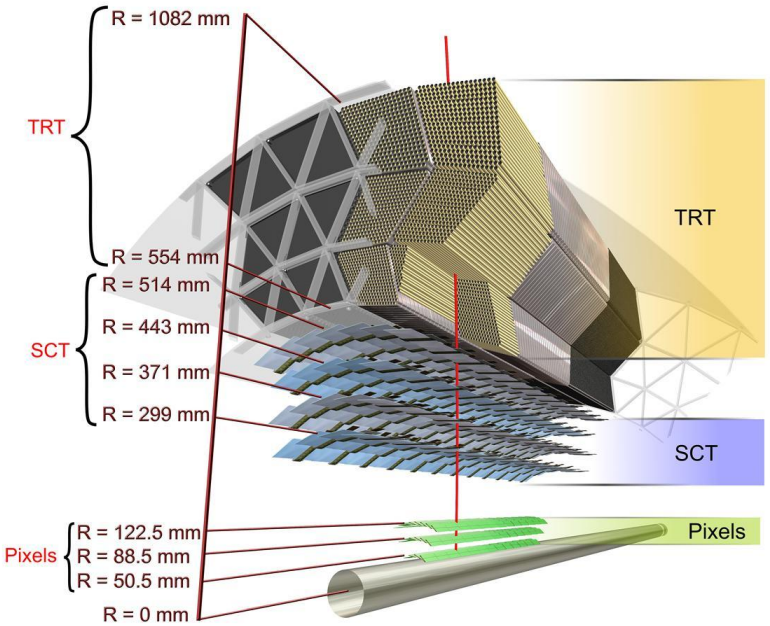

Figure 4.3: Scheme of the ATLAS inner detector barrel being crossed by a high-energy particle, [49].

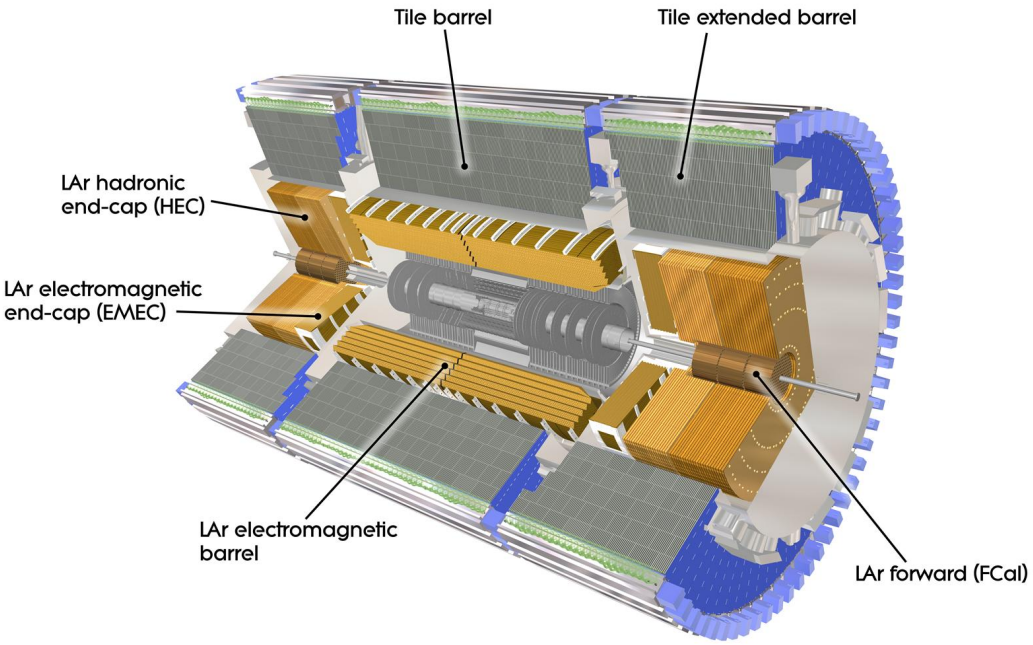

Figure 4.4: A computer generated image of the ATLAS calorimeter system, [50].

The calorimeter has an accordion-shape structure, which provides complete ϕ coverage without azimuthal cracks and fast signal read-out. It consists of a dense absorbing material and an active material to produce an output signal proportional to the input energy. The absorbing material of the EM calorimeter is lead and stainless steel. The gaps between the absorber layers are filled with liquid argon, which acts as the active material. The readout electrodes are located in the gaps between the absorbers and consist of three conductive copper layers separated by insulating polyimide sheets.

The EM calorimeter is designed to measure the energies of electrons and photons. The main mechanism of energy-loss for a high-energy electron passing through a medium is Bremsstrahlung. The electron decelerates losing kinetic energy which causes the emission of photons. High-energy photons lose energy in the material primarily by e^+e^- pair production. Thus a high-energy electron or photon initiates an electromagnetic cascade in the EM calorimeter by producing electron pairs and photons with lower energies. The rate of energy loss depends on the absorber material, which is characterized by its stopping power, and on the energy of the passing particle.

The width of the absorber is measured in radiation lengths X_0, the distance after which an electron looses all but $1/e$ of its energy. After n radiation lengths the total number of particles present in the EM cascade can be approximated as 2^n. The average energy of a shower particle at depth n is then $E(nX_0) = E_0/2^n$, where E_0 is the initial energy of the particle. When the energies of the particles in the cascade drop to the critical energy E_c (the energy at which the losses due to Bremsstrahlung become equal to the losses due to ionization) the shower attains the maximum number of particles, $E_c = E_0/2^{n_{max}}$,

$$n_{max} = \log_2(E_0/E_c) = \frac{\ln(E_0/E_c)}{\ln 2}. \tag{4.1}$$

Within the region with $|\eta| < 1.8$, a presampler detector is used to correct for energy losses in front of the calorimeter. The presampler consists of an active LAr layer of thickness 1.1 cm (0.5 cm) in the barrel (end-cap) region.

Over the central pseudorapidity region ($\eta < 2.5$), the EM calorimeter is segmented in three sections in depth (figure 4.5). The first sampling layer has a depth of 4.3 radiation lengths. It has very fine granularity in η and a relatively coarser granularity in ϕ: $\Delta\eta \times \Delta\phi = 0.0031 \times 0.098$. The high granularity of this layer allows to distinguish energy deposits of photons from converted pions $\pi^0 \to \gamma\gamma$. The second sampling absorbs the majority of the electron and photon energy and has a length of 16 X_0. It is segmented into cells of size $\Delta\eta \times \Delta\phi = 0.0245 \times 0.025$. The third sampling layer is reached only by high energy particles. The cell size is $\Delta\eta \times \Delta\phi = 0.05 \times 0.025$. The end-cap inner wheel is segmented in two sections in depth and has a coarser lateral granularity than the rest of the acceptance.

Hadronic calorimeters

In the region $|\eta| < 3.2$ the hadronic calorimetry is comprised of the Tile and HEC calorimeters.

The Tile calorimeter is made of scintillating tiles which act as active material and steel plates which act as absorbers. It is divided into four partitions, two barrels and two extended barrels, covering the pseudorapidity region $|\eta| < 1.7$. When a particle produced in an interaction of a hadron with the absorber goes through the scintillator it causes luminescence. The radiated photons are read out with wavelength shifting fibres to photomultipliers placed outside of the calorimeter. The tiles are grouped in cells of different size depending on their pseudorapidity and depth. The calorimeter is divided in three layers and the dimensions of the cells are optimized to obtain a structure

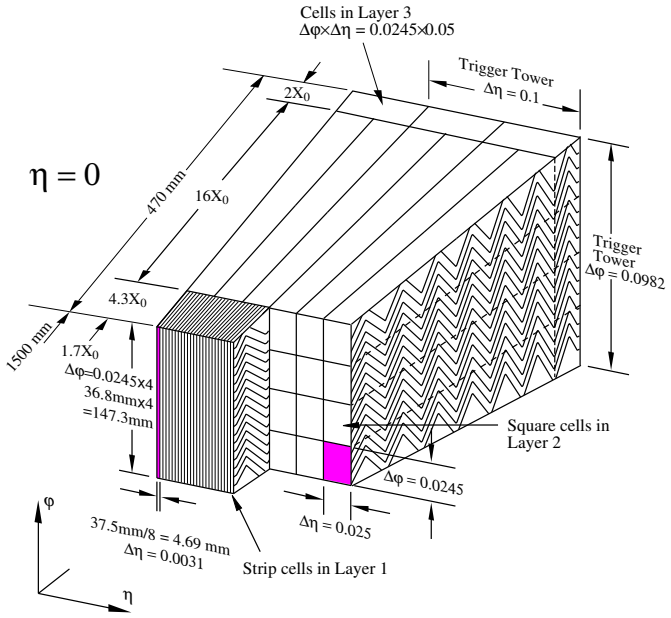

Figure 4.5: The structure of a barrel module of the EM accordion calorimeter, [30].

of towers. The first two layers provide a granularity $\Delta\eta \times \Delta\phi = 0.1 \times 0.1$, and the last layer provides a granularity of $\Delta\eta \times \Delta\phi = 0.2 \times 0.1$. A geometry of a Tile module is sketched in figure 4.6.

The HEC is designed to provide coverage for hadronic showers in the range $1.5 < |\eta| < 3.2$. The HEC is a liquid argon sampling calorimeter with copper-plate absorbers. Liquid argon technology is chosen as the active medium for its robustness against the high radiation levels present in the forward region. The granularity of the HEC calorimeter is $\Delta\eta \times \Delta\phi = 0.1 \times 0.1$ for the region $|\eta| < 2.5$ and $\Delta\eta \times \Delta\phi = 0.2 \times 0.2$ beyond $|\eta| = 2.5$.

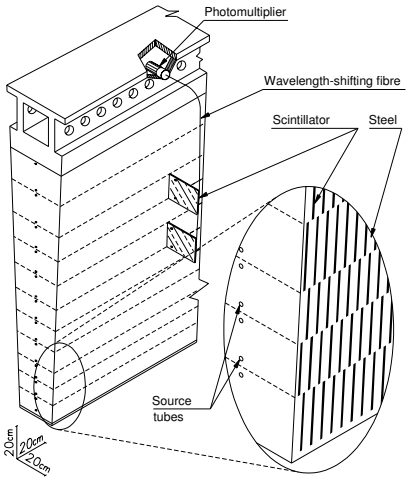

Figure 4.6: A sketch of a Tile calorimeter module geometry, [30].

Forward calorimeter

The FCal covers the detector regions between $3.1 < |\eta| < 4.9$, where the energies and densities of particles are very high. A detailed description of the FCal is given in [51]. The FCal consits of three layers as shown in figure 4.7. The layer closest to the interaction point is FCal1 designed for electromagnetic calorimetry, while FCal2 and FCal3 are hadronic calorimeters.

Each FCal module is a hexagonal absorber matrix in which electrodes are positioned parallel to the beam pipe. The electrodes are formed by a cathode tube and placed inside an anode rod. A gap between the rod and the tube is filled with liquid argon. Particles from the interaction point which hit the calorimeter produce a shower of secondary particles. The charged secondaries crossing the liquid argon gaps ionize the argon atoms. The resulting electrons

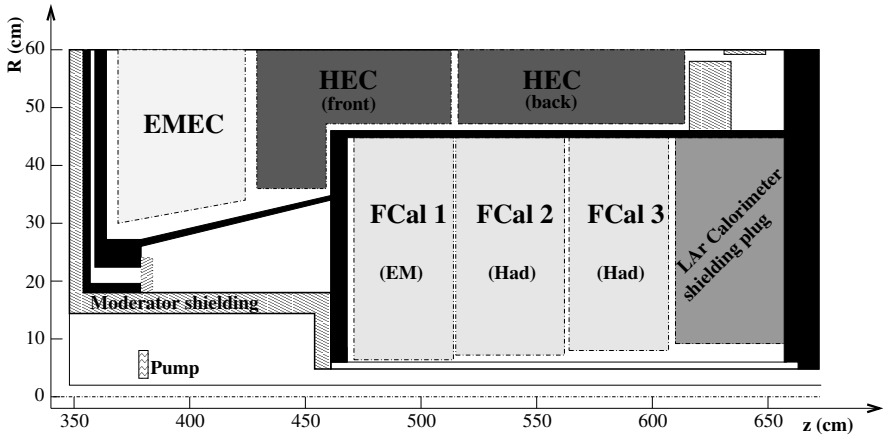

Figure 4.7: Sketch of the three FCal modules, [30].

drift to the rod, producing an electrical pulse. The size of the gap is required to be very small to provide a fast readout. Apart from that, the small gap size allow to avoid signal degradation caused by distortion of the electric field in the gap (see Ref. [52]). The later appears due to accumulation of slowly drifted positive ions, liberated when a charge particle traverse the calorimeter, which is particularly important in the forward regions where particle rate is large. The size of the gap is 0.27 mm, 0.38 mm and 0.50 mm for FCal1, FCal2 and FCal3 respectively.

The structure of the FCal1 is schematically shown in figure 4.8. The FCal1 module is made of copper plates stacked one behind another. The electrodes are placed in the holes of the plates and consist of copper rods and tubes separated by a radiation-hard plastic fibre. The copper is chosen as the absorber to optimise the resolution and the heat removal [30]. FCal1 has a depth of 28 radiation lenghs.

In the hadronic modules FCal2 and FCal3 the amount of tungsten is maximized in order to limit the transverse hadronic shower spread. A copper skeleton is used, consisting of electrode tubes installed between two end-plates. The space between the tubes is filled with tungsten alloy slugs and the anode rods are made of pure tungsten.

Each FCal readout cell is formed from several neighbouring electrodes to achieve a granularity of about $\Delta\eta \times \Delta\phi \approx 0.2 \times 0.2$.

4.2.3 Muon System

Muons can penetrate through the calorimeters and reach the outermost part of ATLAS, the muon system. The muon spectrometer is designed to detect charged particles and measure their momenta. The muon spectrometer components are:

- Monitored Drift Tube (MDT) chambers, which provide a precision measurement of the track coordinates in the pseudorapidity region $|\eta| < 2.7$, (the innermost layer $|\eta| < 2.0$).
- Cathode strip chambers (CSC), which are used for precise momentum measurements in the forward region $2.0 < |\eta| < 2.7$.
- Resistive plate chambers (RPC) triggers, which are placed in the barrel region.

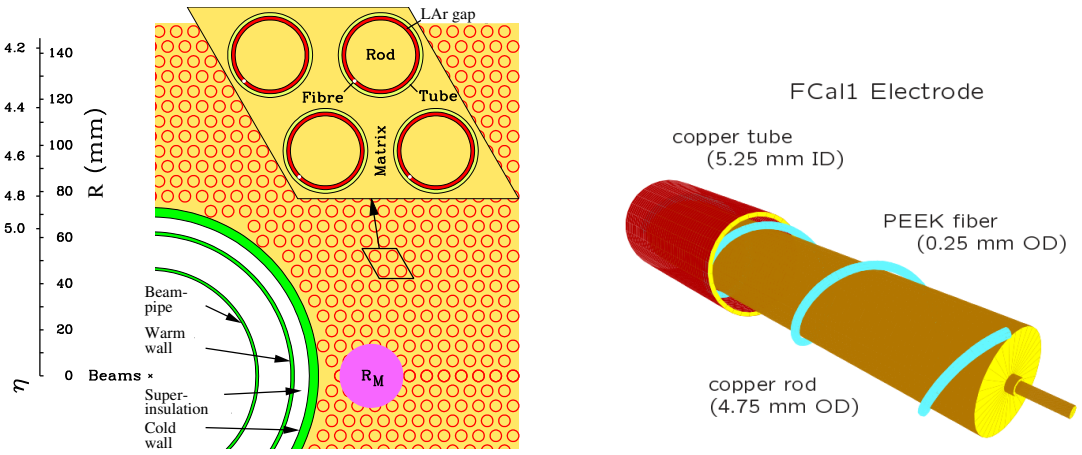

(a) **(b)**

Figure 4.8: Electrode structure of FCal1. The copper tubes and rod are placed in the hexogonal matrix, [30](a), sketch of the FCal1 tubular electrode (b), [53].

- Thin gap chambers (TGC) triggers, which are in the end-cap region.

Particles from the primary vertex traverse three sets of muon chambers. The measurement of the muons' momenta is performed by precision-tracking chambers, based on the deflection of the muon tracks by the magnetic field. In the transition region $1.4 < |\eta| < 1.6$ the magnetic deflection is provided by a combination of barrel and end-cap fields. A system of trigger chambers provide fast information on muon tracks traversing the detector.

4.2.4 The Magnet system

The ATLAS magnet system is formed by solenoid and toroid magnets. The solenoid is located between the inner detector and the EM calorimeter. It is aligned with the beam axis and provides a 2 T axial magnetic field for the inner detector.

Three toroids, one barrel and two end-caps, produce a magnetic field for the muon detectors. The barrel toroid produces approximately a 0.5 T field in the central region, and the two end-caps produce 1 T for the forward region.

4.2.5 Trigger system

The ATLAS trigger system is designed to record events at an average rate of 200 Hz from the bunch-crossing frequency of 40 MHz. This is made by using a three level system of events selection.

The first level (L1) is a hardware-based trigger which uses coarse-granularity information from the calorimeter and muon trigger systems. The High Level Trigger (HLT) is a software based trigger, which is subdivided into the Level-2 (L2) trigger and Event Filter (EF). The L2 uses information from *Regions of Interest* (RoIs) identified by L1. The L2 trigger has access to full granularity from all the detectors. The EF is responsible for the final decision and has access to the full event.

4.3 Luminosity

An important collider characteristic is its luminosity, which defines the event rate $\dot{N} = L\sigma$. For a storage ring, operating at a frequency f_r and with n_b bunch pairs colliding per revolution, the luminosity can be written in terms of the experimentally measured interaction rate per crossing μ_{vis} as

$$L = \frac{\mu_{vis} n_b f_r}{\sigma_{vis}} \tag{4.2}$$

where σ_{vis} is the visible inelastic cross-section, calibrated using the beam parameters.

ATLAS monitors the delivered luminosity by measuring μ_{vis} with a variety of detectors and using different algorithms [54]. The inner detector contributes to the luminosity measurement by the detection of primary vertices produced in inelastic pp interactions. The Beam Condition Monitor (BCM) is used to monitor the beam conditions close to the interaction point. LUCID is a Cherenkov light detector dedicated to the online luminosity monitoring. Its main purpose is to detect inelastic pp scattering in the forward direction, in order to both measure the integrated luminosity and to provide online monitoring for the instantaneous luminosity and beam conditions.

The calibration of σ_{vis} is performed using beam-separation scans, first proposed by van der Meer, and called van der Meer (vdM) scans [55,56]. The delivered luminosity can be derived from the beam parameters and written as

$$L = \frac{n_b f_r n_1 n_2}{2\pi \Sigma_x \Sigma_y} \tag{4.3}$$

where $n_{1,2}$ are the numbers of protons in beams 1 and 2, and $\Sigma_{x,y}$ characterize the horizontal and vertical beam profile widths.

The design luminosity of the LHC is 10^{34} cm^{-2}s^{-1}, providing a bunch collision rate of 40 MHz. The integrated luminosity $\int L dt$ delivered by the LHC in 2011 and 2012 and recorded by ATLAS is shown in figure 4.9.

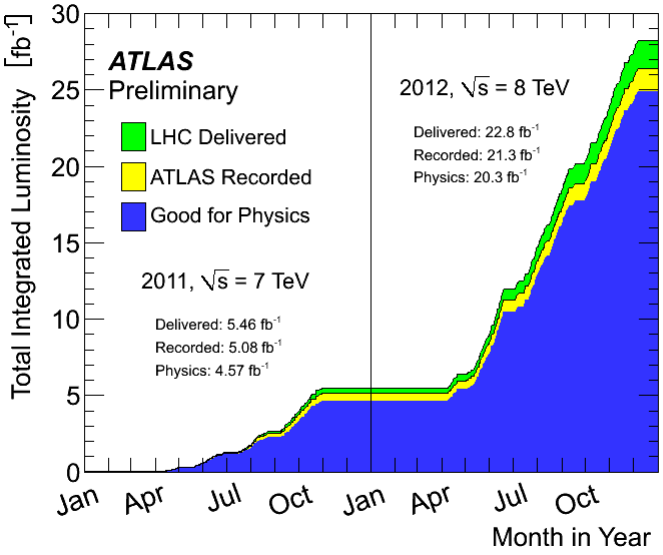

Figure 4.9: Total integrated luminosity delivered and recordered by ATLAS for pp collisions at $\sqrt{s} = 7$ and 8 TeV centre-of-mass energy in 2011 and 2012, [57].

4.4 Phase-0 Upgrade

During the long shutdown 1 (LS1) the LHC prepares for operating at the center-of-mass energy $\sqrt{s} = 13 - 14$ TeV with a bunch spacing of 25 ns. Both the accelerator system and the ATLAS detector are upgraded during this time to prepare for the new running conditions and to allow for a safe increase in beam energy.

The ATLAS upgrade program includes consolidation works, to prepare the detector for the new operation conditions. Among them are the installation of a new ID cooling system, a new diamond beam monitor, an improved shielding of the muon spectrometer between the barrel and end-cap regions, and a new beam pipe.

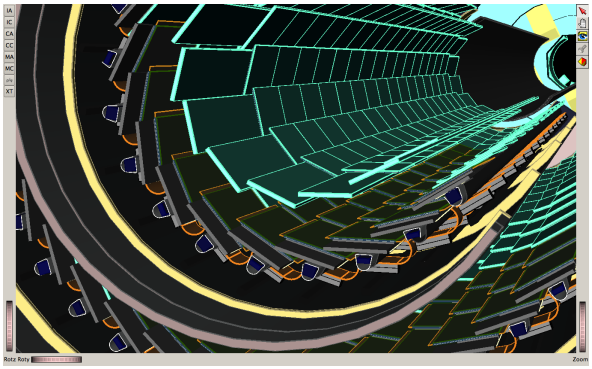

Figure 4.10: 3D view of the IBL inside the Pixel detector illustrating the geometrical arrangement. Taken from [58].

The central ATLAS upgrade activity is the installation of a new barrel layer in the pixel detector. The Insertable B-Layer (IBL) [58] is an additional, fourth pixel layer, which has been installed inside of the present pixel detector (see figure 4.10). Being close to the interaction point the IBL will improve the quality of vertex position measurements, secondary vertex finding and b-tagging. Moreover, as an additional low-occupancy layer, it will help to preserve the tracking performance at high luminosity where increased pile-up levels are expected.

CHAPTER 5

Data and Monte-Carlo samples

5.1 Data sample

The data analysed in this thesis correspond to pp collisions recorded during 2012 at a center-of-mass energy of $\sqrt{s} = 8$ TeV. The data taking efficiency is shown in figure 5.1a. The number of proton-proton interactions per bunch crossing follows a Poisson distribution with a mean value of μ. The average number of interactions per bunch crossing is shown in figure 5.1b.

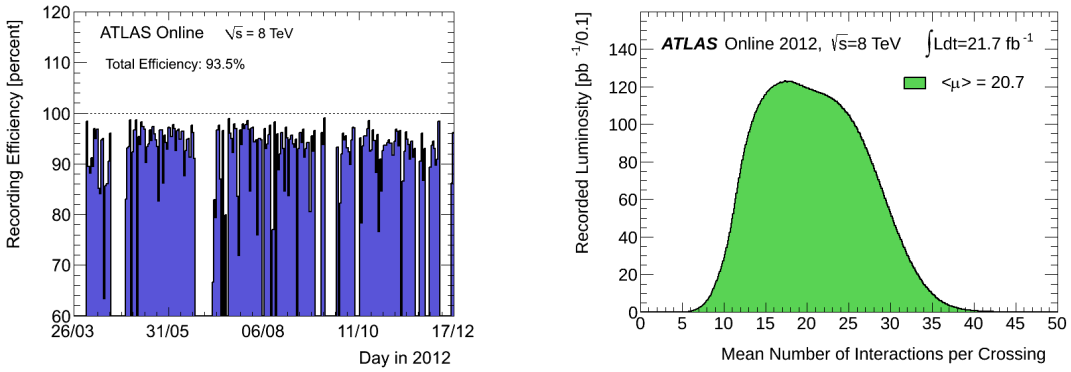

(a) **(b)**

Figure 5.1: ATLAS data taking efficiency in 2012 (a). Number of Interactions per Crossing (b). [57]

The data taking was divided into 10 periods as shown in table 5.1. The periods are formed such that they correspond to a coherent configuration of the detector and the trigger. The data quality is encoded in the GRL (Good Run List). The GRL used in the presented measurements includes information of good quality electron and photon data-taking periods.

Period	A	B	C	D	E	G	H	I	J	L
$\int Ldt$ [fb^{-1}]	0.848	5.300	1.544	3.378	2.658	1.310	1.550	1.066	2.732	0.894
$\int Ldt$ [fb^{-1}] (GRL)	0.794	5.090	1.406	3.290	2.373	1.275	1.446	1.017	2.597	0.841

Table 5.1: Luminosity recordered and satisfied to GRL for 2012 data taking periods.

5.2 Monte-Carlo simulation

Theoretical predictions for the presented analysis are produced using Monte-Carlo event generators. The generation of Monte-Carlo events involves several general steps:

1. Calculation of matrix elements to some order in α_s, α_{EW}.
2. Parton showers, which describe the radiation of gluons and $g \to q\bar{q}$ splittings in the initial and final state from the scale of the hard interaction down to a cutoff scale (of the order of 1 GeV).
3. Hadronization, i.e. transition from the colored partons produced in the previous steps to colorless hadrons. These hadrons can further decay into particles that are ultimately detected in the detector.

The generated events are propagated through a detector simulation, using the GEANT4 package [59]. The simulation step consists of describing the interaction of the different particles that the event generators produce with the detector material. This procedure outputs digitized hits. In order to simulate pile-up interactions, hits from generated minimum bias interactions are sampled according to a Poisson distribution with mean μ, and are overlaid on the hits that the generated hard-scatter interaction produces. The reconstruction of simulated events follows the same procedure as data.

The current analysis uses samples generated with the following generators:

- POWHEG [60–63]: POWHEG is a NLO generator. It is based on the Powheg method for merging NLO calculations with parton showers and it can be interfaced to different parton shower generators.
- PYTHIA [64]: PYTHIA is a LO general purpose event generator for high-energy particle collisions. It contains a library of hard processes and models for parton showers, multiple parton interactions, beam remnants, hadronization and particle decays. The PYTHIA8 version [65] that is used in this thesis uses a model of interleaved evolution for multiparton interactions and parton showers, using p_T as the evolution variable. The hadronization is modeled in terms of the Lund string model [66, 67].
- HERWIG [68]: is also a LO general purpose event generator, consisting of a library of hard processes and containing models for all steps of the event generation outlined above. The main differences with respect to PYTHIA is that HERWIG uses angular ordering in the parton showers (which accounts for color coherence effects) and also models the hadronization step based on cluster fragmentation.
- SHERPA [69]: SHERPA is a LO multi-purpose event generator featuring its own implementation of parton shower and hadronization models (the latter being based on the cluster fragmentation model).
- PHOTOS [70]: is a precision tool for the generation of QED radiative corrections in Z and W decays. The PHOTOS algorithm adds Bremsstrahlung photons to already existing events, generated by a 'host' Monte-Carlo generator.

Monte-Carlo is used to simulate both signal and background processes. A summary of the signal samples used in the analysis is given in table 5.2. The primary signal Monte-Carlo is generated with

POWHEG+PYTHIA8 and is composed of three orthogonal samples $\left(\sum_{i=1,2,3} \varepsilon^{i}_{filter} = 1\right)$. The samples are merged into a single sample by normalizing each part individually using cross-section and event filter information.

Lepton filters	Generator	$\sigma \cdot \varepsilon_{filter} \cdot k^{NNLO/NLO}_{factor}$ [nb] (Unc.)	N_{evnt}
$M_{ee} > 60$ GeV, $1 \times p^{e}_{T} > 15GeV, \lvert\eta^{e}\rvert < 2.7$	POWHEG+PYTHIA8	$1.1099 \cdot 0.31469 \cdot 1.03$ (5%)	20M
$M_{ee} > 60$ GeV, $2 \times p^{e}_{T} > 15GeV, \lvert\eta^{e}\rvert < 2.7$	POWHEG+PYTHIA8	$1.1099 \cdot 0.55648 \cdot 1.03$ (5%)	50M
$M_{ee} > 60$ GeV, $1 \times p^{e}_{T} < 15GeV, \lvert\eta^{e}\rvert > 2.7$	POWHEG+PYTHIA8	$1.1099 \cdot 0.12890 \cdot 1.03$ (5%)	3M
$M_{ee} > 40$ GeV	SHERPA	$1.2079 \cdot 1.03$ (5%)	10M

Table 5.2: Summary of $Z \to ee$ Monte-Carlo samples used in the presented measurements. The uncertainty on the cross-section follows the one defined in Ref. [71].

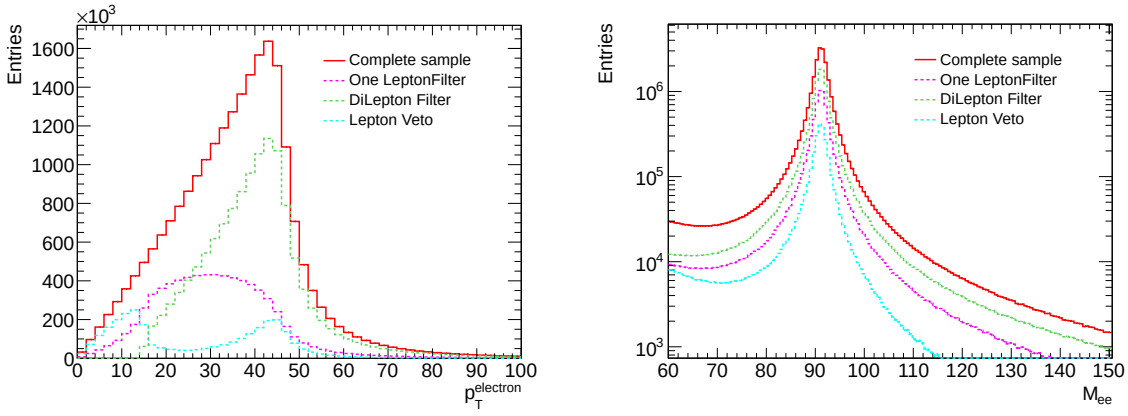

(a) **(b)**

Figure 5.2: The signal Monte-Carlo POWHEG+PYTHIA8 sample assembled from three samples covering orthogonal kinematic regions. Resulting distrubution of an electron transverse momentum (a) and dielectron invariant mass (b).

The sources of background are discussed in chapter 10. The Monte-Carlo samples used for the simulation of the background processes are given in table 5.3.

Process	Generator	$\sigma \cdot \varepsilon_{filter} \cdot k_{factor}^{NNLO/NLO}$ [nb] (Unc.)	N_{events}
$W \to e\nu$+jets	SHERPA	$11.866 \cdot 1.03$ (5%)	40M
$W \to \tau\nu$	SHERPA	$11.858 \cdot 1.03$ (5%)	7 M
$t\bar{t}$	POWHEG+PYTHIA8	$0.21084 \cdot 0.54309 \cdot 1.1994$ $(^{+5.14\%}_{-5.93\%})$	15M
t, t-channel	POWHEG+PYTHIA8	$0.017519 \cdot 1.0 \cdot 1.0500$	5M
$\bar{t}$, t-channel	POWHEG+PYTHIA8	$0.0093964 \cdot 1.0 \cdot 1.0616$	5M
t, s-channel	POWHEG+PYTHIA8	$0.0016424 \cdot 1.0 \cdot 1.1067$	6M
t, Wt channel	POWHEG+PYTHIA8	$0.020461 \cdot 1.0 \cdot 1.0933$ (7%)	1M
$Z \to \tau\tau$	POWHEG+PYTHIA8	$1.1099 \cdot 1.0 \cdot 1.03$ (5%)	5M
WW	HERWIG	$0.032501 \cdot 0.38203 \cdot 1.6833$ (7%)	2.5M
WZ	HERWIG	$0.012009 \cdot 0.30532 \cdot 1.9011$ (7%)	1M
ZZ	HERWIG	$0.0046915 \cdot 0.21154 \cdot 1.5496$ (7%)	0.25M

Table 5.3: The Monte-Carlo samples of the background processes used in the presented measurements.

CHAPTER 6

Electrons in ATLAS

In this chapter the reconstruction and identification (ID) of electrons in the ATLAS experiment is discussed. Depending on the region where an electron is detected two categories are defined: an electron detected in the region $|\eta| < 2.47$ is called central, while an electron detected in the region $2.5 < |\eta| < 4.9$ is called forward.

6.1 Track and vertex reconstruction

The different strategies for track finding used in ATLAS are described in [72]. The primary track reconstruction strategy is the so-called "inside-out", which follows the natural particle direction. The reconstruction starts by finding a track seed in the Pixel and SCT detectors. A seed, formed by three silicon space points, provides the initial parameters for track building - position, direction and bending. These parameters are propagated through the detector layers away from the interaction point and the hits which match the assumed track points are iteratively included in the track candidate fit. A Kalman fitter-smoother formalism [73] is used to simultaneously follow the trajectory and include successive hits in the track fitting. The tracks are formed using the 'pion hypothesis', namely, the track corresponds to the trajectory of a massive particle with a mass equal to the pion mass, whose energy losses due to radiation are negligible. If a track seed is located in one of the EM cluster regions of interest and cannot be successfully extended to a full track using the pion hypothesis, an attempt is made to build the track using an alternative electron hypothesis [74]. In this hypothesis, the electron trajectories are affected by energy losses dominated by Bremsstrahlung when they interact with the detector material. The modified reconstruction algorithm allows for up to 30% energy losses on each material surface.

The reconstructed tracks are extrapolated inside the detector to reconstruct the position of the primary vertex. For vertex reconstruction only tracks with $p_T > 0.5$ GeV are taken into account. Among all vertex candidates the primary vertex is defined as the one having the largest $\sum p_T^2$ of outgoing tracks. The position of the primary vertex is described by the transverse and longitudinal impact parameters and depends on the beam spot parameters.

6.2 Electron reconstruction

The reconstruction of electrons in the region $|\eta| < 2.47$ is based on two sub-detectors: the inner detector, which provides track information and the EM calorimeter, which measures energy deposits. The

reconstruction of forward electrons is based only on calorimeter information. The two reconstruction strategies use different algorithms of calorimeter clustering [75] - the "sliding window" algorithm for central electrons and the "topological" algorithm for forward electrons.

Central electrons

The electron reconstruction starts with building clusters of energy deposits in the EM calorimeter. For that the $\eta - \phi$ space is divided into a grid with a cell size of $\Delta\eta \times \Delta\phi = 0.025 \times 0.025$, which corresponds to the granularity of the middle layer of the calorimeter. Within each grid cell, the energy from all calorimeter layers is summed into an energy tower. The "sliding window" algorithm scans the resulting tower grid with a window of a fixed size $N_{\eta}^{window} \times N_{\phi}^{window} = 3 \times 5$. A seed cluster is formed if the total transverse energy of the window is a local maximum of the scanned region and is above $E_T^{threshold} = 2.5$ GeV. The position of the seed cluster is computed so as to maximise the amount of energy within the cluster. This is done by using a window of a smaller size ($N_{\eta}^{pos} \times N_{\phi}^{pos} = 3 \times 3$) around the central energy tower of the sliding window. The smaller size of the window makes the position computation less sensitive to noise. The resulting seed cluster is positioned around the energy-weighted η and ϕ barycenter of all cells within this window.

A set of electron-track candidates is formed within a cone of $\Delta R = 0.3$ around the barycenter of the seed cluster. If more than one track is matched to a cluster then the track with the most pixel hits and the smallest distance to the cluster barycenter is preferred. An electron is reconstructed if at least one well-reconstructed track is matched to the seed cluster.

The final electron cluster is rebuilt from the seed cluster using $N_{\eta}^{cluster} \times N_{\phi}^{cluster} = 3 \times 7$ and $N_{\eta}^{cluster} \times N_{\phi}^{cluster} = 5 \times 5$ longitudinal towers of cells in the EMB and EMEC respectively. The number of cluster cells is optimized as a compromise between inclusion of the most of the energy from the electromagnetic cascade and minimization of the pile-up and electronic noise contributions. The four-momentum of central electrons is computed using information from both the energy cluster and the best track matched to the original seed cluster. The energy is taken from the cluster energy while the ϕ and η directions are determined from the corresponding track parameters.

Forward electrons

The reconstruction of forward electrons is different from the central ones. It uses information only from the calorimeters, since the forward detection region lays beyond the coverage of the tracking system. Without track information electrons cannot be distinguished from photons, and the charge cannot be measured.

Forward electron reconstruction uses topological clusters which are constructed with a variable number of cells and have a variable border in contrast to the fixed size of the central electron clusters. Neighboring cells are grouped into clusters taking into account their energy contents compared to the expected noise. The average noise in a cell is obtained from calibration runs and data and includes the expected contribution from pile-up. The energy significance of a cell is defined as the signal to noise ratio. The topological cluster is seeded by a cell with an energy significance above a threshold t_{seed}. The cluster is then expanded by examining the neighboring cells in three dimensions. A significance of more than $t_{neighbour}$ is needed for a cell to enter the cluster. If two clusters share a neighboring cell they are merged. The perimeter cells are included in the cluster if the signal to noise ratio is above t_{cell}. The thresholds of signal to noise ratio for the topocluster building $t_{seed}/t_{neighbour}/t_{cell}$ are chosen to be 4/2/0.

The energy of forward electrons is determined by summing the energies in the cluster cells and is then corrected for energy losses in the passive material before the calorimeter. The direction of forward electrons is defined by the barycentre of the cluster cells.

6.3 Electron identification

The reconstructed electromagnetic objects can be not only isolated signal electrons, but also objects, that can be mis-identified as electrons, such as hadronic jets and electrons from photon conversions. A set of criteria is needed to identify real electrons. For the central electrons two approaches are used: cut-based and likelihood identification techniques. Forward electrons are identified using the cut based approach.

Central electrons

The electron identification is based on variables describing the longitudinal and transverse shower shapes and track parameters summarized in table 6.1. The cut-based approach forms three identification levels with increasing background rejection: Loose, Medium and Tight.

The Loose identification criteria use shower shape variables in the first and second layers of the EM calorimeter and the fraction of the energy deposited in the hadronic calorimeter. Additional requirements on the associated track quality and track-cluster matching are applied.

Stricter identification is performed at the Medium level. In addition to the Loose selection, information from the third layer of the EM calorimeter, transverse impact parameter and TRT signals are analyzed. A measured hit in the innermost layer of the pixel detector is required to discriminate against photon conversions.

The Tight level in addition to all variables included in the previous identification levels uses a selection on the ratio between the candidate's cluster energy and its track momentum, stricter requirements on the discriminating variables and TRT information, and a veto on reconstructed photon conversion vertices associated with the cluster.

A Multivariate analysis (MVA) technique is used to perform the likelihood (LH) identification. Three levels are defined here: Loose, Medium and Very Tight. The LH identification makes use of signal and background probability density functions of the discriminating variables for a selection decision. The variables used for the LH ID levels are described in [76].

Forward electrons

The identification of forward electrons is based on cluster moments and differences in the shower shapes of hadronic and electromagnetic deposits. Cluster moments of degree n for a variable x_i are defined as $< x^n >= \frac{\sum_i E_i x_i^n}{\sum_i E_i}$, where i runs over all cluster cells. The clusters built during the reconstruction are described by several variables:

- Shower depth: the distance between the shower barycenter and the calorimeter front face, measured along the shower axis.
- Maximum cell energy: fraction of energy deposited in the most energetic cell with respect to the rest of the cluster energy.

Type	Description	Loose	Medium	Tight
Hadronic leakage	Ratio of the E_T in the first layer of the hadronic calorimeter to E_T of the EM cluster (for $\|\eta\| < 0.8$ and $\|\eta\| > 1.37$) or ratio of the E_T in the hadronic calorimeter to E_T of the EM cluster (for $\|\eta\| > 0.8$ and $\|\eta\| < 1.37$)	x	x	x
Third layer of EM calorimeter	Ratio of the energy in the third layer to the total energy in the EM accordion calorimeter		x	x
Middle layer of EM calorimeter	Lateral shower width	x	x	x
	Ratio of the energy in 3×7 cells over the energy in 7×7 cells centered at the electron cluster position	x	x	x
Strip layer of EM calorimeter	Shower width	x	x	x
	Ratio of the energy difference between the largest and second largest energy deposits in the cluster over the sum of these energies	x	x	x
Track quality	Number of hits in the B-layer (discriminates against photon conversions)		x	x
	Number of hits in the pixel detector	x	x	x
	Number of total hits in the pixel and SCT detectors	x	x	x
	Transverse impact parameter		x	x
TRT	Total number of hits in the TRT		x	x
	Ratio of the number of high-threshold hits to the total number of hits in the TRT		x	x
Track-cluster matching	$\Delta\eta$ between the cluster position in the strip layer of the calorimeter and the extrapolated track	x	x	x
	$\Delta\phi$ between the cluster position in the middle layer of the calorimeter and the extrapolated track			x
	Ratio of the cluster energy to the track momentum			x
Conversions	Veto electron candidates matched to reconstructed photon conversions			x

Table 6.1: Shower shape and track information used for the identification of central electrons. The use of the variables for different identification levels in the cut-based approach is shown. Adapted from [76].

- Longitudinal second moment: measure of the longitudinal extension of the cluster, defined as the second moment of the distance of each cell to the shower center in the longitudinal direction.
- Transverse second moment: measure of the transverse extension of the cluster, defined as the second moment of the distance of each cell to the shower center in the transverse direction.
- Normalized longitudinal moment - modified measure of the longitudinal cluster extension with different weights per cell.
- Normalised lateral moment - modified measure of the lateral cluster extension with different weights per cell.

Three identification levels are defined using a Fisher discriminant [77] and are called FwdLoose, FwdMedium and FwdTight. Similar to the central identification levels the background rejection increases from FwdLoose to FwdTight.

6.4 Energy corrections

Several effects cause the reconstructed energy of the electron cluster to be lower than the true energy of the electron. The electron loses energy in front of the calorimeter while traveling through the different detector regions, such as the inner detector, cryostat, the material between the presampler, etc. Inside the EM calorimeter part of the energy is deposited in dead material and in cells outside of the cluster. Another source of energy losses is leakage into the hadronic calorimeter.

The cluster energy needs to be corrected to account for these effects. The calibration procedure consists of reweighting the cluster energies with correction factors, which are derived in simulation. The overall electron energy response in data is calibrated so that it agrees with the simulation expectations, using a sample of $Z \to e^+e^-$ events. The calibrated electron energy scale is validated with in-situ measurements using $J/\psi \to e^+e^-$ decays, as described in [78].

To account for mismatch between the energy resolution in data and simulation the cluster energy of electrons in Monte-Carlo is smeared to mimic the effects observed in the detector. The fractional energy resolution of the calorimeter can be parametrized as

$$\frac{\sigma_E}{E} = \frac{a}{\sqrt{E}} \oplus \frac{b}{E} \oplus c, \tag{6.1}$$

with the sampling term a, the noise term b and the constant term c. The sampling term depends upon the choice of absorber, active material and thickness of sampling layers. The noise term is coming from electronic noise and pileup and is taken from calibration data runs. The last term is a constant term, which is determined by the depth of detector, crack regions, dead material etc. The constant term limits the calorimeter performance at high energies. The electron resolution corrections are derived under assumption that the simulation is well-modeled up to a Gaussian constant term

$$\left(\frac{\sigma_E}{E}\right)_i^{\text{Data}} = \left(\frac{\sigma_E}{E}\right)_i^{\text{MC}} \oplus c_i, \tag{6.2}$$

where c_i is an η dependent relative resolution correction. While the resolution correction is well-calibrated for the central electrons, as described in [78], an additional smearing correction for forward electrons is required to account for a difference in Z resonance width in the central-forward $Z \to e^+e^-$ data and Monte-Carlo samples. The invariant mass spectrum is one of the observables that is measured in the presented analysis. To avoid the bias of the measurement, the smearing correction factors are derived using the transverse energy distribution of forward electrons. The smearing factor has been varied in the simulation between 0% and 8% for 9 bins of electron η and the optimal value in each bin is obtained using a χ^2 minimization method. The resulting scales are shown in figure 6.1. An additional systematic uncertainty is assigned to the measurement as half of the smearing factor in each bin. The effect of the smearing correction on the energy of forward electrons and on the dielectron mass distributions is shown on figure 6.2.

The total energy of calorimeter cells, surrounding an EM cluster within a certain radius $\Delta R = \sqrt{\Delta\phi^2 + \Delta\eta^2}$, is used in data analyses to judge about the level of isolation of an electron candidate. This isolation quantity is needed to be corrected in the measurements for two effect. The isolation

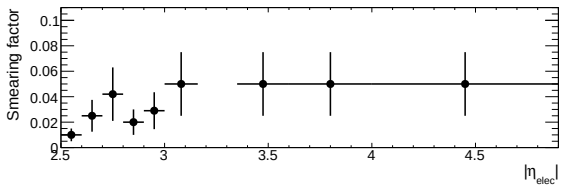

Figure 6.1: Resolution smearing factors applied on the forward electrons cluster energy.

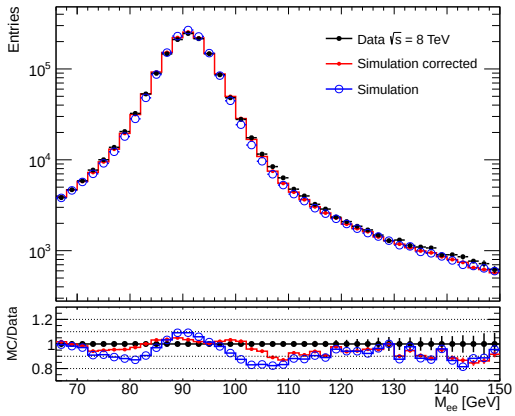

Figure 6.2: Effect of the smearing correction of forward electrons on M_{ee} distribution.

correction accounts for the lateral leakedge of the cluster energy described above, which cause the isolation energy to grow as a function of electron E_T. And, apart from that, the isolation energy can be increased due to soft energy deposits from interactions different from the hard scattering (underlying event and pile-up).

6.5 Efficiency corrections

The electron detection is characterized by its efficiency which is defined as the fraction of electrons which passed the detection criteria. For central electrons, the total efficiency is comprised of reconstruction, identification and trigger components, while for forward electrons only an identification efficiency is defined. The efficiencies are measured (see Ref. [76]) from $Z \to ee$ and $J/\psi \to ee$ decays with the so-called tag-and-probe technique. The reconstruction efficiency is determined with respect to reconstructed EM clusters, the identification efficiency is measured with respect to the number of reconstructed electrons, and the trigger efficiency is defined for reconstructed electrons passing the identification criteria.

It is important for data analyses to have a simulation which reproduces the data efficiency. Scale factors (SF) are introduced to correct for differences between data and simulation efficiencies. They are defined as follows:

$$SF = \frac{\text{Efficiency}^{data}}{\text{Efficiency}^{simulation}}. \tag{6.3}$$

The scale factors correct the reconstruction, trigger, and identification efficiencies in the simula-

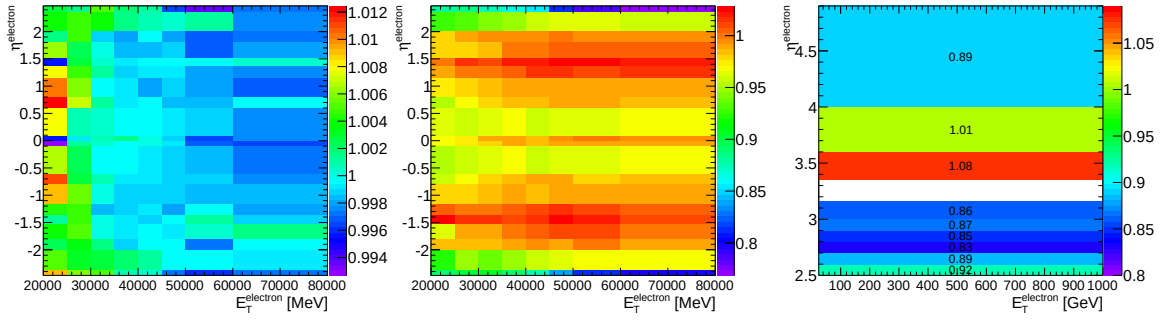

(a) **(b)** **(c)**

Figure 6.3: Reconstruction (a) and identification scale factors for central (b) and forward (c) electrons for tight identification criteria determined as a function of electron p_T and η. Obtained from [76].

tion and the total scale factor is defined as a product of those three contributions:

$$SF_{\text{total}} = SF_{\text{Reconstruction}} \times SF_{\text{Identification}} \times SF_{\text{Trigger}}. \tag{6.4}$$

The electron efficiencies depend on the transverse energy and pseudorapidity of electrons. Following that, the scale factors are determined in two-dimentional bins in $\left(E_T^{\text{elec}}, \eta^{\text{elec}}\right)$. The reconstruction and identification scale factors are shown in figure 6.3. The efficiencies for different levels of electron identification of central electrons are shown in figures 6.4. The measured reconstruction efficiency compared to Monte-Carlo predictions is illustrated in figures 6.5.

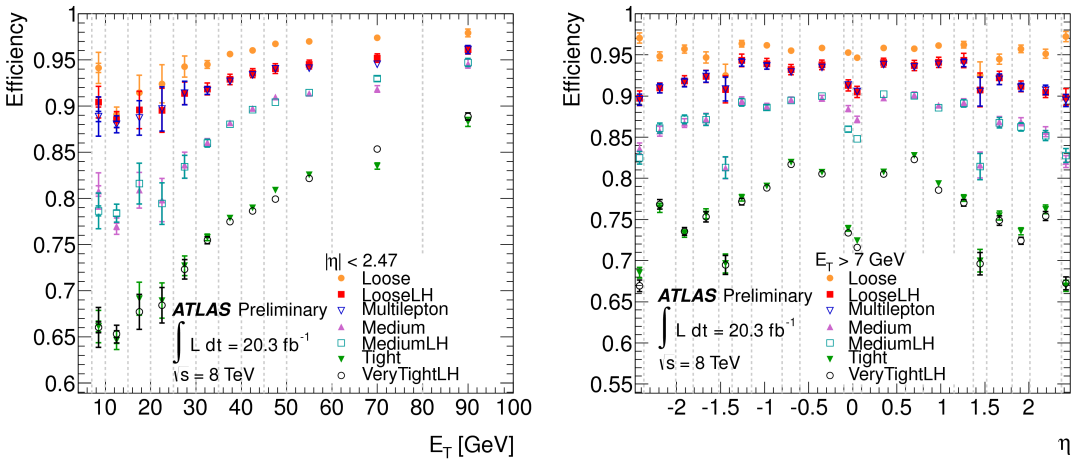

(a) **(b)**

Figure 6.4: Electron identification efficiencies measured for central electrons as a function of E_T (a) and η (b), [76].

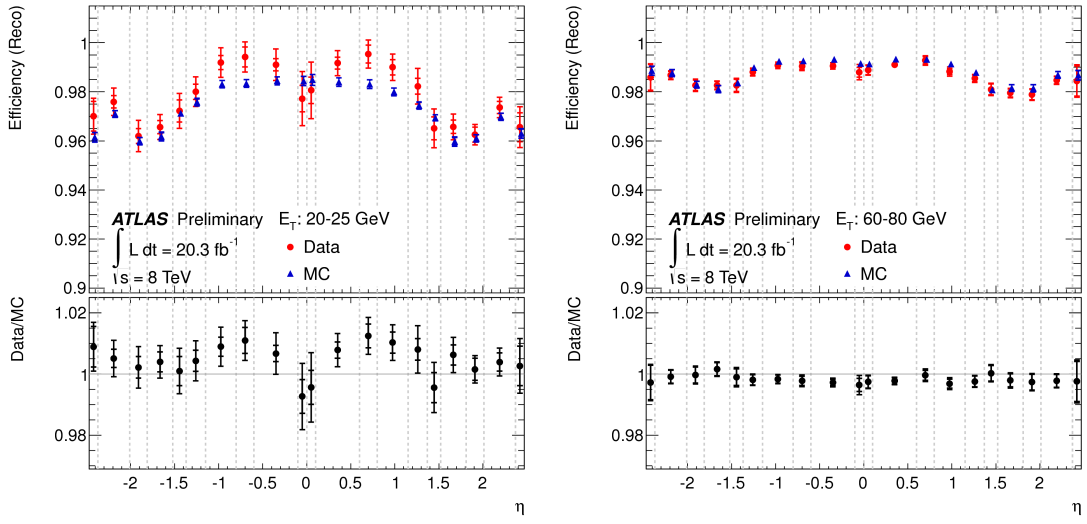

(a) **(b)**

Figure 6.5: Example of electron reconstruction efficiencies measured in two ranges of electron E_T as a function of η, [76].

The measurement

CHAPTER 7

Selection

In this chapter the selection of $pp \to Z/\gamma^* \to e^+e^- + X$ events from the data and Monte-Carlo samples is discussed. The selection requirements, applied on the reconstructed quantities, are denoted as analysis selection. In order to minimize the uncertainties due to the extrapolation of the measured cross-sections to the full phase-space the detector-related effects are taken into account in extrapolating to a fiducial phase-space which is close to the detector acceptance. The selection criteria corresponding to the fiducial phase-space are applied on the Monte-Carlo truth level.

7.1 Analysis selection

A sample of $pp \to Z/\gamma^* \to e^+e^- + X$ events is formed by applying the selection criteria summarised in table 7.1 on collected data and simulated signal and background Monte-Carlo samples. The selection is optimized to suppress contributions from the background processes.

The online event selection is based on the ATLAS trigger system. The analyzed samples are required to be recorded by at least one of two single-electron triggers both requiring one electron candidate passing medium identification criteria and having a transverse energy above a certain threshold. One trigger selects events with electron $E_T > 24$ GeV and another trigger with $E_T > 60$ GeV. The lower energy threshold trigger uses an additional requirement on relative track isolation, which allows to reduce the event rate. However for higher energy electrons this requirement causes inefficiency in event selection, and the complementary information from the second trigger is needed to resolve the inefficiency [79]. An additional requirement, called trigger matching, checks that a selected event was triggered by the electron that passed the selection criteria.

The offline selection of events starts by requiring quality conditions on the recorded data, monitored during the data-taking. Only events which were recorded during a period when the calorimetry and the inner-detector tracker were functioning normally and the solenoidal field had its nominal value are used for the measurement. This information is summarized in a so-called "Good Run List" (GRL). Events with electrons detected in problematic calorimeter regions are excluded from the measurement. These regions include bad quality clusters or fake clusters originating from calorimeter problems.

Events with one of the electrons going into the central detector region, i.e. having $|\eta| < 2.47$ and the other into the forward region, $2.5 < |\eta| < 4.9$, are defined as central-forward and are selected for the measurement. Events with a central electron detected in the crack region between EMB and EMEC ($1.37 < |\eta| < 1.52$) or with a forward electron in the transition region between the EMEC and

Event selection:	
Single electron trigger	
Good Run List	
Reject events with LAr errors	
Number of tracks at primary vertex ≥ 3	
Maximum two good electrons	
Electron selection:	
Central electron	Forward electron
$\lvert\eta\rvert < 2.47$,	$2.5 < \lvert\eta\rvert < 4.9$,
excluding $1.37 < \lvert\eta\rvert < 1.52$	excluding $3.16 < \lvert\eta\rvert < 3.35$
$E_{\mathrm{T}} > 25\,\mathrm{GeV}$	$E_{\mathrm{T}} > 20\,\mathrm{GeV}$
Tight central identification	Tight forward identification
has isolated track	
Boson selection:	
$66 < M_{ee} < 150$ GeV	

Table 7.1: Summary of the analysis selection.

the FCal, $3.16 < |\eta| < 3.35$ are excluded from the measurement. An algorithm used to reconstruct an electron is stored in the "Author" variable and refers to the reconstruction procedures described in section 6.2. The "Author CF" criterion implies that one central and one forward electron were reconstructed. If an event contains more than one central and more than one forward electrons passing the corresponding identification, η and p_T requirements, the event is rejected in order to suppress background contributions from multi-electron processes, including the Higgs boson decay to four leptons. Further background rejection is achieved by requiring of at least three tracks coming from the reconstructed primary vertex, which allow to suppress the contribution from photon induced process (see chapter 10).

The transverse energy of the offline electrons is required to be more than 25 GeV for the central electron and more than 20 GeV for the forward electron. The tighter cut for the central electron is driven by the E_T threshold of the single electron trigger. The electron energy is taken from the calorimeter cluster corrected as described in chapter 6, while the direction of the electron is defined taking into account the available cluster and track information. More precisely, if the electron track has at least four hits in the pixel and SCT detectors, the electron direction is taken from the track. The transverse energy is then $E_{\mathrm{T}} = \frac{E}{\cosh(\eta_e^{track})}$. If there are less than four silicon hits or there is no track information available, like for forward electrons, the direction is taken from the cluster and the transverse energy is calculated as $E_{\mathrm{T}} = \frac{E}{\cosh(\eta_e^{cluster})}$.

Tight identification criteria, defined for central and forward electrons as described in section 6.3, are applied for both electrons for high background rejection. The track of the central electron candi-

date is required to be isolated to further reject jets misidentified as electrons. The transverse momentum of the tracks around the electron candidate are summed into a p_T^{Cone} variable. These tracks are required to have $p_T > 0.4$ GeV and come from the primary vertex associated to the electron track. The tracks enter the sum if they are reconstructed within a cone of radius $\Delta R = 0.2$ around the electron candidate. Only electrons with track isolation requirement $p_T^{Cone}/p_T^{elec} < 0.14$ pass the selection.

The reconstructed electron candidate pairs are required to have an invariant mass between 66 and 150 GeV. The upper limit of the mass window is extended above the Z mass peak to allow for the measurement of the Drell-Yan production cross-section dominated by the photon exchange. Apart from that in this region Forward-Backward asymmetry is large compare to the Z peak-region (see figure 3.10). Both upper and bottom limits of the mass window are defined to exclude regions with high background contamination and low statistics of the data sample.

7.2 Cut Flow

The results of the analysis selection applied on the data and simulation samples are summarized in the cut flow table 7.2. The fraction of events passing the selection criteria with respect to the initial number of events, and the efficiencies with respect to the previous cut are shown as well. The event weights of the Monte-Carlo samples are applied as described in chapter 8. Most of the selection criteria have similar effect on both data and simulation. At the same time tight and forward tight identification requirements reject background, they thus reject a bigger fraction of events in data than in Monte-Carlo. The E_T requirements on central and forward electrons has a similar effect. The flow of the background rejection at the different stages of the analysis selection is demonstrated in figures 7.1, where the mass distribution, formed by the candidate events in data, is shown after each analysis cut.

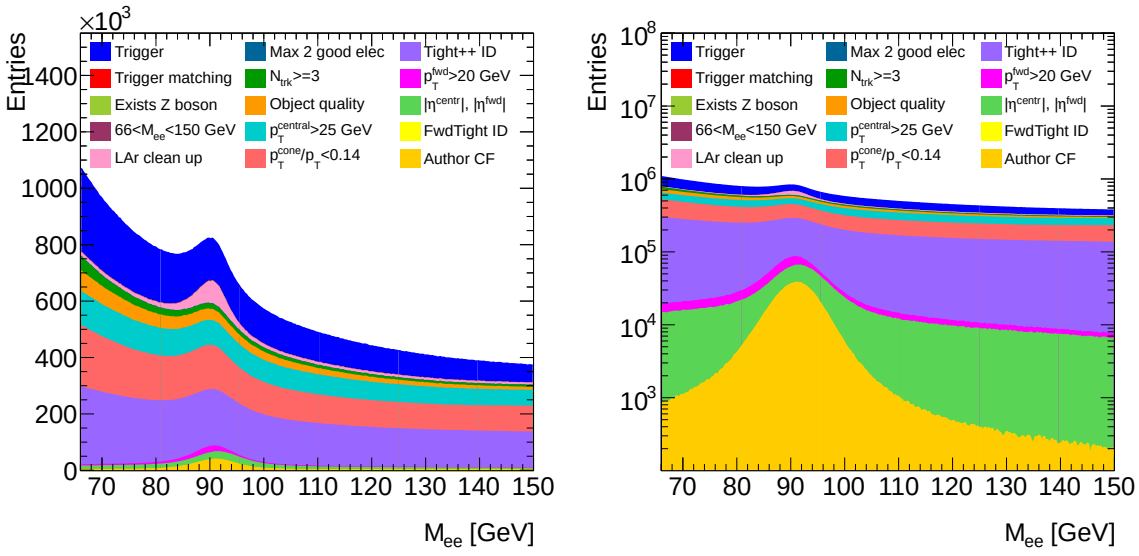

Figure 7.1: M_{ee} distribution in linear (left) and logarithmic (right) scales formed by candidate events at the different stages of the analysis selection. At each stage an analysis cut is applied additionally to all previous cuts.

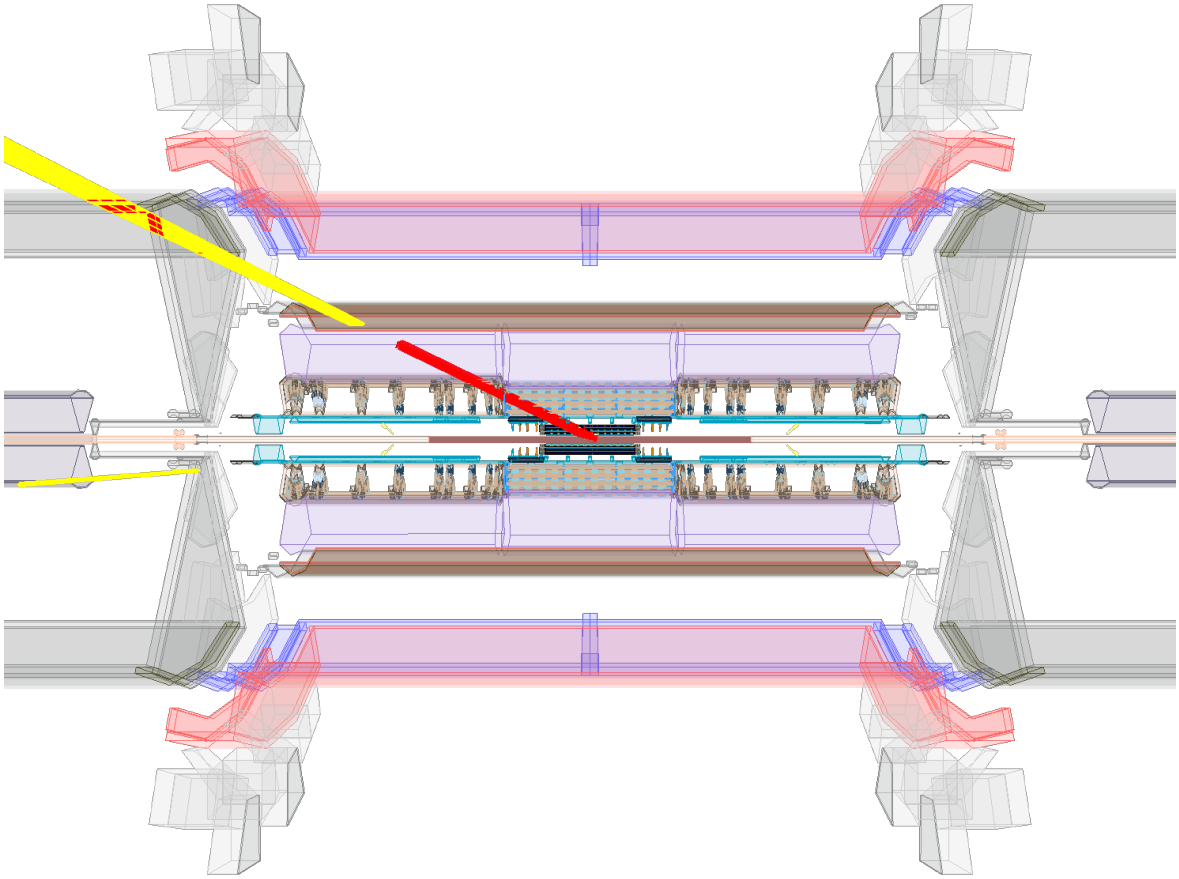

Figure 7.2: VP1 event display of a central-forward candidate event. The energy deposition of the electron candidates is shown in yellow and the track of the central electron candidate is in red. The event was recorded 2012-12-03, during run 215473 (event 139838400).

The trigger requirements lead to some event loss in Monte-Carlo due to the inefficiency around the threshold of 24 GeV. This is not seen in data since the single electron trigger is the dominant trigger to select events with the forward-backward topology online.

An example of a data event passing the selection criteria is shown in figure 7.2. It has been visualized using the Virtual Point 1 (VP1) event display [80]. In this event the central electron candidate is detected with $E_T = 32.8$ GeV and $\eta =$ -1.36. The forward electron candidate with $\eta =$ -2.97 is detected by the EMEC calorimeter with a transverse energy of about 35 GeV.

7.3 Fiducial phase space

The target phase-space region for measuring the cross-section and for comparing with the theoretical predictions is the fiducial phase-space. This phase-space is defined to be as close as possible to the detector acceptance and to the analysis selection. The selection criteria defining the fiducial volume are shown in table 7.3. The final-state electrons in the fiducial phase-space are defined with the so-called Born kinematics, which is defined from the decay kinematics before QED final state radiation.

Analysis cut	N_{events}^{data}	ε_{abs}^{data} [%]	ε_{rel}^{data}[%]	N_{events}^{MC}	ε_{abs}^{MC}[%]	ε_{rel}^{MC}[%]
Good Run List	6.943×10^8	100.00	100.00	2.137×10^7	100.00	100.00
Exists Z boson	6.640×10^8	95.64	95.64	2.120×10^7	99.22	99.22
$66 < M_{ee} < 150$ GeV	4.504×10^8	64.87	67.82	1.883×10^7	88.12	88.82
$E_{\mathrm{T}}^{\mathrm{central}} > 25$ GeV	2.722×10^8	39.20	60.44	1.323×10^7	61.90	70.24
$E_{\mathrm{T}}^{\mathrm{forward}} > 20$ GeV	4.910×10^6	7.07	18.04	6.728×10^6	31.48	50.86
$\eta^{\mathrm{cntr}} < 2.47$, $2.5 < \eta^{\mathrm{fwd}} < 4.9$	2.584×10^6	3.72	52.62	3.337×10^6	15.62	49.60
Exclude $1.37 < \lvert\eta\rvert < 1.52$	2.353×10^6	3.39	91.06	3.133×10^6	14.66	93.86
Exclude $3.16 < \lvert\eta\rvert < 3.35$	2.241×10^6	3.23	95.24	3.133×10^6	14.66	100.00
Vertex with ≥ 3 tracks	2.237×10^8	3.22	99.83	3.111×10^6	14.56	99.31
One central-forward pair	2.228×10^8	3.21	99.59	3.032×10^6	14.19	97.45
Author central-forward	2.200×10^6	3.17	98.75	3.026×10^6	14.16	99.81
Tight++ ID	6.850×10^7	0.99	31.14	2.276×10^6	10.65	75.22
Forward Tight ID	1.542×10^6	0.22	22.50	1.596×10^6	7.47	70.10
Track isolation	1.518×10^8	0.22	98.50	1.590×10^6	7.44	99.66
LAr problematic regions	1.515×10^8	0.22	99.78	1.590×10^6	7.44	100.00
Object quality	1.506×10^8	0.22	99.42	1.584×10^6	7.41	99.61
Trigger	1.496×10^6	0.22	99.34	1.459×10^6	6.83	92.13
Trigger matching	1.496×10^6	0.22	100.00	1.459×10^6	6.83	100.00

Table 7.2: Number of events in data and signal Monte-Carlo samples at different stages of the analysis selection. ε_{abs} shows relative number of events remaining after a cut with respect to initial number of events. ε_{rel} is a fraction of event with respect to the previous selection criteria.

$66 < M_{ee} < 150$ GeV
Central electron $E_T > 25$ GeV
Forward electron $E_T > 20$ GeV
Central electron $\lvert\eta\rvert < 2.47$
Forward electron $2.5 < \lvert\eta\rvert < 4.9$

Table 7.3: Definition of the fiducial phase space for the cross-section calculation.

CHAPTER 8

Event weights

The agreement between data and simulation shows our level of understanding of the physics processes in the collision events. The Monte-Carlo simulation does not describe all the known effects in data and a number of corrections are required. The necessary corrections are either implemented in the form of a reweighting procedure which changes the weights of the generated and reconstructed events, or as a shift of reconstructed distributions. The corrections are applied at different stages of the analysis. At the reconstructed level the simulation is corrected for the difference between data and Monte-Carlo in efficiency, energy resolution, and isolation, as described in sections 6.4, 6.5. The following corrections are applied at the level of generated events:

- z position of primary vertex.
  The Monte-Carlo samples used in this analysis were simulated with broader beam spot parameters than that in data. In particular the distribution of the position of the reconstructed primary vertex along the z axis is wider in simulation than it is in data. It follows a Gaussian distribution with a mean of 0. In order to match the data, the Monte-Carlo samples are reweighted as shown in figure 8.1.

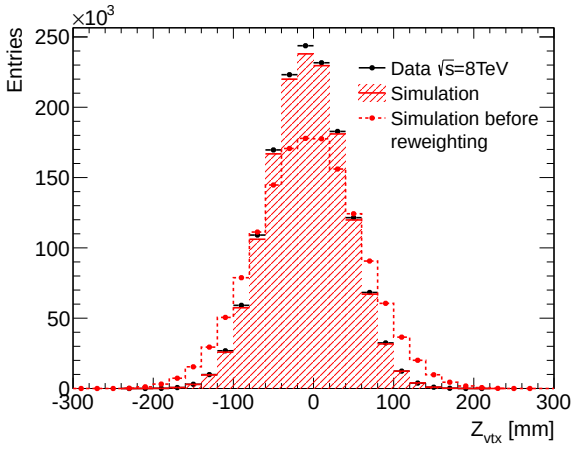

Figure 8.1: The z component of the primary vertex position. Effect of the reweighting applied on the simulation is shown.

- Lineshape correction.
  Higher order electroweak effects are included in the simulation by using the so-called Improved Born Approximation (IBA), which consists in making the tree-level photon coupling scale-dependent $\alpha_{\mathrm{EM}} \to \alpha_{\mathrm{EM}}(s)$ and rescaling the Z coupling according to

$$\frac{\pi\alpha}{\sqrt{2}\sin^2\theta_W\cos^2\theta_W} \to \frac{\pi\alpha(1+\Delta\rho)}{\sqrt{2}\sin^2\theta_W\cos^2\theta_W} \tag{8.1}$$

  Since the input electroweak parameters differ among generators, a reweighting procedure is devised in order to unify the different input parameters and make them consistent with the IBA. More specifically, the Breit-Wigner form is reweighted according to

$$m_Z\Gamma_Z \to \frac{s}{m_Z}\Gamma_Z. \tag{8.2}$$

  The effect of the lineshape reweighting on the POWHEG+PYTHIA8 Monte-Carlo is shown in figure 8.2

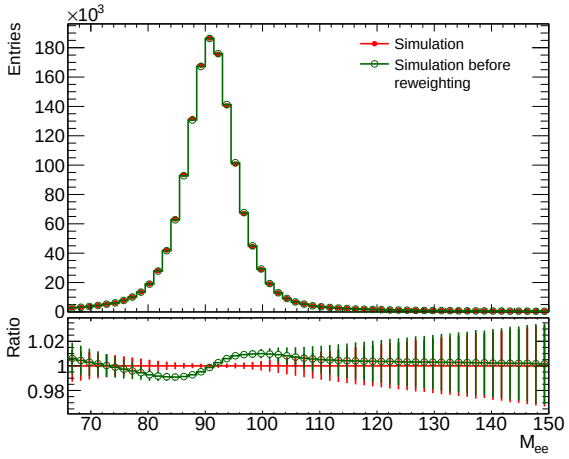

Figure 8.2: Effect of the lineshape correction on the mass distribution applied to the POWHEG+PYTHIA8 $Z \to ee$ sample.

- Pile-up correction.
  The data-taking in 2012 at the LHC is characterised by high pile-up, i.e. the presence of additional to the hard-scattering event proton-proton collisions. Since most of the particles produced in the pile-up collisions are soft, e.g. have low transverse momenta, they go to the forward region. This can potentially affect the Drell-Yan measurements with the central-forward kinematics. The pile-up interactions may occur in the same bunch crossing as the $Z \to ee$ decay (in-time pile-up) or in a different bunch crossing (out-of-time pile-up). The total level of pile-up is quantified by the variable μ while the in-time pile-up can be estimated from the number of the reconstructed primary vertices. The dilepton invariant mass distribution in the presence of low and high pile-up is shown in figure 8.3.

  The Monte-Carlo samples are produced with an average number of interactions per bunch crossing close to the one in data. A small correction is applied on simulation which affects the

distributions of μ and number of primary vertices as shown in figures 8.4, 8.5. The correction is optimized to provide the best match for both in-time and out-of-time pile-up. This include an additional rescaling factor of $1/1.09$ to account for mismatch between simulation and data in the vertex multiplicity.

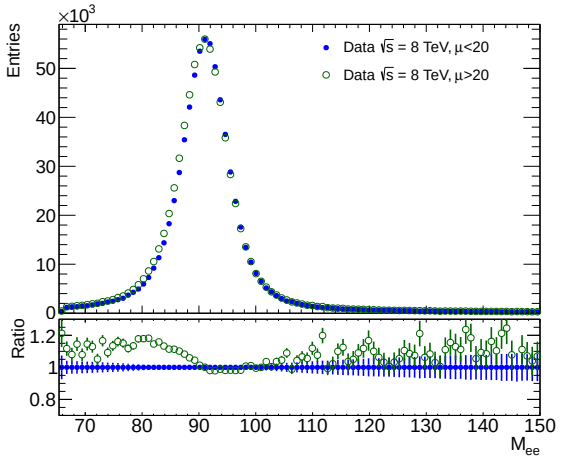

Figure 8.3: M_{ee} distribution in presence of high pile-up ($\mu > 20$) and low pile-up ($\mu < 20$).

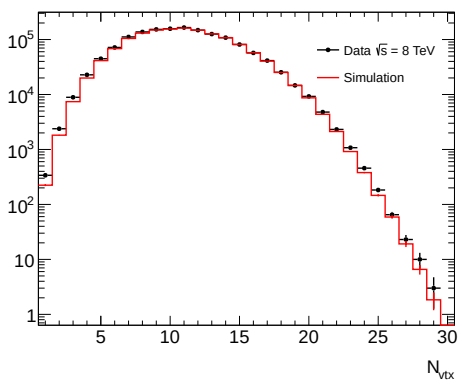

Figure 8.4: Number of reconstructed primary vertices. The Monte-Carlo distribution is rescaled on 1/1.09 to account for mismatch between simulation and data in the vertex multiplicity.

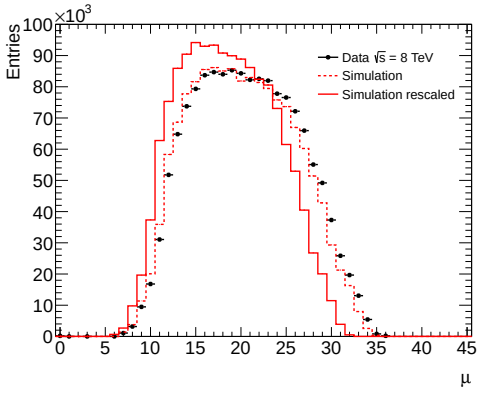

Figure 8.5: Average number of interactions per bunch crossing. The Monte-Carlo distribution is shown after pile-up reweighting with and without applying rescaling of 1/1.09.

CHAPTER 9

Binning definition and bin-to-bin migration effects

The large data sample collected with the ATLAS detector in 2012 allows to study the cross-section in multiple dimensions. The choice of binning for the differential cross-section measurement is an important part of the analysis optimization. It affects the statistical precision of the measurement and the choice of the cross-section unfolding method. The binning should be coarse enough to take into account the limited resolution of the detector and the effects of the corrections applied to the simulation. On the other hand the binning should be fine enough to reflect the dependency of the cross-section on the chosen dimensions.

The binning for the triple-differential cross-section measurement is formed by the edges of the dielectron invariant mass, rapidity and $\cos\theta^*_{CS}$ distributions as shown in table 9.1. The choice of the dielectron invariant mass region between 66 and 150 GeV follows the analysis selection and is explained in section 7.1. The dielectron rapidity range partially overlaps with the central-central measurement, which spans the rapidity range up to $|y_{Z/\gamma^*}| = 2.4$. The limit of $|y_{Z/\gamma^*}| = 3.6$ is due to the coverage of the ATLAS detector. The $\cos\theta^*_{CS}$ distribution covers the entire acceptance. The measurements of the single-differential cross-section as a function of M_{ee}, $|y_{Z/\gamma^*}|$ and $\cos\theta^*_{CS}$ follow the same binning.

Measurement dimension	Bin edges
M_{ee} [GeV]	66, 80, 91, 102, 116, 150
$\lvert y_{Z/\gamma^*}\rvert$	1.2, 1.6, 2.0, 2.4, 2.8, 3.6
$\cos\theta^*_{CS}$	-1.0, -0.7, -0.4, 0.0, 0.4, 0.7, 1.0

Table 9.1: The binning definition for the triple-differential and single-differential cross-section measurements.

The limited detector resolution and the corrections applied cause migrations of events between bins. Two effects can be distinguished: (i) the migration of events from different bins at the generated level into a given bin i at reconstruction level, measured in terms of the bin purity and (ii) the migration

of events out of a given bin i at the generated level, measured in terms of the bin stability:

$$\begin{aligned} \text{Purity}^i &= \frac{N^i_{\text{rec\&gen}}}{N^i_{\text{rec}}}, \\ \text{Stability}^i &= \frac{N^i_{\text{rec\&gen}}}{N^i_{\text{gen}}}, \end{aligned} \tag{9.1}$$

here $N^i_{\text{rec\&gen}}$ is the number of reconstructed events in bin i which are generated in this bin, N^i_{rec} is the total number of events reconstructed in the bin i, and N^i_{gen} is the total number of events generated in the same bin.

The binning is optimized to reduce the migration effects by increasing the purity and stability distributions, shown in figures 9.2 and 9.3. The distributions containing simulated events are normalised to the data luminosity. The purity of the bins changes significantly as a function of the dielectron invariant mass, being quite low for the first mass bin due to the migration of events generated near the Z mass peak region. The stability of the same region is relatively high, above 0.6, which indicates the dominant direction of the event migrations: from the Z mass peak to the regions around the peak. The main source of such a migration is the smearing due to the energy resolution correction, the effect of which is described in section 13.2. The highest purity and stability are observed for the mass bin $116 < M_{ee} < 150$. In this region the cross-section is relatively flat as a function of the invariant mass and thus corrections, which shift the mass distribution, cause lower migration of the events. The amount of migration has a small dependence on the $\cos\theta^*_{CS}$ and rapidity distributions, although the purity and stability tend to be slightly higher at central $\cos\theta^*_{CS}$.

The low purity of the first mass bin ($66 < M_{ee} < 80$) does not allow for a bin-by-bin correction of the cross-section for the detector effects. As discussed in chapter 12, the Bayesian unfolding technique is needed to handle the migrations.

With the defined binning the available number of events is not distributed uniformly among the bins. To keep the precision of the cross-section measurements high, bins with too few events, which do not allow for a reliable background estimation, are rejected (shown in white in the purity and stability plots). Such bins include in particular regions of low rapidity at low $\cos\theta^*_{CS}$, which are kinematically not accessible with the central-forward configuration (these are more easily accessible by the the central-central measurements). The amount of events available for the chosen binning is visualised in figure 9.4. There are 118 bins available for the cross-section calculations.

Representing of distributions with the triple-differential binning is not always straightforward, especially when multiple curves need to be shown. In addition to the standard 1d, 2d and 3d histograms two conventions for the binning representation are used in this work.

- $2d \rightarrow 1d$ representation. Within each mass bin, the bins in rapidity and $\cos\theta^*_{CS}$ are enumerated from 1 to 30[1] and ordered as shown in table 9.2.

- $3d \rightarrow 1d$ representation uses an axis with 150 bins[1]. The bins are ordered to first run over rapidity, then over $\cos\theta^*_{CS}$ and lastly over the mass bins. The graphical representation of this scheme is shown in figure 9.1 and the complete table of the $3d \rightarrow 1d$ bin number meaning is given in Appendix B.

[1] The bins that are excluded from the measurement still have their positions in both conventional representations, but they are not filled.

$\cos\theta^*_{CS}$ \ $\lvert y_{Z/\gamma^*}\rvert$	1.2 – 1.6	1.6 – 2.0	2.0 – 2.4	2.4 – 2.8	2.8 – 3.6
-1.0 – -0.7	1	2	3	4	5
-0.7 – -0.4	6	7	8	9	10
-0.4 – 0.0	11	12	13	14	15
0.0 – 0.4	16	17	18	19	20
0.4 – 0.7	21	22	23	24	25
0.7 – 1.0	26	27	28	29	30

Table 9.2: $2d \rightarrow 1d$ bin number convention for representation of the triple-differential binning. Within each mass bin the binning of $|y_{ee}|$ and $\cos\theta^*_{CS}$ can be formed using the corresponding bin number.

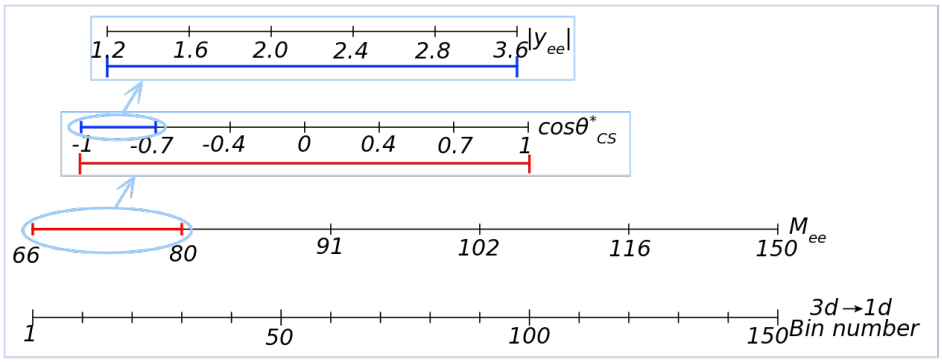

Figure 9.1: $3d \rightarrow 1d$ binning representation. A unique number is assigned to each analysis bin, from 1 to 150. The numbers are assigned by sorting the bins first by their mass window, then by $\cos\theta^*_{CS}$ region, and lastly by their rapidity bin. The one-to-one correspondence is shown in Appendix B.

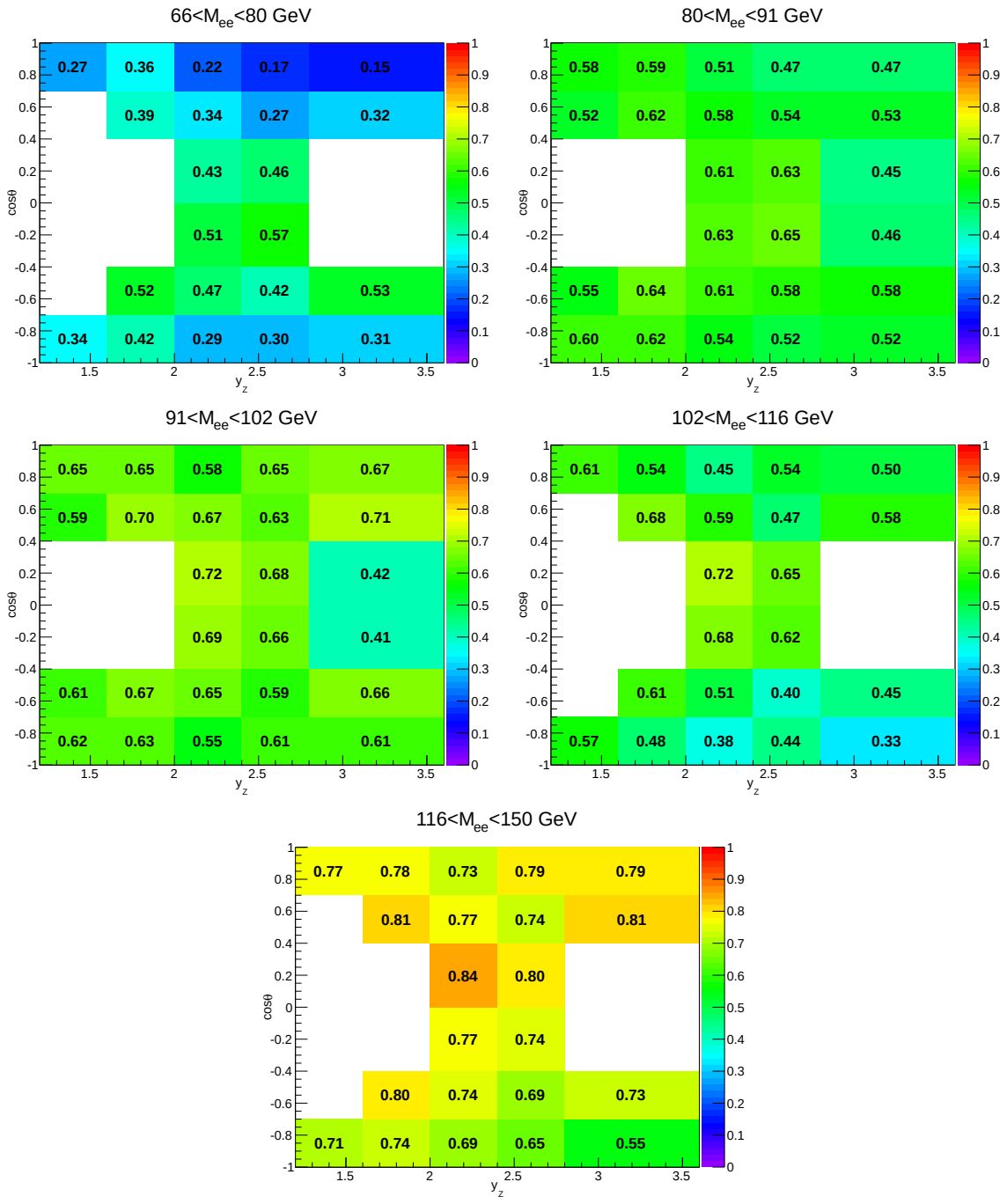

Figure 9.2: Purity of the binning describing the migration of events into the bins. Purity shows the fraction of reconstructed events that were generated in the same bin, from the total number of events reconstructed in this bin.

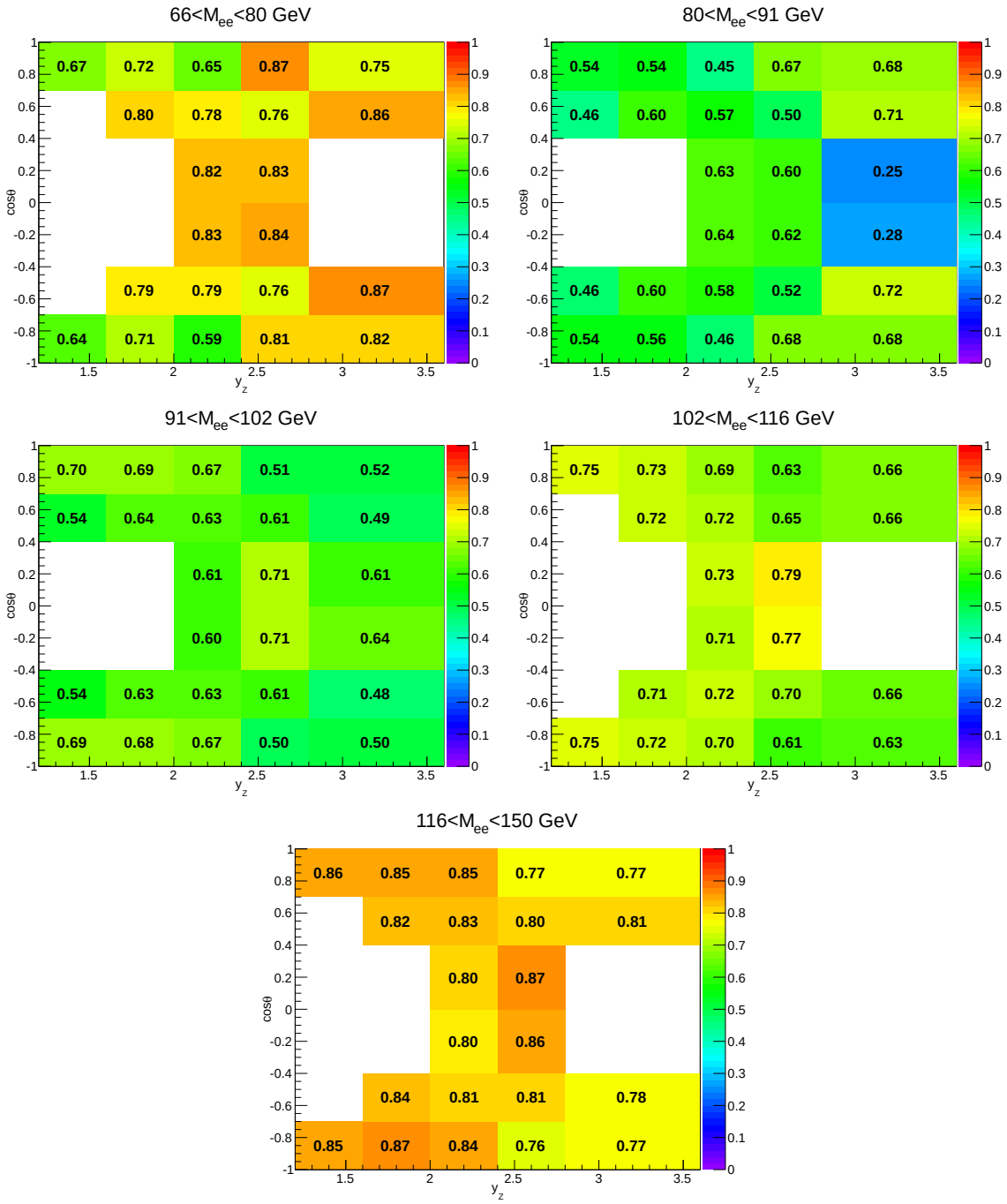

Figure 9.3: Stability of the binning shows the fraction of generated events remaining in the bin after reconstruction.

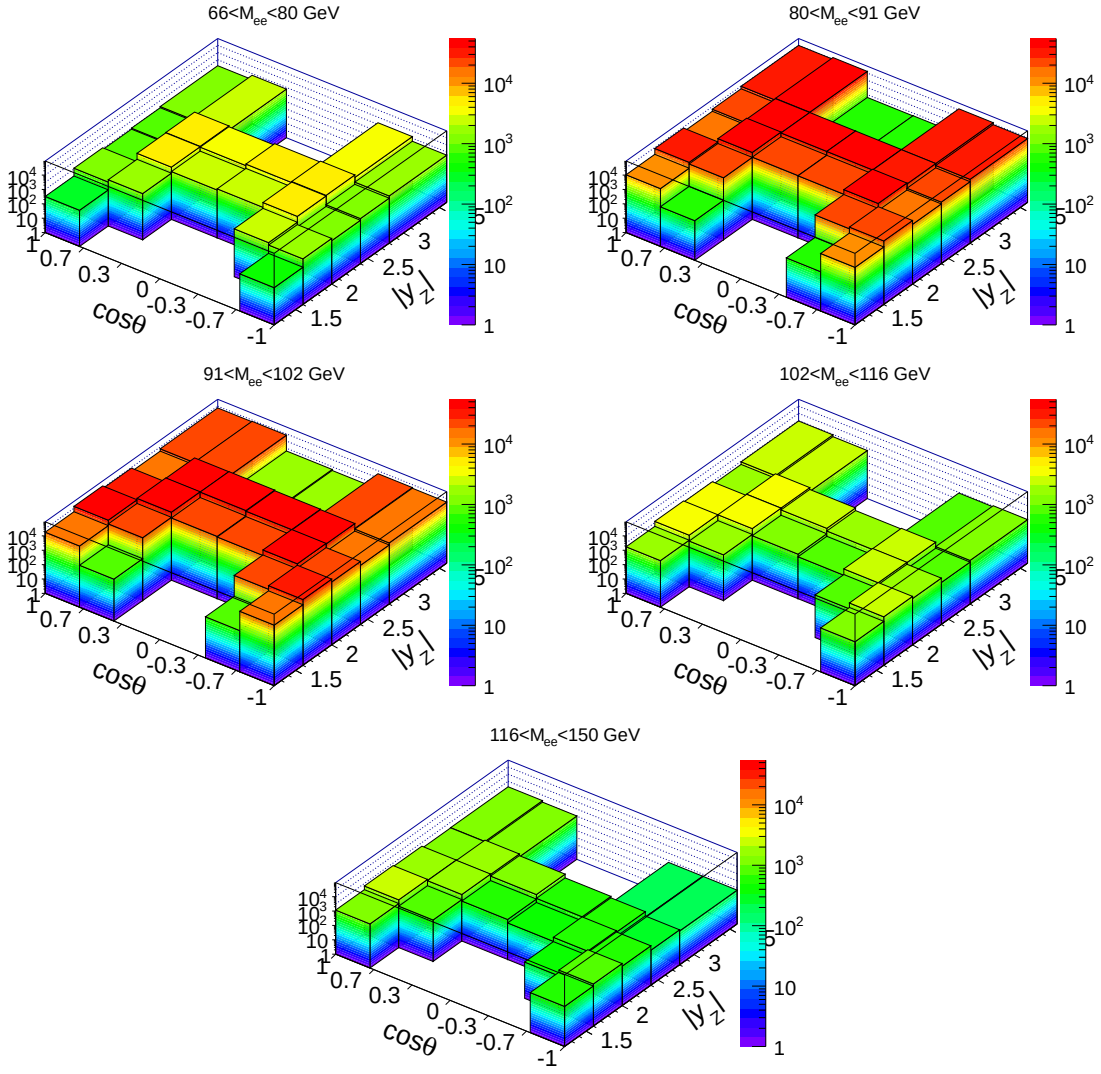

Figure 9.4: Available statistics for the measurements. Number of events in each bin is obtained from Monte-Carlo simulation normalized to the data luminosity.

CHAPTER 10

Background estimation

The processes that constitute the background to $pp \to Z/\gamma^* \to e^+e^-$ can be combined into four categories with respect to their final-state configuration, schematically shown in figure 10.1.

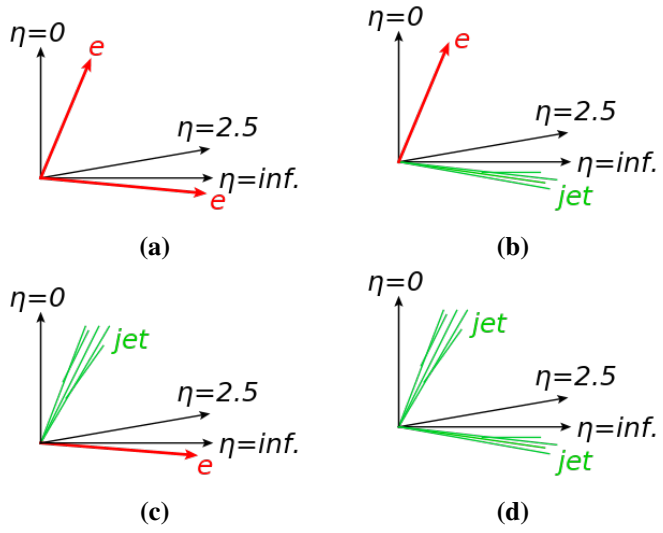

Figure 10.1: Possible configurations of final states for background events. The dielectron pair can be formed by real electrons or hadronic jets mis-identified as electrons.

The first category consists of processes with two or more electrons in the final state (figure 10.1a). These contain

- $t\bar{t}$ events which may decay as $t\bar{t} \to W^+W^-b\bar{b} \to e^+\nu_e e^-\bar{\nu}_e b\bar{b}$;
- single top production in the Wt channel ($bg \to tW^-$) where the W^- boson and the top quark decay as $W^- \to e\bar{\nu}_e$, $t \to W^+b \to e^+\nu_e b$;
- Drell-Yan production $Z \to \tau^+\tau^-$, with both τ-leptons decaying into electrons and neutrinos: $\tau^- \to W^-\nu_\tau \to \bar{\nu}_e e^-\nu_\tau$, $\tau^+ \to W^+\bar{\nu}_\tau \to \nu_e e^+\bar{\nu}_\tau$;
- diboson processes: ZZ, WZ and WW, which lead to two, three or four electrons from the decay of W and Z bosons;
- background from $\gamma\gamma \to e^+e^-$ processes.

The next two categories (figures 10.1b, 10.1c) contain processes with one real electron, and one jet which passed the electron identification criteria. Such processes are coming from

- $W^{\pm} \to e^{\pm}\nu_e$ + jets production;
- $W^{\pm} \to \tau^{\pm}\nu_\tau$ + jets, where the τ decays into an electron and neutrinos;
- single-top production in s- and t-channels with the top quarks decaying into electrons.

The processes from the first category containing semi-leptonic decays also contribute here.

The last category consists of events where two jets are misidentified as electrons (figure 10.1d). This multi-jet background is highly suppressed by the tight identification criteria applied on electrons. However this background has a large cross-section which leads to a relatively high contribution to the selected data sample. Among the QCD processes that contribute to the background are semi-leptonic heavy-flavor decays and Dalitz decay.

Therefore the main background processes to the Drell-Yan process are: multi-jets, $W \to e\nu$ + jets; $W \to \tau\nu$ + jets, $Z \to \tau^+\tau^-$, WW, WZ, ZZ, top production. The background events with final states of types (a) and (b) are estimated from simulation normalized to the data luminosity. Category (b) consists mainly of $W \to e\nu$ events. A data-driven method is used to account for background of types (c) and (d). In this data-driven method the central electron isolation is used as a discriminating variable, as explained in section 10.1.2.

10.1 Data-driven template method

Multi-jet events have large cross-sections and the simulation of such processes has a large statistical uncertainty (following $N = \int dtL\sigma$). The background due to multi-jet production can instead be estimated from data. The sample obtained from data by suppressing the signal events is called the template sample. Another component of the template method is the discriminating variable which allows to distinguish between signal and background events and normalize the template sample.

10.1.1 Purity of the template selection

The template sample is formed by modifying the signal selection. Multi-jet events require to fulfil the same kinematic criteria, but the identification requirements are inverted in order to suppress the signal events. The normalization of this sample to the data differs from the normalization of the electroweak background processes estimated from simulation, as described in section 10.1.3.

The template sample is built by requiring the central electron candidate to fail the tight identification criteria, but to pass the medium selection. The forward electron candidate is required to fail the tight forward identification.

The sample extracted from data contains not only multi-jet events, but also events from other background processes. Non-negligible contributions are mostly from $W \to e\nu$ events. In order to avoid double-counting the background events from electroweak processes and top production, the template selection is additionally applied to the background Monte-Carlo simulation. The resulting samples are subtracted from the final data template sample. Due to imperfections in the template selection some signal events can also pass the template criteria. This effect is taken into account by applying the template selection on the signal Monte-Carlo and excluding the resulting sample from the data template sample. The purity of the template sample P_{Template} can be quantified from

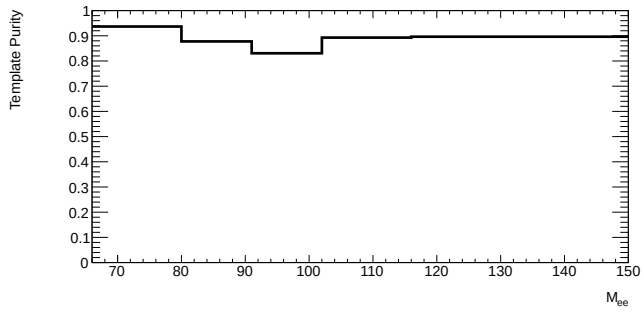

Figure 10.2: Purity of the template sample as a function of the dielectron invariant mass.

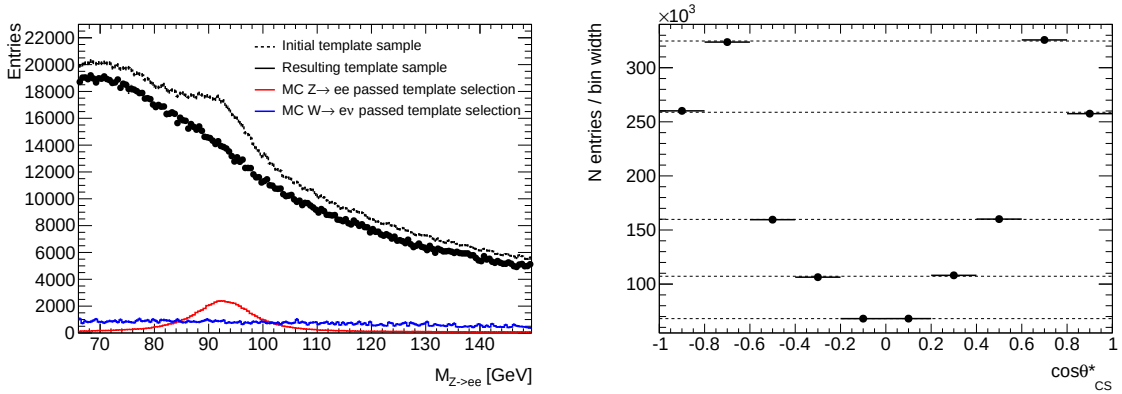

Figure 10.3: The mass (left) and $\cos\theta^*_{CS}$ (right) distributions of the the resulting template sample.

the number of data events $N_{data\,templ.}$ and the sum of the simulated signal and background events $\sum N_{templ.MC} = N_{templ.sig.MC} + \sum N_{templ.bkg.MC}$ which passed the template selection as follows:

$$P_{\text{Template}} = \frac{N_{data\,templ.} - \sum N_{templ.MC}}{N_{data\,templ.}}. \tag{10.1}$$

The purity of the template sample as a function of M_{ee} is shown in figure 10.2. Figure 10.3 shows the control distributions of the template sample. The shape of the mass distribution is expected to be smooth with the number of events decreasing as the energy grows. The Forward-Backward asymmetry is not a property of multi-jet events, thus the distribution of the template sample as a function of $\cos\theta^*_{CS}$ is expected to be symmetric with respect to zero.

10.1.2 Choice of discriminating variable

The estimation of the multi-jet background is based on our understanding of the isolation of electrons and hadronic jets. In the calorimeter an electron should be surrounded by smaller energy deposits within a cone centered around the cluster barycenter as shown in figure 10.4. Within a cone of a certain radius ΔR the cell energy is summed, (excluding the electron cluster energy) and stored in an energy cone variable $E_T Cone$. A relative isolation variable is then defined as the ratio of the energy inside the cone to the transverse energy of the electron: $Isolation = \frac{E_T Cone}{E_T^{elec}}$. Energy cone variables

of radius $\Delta R = 0.2$ and $\Delta R = 0.3$ were tested and found to give similar results for the background estimate. A cone of a radius $\Delta R = 0.3$ is used in the current measurement for the background studies.

The peak of the isolation distribution is formed by electrons whose cluster energy dominates over the energy in the cone. For the low dielectron invariant masses and high rapidities, Bremsstrahlung photons can be emitted from electrons at high angles. The energy of such photons will then be reconstructed within the $E_T Cone$ and not as part of the electron cluster energy. Another effect giving rise to the isolation tail is lateral leakage of the energy outside the reconstructed cluster. This effect is minimized by applying a correction on the isolation variable, as described in section 6.4. Due to aforementioned effects the tail of the isolation distribution contains contributions from both signal and multi-jet processes.

Apart from the isolation distribution, the multi-jets background can be normalized using the di-electron invariant mass spectrum, where the normalization is based on the difference between the shapes of the template sample (see figure 10.3) and $Z \to ee$ events. However the invariant mass distribution is one the measured quantities in the presented analyses and its direct use in the multi-jets background estimation is avoided in order to prevent biasing the measurements. Other possible discriminating variables can be defined using the momentum distributions of the electrons. The use of transverse momentum of the forward electrons is discussed in the following section.

10.1.3 Methodology of the template sample normalization

The template sample is normalized to the data in the tail of the isolation distribution where the multi-jets contribution is expected to have a bigger impact. The choice of the right edge of the normalization region is driven by the isolation distribution of the data sample and is fixed to the last non-empty bin. In order to take into account the presence of signal in the tail, the left edge is determined dynamically for each individual bin by adapting the discriminating requirement. The initial requirement is that the data is higher than the signal Monte-Carlo in the normalization region by at least factor of two. The size of the normalization region is determined by an iterative procedure, whereby, starting from $Isolation = 0.1$ (where the multi-jet background starts to grow) the left edge is shifted towards the right until the discriminating requirement is fulfilled. The normalization region is required to be wide enough to avoid statistical fluctuations, which is particularly important for three-dimensional binning. If a region is found to be too narrow, namely less than $\Delta Isolation = 0.1$, the requirement of data to Monte-Carlo ratio in the normalization region is lowered and the scan is repeated.

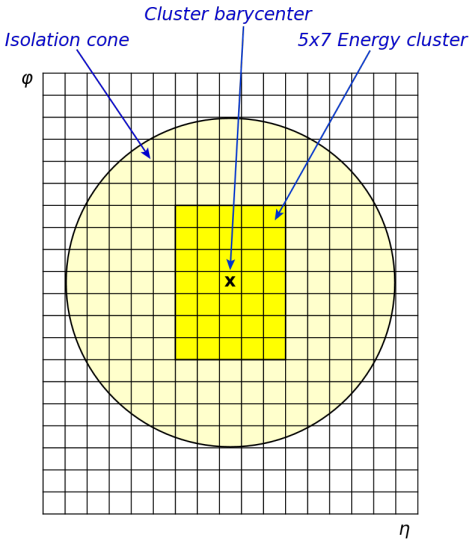

Figure 10.4: Sketch of energy isolation cone.

The number of multi-jet events $N_{multi\text{-}jets}$ is calculated as

$$N_{multi\text{-}jets} = scale_{multi\text{-}jets} \cdot \left(N_{data\ templ.} - \sum N_{templ.bkg.MC} - N_{templ.sig.MC} \cdot scale^{k}_{sig.MC} \right). \qquad (10.2)$$

The normalization scale $scale_{multi\text{-}jets}$ for the template selection is calculated using the number of

events in the tail of the isolation distribution for data N^{tail}_{data}, and for data, signal and background Monte-Carlo events passing the template selection $N^{tail}_{templ.}$, $N^{tail}_{sig.MC}$ and $N^{tail}_{bkg.MC}$ respectively, according to

$$scale_{multi\text{-}jets} = \frac{N^{tail}_{data} - (scale^{k}_{sig.MC} \cdot N^{tail}_{sig.MC} + \sum N^{tail}_{bkg.MC})}{N^{tail}_{data\ templ.} - \left(scale^{k}_{sig.MC} \cdot N^{tail}_{templ.sig.MC} + \sum N^{tail}_{templ.bkg.MC}\right)}, \tag{10.3}$$

where

$$scale^{k}_{sig.MC} = \frac{N_{data} - \sum N_{bkg.MC} - N_{multi\text{-}jets}}{N_{sig.MC}}. \tag{10.4}$$

Here $scale^{k}_{sig.MC}$ is estimated iteratively starting with $scale^{k=1}_{sig.MC} = 1$, which corresponds to the normalization of the signal Monte-Carlo using the NNLO cross-section. As a next step, the Monte-Carlo expectations are normalized to the measured cross-section. This procedure converges typically after three iterations, when the change of $scale^{k}_{sig.MC}$ becomes less than 0.1%. It avoids bias of the measurement to the theoretical prediction for the cross-section.

The background estimation is tested on the integrated distribution and in two bins of forward electron rapidity: $2.5 < |\eta^{\text{elec. fwd}}| < 3.16$ (EMEC) and $3.25 < |\eta^{\text{elec. fwd}}| < 4.9$ (FCal). The result of the estimation is shown in figures 10.5 together with derived scale factors $scale_{multi\text{-}jets}$ in each of the three cases.

The background is estimated both triple and single-differentially as a function of M_{ee}, $|y_{Z/\gamma^*}|$ and $|\cos\theta^*_{CS}|$. The absolute value of $\cos\theta^*_{CS}$ it taken as no asymmetry is expected for background events. The increased statistics allows to reduce the uncertainty on the background estimation, which is important for the triple-differential measurement. The result of the multi-jet background normalization for each bin of the triple-differential measurement is given in Appendix C.

Additionally the background is estimated using forward electrons. This estimate exploits the fact that the p_T distribution for electrons from $Z \to ee$ events has a different shape compared to the multi-jets background, which peaks at zero. Thus the $p_T^{\text{elec. fwd}}$ distribution is used as a discriminating variable. The analysis selection require $p_T^{\text{elec. fwd}}$ above 20 GeV (see chapter 7), where the discrimination between data and background is reduced compared to low $p_T^{\text{elec fwd}}$ regions. The data-driven estimation techniques require to have high enough data-to-background fraction of events in the normalization region for reliable results, following that the $p_T^{\text{elec. fwd}}$ method give the best estimates in regions with a high background contamination. An example of the background estimation based on the p_T shape of forward electrons at the edges of the M_{ee} distribution is shown in figure 10.6. The two discriminating variables give similar results for the multi-jet background estimation. However in regions of low invariant masses, the $p_T^{\text{elec. fwd}}$ method is found to give higher estimate on the number of multi-jets events. This is taken into account by averaging the two estimates and assigning an additional uncertainty, derived from the difference of the two methods.

The estimation of the background for the single-differential M_{ee} cross-section measurement is shown in figures 10.7. Similar collection of figures for the $|y_{Z/\gamma^*}|$ and $|\cos\theta^*_{CS}|$ single-differential cases and for the triple-differential measurements, together with the adaptation of the method for the triple-differential case, are given in Appendix C.

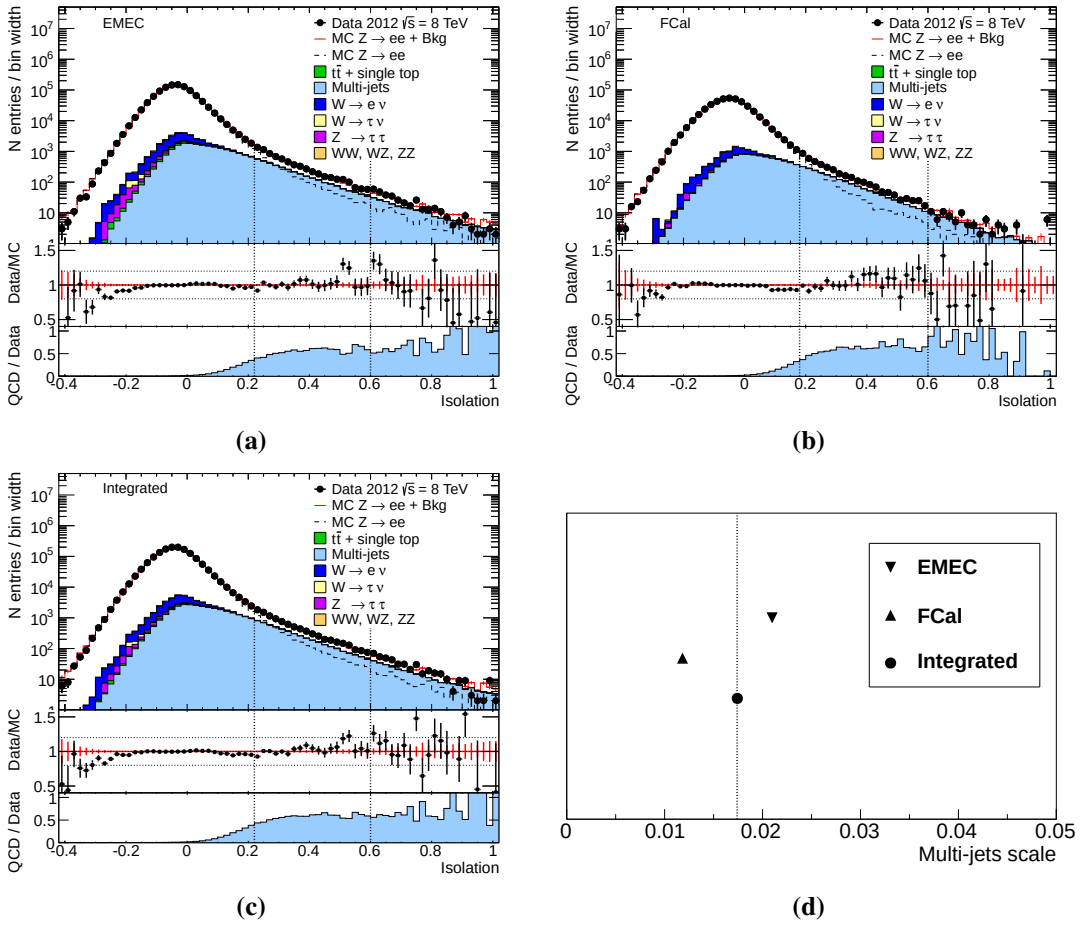

Figure 10.5: The multi-jet background estimation in cases when forward electron is detected by EMEC ($2.5 < |\eta^{fwdelec}| < 3.16$) (a) and FCal ($3.25 < |\eta^{fwdelec}| < 4.9$) (b), and the integrated case (c). The resulting scale factors are given in (d).

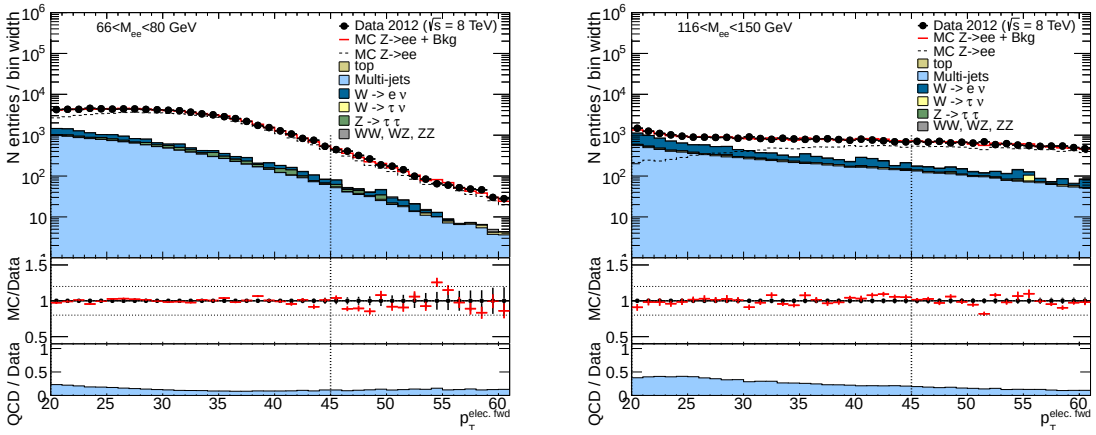

Figure 10.6: Estimation of the multi-jets background as a function of forward electron p_T. Two mass regions are shown, $66 < M_{ee} < 80$ GeV and $116 < M_{ee} < 150$ GeV.

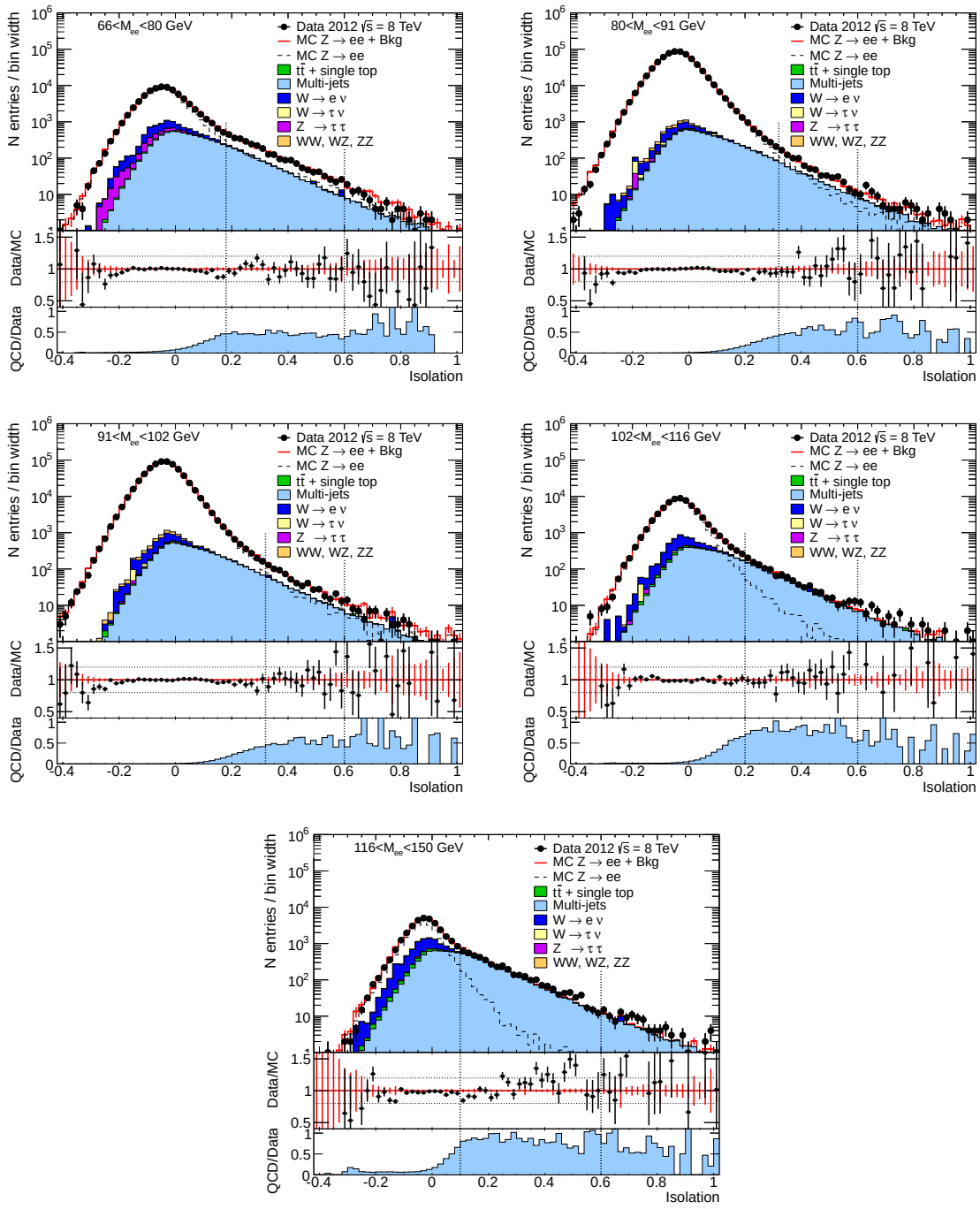

Figure 10.7: The multi-jets background estimation using *Isolation* distribution in different bins of M_{ee} integrated over rapidity and $\cos\theta^*_{CS}$.

10.2 Uncertainties on the data-driven method

The uncertainty of the multi-jets background estimation $\delta_{Multi\text{-}jets}$ is given by

$$\delta_{Multi\text{-}jets} = \sqrt{(\delta_{stat.})^2 + (\delta_{norm.region})^2 + (\delta_{templ.shape})^2} \tag{10.5}$$

and is comprised of

- statistical component $\delta_{stat.}$,
- uncertainty due to the choice of a normalization region $\delta_{norm.region}$,
- uncertainty from the template formation $\delta_{templ.shape}$.

The statistical component of the uncertainty is evaluated using the bootstrap method described in section 13.1.3. The data and template samples are resampled into 200 bootstrap replicas, and the background estimation is repeated in each bin using the resulting distributions. In order to avoid double counting the uncertainties related to the choice of the normalization region, the region used for the original sample is kept fixed for all replicas in a given bin.

The second component of the uncertainty on the multi-jet background estimation is evaluated from the difference of the template fit results using different normalization regions. The variation of the normalization region is obtained by systematically shifting the left edge towards the right edge as it is schematically shown in figure 10.8. The left edge is shifted towards the center of the initial region within 10 iterations, so that each step is equal to

$$\text{Step} = \frac{\frac{1}{2}(\text{Edge}^{Left} - \text{Edge}^{Right})}{10}. \tag{10.6}$$

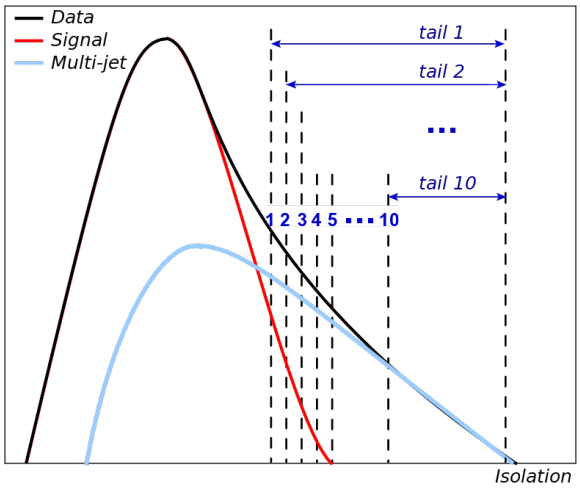

Figure 10.8: Schematic illustration of the normalization tail scan. Left edge of the tail is shifted towards the right edge within ten iterations until it reaches the middle of the normalization region. Multi-jet scale factor is calculated for each of the ten normalization tails.

The scan stops in the middle of the tail to minimize the effects from statistical fluctuations in the poorly populated end of the isolation distribution. For the same reason the right edge is not varied for the uncertainty determination. After each iteration the multi-jet scale factor is recalculated. The uncertainty is taken to cover all the observed values of the normalization scale. The size of the systematic uncertainty estimated from the scan of the integrated mass bins is shown in figure 10.9. The scans of the normalization regions for the single-differential $|y_{Z/\gamma^*}|$ and $\cos\theta^*_{CS}$ measurements are shown in Appendix C. In the triple-differential case only very few measured bins around the Z mass peak allow for the scan of the normalization region. Due to the limited statistics the uncertainty in this case is given by the difference of the background estimate obtained with two different discriminating variables, *Isolation* and p_T of forward electron. The uncertainties of the triple-differential measurements are discussed in Appendix C.

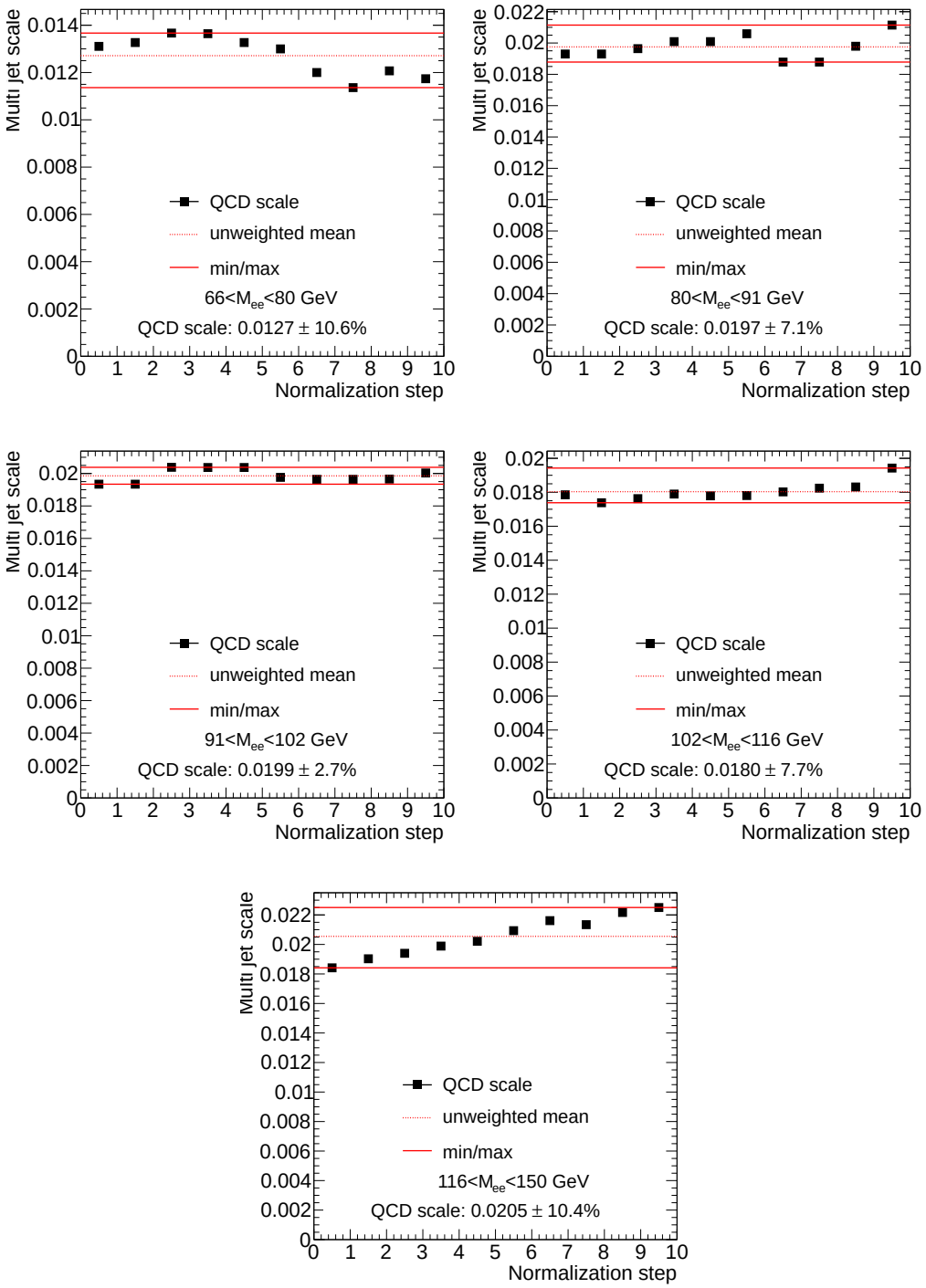

Figure 10.9: The correlated systematic uncertainty of the multi-jet background estimation obtained from the scan of the normalization region. The uncertainty is estimated in the mass regions integrated over rapidity and $\cos\theta^*_{CS}$.

Monte-Carlo simulation is used to estimate the number of non-multi-jets events in the template sample as is described in section 10.1.1. The uncertainties of the Monte-Carlo cross-section, given in tables 5.2, 5.3, affect the background estimation through the size and shape of the resulting template sample. Since the purity of the template sample is high (figure 10.2) this source of uncertainty is small compared to the previously discussed sources.

The results on the multi-jet background scale are shown in figure 10.10. The statistical and systematic variations of the scale are propagated to the cross-section as described in section 13.2. The fraction of the estimated background events for the single-differential measurements is shown in figures 10.11, and for the triple-differential case is given in Appendix C.

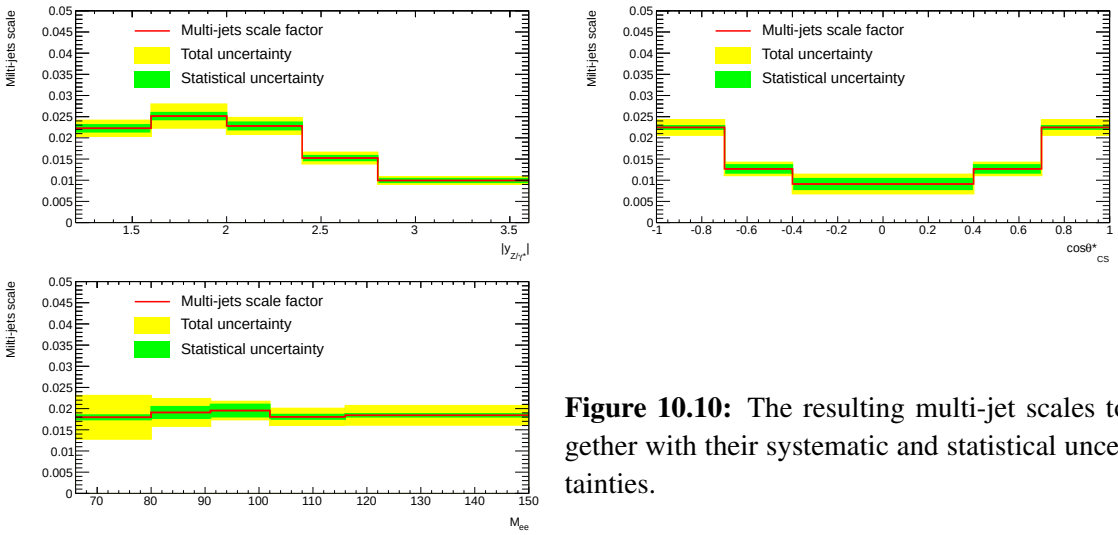

Figure 10.10: The resulting multi-jet scales together with their systematic and statistical uncertainties.

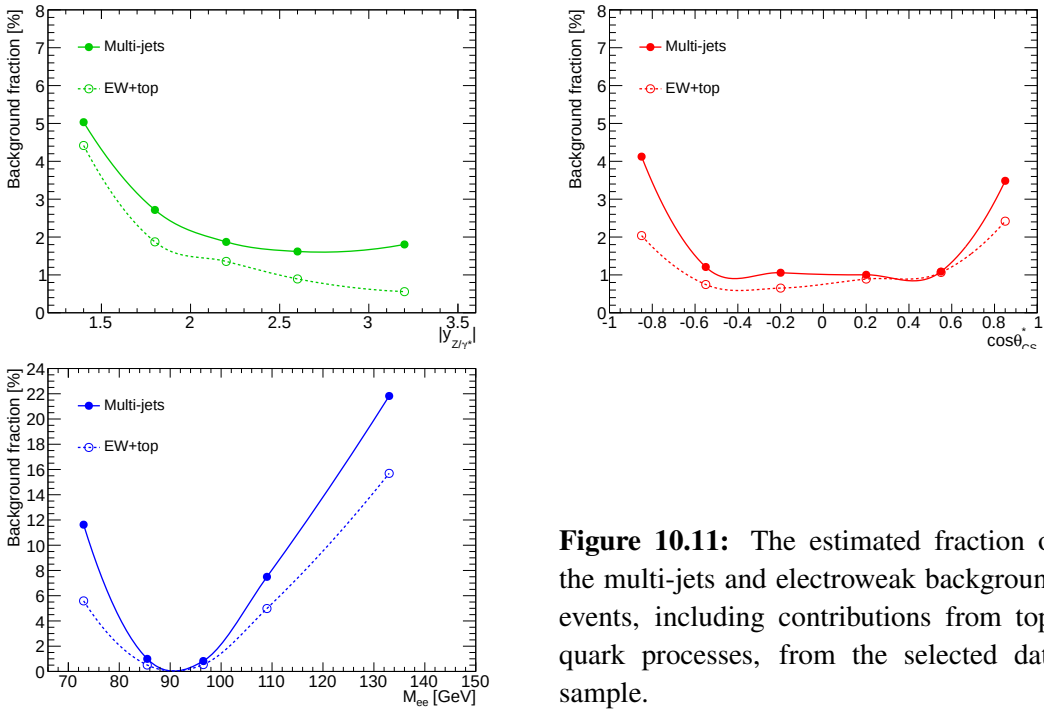

Figure 10.11: The estimated fraction of the multi-jets and electroweak background events, including contributions from top-quark processes, from the selected data sample.

CHAPTER 11

Control distributions

Once the background is estimated and all the corrections are applied to data and simulation, the agreement between data and Monte-Carlo is examined. Figure 11.1 shows control observables used for the cross-section measurement, plotted as single-differential distributions of M_{ee}, $|y_{Z/\gamma^*}|$ and $\cos\theta^*_{CS}$. The data is compared to the signal simulation and the background contribution from different processes is overlaid on the signal. The multi-jets background is normalized using an average scale of 0.0174 derived from the isolation distribution integrated over M_{ee}, $|y_{Z/\gamma^*}|$ and $\cos\theta^*_{CS}$ (see figure 10.5). The ratio distributions contain the statistical uncertainty of the simulation shown as a yellow band. The first set of control plots (figure 11.1) also contains the systematic uncertainty added in quadrature to the statistical one, which is shown as a green band. The uncertainties include all the sources described in chapter 13, except of those related to the PDF reweighting and multi-jets background determination, which requieres estimation in each bin, while an integrated scale is used for the control distributions.

The simulation is found to describe the dielectron invariant mass spectrum within 5% around the Z pole and within 13% at the edges of the distribution. An improvement in the data to Monte-Carlo agreement is achieved by applying additional smearing correction factors for forward electron energy to the simulation (see figure 6.2). However the residual discrepancy require further updates of the corrections, due to change of the geometry modeling in the GEANT4 simulation. The rapidity distribution lies within the uncertainties, except of the regions close to central rapidity, which have low statistics in the central-forward configuration. An agreement within 5% is found between the data and the simulated distributions for $\cos\theta^*_{CS}$. The large longitudinal momentum that the Z boson acquires in the central-forward configuration, shown in figure 11.2a, is well modeled by the simulation over the entire distribution. The transverse momentum of the Z boson (figure 11.2b) is modeled well, within 5%, up to Z $p_T \approx 90$ GeV, however the overestimate of the distribution near the Z p_T peak leads to a deficit of events at higher p_T values. The missing transverse energy is shown in figure 11.2c and is described well by the simulation, including high E_T^{miss} values where background processes dominate.

The transverse and longitudinal momentum distributions of central and forward electrons are shown in figures 11.3. Central electrons are well modeled over the entire p_T range. For forward electrons, good agreement between data and simulation is found up to $p_T \approx 55$ GeV, however the tail of the p_T distribution is mis-modeled despite the resolution corrections. This in turn induces a mis-modeling of the dielectron invariant mass spectrum. The longitudinal momentum distributions of the electrons are well modeled, up to large values of p_Z for forward electrons. The pseudorapidity η^{electron} and angular distributions ϕ^{electron} built from both central and forward electrons, are well described by the simulation (see figures 11.4).

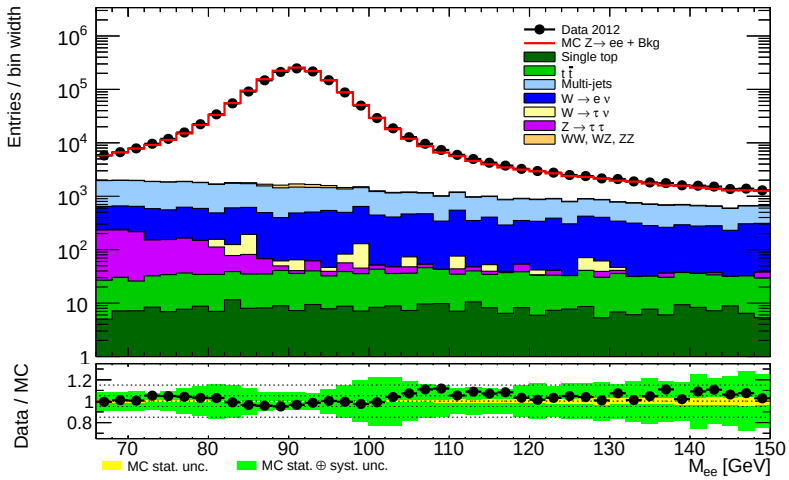

(a)

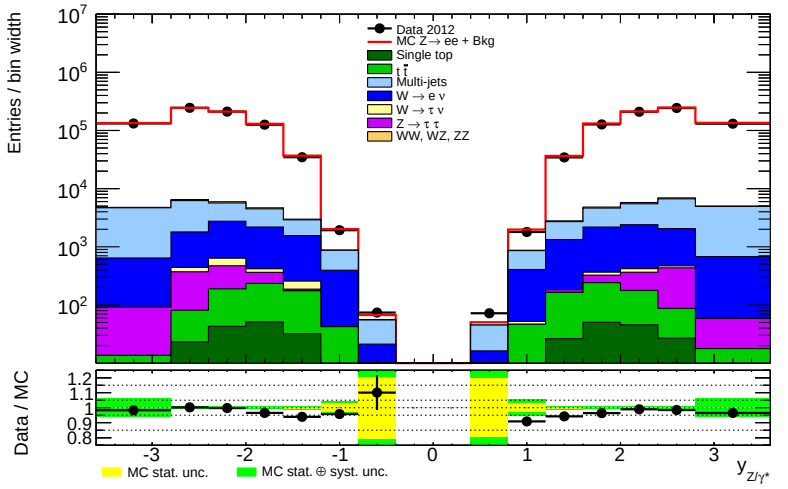

(b)

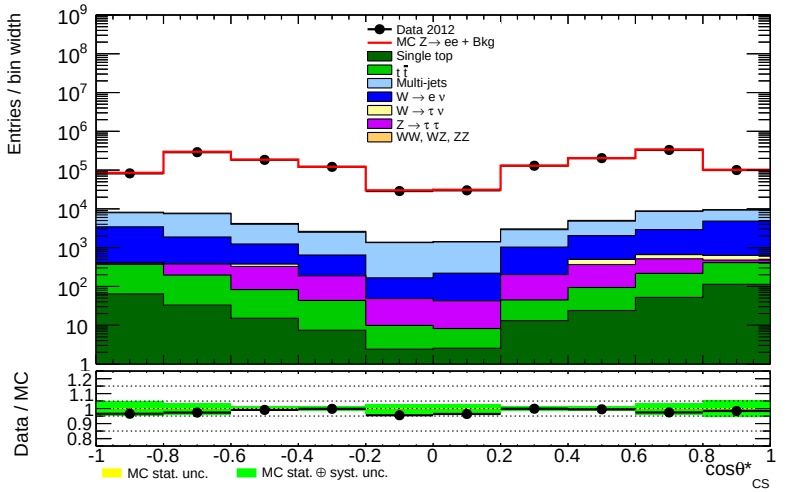

(c)

Figure 11.1: Distributions of the dilepton invariant mass (a), boson rapidity (b), and $\cos\theta^*_{CS}$ (c).

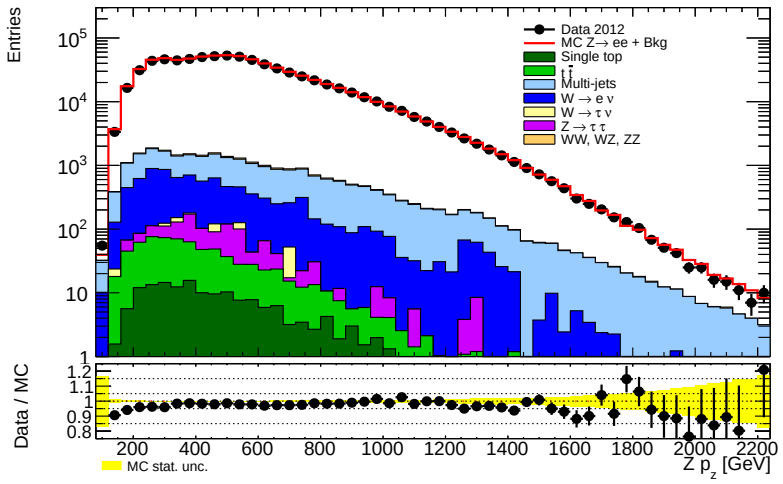

(a)

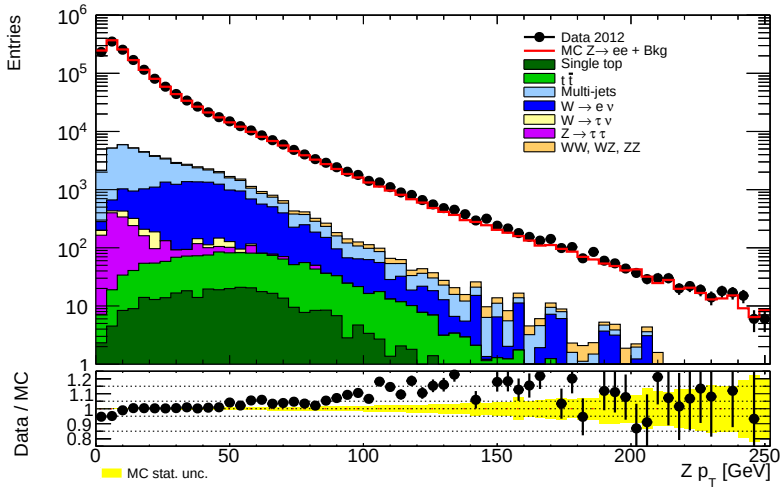

(b)

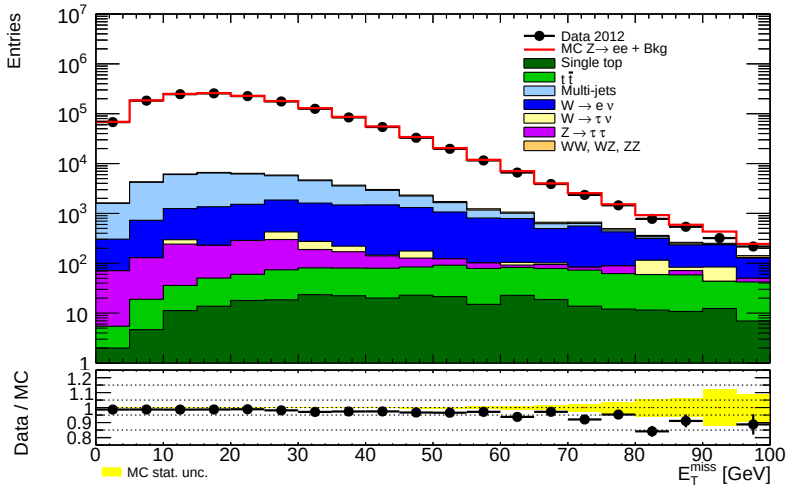

(c)

Figure 11.2: Distributions of the longitudinal (a) and transverse (b) momentum of the Z boson. Missing transverse energy (c).

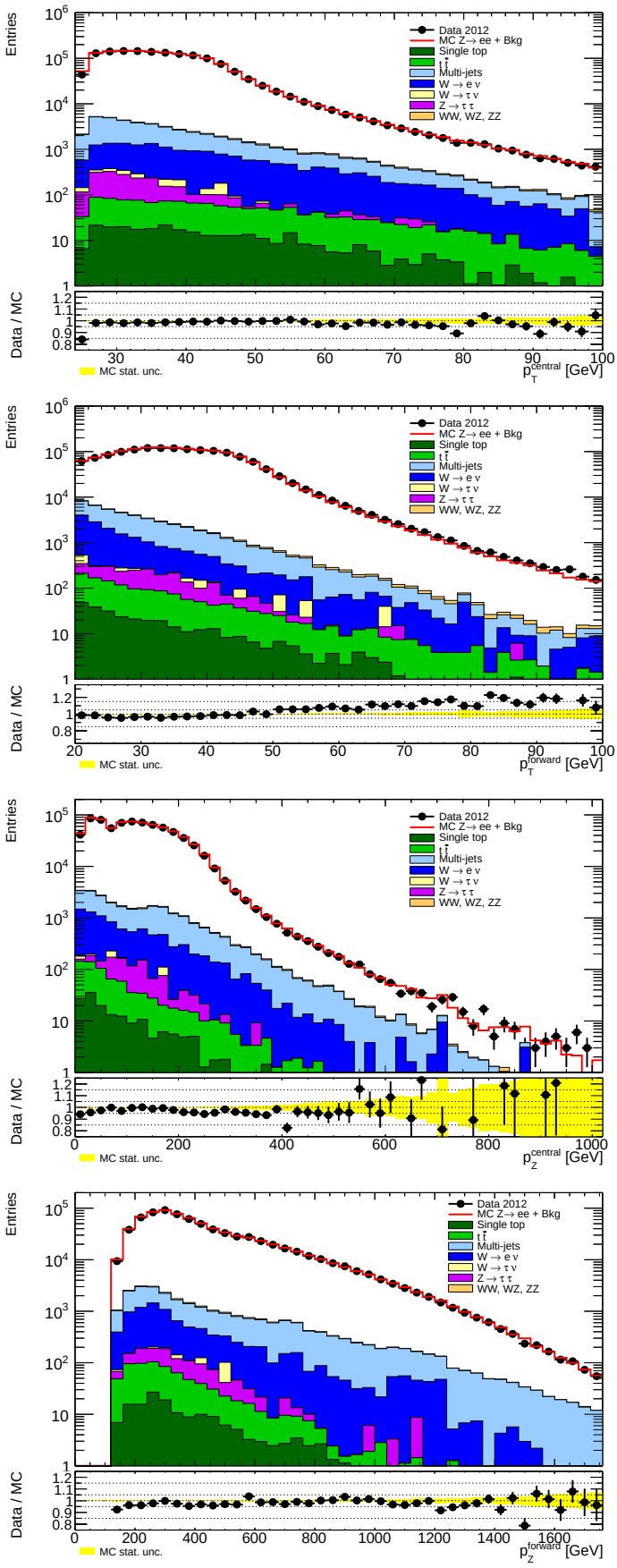

Figure 11.3: Transverse and longitudinal components of central and forward electron momentum.

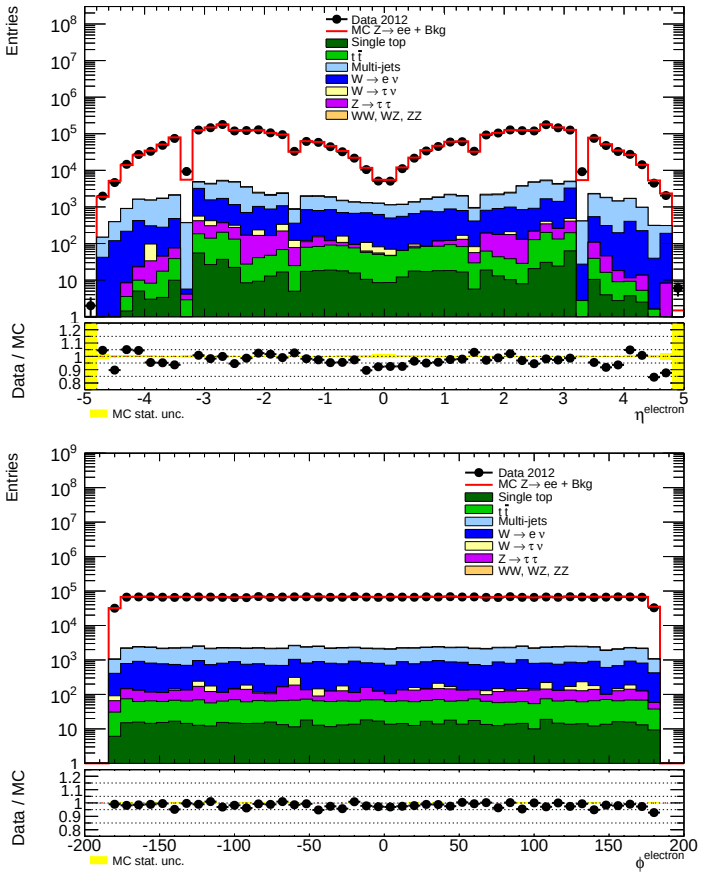

Figure 11.4: Distributions of electron pseudorapidity η^{electron} and azimutal angle ϕ^{electron}.

CHAPTER 12

Unfolding

The ultimate goal of the experimental measurement is to infer the 'true' distribution of an observable quantity from the measured one. The latter is distorted from a series of detector limitations such as electronic noise, finite detector resolution, etc. The procedure of deriving the 'true' distribution from the observed one is called unfolding.

The two most widely used unfolding techniques in ATLAS measurements are bin-by-bin correction factors and the iterative Bayesian method [81, 82]. The bin-by-bin unfolding method consists of calculating correction factors C_i in every bin i of the measured distribution according to

$$C_i = \frac{N_{i,\text{Reco}}}{N_{i,\text{Truth}}}, \tag{12.1}$$

where $N_{i,\text{Truth}}$ is the predicted number of events at the truth-level and $N_{i,\text{Reco}}$ is the predicted number of events at the reconstruction level accounting for all detector effects. The unfolded distribution in each bin is then derived as

$$N_{i,\text{Unfolded}} = \frac{N_{i,\text{Measured}}}{C_i}, \tag{12.2}$$

where $N_{i,\text{Measured}}$ is the spectrum obtained from data. The bin-by-bin method requires very good description of the data by Monte-Carlo and small level of migrations to yield reliable results.

A different approach for deriving the unfolded distribution is based on Bayes' theorem. The number of events $n(T_i)$ in bin i of the unfolded spectrum T, given an observed number of events $n(R_j)$ in bin j of the measured spectrum R is given by

$$n(T_i)|_{n(R_j)} \approx P(T_i|R_j)n(R_j), \tag{12.3}$$

where $P(T_i|R_j)$ is the probability that an observation R_j is due to the true spectrum T_i and according to Bayes' theorem is given by

$$P(T_i|R_j) = \frac{P(R_j|T_i)\,P(T_i)}{P(R_j)}. \tag{12.4}$$

In eq. (12.4), $P(R_j|T_i)$ is called the likelihood function and expresses the probability to reconstruct the spectrum R_j given the true spectrum T_i, and $P(T_i)$ is known as the prior probability. The prior probability expresses the degree of belief about the true spectrum T_i. The likelihood function is usually estimated from simulation according to the following formula:

$$P(R_j|T_i) \equiv \lambda_{ji} \approx \frac{n(R_j)^{\text{MC}}}{n(T_i)^{\text{MC}}}, \tag{12.5}$$

where $n(T_i)^{\mathrm{MC}}$ is the number of events generated according to the true spectrum T in bin i and $n(R_j)^{\mathrm{MC}}$ is the number of events reconstructed in bin j of the measured spectrum R, after simulation of the detector effects. The quantity λ_{ji} is known as response matrix.

The simplest choice for selecting the prior in eq. (12.4) is to assume $P(C_i) = const$, i.e. a *flat* true spectrum. This is a strong assumption which is rarely true in physical situations and leads to an unfolded spectrum which will be biased towards the flat spectrum. In order to decrease this bias, an iterative unfolding procedure is devised, in which at each iteration step, one replaces the prior probability of the current step with the posterior probability of the previous step. It has been shown that a small number of steps are sufficient to obtain a good description of the underlying true spectrum [82]. The initial prior can be taken as the truth distribution generated by the Monte-Carlo, in which case an optimum could be reached with fewer iterations [83]. This strategy is exploited by the RooUnfold package [84] which is used [85] to unfold the cross-section measurement.

For the Z/γ^* production cross-section measurement the one-dimensional distributions of M_{ee}, $|y_{Z/\gamma^*}|$ and $\cos\theta^*_{CS}$ lead to the response matrices shown in figure 12.1. Each matrix maps a reconstructed distribution (x-axis) onto a generated one (y-axis). The response matrix for the dielectron invariant mass distribution has sizable off-diagonal elements due to large events migrations (discussed in chapter 9). At the same time, the $|y_{Z/\gamma^*}|$ and $\cos\theta^*_{CS}$ matrices are more diagonal, since the corresponding migrations of events are smaller. The opposite diagonal in the $\cos\theta^*_{CS}$ response matrix is due to both the dilution effect and the charge misidentification of central electrons. The later appear when electron energy cluster is associated with a track of oppositely charged electron originating from a decay of Bremsstrahlung photon. The three-dimensional distribution is presented in a single-dimensional form following the convention described in Appendix B. The response matrix in this representation is shown in figure 12.2.

The initial distribution for the presented measurement is predicted by the POWHEG+PYTHIA8 Monte-Carlo. The truth distribution, in addition to the events which pass the reconstruction selection (i.e. events which enter the response matrix), contains events which were not measured due to detection inefficiency. The measured distribution in addition to events described by the response matrix, contains entries which have no corresponding truth events (e.g. due to event migrations). Both this and the inefficiency information are taken into account by the RooUnfold for the construction of the unfolded distribution.

The choice of the number of iterations in Bayesian unfolding is a compromise between reducing the bias towards the prior distribution and reducing the uncertainty due to the unfolding procedure. For the one-dimensional distributions in the current measurement 3 iterations are found to be the optimal choice for the unfolding. The studies of number of iteration for Bayesian unfolding and corresponding change of statistical uncertainty are shown in figures 12.3. In the three-dimensional case however the growth of the statistical fluctuations allows only for one iteration. The study of the unfolding method choice for the triple-differential measurement is given in appendix D.

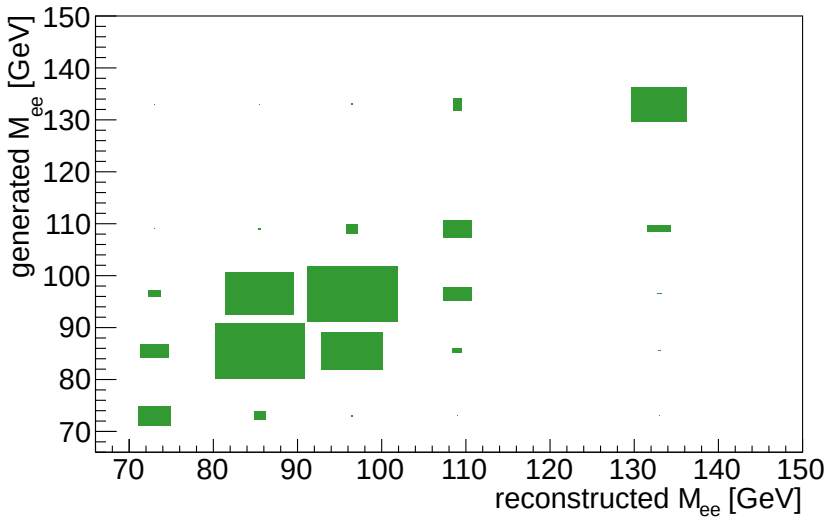

(a)

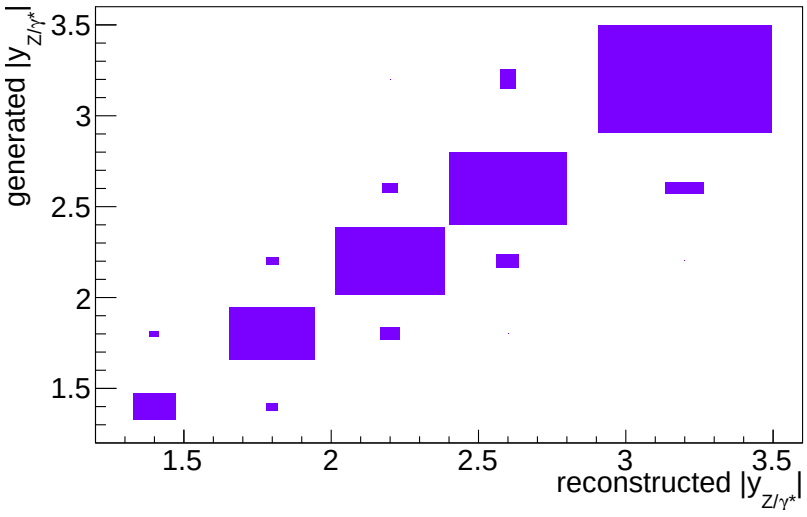

(b)

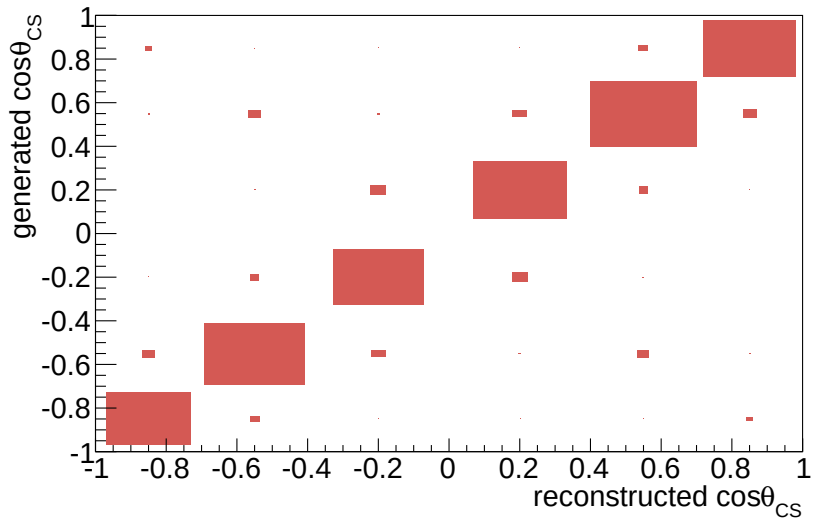

(c)

Figure 12.1: Response matrices of single-dimensional distributions: dilepton invariant mass (a), boson rapidity $|y_{Z/\gamma^*}|$ (b) and angular distribution $\cos\theta^*_{CS}$ (c).

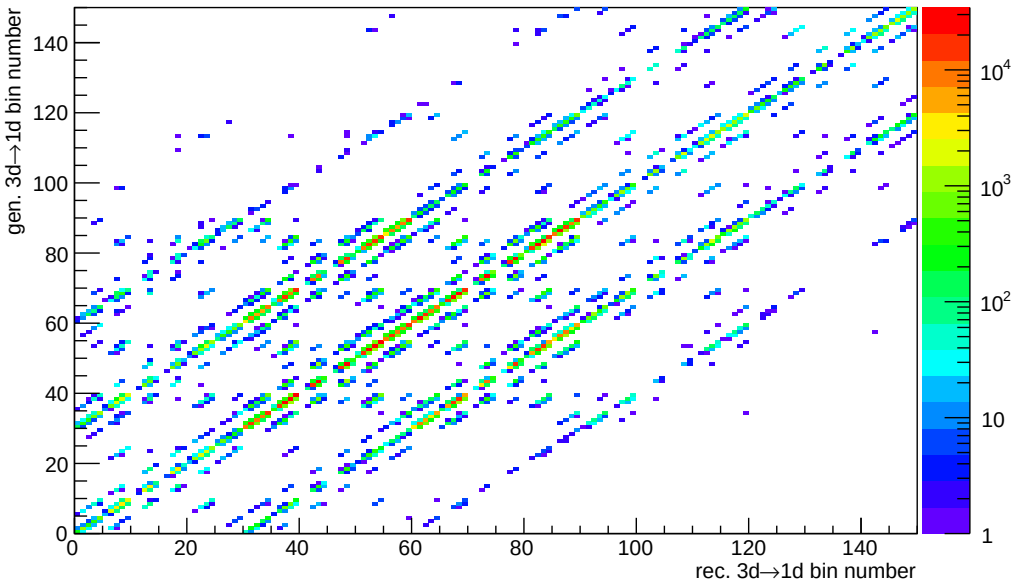

Figure 12.2: Response matrix constructed for the triple-differential cross-section measurement. The 3d binning is presented using the one-dimensional convention (see appendix B).

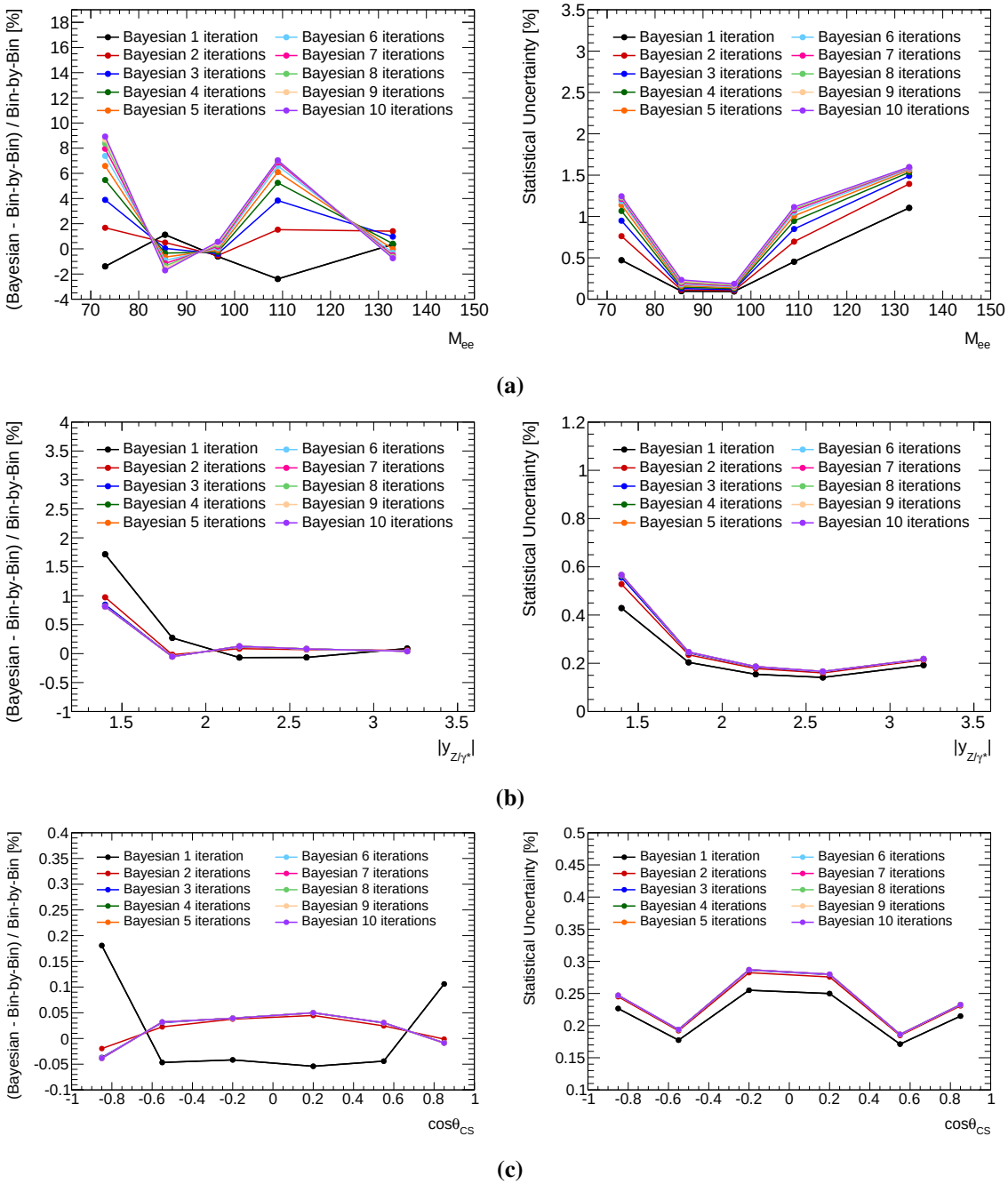

Figure 12.3: Deviation of unfolded result using Bayesian unfolding with different number of iterations from bin-by-bin unfolding (left) and relative statistical uncertainty (right) for the dilepton invariant mass (a), boson rapidity $|y_{Z/\gamma^*}|$ (b) and angular distribution $\cos\theta^*_{CS}$ (c).

CHAPTER 13

Uncertainties of the measurement

This chapter describes uncertainties of the cross-section measurement. The methodology for the uncertainty propagation, the uncertainty sources and their effects on the measured distributions are discussed.

13.1 Methods of the uncertainty propagation

The cross-section measurement relies on a number of corrections, which introduce uncertainties in the calculation. These uncertainties need to be properly propagated to the final result. There are three main methods which are used to propagate the uncertainties in the presented measurement: the offset method, the combined Toy MC and the "bootstrap" method which are discussed below.

13.1.1 The offset method

The offset method is based on the symmetrization of a propagated uncertainty around the central value. For that the cross-section calculation is repeated taking into account the corresponding variations in order to form the lower and upper cross-section limits σ^{up} and σ^{down}. The uncertainty U^{Offset} is calculated as the average deviation from the central cross-section value in each bin i:

$$U_i^{\text{Offset}} = \frac{\sigma_i^{up} - \sigma_i^{down}}{2}. \tag{13.1}$$

13.1.2 The combined Toy MC method

The combined toy MC method consists of making a set of pseudo-experiments, where the whole analysis chain is rerun with modified input parameters, corresponding to the different uncertainty sources under study. The toy MC method is typically used for the propagation of uncorrelated uncertainties. The 'combined' refers to the simultaneous treatment of the bin-to-bin correlated uncertainties with the uncorrelated ones.

The combined toy MC method is used in particular to propagate uncertainties on the scale factors to the final result of the analysis. The scale factors are binned in electron p_T and η and contain correlated and uncorrelated systematic components and a statistical uncertainty:

$$\text{SF}_i \pm \Delta\text{SF}_i^{\text{corr}} \pm \Delta\text{SF}_i^{\text{uncorr}} \pm \Delta\text{SF}_i^{\text{stat}}. \tag{13.2}$$

In order to properly take into account the correlation information across the bins, instead of using one table of scale factors with fixed uncertainties, N tables of toy scale factors are prepared. The scale factors in each pseudo-experiment are comprised of three parts: the central value of the scale factor in the given bin, the correlated component of the scale factor uncertainty and the uncorrelated and statistical components of the uncertainty. The uncorrelated and statistical components are sampled independently in each pseudo-experiment from a Gaussian distribution with a mean of 0 and a width equal to the sum of the uncorrelated and statistical uncertainty of the scale factor. For all sources of correlated uncertainties c the Gaussian distributions are synchronized by using the same random number in each bin. Thus for each Toy_n experiment the scale factor is taken as follows:

$$\text{SF}_i^{\text{Toy}_n} = \text{SF}_i + \text{Gauss}\left(0, \Delta\text{SF}_i^{\text{uncorr+stat}}\right) + \sum_{c=1}^{C} \Delta\text{SF}_{i,c}^{\text{corr}} \cdot \text{Gauss}\left(0,1\right). \tag{13.3}$$

The total uncertainty on an observable σ obtained with the combined toy MC method, is given by the standard deviation of the values of σ in all pseudo-experiments:

$$U_i^{\text{CombToyMC}} = \sqrt{\frac{\sum\limits_{\text{Toy}_n=1}^{N} \sigma_i^2}{N} - \left(\frac{\sum\limits_{\text{Toy}_n=1}^{N} \sigma_i}{N}\right)^2}. \tag{13.4}$$

The number N of the pseudo experiments should be sufficiently large to avoid a bias in the uncertainty estimation. In the current analysis 100 pseudo-experiments are used for the uncertainty estimation with the combined toy MC method.

13.1.3 The bootstrap method

The "bootstrap method" allows to estimate the statistical uncertainty of a sample of limited size and also to estimate the statistical component of the systematic uncertainties [86,87]. The method is based on resampling from the original $\mathbf{x} = \{x_1, x_2, \ldots, x_n\}$ sample.

A bootstrap replica $\mathbf{x}^* = \{x_1, x_2, \ldots, x_n\}$ is obtained from the original sample by randomly sampling with replacement. The resampling is performed using a Poisson distribution of N positive integer numbers with a mean of one. The way in which each event enters the bootstrap replica is described by a vector of random numbers which are assigned to an event as weights. Sampling with replacement means that each event can enter a sample more than once, but can also be rejected from a sample.

After N bootstrap samples $\mathbf{x}_1^*$, $\mathbf{x}_2^*$, $\mathbf{x}_N^*$ have been formed, the bootstrap estimate of the standard error for a parameter ξ is taken as the standard deviation of the bootstrap replications.

$$\text{standard error}_{bootstrap}(\xi) = \left[\frac{1}{N-1}\sum_{i=1}^{N}(\xi(\mathbf{x}_i^*) - \bar{\xi})^2\right]^{\frac{1}{2}}, \tag{13.5}$$

where $\bar{\xi} = \frac{\sum_{i=1}^{N} \xi x_i^*}{N}$. The number of replicas N formed with the bootstrap method need to be large enough to obtain reliable estimate of the uncertainty, typically not less than $N = 100$. The current measurement uses 1000 replicas for the propagation of the statistical uncertainties.

13.2 Uncertainty sources

The sources of experimental uncertainties are listed in table 13.1. The relative size of the uncertainties for the distributions of the cross-section dimensions is shown in figure 13.1.

Source of uncertainty	Propagation method
Identification of central electron	Combined Toy MC
Identification of forward electron	Combined Toy MC
Reconstruction efficiency	Combined Toy MC
Trigger efficiency	Combined Toy MC
Energy scale for central electron	Offset
Energy scale for forward electron	Offset
Energy resolution for central electron	Offset
Energy resolution for forward electron	Offset
Electroweak and top background	Offset
Multi-jet background	Offset and bootstrap
Pile-up modeling	Offset
Lineshape correction	Offset
PDF uncertainty	CT10 prescription
Unfolding statistics	Bootstrap
Unfolding method	Offset
Data statistics	Bootstrap

Table 13.1: Sources and propagation methods of the experimental uncertainties of the cross-section measurement.

The size of the uncertainties in each of the measured single-differential distributions after unfolding are summarized in tables 13.3 - 13.4. For the triple-differential measurement the uncertainties are given in appendix F. The statistical uncertainties of the data is estimated using the bootstrap method. The size of the uncertainty does not exceed 1.12% for the one-dimensional distributions. The uncertainties on the electroweak and top background estimation are due to the limited statistics of the Monte-Carlo samples and due to the uncertainty of their cross-sections. These uncertainties are propagated with the offset method.

The sources of the uncertainties related to the efficiency scale factors are described in Ref. [76] and are mostly due to the choice of model and background estimation techniques used for the scale factors determination. Those uncertainties are propagated to the cross-section calculation using the combined toy MC method independently for the trigger, reconstruction and identification efficiency scale factors. In particular the uncertainties due to the identification efficiency of central and forward electrons are taken separately since the identification in these cases is based on information from different parts of the detector. The uncertainty of the reconstruction efficiency in the one-dimensional

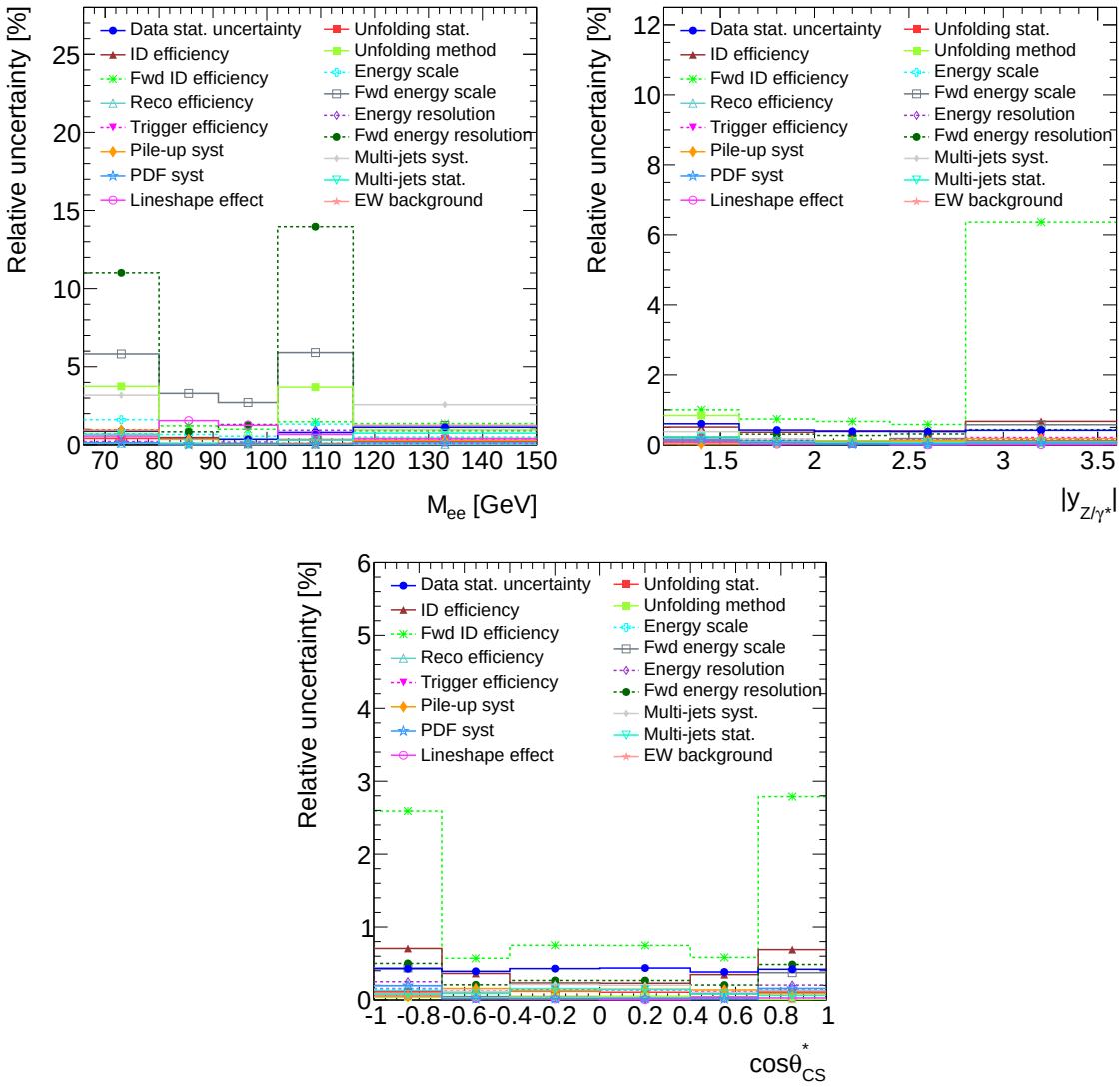

Figure 13.1: Relative size of the systematic uncertainties as functions of the Z/γ^* boson rapidity, invariant mass, and $\cos\theta^*_{CS}$.

distributions is within 0.13%. The uncertainty coming from the trigger efficiency is small for all the studied distributions and lays within 0.21%. While the uncertainty due to the central electron identification is smaller than 0.9%, the corresponding uncertainty for forward electrons has a big effect on the entire measurement being the dominant uncertainty in the last rapidity bin, where it reaches 6.38%.

The uncertainties due to the energy scale and resolution corrections are applied for the central and forward electrons. The energy scale uncertainty is due to the method of the energy scale extraction, statistical limitations, knowledge of the internal calorimeter geometry, material uncertainties, etc. (see Ref. [78]) The uncertainties are presented as up and down variations. Each pair of uncertainties is propagated to the cross-section using the offset method and the results are summed in quadrature. The forward resolution and energy scale corrections are the dominant sources of uncertainties for the

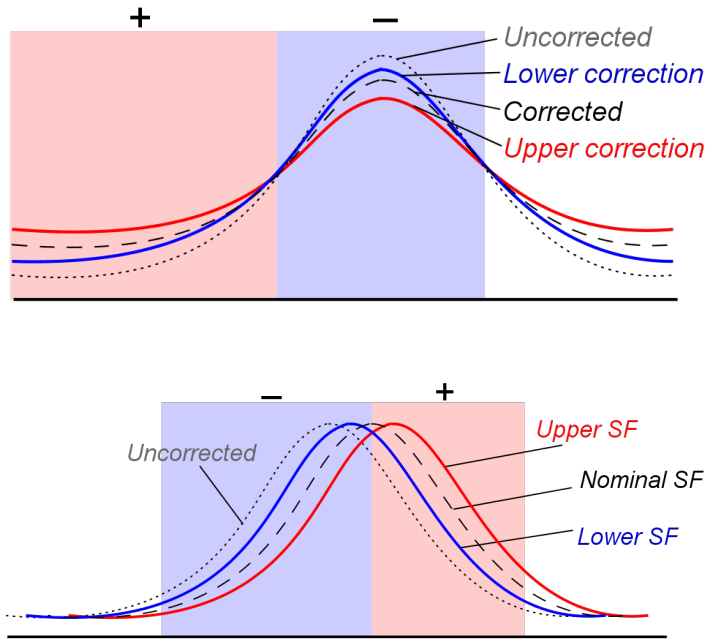

Figure 13.2: En example of a smearing correction (top) and a correction which shifts a distribution (bottom). The uncertainties due to the corrections can have either negative or positive sign depending on the region and the shape of the distribution.

cross-section measurement as a function of M_{ee}. The big impact on this distribution is expected due to the sensitivity of the dielectron mass distribution to the electron energy, in contrast to the measurements as a function of $|y_{Z/\gamma^*}|$ and $\cos\theta^*_{CS}$. The uncertainties of corrections that smear the analyzed distribution, such as resolution correction, and corrections that cause a shift of the reconstructed observables, such as energy scale, lead to a change of a sign of the uncertainty shift with respect to the upper and lower variation of the corrections. An example of the sign dependence on the distribution shape is schematically shown in figures 13.2. The sign of the uncertainty is taken into account, for example, when the measured distribution is fitted to PDFs and can reduce the impact of the uncertainty on the fits.

The uncertainty due to the pile-up modeling has a small impact on the rapidity and $\cos\theta^*_{CS}$ distributions not exceeding 0.18%. The mass distribution giving rise to an uncertainty up to 1% in both the single-differential M_{ee} and triple-differential measurements.

The uncertainty of the unfolding procedure is composed of two components. The first component is related to the limited statistics of the Monte-Carlo samples and is estimated using the bootstrap method with 1000 Monte-Carlo replicas. The second component is due to the choice of the unfolding method. This component is minor for the single-differential distributions $|y_{Z/\gamma^*}|$ and $\cos\theta^*_{CS}$ as the Bayesian unfolding give a stable result for a high enough number of iterations (see figures 12.3), while for the M_{ee} and triple-differential measurements the cross-section has bigger depends on the unfolding method (see figures in appendix D). The uncertainty is estimated from the difference between the Bayesian method and the bin-by-bin method.

The signal Monte-Carlo simulation used for the measurement is generated with the CT10 PDF [88]. This PDF contains a central set and 52 error sets. In order to estimate the corresponding un-

certainty the error sets are propagated to the cross-section by re-weighting the Monte-Carlo samples using an interface to the LHAPDF library [89]. The uncertainty is estimated at 68% confidence level. The variation acts in a similar way on both reconstruction and generated levels shifting the distributions in the same direction. This leads to the reduction of the uncertainty after unfolding as shown in figure 13.3. The resulting uncertainty is symmetrized using the offset method.

The uncertainty on the integrated luminosity is $\pm 2.8\%$. It is derived, following the same methodology as that detailed in Ref. [90], from a preliminary calibration of the luminosity scale derived from beam-separation scans performed in November 2012. This source of uncertainty is not shown in the presented distributions.

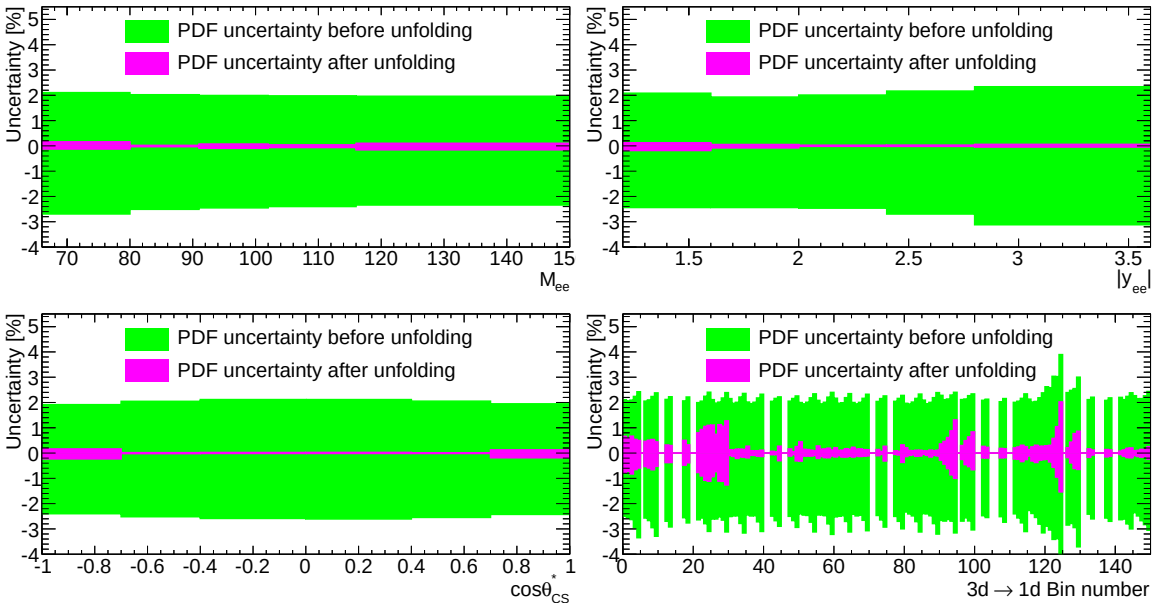

Figure 13.3: Reduction of PDF uncertainty ufter the unfolding procedure.

Systematic source [%]	$\lvert y_{Z/\gamma^*} \rvert$				
	(1.2, 1.6)	(1.6, 2.0)	(2.0, 2.4)	(2.4, 2.8)	(2.8, 3.6)
Reco. efficiency	0.12	0.11	0.06	0.04	0.08
Trig. efficiency	0.09	0.17	0.10	0.15	0.21
ID efficiency	0.51	0.36	0.40	0.40	0.67
Fwd ID efficiency	1.00	0.74	0.67	0.58	6.38
Energy scale	0.23	0.14	0.08	0.08	0.12
Fwd Energy scale	0.11	0.10	0.04	0.18	0.57
Energy resolution	0.22	0.13	0.07	0.08	0.14
Fwd energy resolution	0.22	0.31	0.27	0.31	0.43
EW and top bkg	0.22	0.07	0.05	0.03	0.02
Multi-jets stat.	0.23	0.09	0.07	0.06	0.08
Multi-jets syst.	0.30	0.14	0.09	0.07	0.08
Pile-up modelling	0.03	0.07	0.11	0.13	0.18
PDF	0.15	0.07	0.02	0.03	0.05
Lineshape	0.08	0.02	0.05	0.00	0.01
Unfolding stat.	0.20	0.10	0.08	0.08	0.11
Unfolding method	0.84	0.05	0.12	0.08	0.04
Data stat	0.60	0.42	0.38	0.38	0.42
Total	1.66	1.05	0.95	0.92	6.48

Table 13.2: Relative uncertainties on the single-differential cross-section measurements as a function of $\lvert y_{Z/\gamma^*} \rvert$.

Systematic source [%]	M_{ee} [GeV]				
	(66, 80)	(80, 91)	(91, 102)	(102, 116)	(116, 150)
Reco. efficiency	0.10	0.07	0.06	0.04	0.03
Trig. efficiency	0.21	0.13	0.12	0.10	0.10
ID efficiency	0.87	0.47	0.39	0.30	0.23
Fwd ID efficiency	0.71	1.22	1.00	1.48	1.36
Energy scale	1.61	0.66	0.55	1.33	0.50
Fwd Energy scale	5.82	3.30	2.71	5.91	1.24
Energy resolution	0.97	0.13	0.18	0.93	0.30
Fwd energy resolution	11.01	0.83	1.30	13.96	0.91
EW and top bkg	0.41	0.02	0.01	0.30	1.21
Multi-jets stat.	0.68	0.08	0.06	0.31	0.75
Multi-jets syst.	3.11	0.12	0.01	0.56	2.46
Pile-up modelling	0.94	0.35	0.10	0.10	0.27
PDF	0.14	0.03	0.08	0.05	0.13
Lineshape	0.56	1.55	1.25	0.68	0.39
Unfolding stat.	0.42	0.07	0.06	0.35	0.41
Unfolding method	3.75	0.04	0.40	3.70	0.96
Data stat	0.89	0.36	0.35	0.80	1.12
Total	13.66	4.06	3.52	15.82	3.91

Table 13.3: Relative uncertainties on the single-differential cross-section measurements as a function of M_{ee}.

Systematic source [%]	$\cos\theta^*_{CS}$					
	(-1.0, -0.7)	(-0.7, -0.4)	(-0.4, 0.0)	(0.0, 0.4)	(0.4, 0.7)	(0.7, 1.0)
Reco. efficiency	0.13	0.04	0.03	0.03	0.04	0.12
Trig. efficiency	0.16	0.12	0.14	0.14	0.12	0.15
ID efficiency	0.71	0.36	0.23	0.23	0.35	0.69
Fwd ID efficiency	2.59	0.57	0.75	0.75	0.58	2.79
Energy scale	0.15	0.04	0.04	0.04	0.04	0.11
Fwd Energy scale	0.44	0.05	0.05	0.03	0.04	0.37
Energy resolution	0.25	0.02	0.03	0.01	0.02	0.20
Fwd energy resolution	0.50	0.21	0.27	0.27	0.2	0.49
EW and top bkg	0.09	0.02	0.02	0.03	0.04	0.11
Multi-jets stat.	0.08	0.09	0.15	0.14	0.08	0.06
Multi-jets syst.	0.18	0.07	0.15	0.14	0.06	0.15
Pile-up modelling	0.05	0.16	0.12	0.15	0.14	0.09
PDF	0.20	0.02	0.02	0.02	0.01	0.16
Lineshape	0.05	0.02	0.01	0.00	0.03	0.03
Unfolding stat.	0.11	0.09	0.11	0.12	0.08	0.10
Unfolding method	0.04	0.03	0.04	0.05	0.03	0.01
Data stat	0.43	0.39	0.43	0.44	0.38	0.42
Total	2.84	0.85	0.99	0.99	0.84	3.00

Table 13.4: Relative uncertainties on the single-differential cross-section measurements as a function of $\cos\theta^*_{CS}$.

CHAPTER 14

Theoretical predictions

Theoretical predictions for the Drell-Yan production are obtained at NLO QCD with the MCFM [91] program interfaced to APPLGRID [92]. MCFM is a parton-level Monte-Carlo generator, which provides calculations at LO and NLO. The partonic cross-section calculated as a function of x and Q^2 can be stored as a grid. In order to obtain the hadronic cross-section, this grid has to be convolved with a PDF. This principle of a posteriori PDF inclusion is used by the APPLGRID program, which allows for a fast calculation of the hadronic cross-section.

The calculation uses the G_μ electroweak parameter scheme, in which the Fermi constant measured from the muon lifetime, together with the masses of the Z and W bosons, is used as an input. The electroweak parameters used for the production of the grids are summarized in table 14.1. The grid parameters, shown in table 14.2, are chosen to provide a detailed enough binning and reasonable interpolation order of x and Q^2 distributions. This is important for obtaining an unbiased result after the convolution of the grids with the PDFs. The quality of the grids is checked by comparing them to the MCFM predictions. For this the grids are convolved with the same PDF which was used for the production. Figure 14.1 shows an example of such a check, where the level of agreement between the two calculations is shown to be better than half per mille. The computations using APPLGRID are very fast which is important for PDF fits to the data since the computation needs to be repeated many times using modified PDF parametrizations.

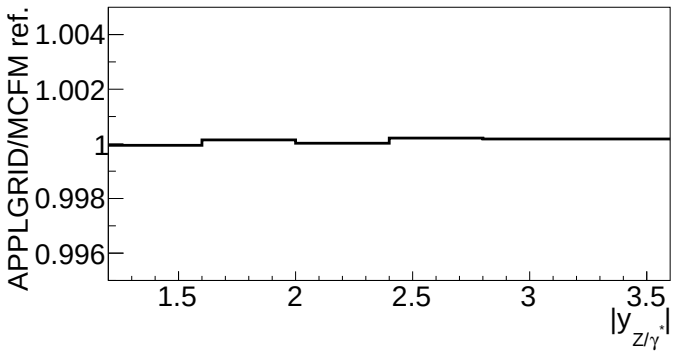

Figure 14.1: The ratio between the single-differential cross-section as a function of $|y_{Z/\gamma^*}|$ obtained by convolving (x, Q^2) grid prepared by APPLGRID with CTEQ6.6 PDF [93] and MCFM hadronic cross-section calculated as a reference.

Z boson mass	91.1876 GeV
Decay width Γ_Z	2.4949 GeV
W boson mass	80.385 GeV
Decay width Γ_W	2.0906 GeV
top quark mass	173.5 GeV
H boson mass	125 GeV
Fermi coupling constant G_F	1.1663787×10^{-5} GeV^{-2}
Weak-mixing angle $\sin^2\theta_W$	0.2228972

Table 14.1: Electroweak parameters used for evaluation of the theoretical predictions for the Drell-Yan production cross-section.

Number of x bins	x range	x interpolation order
30	$1 \times 10^{-6} - 1$	6
Number of Q^2 bins	Q^2 range [GeV^2]	Q^2 interpolation order
20	$66^2 - 8000^2$	4

Table 14.2: Bin grid settings for the Drell-Yan production.

The calculations of the theoretical predictions are performed single-differentially and triple-differentially following the fiducial selection criteria described in table 7.3.

14.1 Scale scan

The grids are constructed with dynamic factorization and normalization scales, which change on an event-by-event basis and are set equal to the invariant mass of the dielectron pair: $\mu_r = \mu_f = M_{ee}$.

In order to investigate the stability of the derived grids a scale scan was performed. There μ_R and μ_F were scaled independently within a range of $1/2^4$ - 2^4:

$$\frac{1}{2^4}\mu_F \leq \mu_F \leq 2^4\mu_F, \ \frac{1}{2^4}\mu_R \leq \mu_R \leq 2^4\mu_R. \tag{14.1}$$

Nine multiplicative factors were tested for μ_R and μ_F scales, and the cross-section was recalculated for each variation. Thus 81 cross-section results for each of the studied bins were stored as a function of μ_R and μ_F. Figure 14.2 shows an example of two bins with the performed scale scan. A clear 'saddle' point is observed in the left plot. The appearance of a saddle point denotes the presence of a 'stable region' where a relatively small change of the factorization and normalization scales does not lead to a significant change of the cross-section. The bin without a saddle point behaviour gives an 'unstable' distribution when the scales are varied. The 'unstable' bins thus have a large theoretical uncertainty on the calculated cross-section. Figures 14.3-14.5 show the result of the scale scan for

each of the studied bins in M_{ee}, $|y_{Z/\gamma^*}|$ and $\cos\theta^*_{CS}$. The scale scan is performed by convolving the grids with the CTEQ6.6 PDF. The choice of PDF does not lead to a significant change in the scan distributions. Due to certain kinematic constraints, such as the requirement of low boson rapidity at high $\cos\theta^*_{CS}$ values, the unstable behavior observed in a number of calculated bins is expected. This can be seen for example in the rapidity distribution for $80 < M_{ee} < 91$ GeV and $0.4 < \cos\theta^*_{CS} < 0.7$ (figure 14.6), where the NLO/LO k-factor are shown. This distribution corresponds to the second row in figure 14.3b. In the bin with $1.2 < |y_{Z/\gamma^*}| < 1.6$, $80 < M_{ee} < 91$ GeV, $0.4 < \cos\theta^*_{CS} < 0.7$ the LO contribution is absent. In such bins higher order corrections become sizable and calculations at NNLO are required, which is however outside of the scope of the current thesis. A similar effect is observed in the Drell-Yan measurement with $\sqrt{s} = 7$ TeV ATLAS data [94] below the Z mass peak, where a region with tight kinematic constraints is purely described by NLO theoretical calculations (see appendix A).

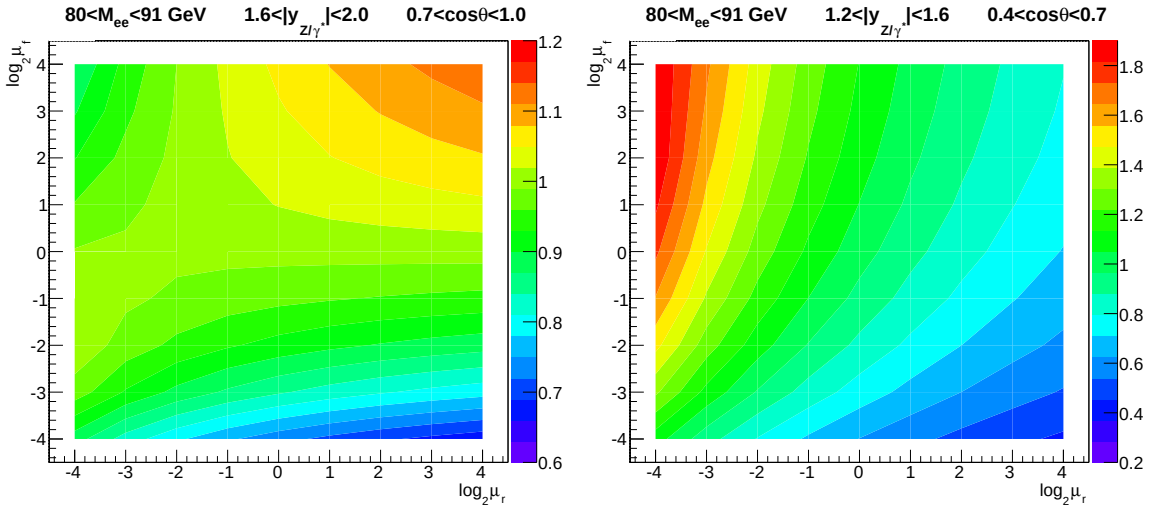

Figure 14.2: An example of a 'stable' (left) and 'unstable' (right) bins obtained via the variation of renormalization and factorization scales. The colour map denotes the difference of the varied cross-section from the central case. The 'stable' bin is characterized by a saddle point close to the central cross-section. In this region the cross-section does not change significantly as a function of μ_R and μ_F.

14.2 Theoretical uncertainties

The uncertainty of the theoretical predictions are comprised of the statistical uncertainty, uncertainty due to the μ_r and μ_f scale variation and PDF-driven components. Table 14.3 summarizes uncertainties for the single-dimensional distributions M_{ee}, $|y_{Z/\gamma^*}|$ and $\cos\theta^*_{CS}$. For the triple-differential binning the same information is given in appendix E. The statistical uncertainty is taken as the standard deviation of the mean value and is estimated using the toy MC method. The grids were calculated 100 times with different seeds of random numbers. The statistical uncertainty is found to be small (typically less than 0.1%) for all of the analyzed distributions.

The scale uncertainties are derived from independent variations of the renormalization and factorization scales by factor of two up and down:

$$(\mu_f, 2\mu_r),\ (\mu_f, \tfrac{1}{2}\mu_r),\ (\tfrac{1}{2}\mu_f, \mu_r),\ (\tfrac{1}{2}\mu_f, \tfrac{1}{2}\mu_r),\ (2\mu_f, \mu_r),\ (2\mu_f, 2\mu_r).$$

The six combinations are propagated to the cross-section level, and the biggest deviations from the central value are taken as up and down uncertainties.

The PDF uncertainties are generally coming from theoretical and experimental constraints. The theoretical component refers to the choice of the input parametrization form and uncertainty of the input parameters for the theoretical calculations, while the experimental uncertainties are defined from the data used for the PDF fits. The treatment of the uncertainties depends on the particular PDF set. The uncertainties presented in the tables 14.3 are estimated using MSTW2008nlo PDF [95] at 68% confidence level.

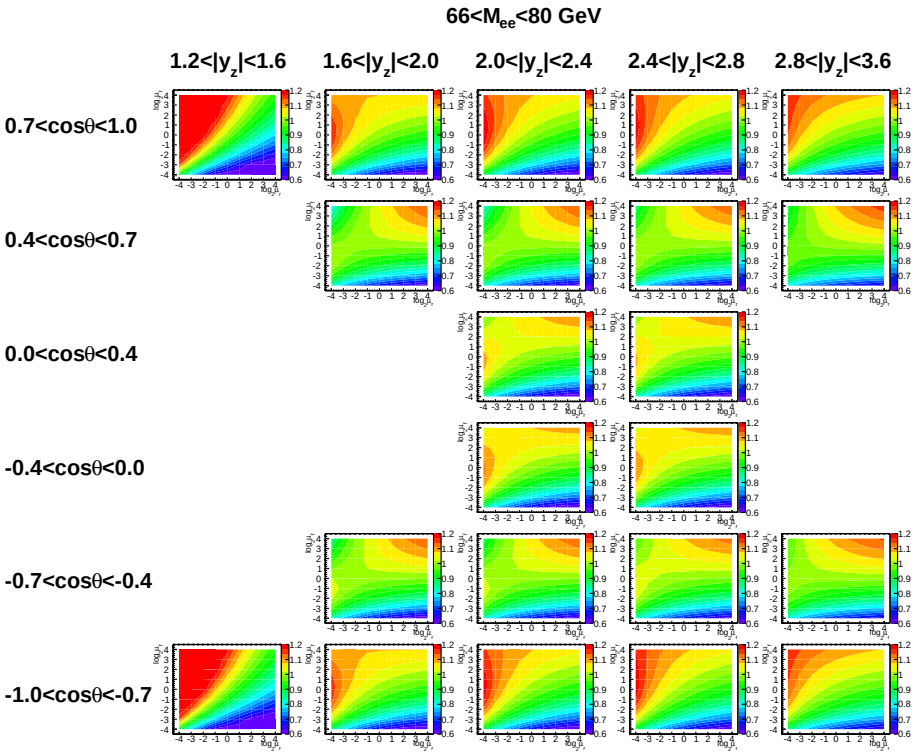

(a)

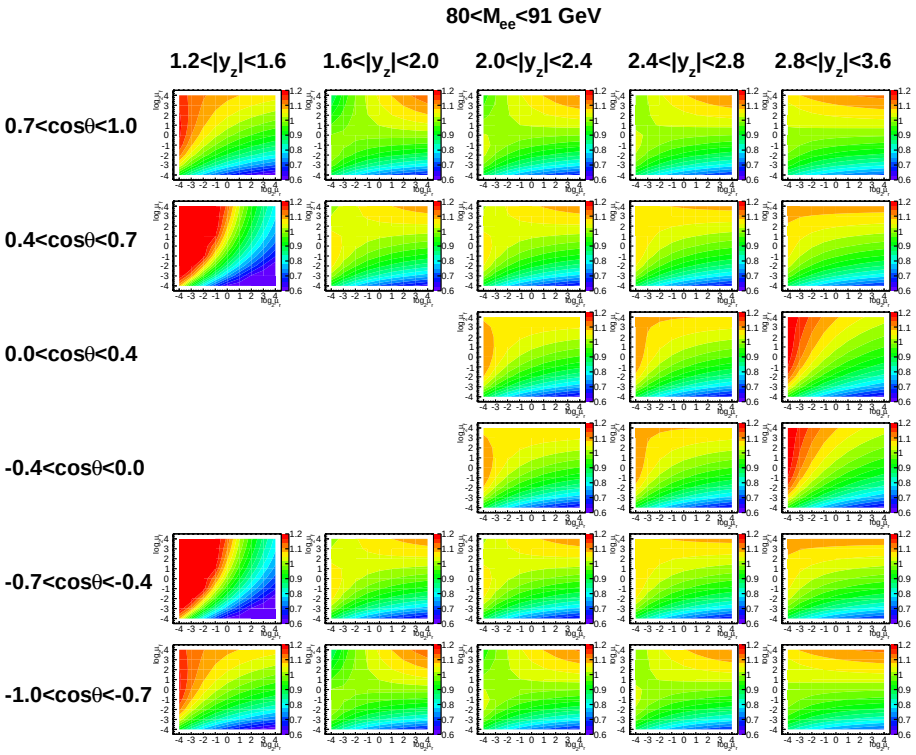

(b)

Figure 14.3: The cross-section scan with variation of μ_r and μ_f. The result for each variation is shown as a ratio to the default scale choice. Two regions of dielectron invariant mass are scanned: $66 < M_{ee} < 80$ GeV (a) and $80 < M_{ee} < 91$ GeV (b).

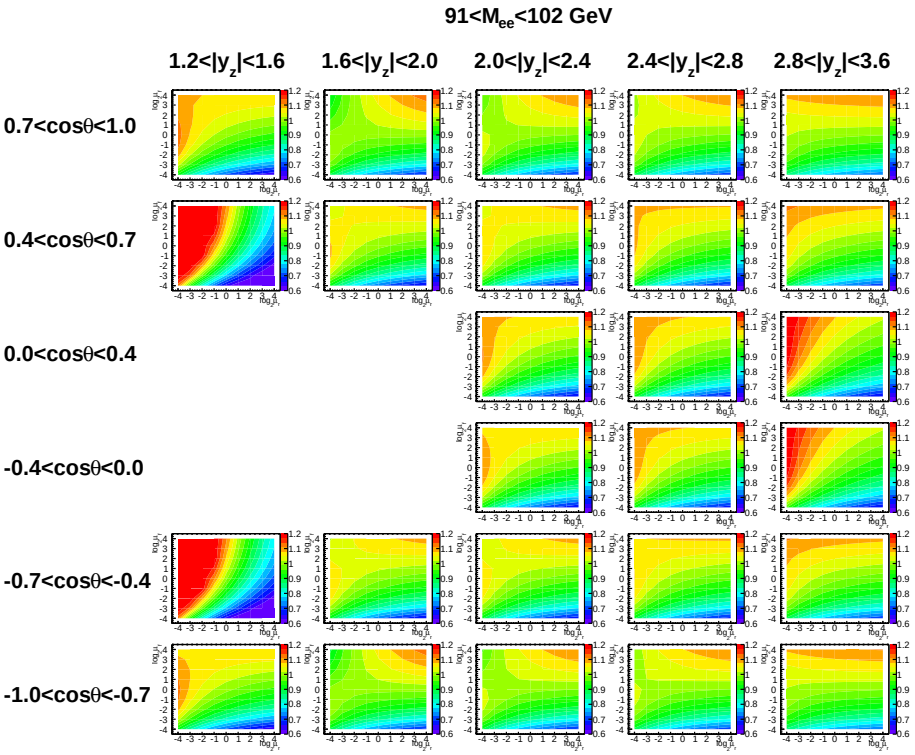

(a)

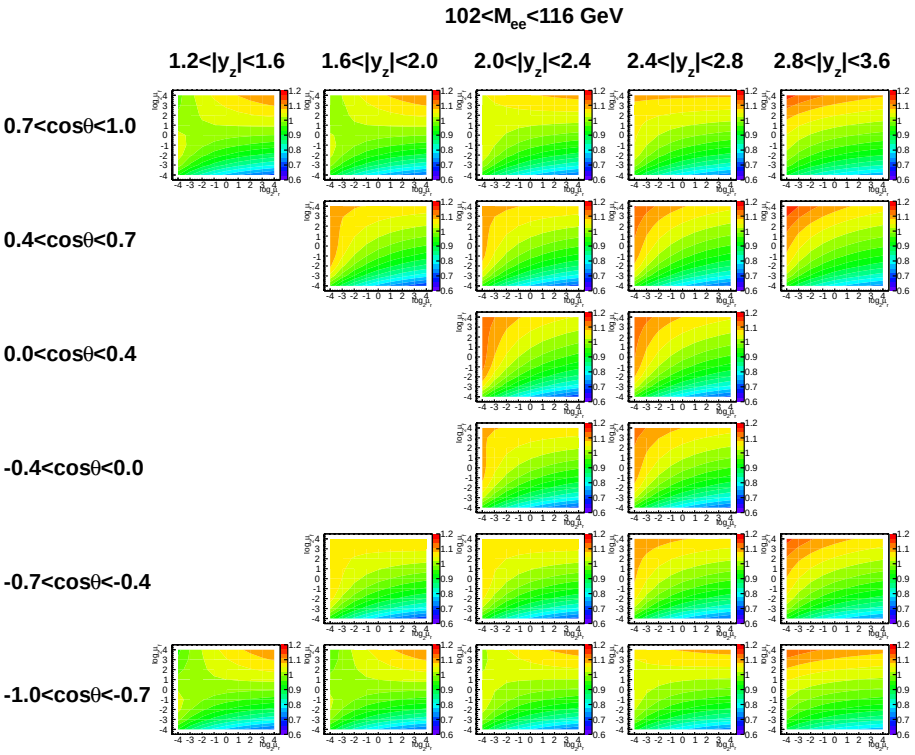

(b)

Figure 14.4: The cross-section scan with variation of μ_r and μ_f. The result for each variation is shown as a ratio to the default scale choice. Two regions of dielectron invariant mass are scanned: $91 < M_{ee} < 102$ GeV (a) and $102 < M_{ee} < 116$ GeV (b).

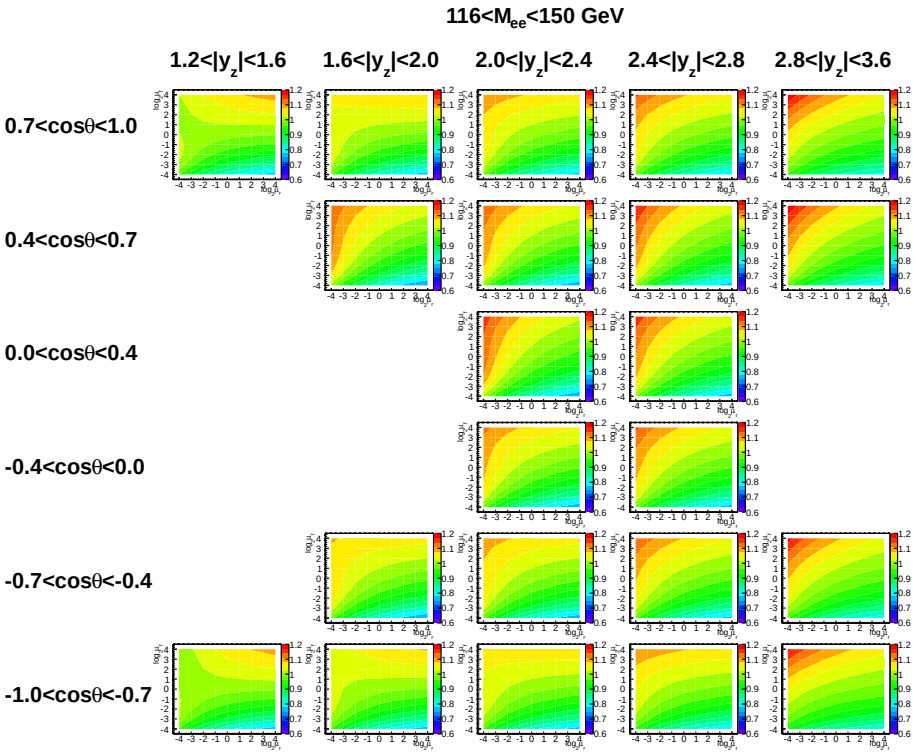

Figure 14.5: The cross-section scan with variation of μ_r and μ_f. The result for each variation is shown as a ratio to the default scale choice. The dielectron invariant mass region of $116 < M_{ee} < 150$ GeV is scanned.

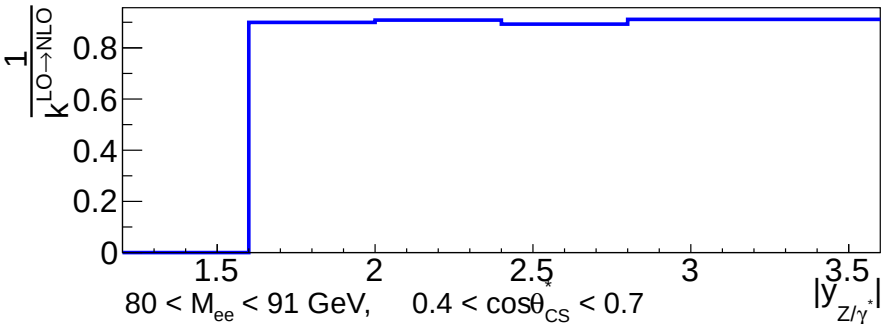

Figure 14.6: An example of inverted LO to NLO k-factor calculated with MCFM and APPLGRID.

M_{ee} bin [GeV]	$\mathrm{Unc}_{\mathrm{Stat}}$ [%]	$\mathrm{Unc}^{\mathrm{scale}}_{Up}$ [%]	$\mathrm{Unc}^{\mathrm{scale}}_{Down}$ [%]	$\mathrm{Unc}^{\mathrm{PDF}}_{Up}$ [%]	$\mathrm{Unc}^{\mathrm{PDF}}_{Down}$ [%]
66-80	0.090	2.89	4.33	2.39	1.95
80-91	0.015	2.64	3.65	2.43	1.87
91-102	0.014	2.57	3.51	2.44	1.85
102-116	0.094	2.33	3.02	2.45	1.78
116-150	0.166	2.05	2.48	2.48	1.72

(a)

$\lvert y_{Z/\gamma^*}\rvert$ bin	$\mathrm{Unc}_{\mathrm{Stat}}$ [%]	$\mathrm{Unc}^{\mathrm{scale}}_{Up}$ [%]	$\mathrm{Unc}^{\mathrm{scale}}_{Down}$ [%]	$\mathrm{Unc}^{\mathrm{PDF}}_{Up}$ [%]	$\mathrm{Unc}^{\mathrm{PDF}}_{Down}$ [%]
1.2 - 1.6	0.097	3.01	4.22	2.06	1.51
1.6 - 2.0	0.032	2.51	3.44	2.36	1.68
2.0 - 2.4	0.026	2.50	3.55	2.42	1.82
2.4 - 2.8	0.019	2.63	3.57	2.54	1.95
2.8 - 3.6	0.030	2.81	3.51	2.65	2.12

(b)

$\cos\theta^*_{CS}$ bin	$\mathrm{Unc}_{\mathrm{Stat}}$ [%]	$\mathrm{Unc}^{\mathrm{scale}}_{Up}$ [%]	$\mathrm{Unc}^{\mathrm{scale}}_{Down}$ [%]	$\mathrm{Unc}^{\mathrm{PDF}}_{Up}$ [%]	$\mathrm{Unc}^{\mathrm{PDF}}_{Down}$ [%]
-1.0 - -0.7	0.032	2.54	3.46	2.29	1.75
-0.7 - -0.4	0.017	2.66	3.66	2.35	1.82
-0.4 - 0.0	0.031	2.67	3.69	2.40	1.84
0.0 - 0.4	0.031	2.65	3.65	2.51	1.91
0.4 - 0.7	0.021	2.64	3.61	2.54	1.92
0.7 - 1.0	0.031	2.54	3.39	2.52	1.89

(c)

Table 14.3: Uncertainties associated with the theoretical predictions of the Drell-Yan production cross-section as a function of M_{ee} (a), $|y_{Z/\gamma^*}|$ (b) and $\cos\theta^*_{CS}$ (c). The calculations are performed with MCFM and APPLgrid at NLO and convolved with MSTW2008nlo PDF.

CHAPTER 15

Cross-section results

The cross-sections are calculated single- and triple-differentially in bins of $y_{Z/\gamma^*}, M_{ee}$ and $\cos\theta^*_{CS}$ using the following formulas

$$\frac{\mathrm{d}\sigma}{\mathrm{d}|y_{Z/\gamma^*}|} = \frac{N-B}{L_{int}}\frac{1}{\Delta|y_{Z/\gamma^*}|}, \tag{15.1}$$

$$\frac{\mathrm{d}\sigma}{\mathrm{d}M_{ee}} = \frac{N-B}{L_{int}}\frac{1}{\Delta M_{ee}}, \tag{15.2}$$

$$\frac{\mathrm{d}\sigma}{\mathrm{d}\cos\theta^*_{CS}} = \frac{N-B}{L_{int}}\frac{1}{\Delta\cos\theta^*_{CS}}, \tag{15.3}$$

$$\frac{\mathrm{d}\sigma}{\mathrm{d}|y_{Z/\gamma^*}|\mathrm{d}M_{ee}\mathrm{d}\cos\theta^*_{CS}} = \frac{N-B}{L_{int}}\frac{1}{\Delta|y_{Z/\gamma^*}|\Delta M_{ee}\Delta\cos\theta^*_{CS}}, \tag{15.4}$$

where $\Delta|y_{Z/\gamma^*}|$, ΔM_{ee} and $\Delta\cos\theta^*_{CS}$ denote corresponding widths of a given bin, N is the total number of events observed in a given bin, B is the estimated number of background events in this bin and L_{int} is the total integrated luminosity of the analyzed data sample (20.1 fb^{-1}). The number of signal events is obtained by unfolding the reconstructed quantities to the the fiducial phase-space at Born level. The results on the cross-section measurements are summarized in tables 15.1-15.3 and in Appendix F.

The total uncertainty of the measurement consists of the statistical and systematic components. The dominant uncertainty that affects the $|y_{Z/\gamma^*}|$ spectrum is coming from the identification efficiency of the forward electrons, which increases at high rapidity values. The dielectron invariant mass measurement is affected primarily by the uncertainties coming from the forward electon energy scale and resolution corrections, unfolding procedure and multi-jets background modeling. In particular in bins $66 < M_{ee} < 80$ GeV and $102 < M_{ee} < 116$ GeV the smearing resolution correction cause large migration of events from the Z pole. The $\cos\theta^*_{CS}$ measurement in general is very precise, however a non-negligible uncertainty at the edges of the distribution is coming from the identification efficiency of forward electrons. The described sources of uncertainties are dominant for both single- and triple-differential cross-section measurements. The uncertainty from the multi-jets background modeling is generally high for the triple-differential measurement, especially in the bins with low cross-section and high level of background contamination.

The theoretical predictions for the cross-section measurements are obtained at NLO QCD from POWHEG+PYTHIA8 and MCFM/APPLGRID calculations using different PDF sets: CT10 NLO, HERAPDF 1.5 NLO, MSTW2008 NLO, ATLAS WZ [96], ABM11 NLO 5fl [97]. While both the POWHEG+PYTHIA8 and MCFM predictions provide the same level of accuracy (i.e. $O(\alpha_s)$), the

former contains a ressumation of leading logarithmic terms provided by the parton shower, which can potentially improve description in kinematically restricted phase-space regions. The uncertainties of the theoretical predictions calculated with MCFM and APPLGRID are comprised of the μ_R and μ_F scale variations (see chapter 14) and PDF uncertainties at 68% confidence level. The theoretical uncertainties are symmetrized for the comparison with the measured cross-sections. The POWHEG+PYTHIA8 predictions are given together with their statistical uncertainties.

The comparison of the measured cross-sections with the theoretical predictions is shown in figures 15.1, 15.2, 15.3, which show the single-differential cross-sections as a function of $|y_{Z/\gamma^*}|$, $\cos\theta^*_{CS}$ and M_{ee} respectively. The triple-differential cross-section measurements are shown in figures 15.4 - 15.8, where each set of plots corresponds to a certain M_{ee} region. Within each set of figures the dependence of the cross-section on $\cos\theta^*_{CS}$ is shown for different regions of $|y_{Z/\gamma^*}|$. The cross-section measurements agrees with the theoretical predictions within the uncertainty in the most of the measured bins, however the triple-differential measurement deviates from the theoretical predictions in certain regions of phase space. This can be attributed to the absence of higher order electroweak and QCD corrections and is discussed in section 14.1. The predominance of events with $\cos\theta^*_{CS} < 0$ ($\cos\theta^*_{CS} > 0$) in the low (high) dielectron mass region, observed in the triple-differential distributions, is a manifestation of the change of the preferable direction of the outgoing electron from backward to forward (section 3.1).

$\lvert y_{Z/\gamma^*}\rvert$	$\mathrm{d}\sigma/\mathrm{d}\lvert y_{Z/\gamma^*}\rvert$ [pb]	Total unc. [pb]	Stat unc. [pb]	Syst unc. [pb]
1.2 - 1.6	8.940	0.148	0.054	0.138
1.6 - 2.0	36.028	0.378	0.152	0.346
2.0 - 2.4	76.654	0.728	0.294	0.666
2.4 - 2.8	86.835	0.799	0.329	0.728
2.8 - 3.6	23.727	1.538	0.099	1.534

Table 15.1: Results of the single-differential cross-section measurements as a function of $|y_{Z/\gamma^*}|$, unfolded to the fiducial phase-space at Born level.

M_{ee} [GeV]	$\mathrm{d}\sigma/\mathrm{d}M_{ee}$ [pb/GeV]	Total unc. [pb/GeV]	Stat unc. [pb/GeV]	Syst unc. [pb/GeV]
66 - 80	0.377	0.051	0.003	0.051
80 - 91	7.739	0.314	0.028	0.313
91 - 102	9.582	0.337	0.034	0.336
102 - 116	0.402	0.064	0.003	0.064
116 - 150	0.082	0.003	0.001	0.003

Table 15.2: Results of the single-differential cross-section measurements as a function of M_{ee}, unfolded to the fiducial phase-space at Born level.

$\cos\theta^*_{CS}$	$d\sigma/d\cos\theta^*_{CS}$ [pb]	Total unc. [pb]	Stat unc. [pb]	Syst unc. [pb]
-1.0 - -0.7	110.316	3.133	0.472	3.097
-0.7 - -0.4	151.906	1.291	0.596	1.146
-0.4 - 0.0	43.784	0.433	0.188	0.391
0.0 - 0.4	46.566	0.461	0.204	0.414
0.4 - 0.7	168.863	1.418	0.647	1.263
0.7 - 1.0	130.674	3.920	0.549	3.882

Table 15.3: Results of the single-differential cross-section measurements as a function of $\cos\theta^*_{CS}$, unfolded to the fiducial phase-space at Born level.

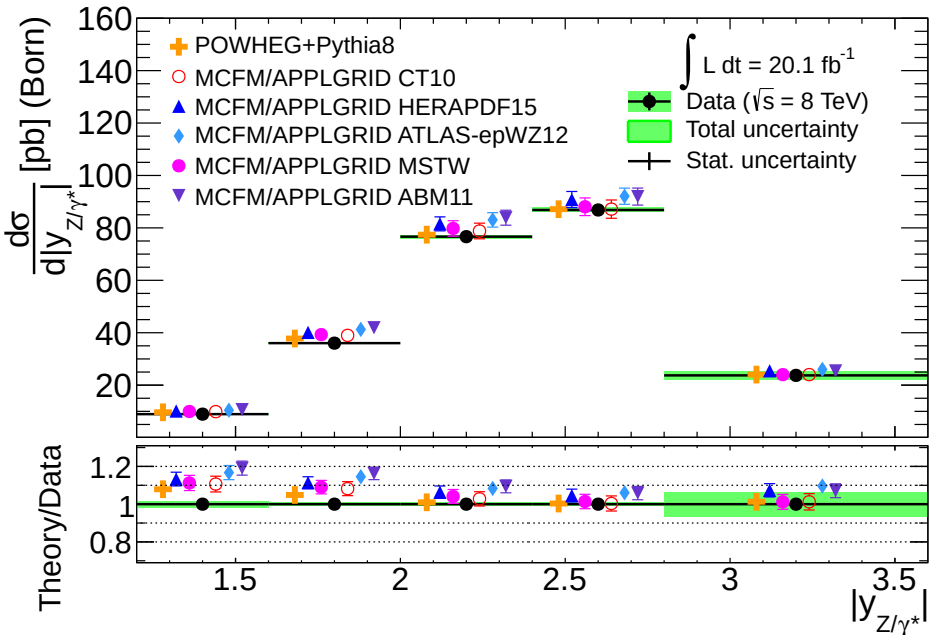

Figure 15.1: The single-differential cross-section as a function of $|y_{Z/\gamma^*}|$ unfolded to the fiducial phase-space at Born level.

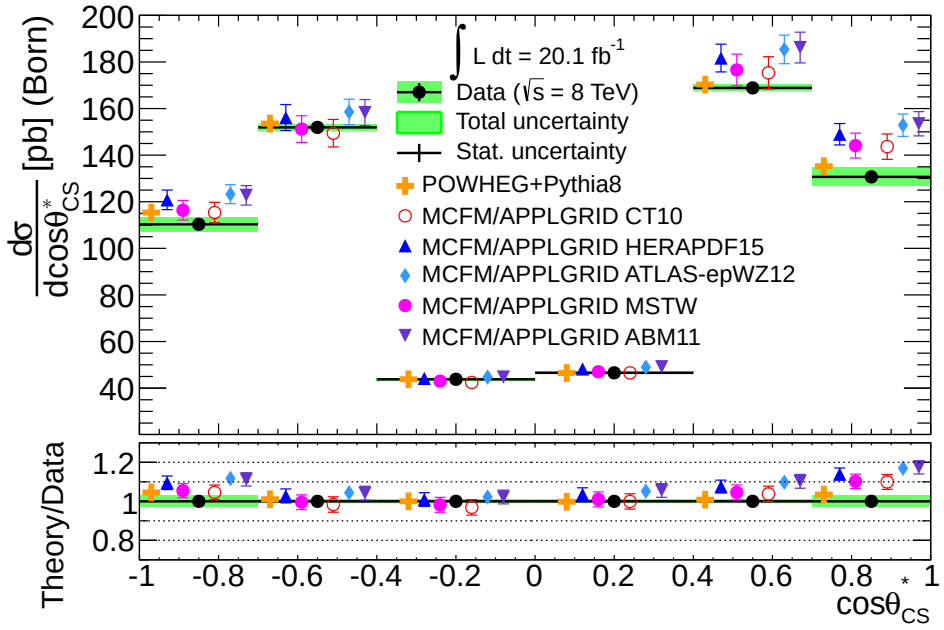

Figure 15.2: The single-differential cross-section as a function of $\cos\theta^*_{CS}$ unfolded to the fiducial phase-space at Born level.

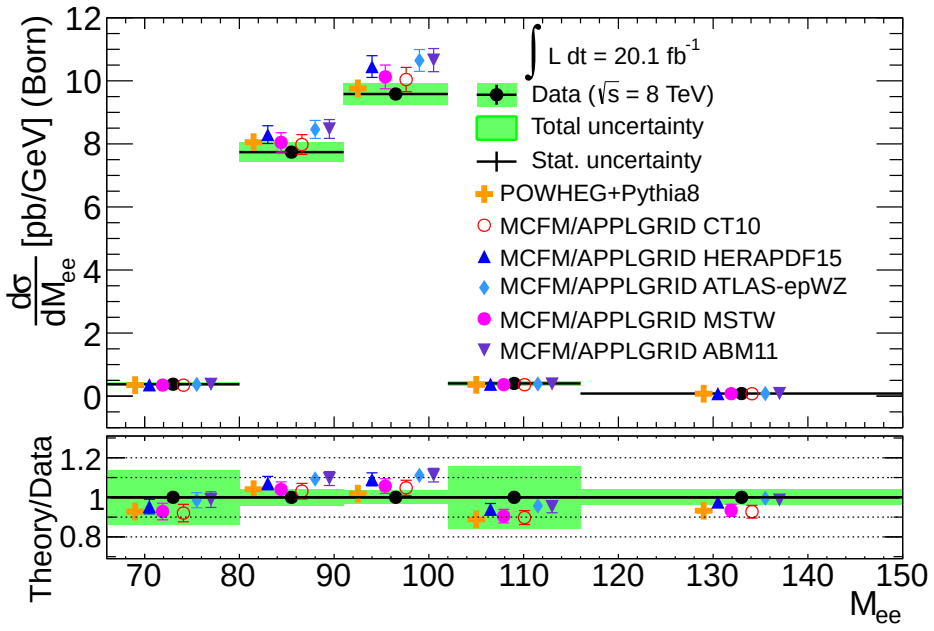

Figure 15.3: The single-differential cross-section as a function of M_{ee} unfolded to the fiducial phase-space at Born level.

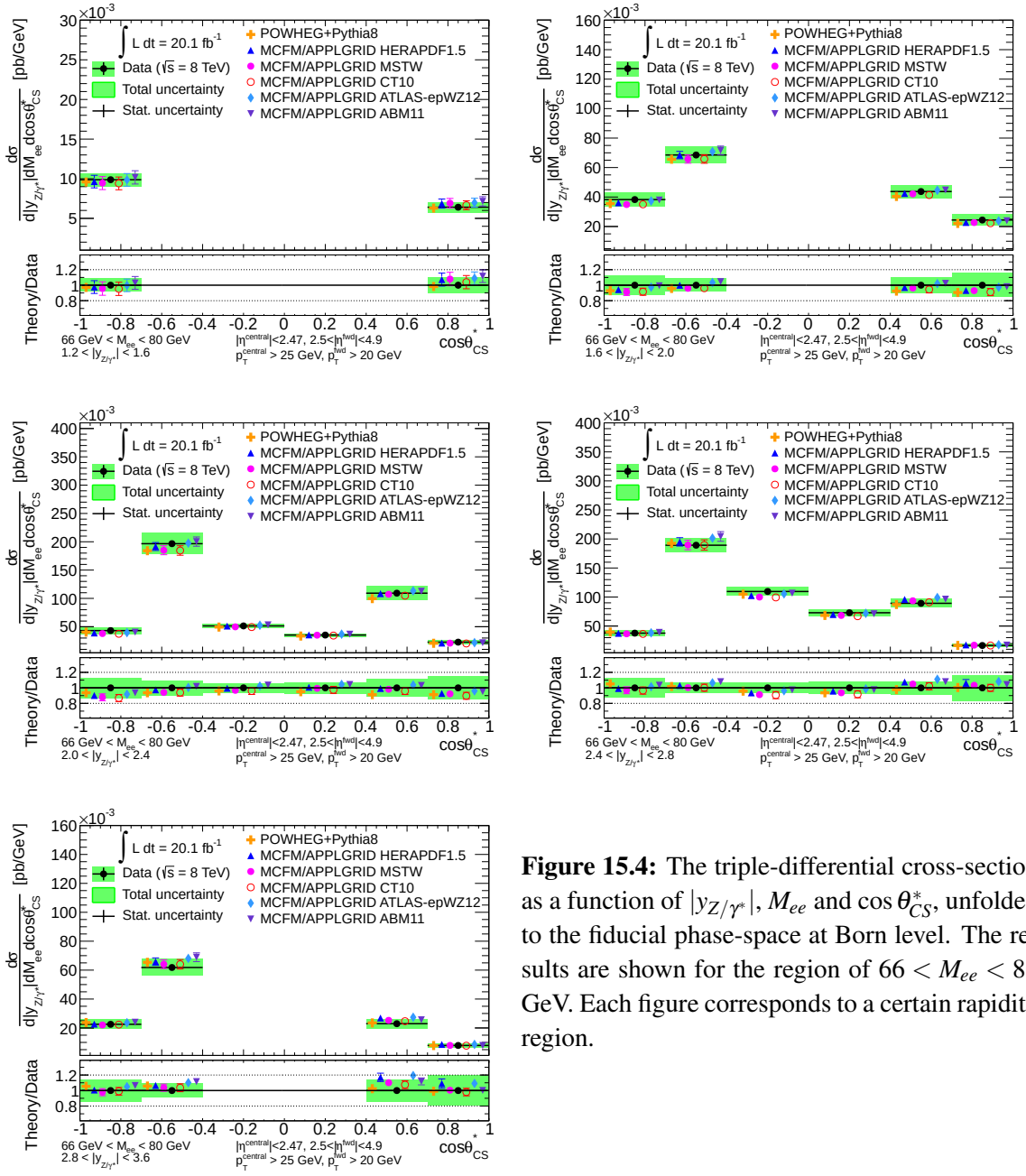

Figure 15.4: The triple-differential cross-section as a function of $|y_{Z/\gamma^*}|$, M_{ee} and $\cos\theta^*_{CS}$, unfolded to the fiducial phase-space at Born level. The results are shown for the region of $66 < M_{ee} < 80$ GeV. Each figure corresponds to a certain rapidity region.

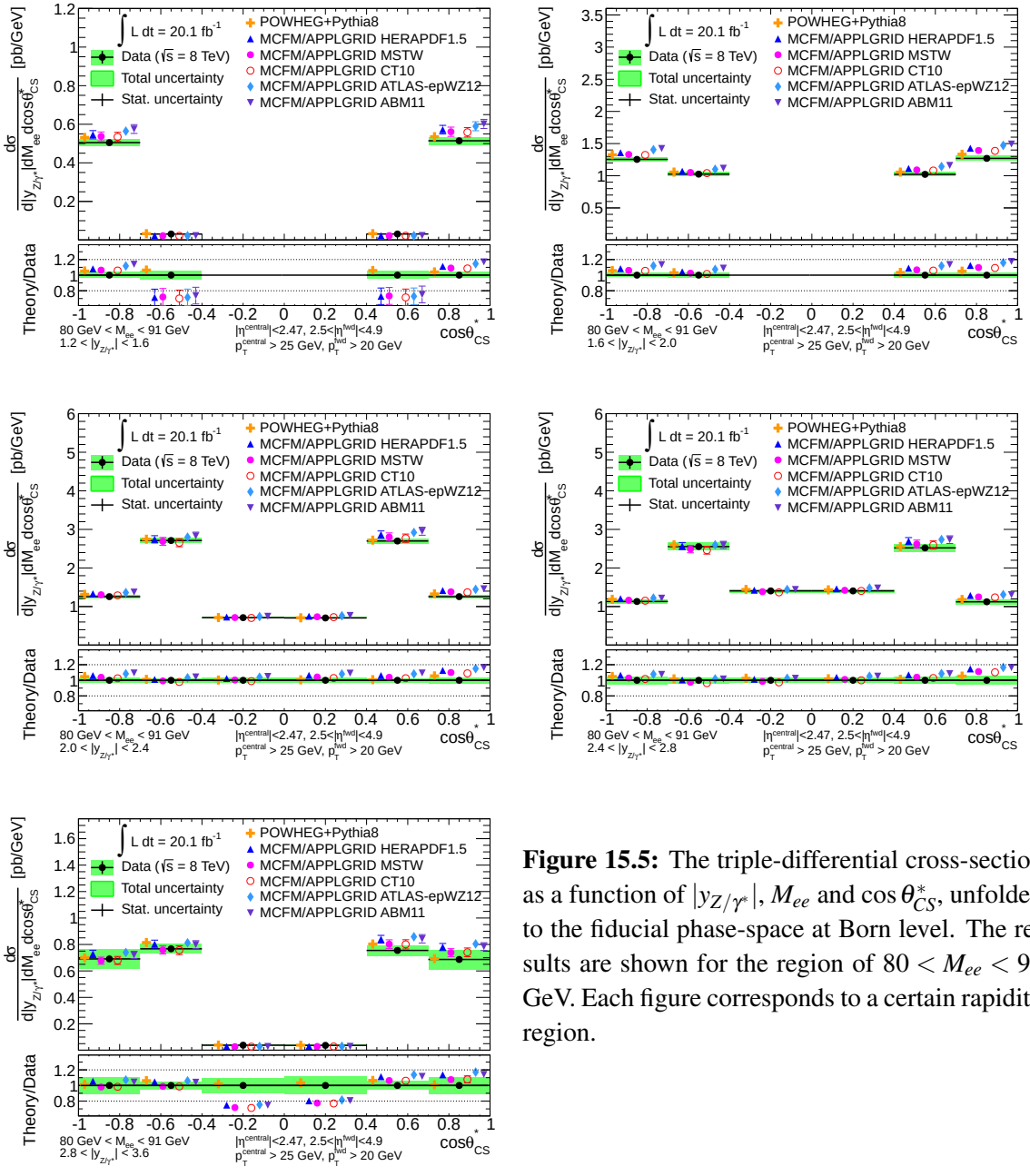

Figure 15.5: The triple-differential cross-section as a function of $|y_{Z/\gamma^*}|$, M_{ee} and $\cos\theta^*_{CS}$, unfolded to the fiducial phase-space at Born level. The results are shown for the region of $80 < M_{ee} < 91$ GeV. Each figure corresponds to a certain rapidity region.

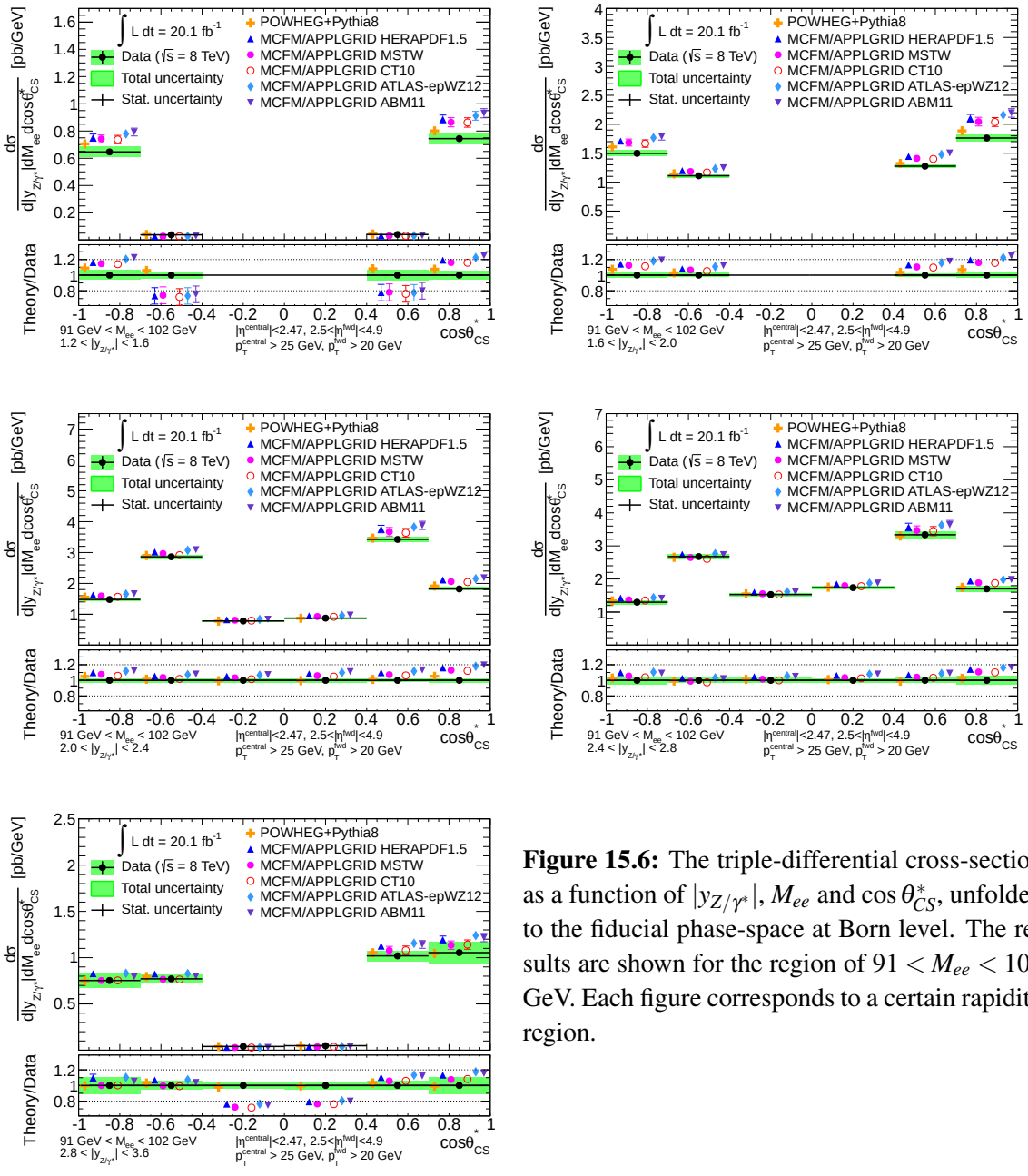

Figure 15.6: The triple-differential cross-section as a function of $|y_{Z/\gamma^*}|$, M_{ee} and $\cos\theta^*_{CS}$, unfolded to the fiducial phase-space at Born level. The results are shown for the region of $91 < M_{ee} < 102$ GeV. Each figure corresponds to a certain rapidity region.

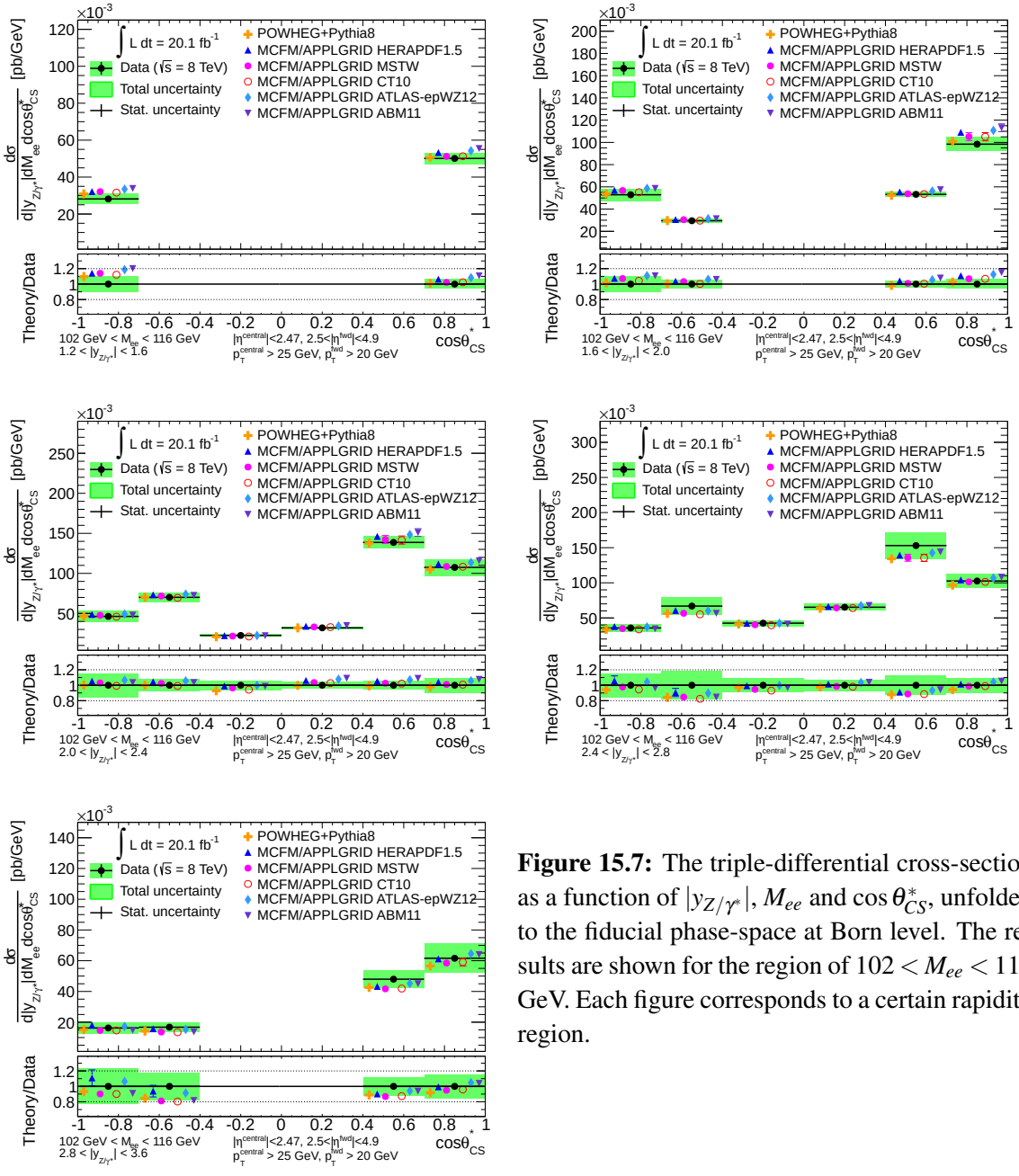

Figure 15.7: The triple-differential cross-section as a function of $|y_{Z/\gamma^*}|$, M_{ee} and $\cos\theta^*_{CS}$, unfolded to the fiducial phase-space at Born level. The results are shown for the region of $102 < M_{ee} < 116$ GeV. Each figure corresponds to a certain rapidity region.

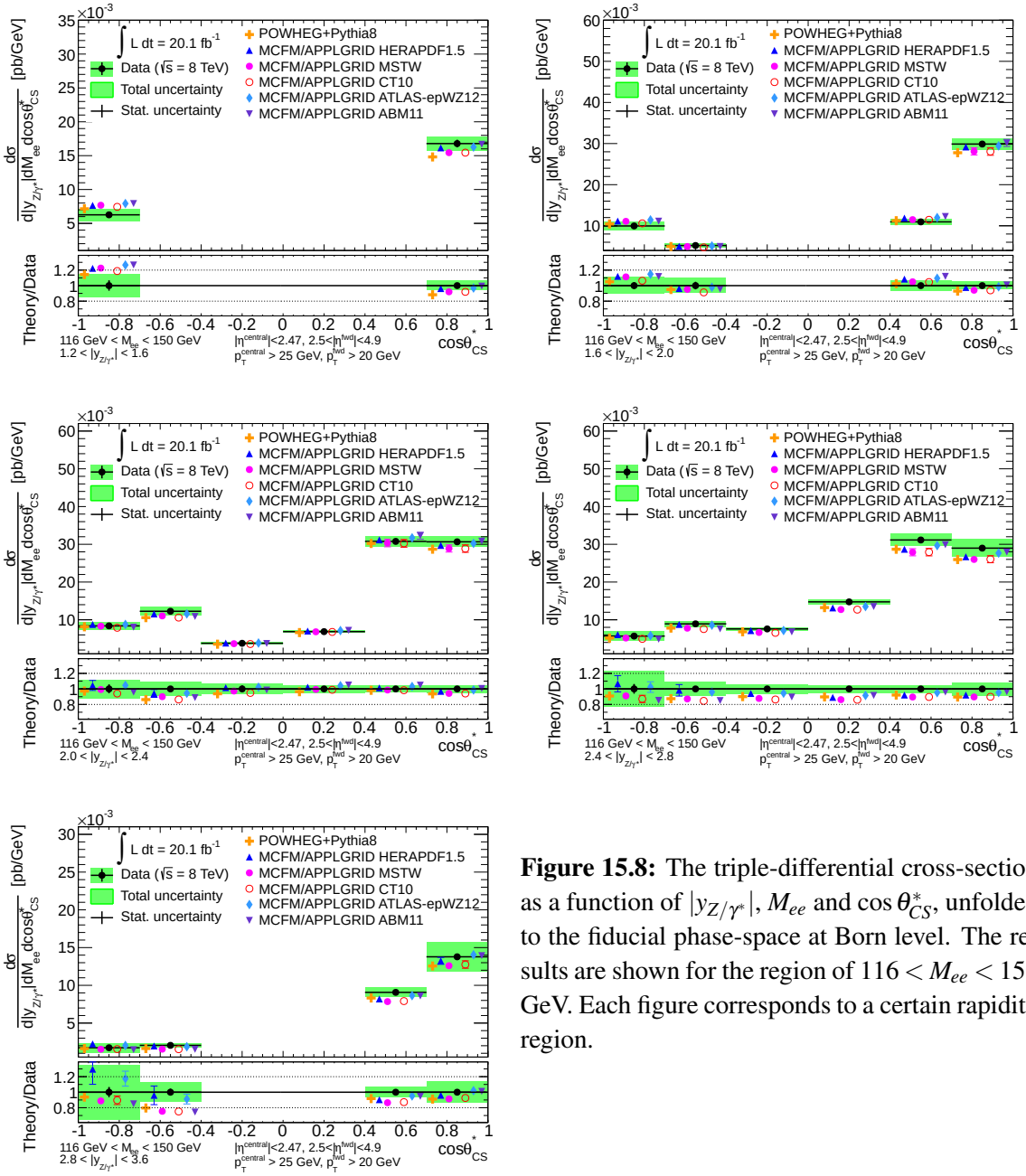

Figure 15.8: The triple-differential cross-section as a function of $|y_{Z/\gamma^*}|$, M_{ee} and $\cos\theta^*_{CS}$, unfolded to the fiducial phase-space at Born level. The results are shown for the region of $116 < M_{ee} < 150$ GeV. Each figure corresponds to a certain rapidity region.

CHAPTER 16

Forward-Backward asymmetry measurement

The Forward-Backward asymmetry is measured double-differentially as a function of the dielectron invariant mass and rapidity. The measurement is unfolded to the fiducial phase-space at the Born level. The A_{FB} is extracted from the triple-differential cross-section measurement (see chapter 15). The results on the A_{FB} measurement are listed in the table 16.1 as a function of M_{ee} for different $|y_{Z/\gamma^*}|$ regions. Each uncertainty source that affects the triple-differential cross-section measurement is individually propagated to A_{FB}. The uncorrelated and correlated uncertainties are treated differently. The uncorrelated uncertainties are propagated as

$$\delta_{A_{FB}}^{\text{uncorr}} = \sqrt{\sum_{i=1}^{3}\left(\frac{df(\sigma^F,\sigma^B)}{d\sigma_i^F}\sigma_i^F\right)^2 + \sum_{i=1}^{3}\left(\frac{df(\sigma^F,\sigma^B)}{d\sigma_i^B}\sigma_i^B\right)^2}, \tag{16.1}$$

where F and B denote the bins with $\cos\theta^*_{CS} > 0$ and $\cos\theta^*_{CS} < 0$ respectively, their indices 1 to 3 represent the $\cos\theta^*_{CS}$ bins in order of increasing $\cos\theta^*_{CS}$ and

$$\begin{aligned} f(\sigma^F,\sigma^B) &= \frac{\sigma_1^F+\sigma_2^F+\sigma_3^F-\sigma_1^B-\sigma_2^B-\sigma_3^B}{\sigma_1^F+\sigma_2^F+\sigma_3^F+\sigma_1^B+\sigma_2^B+\sigma_3^B} = \\ &= \frac{\int_0^1 \frac{\mathrm{d}\sigma}{\mathrm{d}|y_{Z/\gamma^*}|\mathrm{d}M_{ee}\mathrm{d}\cos\theta^*_{CS}}\mathrm{d}\cos\theta^*_{CS} - \int_{-1}^0 \frac{\mathrm{d}\sigma}{\mathrm{d}|y_{Z/\gamma^*}|\mathrm{d}M_{ee}\mathrm{d}\cos\theta^*_{CS}}\mathrm{d}\cos\theta^*_{CS}}{\int_0^1 \frac{\mathrm{d}\sigma}{\mathrm{d}|y_{Z/\gamma^*}|\mathrm{d}M_{ee}\mathrm{d}\cos\theta^*_{CS}}\mathrm{d}\cos\theta^*_{CS} + \int_{-1}^0 \frac{\mathrm{d}\sigma}{\mathrm{d}|y_{Z/\gamma^*}|\mathrm{d}M_{ee}\mathrm{d}\cos\theta^*_{CS}}\mathrm{d}\cos\theta^*_{CS}}. \end{aligned} \tag{16.2}$$

The correlated systematic uncertainties are propagated to A_{FB} measurement using simultaneous shift of the forward and backward components:

$$\delta_{A_{FB}}^{\text{corr}} = f(\sigma^F_{\text{corr}},\sigma^B_{\text{corr}}) - f(\sigma^F,\sigma^B), \tag{16.3}$$

with $\sigma^{F/B}_{\text{corr}} = \sigma^{F/B} + \delta^{F/B}_{\text{corr}}$, where δ_{corr} is a correlated uncertainty.

The uncertainty of the A_{FB} measurement dominates by the statistical uncertainty of the data sample, the uncertainties due to the unfolding procedure, and by the statistical component of the uncertainty on the multi-jets background modeling. The propagation of the correlated uncertainties leads to their reduction. This is observed when an uncertainty does not depend significantly on the sign of the $\cos\theta^*_{CS}$. As an example, an uncertainty which is equal for forward an backward parts, $\delta^F = \delta^B$, will reduce according to

$$\frac{\sigma^F+\delta^F-\sigma^B-\delta^B}{\sigma^F+\delta^F+\sigma^B+\delta^B} - \frac{\sigma^F-\sigma^B}{\sigma^F+\sigma^B} = \frac{\sigma^F-\sigma^B}{\sigma^F+\sigma^B+2\delta^F} - \frac{\sigma^F-\sigma^B}{\sigma^F+\sigma^B}. \tag{16.4}$$

A significant reduction is observed for the uncertainties due to the forward electron energy scale and resolution corrections, which were among the dominant uncertainty sources for the cross-section measurements. The systematic uncertainty due to the background modeling is reduced, however a non-negligible uncertainty from this source affects the A_{FB} measurement. The multi-jets background has no Forward-Backward asymmetry (see figure 10.3). However a large background contamination dilutes the measured asymmetry. Uncertainty in this contamination remains sizable for low and high mass regions.

The theoretical predictions for the A_{FB} are obtained from the cross-section predictions derived with POWHEG+PYTHIA8 and MCFM/APPLGRID using eq. (16.2). The used PDF sets are CT10 NLO, HERAPDF 1.5 NLO, MSTW2008 NLO, ATLAS WZ and ABM11 NLO 5fl. The predictions are sensitive to the choice of PDF, since the asymmetry spectrum differs for up- and down-quark densities. The uncertainty for the POWHEG+PYTHIA8 predictions is taken from the statistical limitations of the Monte-Carlo sample. The uncertainties for the MCFM/APPLGRID predictions are coming from the μ_R and μ_F scale variations and from the corresponding PDF uncertainties at 68% confidence level.

The comparison of the measured A_{FB} with the theoretical predictions is shown in figures 16.1, 16.2. The results of the measurement are in good agreement with the theory. The deviations in the rapidity bin of $1.2 < |y_{Z/\gamma^*}| < 1.6$ are however observed, which follows the deviation of the measured cross-section (figure 15.1), more precise measurement of this region is rather expected with central-central configurations. The observed increase of the A_{FB} at higher rapidities is related to more precise determination of the incoming quark directions, which reduces the asymmetry dilution, as discussed in section 3.3. The change of the A_{FB} sign across the Z mass peak is due to the reversal of sign of the γZ interference term in eq. (3.8). At high rapidity region the uncertainty on the A_{FB} measurement is found to be smaller than the difference between the theoretical predictions, so that the data is expected to have constraining power for PDF fits.

Bin $\lvert y_{Z/\gamma^*}\rvert$	Bin M_{ee}	A_{FB}	Total unc.	Stat. unc	Syst unc.
1.2 - 1.6	66 - 80	-0.213	0.043	0.019	0.039
1.2 - 1.6	80 - 91	0.009	0.009	0.004	0.008
1.2 - 1.6	91 - 102	0.068	0.008	0.004	0.008
1.2 - 1.6	102 - 116	0.280	0.029	0.010	0.028
1.2 - 1.6	116 - 150	0.456	0.044	0.011	0.042
1.6 - 2.0	66 - 80	-0.221	0.019	0.006	0.018
1.6 - 2.0	80 - 91	0.003	0.005	0.002	0.005
1.6 - 2.0	91 - 102	0.076	0.005	0.002	0.005
1.6 - 2.0	102 - 116	0.296	0.019	0.006	0.018
1.6 - 2.0	116 - 150	0.458	0.026	0.008	0.025
2.0 - 2.4	66 - 80	-0.265	0.014	0.004	0.013
2.0 - 2.4	80 - 91	-0.002	0.005	0.002	0.004
2.0 - 2.4	91 - 102	0.087	0.004	0.002	0.004
2.0 - 2.4	102 - 116	0.327	0.016	0.005	0.015
2.0 - 2.4	116 - 150	0.467	0.022	0.007	0.021
2.4 - 2.8	66 - 80	-0.295	0.012	0.004	0.012
2.4 - 2.8	80 - 91	-0.004	0.005	0.002	0.004
2.4 - 2.8	91 - 102	0.100	0.005	0.002	0.005
2.4 - 2.8	102 - 116	0.365	0.019	0.005	0.018
2.4 - 2.8	116 - 150	0.527	0.023	0.007	0.022
2.8 - 3.6	66 - 80	-0.465	0.024	0.005	0.023
2.8 - 3.6	80 - 91	-0.006	0.007	0.002	0.006
2.8 - 3.6	91 - 102	0.151	0.006	0.002	0.006
2.8 - 3.6	102 - 116	0.537	0.026	0.005	0.026
2.8 - 3.6	116 - 150	0.716	0.034	0.008	0.033

Table 16.1: The results of the double-differential measurements of A_{FB} as a function of $\lvert y_{Z/\gamma^*}\rvert$ and M_{ee}. The measurement is unfolded to the fiducial phase-space at Born level.

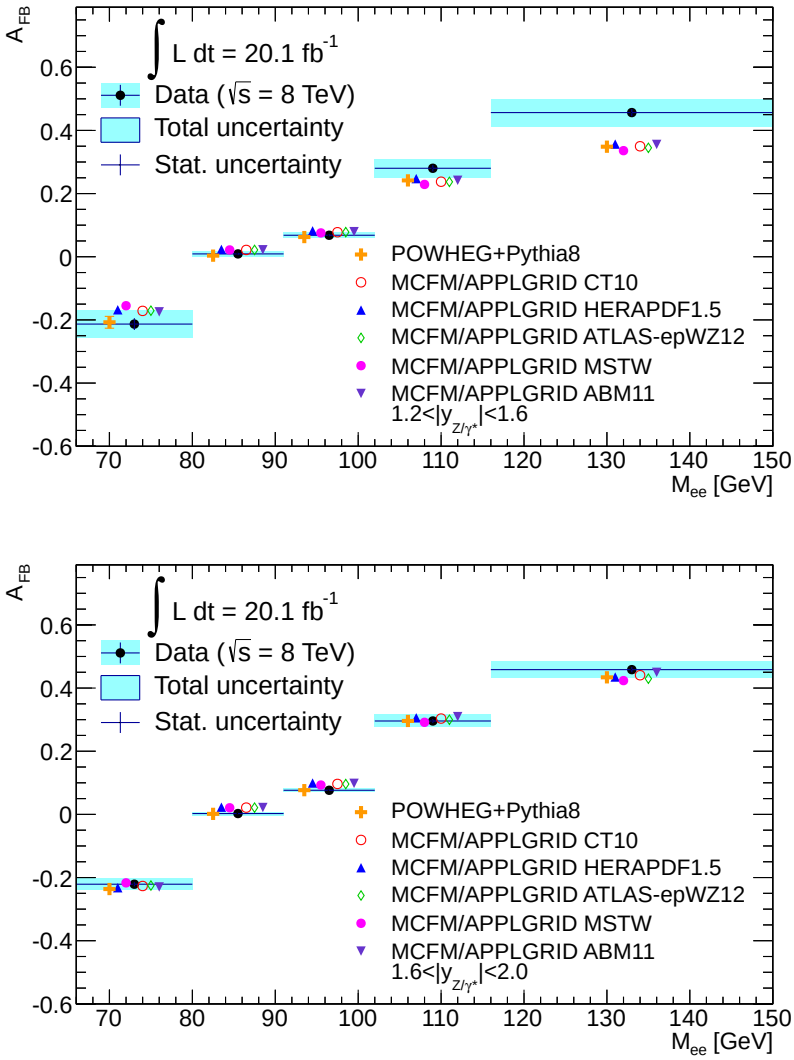

Figure 16.1: The A_{FB} measured double-differentialy as a function of $|y_{Z/\gamma^*}|$ and M_{ee}. Two rapidity regions are shown: $1.2 < |y_{Z/\gamma^*}| < 1.6$ (top) and $1.6 < |y_{Z/\gamma^*}| < 2.0$ (bottom). The results are unfolded to the fiducial phase-space at Born level.

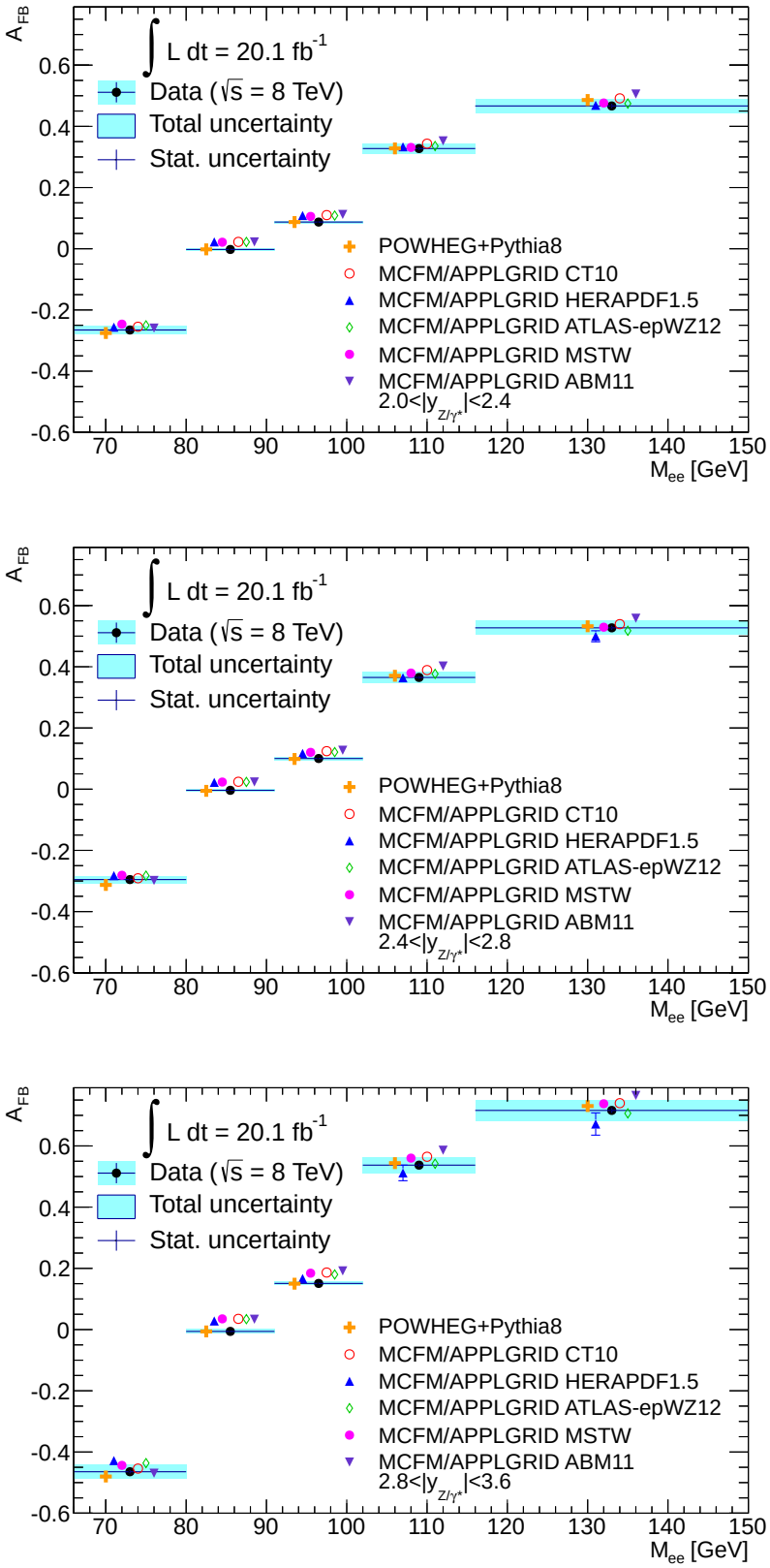

Figure 16.2: The A_{FB} measured double-differentialy as a function of $|y_{Z/\gamma^*}|$ and M_{ee}. Three rapidity regions are shown: $2.0 < |y_{Z/\gamma^*}| < 2.4$ (top), $2.4 < |y_{Z/\gamma^*}| < 2.8$ (middle) and $2.8 < |y_{Z/\gamma^*}| < 3.6$ (bottom). The results are unfolded to the fiducial phase-space at Born level.

CHAPTER 17

Summary

This thesis presented the measurements of the differential cross-section and Forward-Backward asymmetry of the inclusive $pp \to Z/\gamma^* \to e^+e^-$ process in the central-forward final-state configuration. The cross-section has been measured single- and triple-differentially as a function of the Z/γ^* boson rapidity, invariant mass and electron scattering angle. The measurement of the Forward-Backward asymmetry is performed double-differentially as a function of Z/γ^* boson rapidity and dielectron invariant mass. Both measurements are based on data collected with the ATLAS detector in 2012 at a center-of-mass energy of $\sqrt{s} = 8$ TeV.

The contribution of background processes to the cross-section and A_{FB} measurements is estimated using both simulation and data-driven techniques. The dominant background to the signal process is coming from multi-jets and $W \to e\nu$ + jets processes. Systematic uncertainties related to both the experimental and theoretical aspects of the measurements are considered. The major uncertainties of the cross-section measurements are due to the energy resolution correction and the identification efficiency of forward electrons and the multi-jets background estimation. The accuracy of the A_{FB} measurement is affected dominantly by the statistical limitations of the data sample, unfolding procedure and the multi-jets background modeling.

The results are found to agree with the NLO QCD predictions in the bulk of the measured phase space. A discrepancy is observed in certain phase space regions which can be attributed to higher order electroweak and QCD effects. The measurements extend the kinematic range towards lower and higher x values, compared to the central-central configuration. Moreover, the sensitivity of the central-forward data to the parton densities and to the electroweak parameters, can be exploited in PDF fits and can also be used for extracting the effective weak mixing angle.

APPENDIX A

QCD analysis of the low-mass Drell-Yan data at $\sqrt{s} = 7$ TeV

In the region below the Z mass peak, referred to throughout the text as "low-mass", the Drell-Yan cross-section is dominated by the electromagnetic coupling of $q\bar{q}$ pairs to the virtual photon. As discussed in chapter 3, the flavor decomposition of photon exchange processes differs from the one near the Z pole. A QCD fit study which investigates the impact of the low-mass Drell-Yan data on proton PDFs is presented in this section.

The low-mass Drell-Yan production cross-section has been measured as a function of the dilepton invariant mass by the ATLAS Collaboration using $\sqrt{s} = 7$ TeV data [94]. Two regions below the Z mass peak have been analyzed. The first measurement, termed *nominal*, is performed in the region $26 < M_{\ell\ell} < 66$ GeV and it is based on electron and muon Drell-Yan data collected in 2011. The second measurement benefits from the low-threshold muon trigger used in 2010 and covers a wider kinematic region spanning $12 < M_{\ell\ell} < 66$ GeV. The measurements are performed in the fiducial phase space regions described in Table A.1. The corresponding kinematic coverage on the (x, Q^2) plane is shown in figure A.1.

Nominal measurement	*Extended* measurement
$26 < M_{\ell\ell} < 66$ GeV	$12 < M_{\mu\mu} < 66 GeV$
$p_T^{\ell,\text{leading}} > 15$ GeV, $p_T^{\ell,\text{sub-leading}} > 12$ GeV	$p_T^{\ell,\text{leading}} > 9$ GeV, $p_T^{\ell,\text{sub-leading}} > 6$ GeV
$\lvert\eta^{\ell}\rvert < 2.4$	$\lvert\eta^{\mu}\rvert < 2.4$

Table A.1: The definition of the fiducial phase space for the *nominal* and *extended* ATLAS Drell-Yan measurements.

In the QCD fit studies, DIS measurements from HERA-I [98] are used as a base layer to allow for the extraction of the complete set of PDFs and are taken as a reference for the impact of the *nominal* and *extended* Drell-Yan measurements. The fits are performed at NLO and NNLO QCD using the HERAFitter platform [98–100]. The framework uses QCDNUM [101] for PDF evolution and MINUIT [102] for minimization.

Theoretical predictions for the QCD fit studies are made using the MCFM program and the APPLGRID interface. The procedure follows closely the one described in chapter 14. The predictions are made at NLO. In order to perform NNLO QCD fits, NNLO/NLO "k-factors" are estimated using

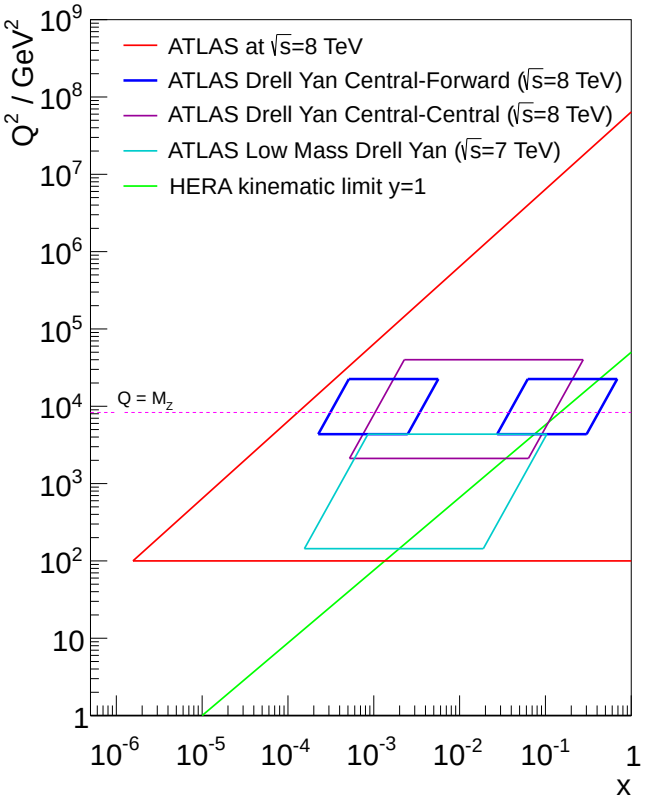

Figure A.1: Kinematic plane in Q^2, x bins. The kinematic coverage of the low-mass DY data measured by ATLAS at $\sqrt{s} = 7$ TeV TeV is shown in comparison with $\sqrt{s} = 8$ TeV DY measurements. The low-mass DY kinematic region is comprised of both *nominal* and *extended* measurements. The ATLAS kinematic limits are shown at $\sqrt{s} = 8$ TeV and the kinematic region of HERA experiments is below the inelasticity limit of $y = 1$.

the FEWZ program [103], which provides fixed-order NNLO predictions:

$$k^{NLO\to NNLO} = \frac{NNLO_{FEWZ}}{NLO_{MCFM/APPLGRID}}. \tag{A.1}$$

The PDFs are parametrized as a function of x with a starting scale $Q^2 = 1.9\,\text{GeV}^2$ using the functional forms described in [104]. The initial scale is chosen to be below the charm mass tresshold m_c^2 and at higher values of Q^2 the PDFs are obtained using the evolution equation (2.19). The generic forms for the quark distributions are expanded by adding polynomial terms only if required by the data following the procedure described in [98]. The optimal functional forms are found to be:

$$\begin{aligned}
xu_v(x) &= A_{u_v} x^{B_{u_v}} (1-x)^{C_{u_v}} (1 + E_{u_v} x^2) \\
xd_v(x) &= A d_v x^{B_{d_v}} (1-x)^{C_{s_v}} \\
x\bar{U}(x) &= A_{\bar{U}} x^{B_{\bar{U}}} (1-x)^{C_{\bar{U}}} \\
x\bar{D}(x) &= A_{\bar{D}} x^{B_{\bar{D}}} (1-x)^{C_{\bar{D}}} \\
xg(x) &= A_g x^{B_g} (1-x)^{C_g} - A'_g x^{B'_g} (1 - x^{C'_g})
\end{aligned} \tag{A.2}$$

The normalization parameters of the valence quarks A_{u_v} and B_{u_v} are fixed by the quark counting rule, and the normalization parameter of the gluon density, A_g, is fixed by the momentum sum rule. The sum rules ensure that the proton valence structure corresponds to *uud* and the proton momentum is conserved:

$$\int_0^1 [u(x) - \bar{u}(x)]\, dx = 2, \quad \int_0^1 \left[d(x) - \bar{d}(x)\right] dx = 1, \tag{A.3}$$

$$\int_0^1 [q(x) - \bar{q}(x)]\, dx = 0 \ (q = s, c, b), \tag{A.4}$$

$$\int_0^1 \sum_i x\,[q_i(x) + \bar{q}_i(x)] + xg(x) dx = 1. \tag{A.5}$$

The strange sea density is taken as the fraction of the d sea density, $x\bar{s} = r_s\bar{d}$, with r_s fixed to 1 following a recent ATLAS determination of the strage quark density [104]. The A and B, normalization and slope parameters of $x\bar{U} = x\bar{u}$ and $x\bar{D} = x\bar{d} + x\bar{s}$, are constrained by the requirement that $x\bar{u} = x\bar{d}$ at $x \to 0$. The gluon distributions are parametrized using so-called "flexible" form suggested by MSTW analyses with $C_g' = 25$ to suppress negative contributions at high x. With all these additional constraints applied, both NLO and NNLO fits use 13 parameters to describe the parton densities.

PDF fits are obtained by minimising a χ^2 function, which allows to take into account both bin-to-bin correlated and uncorrelated uncertainties of the data included in the QCD fit studies:

$$\chi^2 = \sum_i \frac{\left[\mu_i - m_i\left(1 - \sum_j \gamma_j^i b_j\right)\right]^2}{\delta_{i,\mathrm{unc}}^2 m_i^2 + \delta_{i,\mathrm{stat}}^2 \mu_i m_i \left(1 - \sum_j \gamma_j^i b_j\right)} + \sum_j b_j^2 + \sum_i \ln \frac{\delta_{i,\mathrm{unc}}^2 m_i^2 + \delta_{i,\mathrm{stat}}^2 \mu_i m_i}{\delta_{i,\mathrm{unc}}^2 \mu_i^2 + \delta_{i,\mathrm{stat}}^2 \mu_i^2}, \tag{A.6}$$

where m_i is the theoretical prediction and μ_i is the measured cross-section at point i, (Q^2, x, s) with the relative statistical and uncorrelated systematic uncertainties $\delta_{i,\mathrm{stat}}$, $\delta_{i,\mathrm{unc}}$, respectively. γ_j^i denotes the relative correlated systematic uncertainties and b_j their shifts with a penalty term $\sum_j b_j^2$ added. To avoid a bias introduced by statistical fluctuations, the expected rather than observed number of events are used, with the corresponding errors scaled accordingly. This scaling of errors introduces a logarithmic term, coming from the likelihood transition to χ^2. Neglecting the ln term gives very similar results and does not alter any of the conclusions. The *nominal* data of the ATLAS low mass Drell-Yan data measurement contains 13 sources of correlated systematic uncertainties and a global luminosity uncertainty of 1.8%. The *extended* data contains seven sources of correlated systematic uncertainties and a luminosity uncertainty of 3.5%.

The results of the NLO and NNLO fits to the low-mass ATLAS data are summarized in table A.2.

Prediction	χ^2 (8 points) Nominal	χ^2 (6 points) Extended
NLO Fit	40.7	117.1
NNLO Fit	8.5	7.8

Table A.2: The χ^2 values.

One of the goals of this study was to investigate to what extent the disagreement with a pure NLO calculation depends on the PDF used. As shown in figures A.2 inclusion of the low-mass DY data in the PDF fit does not lead to improvement of the data to theory comparison. The poor description of the data by the NLO predictions in the lowest mass bins can be explained by the kinematic constraint created by the lepton transverse momentum requirements. In both the *nominal* and *extended* fiducial regions in lowest mass bins $M_{\ell\ell} \sim p_T^{\ell_1} + p_T^{\ell_2}$. In this regime leptons are not produced back-to-back

as the LO calculations imply and the first order contribution arises at NLO. A similar behaviour is seen in the μ_r, μ_f scale scan of the NLO predictions following the procedure described in chapter 14. The results of the scan are shown in figures A.3, A.4. In both measurements the first two mass bins display an unstable behaviour, i.e. an absence of a stable region with low dependence on the factorization and normalization scales.

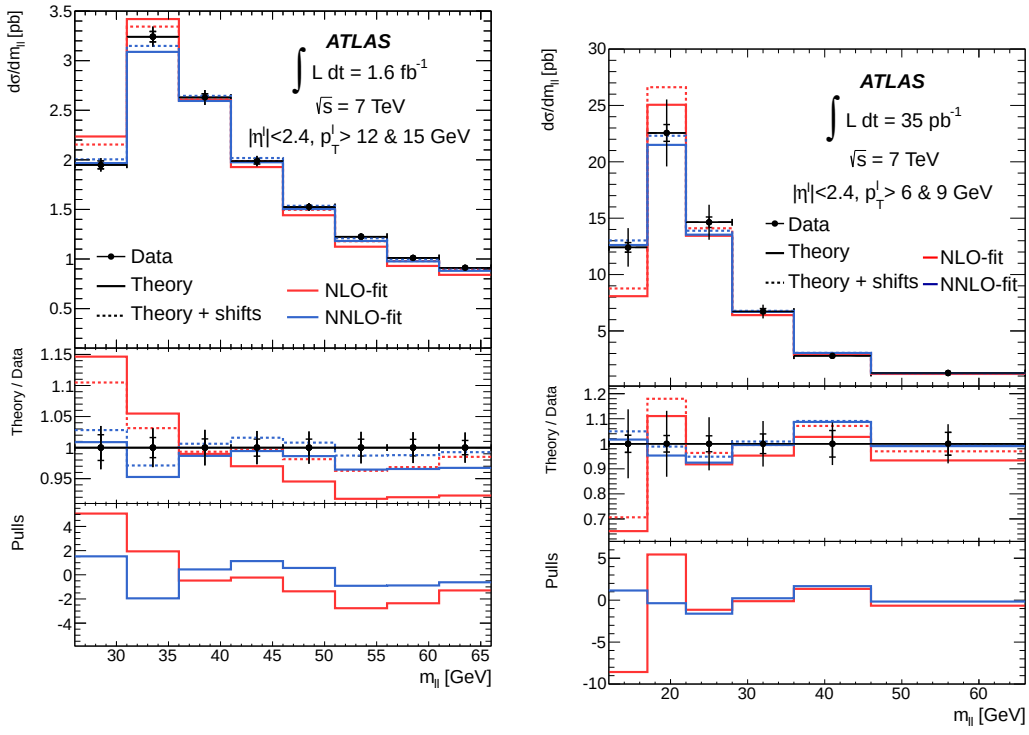

(a) **(b)**

Figure A.2: The *nominal* (a) and *extended* (b) differential cross-section as a function of invariant mass compared to the NLO and NNLO QCD fits, [94].

The impact on PDF is shown in figures A.5, where parton densities obtained at NNLO with only HERA data, quoted as reference, are compared to the fit with low mass Drell-Yan data included. The experimental uncertainties on the extracted PDFs is evaluated using the Hessian method [105], based on linear error propagation, with a tolerance criteria of $\Delta\chi^2 = 1$. The impact of the Drell-Yan data on the experimental uncertainties is marginal with the current experimental precision, however a slight improvement of the valence quark and sea quarks densities can be observed in figures A.5.

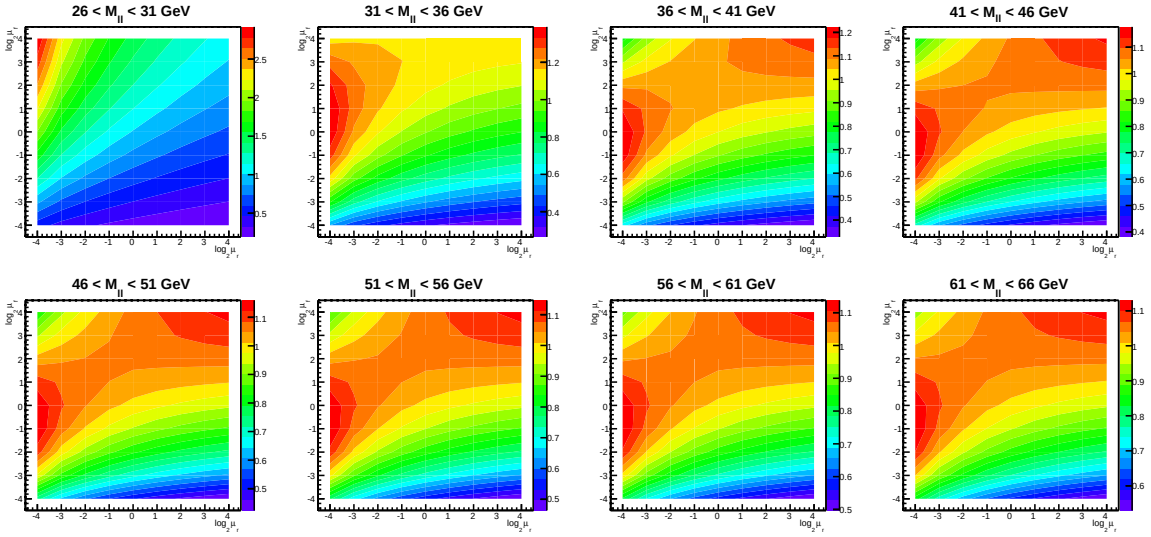

Figure A.3: Variation of the predicted at NLO QCD *nominal* DY cross-section as a function of renormalization μ_r and factorization μ_f scale factors.

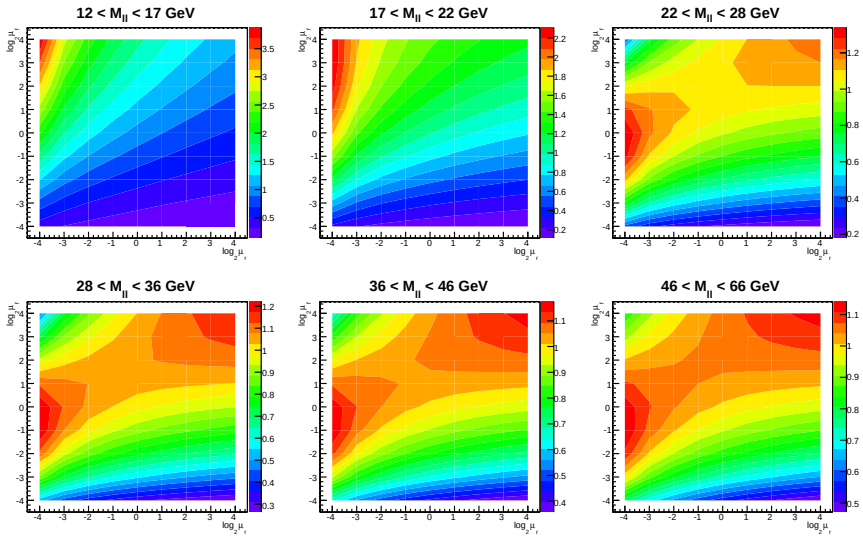

Figure A.4: Variation of the predicted at NLO QCD *extended* DY cross-section as a function of renormalization μ_r and factorization μ_f scale factors.

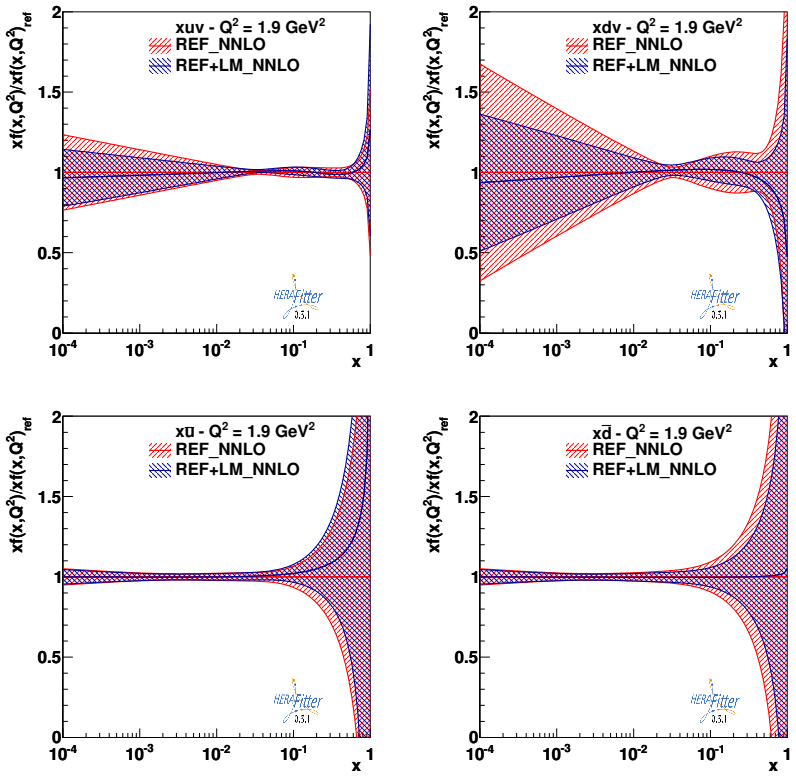

Figure A.5: Relative experimental uncertainties for valence and sea quark densities as a function of x at scale $Q^2 = 1.9\,\mathrm{GeV}^2$. The red band denotes the reference NNLO fit obtained with the HERA-I data only. The impact on the uncertainties after adding the *nominal* and *extended* Drell-Yan data to the NNLO fit is shown by blue boundaries, [106].

APPENDIX B

Binning Representation

The unfolding of the triple-differential binning into one dimention used for both, the measurement and histogram representation.

Table B.1: $2d \rightarrow 1d$ The bin number convention for the triple-binning representation. Withing each mass bin the binning of $|y_{Z/\gamma^*}|$ and $\cos\theta^*_{CS}$ can be formed using the corresponding bin number.

$3d \rightarrow 1d$ Bin number	Bin edges		
1	$1.2 < \|y_{Z/\gamma^*}\| < 1.6$	$-1.0 < \cos\theta^*_{CS} < -0.7$	$66 < M_{ee} < 80$ GeV
2	$1.6 < \|y_{Z/\gamma^*}\| < 2.0$	$-1.0 < \cos\theta^*_{CS} < -0.7$	$66 < M_{ee} < 80$ GeV
3	$2.0 < \|y_{Z/\gamma^*}\| < 2.4$	$-1.0 < \cos\theta^*_{CS} < -0.7$	$66 < M_{ee} < 80$ GeV
4	$2.4 < \|y_{Z/\gamma^*}\| < 2.8$	$-1.0 < \cos\theta^*_{CS} < -0.7$	$66 < M_{ee} < 80$ GeV
5	$2.8 < \|y_{Z/\gamma^*}\| < 3.6$	$-1.0 < \cos\theta^*_{CS} < -0.7$	$66 < M_{ee} < 80$ GeV
6[1]	$1.2 < \|y_{Z/\gamma^*}\| < 1.6$	$-0.7 < \cos\theta^*_{CS} < -0.4$	$66 < M_{ee} < 80$ GeV
7	$1.6 < \|y_{Z/\gamma^*}\| < 2.0$	$-0.7 < \cos\theta^*_{CS} < -0.4$	$66 < M_{ee} < 80$ GeV
8	$2.0 < \|y_{Z/\gamma^*}\| < 2.4$	$-0.7 < \cos\theta^*_{CS} < -0.4$	$66 < M_{ee} < 80$ GeV
9	$2.4 < \|y_{Z/\gamma^*}\| < 2.8$	$-0.7 < \cos\theta^*_{CS} < -0.4$	$66 < M_{ee} < 80$ GeV
10	$2.8 < \|y_{Z/\gamma^*}\| < 3.6$	$-0.7 < \cos\theta^*_{CS} < -0.4$	$66 < M_{ee} < 80$ GeV
11[1]	$1.2 < \|y_{Z/\gamma^*}\| < 1.6$	$-0.4 < \cos\theta^*_{CS} < 0.0$	$66 < M_{ee} < 80$ GeV
12[1]	$1.6 < \|y_{Z/\gamma^*}\| < 2.0$	$-0.4 < \cos\theta^*_{CS} < 0.0$	$66 < M_{ee} < 80$ GeV
13	$2.0 < \|y_{Z/\gamma^*}\| < 2.4$	$-0.4 < \cos\theta^*_{CS} < 0.0$	$66 < M_{ee} < 80$ GeV
14	$2.4 < \|y_{Z/\gamma^*}\| < 2.8$	$-0.4 < \cos\theta^*_{CS} < 0.0$	$66 < M_{ee} < 80$ GeV
15[1]	$2.8 < \|y_{Z/\gamma^*}\| < 3.6$	$-0.4 < \cos\theta^*_{CS} < 0.0$	$66 < M_{ee} < 80$ GeV
16[1]	$1.2 < \|y_{Z/\gamma^*}\| < 1.6$	$0.0 < \cos\theta^*_{CS} < 0.4$	$66 < M_{ee} < 80$ GeV
17[1]	$1.6 < \|y_{Z/\gamma^*}\| < 2.0$	$0.0 < \cos\theta^*_{CS} < 0.4$	$66 < M_{ee} < 80$ GeV
18	$2.0 < \|y_{Z/\gamma^*}\| < 2.4$	$0.0 < \cos\theta^*_{CS} < 0.4$	$66 < M_{ee} < 80$ GeV
19	$2.4 < \|y_{Z/\gamma^*}\| < 2.8$	$0.0 < \cos\theta^*_{CS} < 0.4$	$66 < M_{ee} < 80$ GeV
20[1]	$2.8 < \|y_{Z/\gamma^*}\| < 3.6$	$0.0 < \cos\theta^*_{CS} < 0.4$	$66 < M_{ee} < 80$ GeV
21[1]	$1.2 < \|y_{Z/\gamma^*}\| < 1.6$	$0.4 < \cos\theta^*_{CS} < 0.7$	$66 < M_{ee} < 80$ GeV

[1] Bins are excluded from the analysis as explained in chapter 9.

$3d \rightarrow 1d$ Bin number	Bin boundaries		
22	$1.6 < \lvert y_{Z/\gamma^*} \rvert < 2.0$	$0.4 < \cos\theta^*_{CS} < 0.7$	$66 < M_{ee} < 80$ GeV
23	$2.0 < \lvert y_{Z/\gamma^*} \rvert < 2.4$	$0.4 < \cos\theta^*_{CS} < 0.7$	$66 < M_{ee} < 80$ GeV
24	$2.4 < \lvert y_{Z/\gamma^*} \rvert < 2.8$	$0.4 < \cos\theta^*_{CS} < 0.7$	$66 < M_{ee} < 80$ GeV
25	$2.8 < \lvert y_{Z/\gamma^*} \rvert < 3.6$	$0.4 < \cos\theta^*_{CS} < 0.7$	$66 < M_{ee} < 80$ GeV
26	$1.2 < \lvert y_{Z/\gamma^*} \rvert < 1.6$	$0.7 < \cos\theta^*_{CS} < 1.0$	$66 < M_{ee} < 80$ GeV
27	$1.6 < \lvert y_{Z/\gamma^*} \rvert < 2.0$	$0.7 < \cos\theta^*_{CS} < 1.0$	$66 < M_{ee} < 80$ GeV
28	$2.0 < \lvert y_{Z/\gamma^*} \rvert < 2.4$	$0.7 < \cos\theta^*_{CS} < 1.0$	$66 < M_{ee} < 80$ GeV
29	$2.4 < \lvert y_{Z/\gamma^*} \rvert < 2.8$	$0.7 < \cos\theta^*_{CS} < 1.0$	$66 < M_{ee} < 80$ GeV
30	$2.8 < \lvert y_{Z/\gamma^*} \rvert < 3.6$	$0.7 < \cos\theta^*_{CS} < 1.0$	$66 < M_{ee} < 80$ GeV
31	$1.2 < \lvert y_{Z/\gamma^*} \rvert < 1.6$	$-1.0 < \cos\theta^*_{CS} < -0.7$	$80 < M_{ee} < 91$ GeV
32	$1.6 < \lvert y_{Z/\gamma^*} \rvert < 2.0$	$-1.0 < \cos\theta^*_{CS} < -0.7$	$80 < M_{ee} < 91$ GeV
33	$2.0 < \lvert y_{Z/\gamma^*} \rvert < 2.4$	$-1.0 < \cos\theta^*_{CS} < -0.7$	$80 < M_{ee} < 91$ GeV
34	$2.4 < \lvert y_{Z/\gamma^*} \rvert < 2.8$	$-1.0 < \cos\theta^*_{CS} < -0.7$	$80 < M_{ee} < 91$ GeV
35	$2.8 < \lvert y_{Z/\gamma^*} \rvert < 3.6$	$-1.0 < \cos\theta^*_{CS} < -0.7$	$80 < M_{ee} < 91$ GeV
36	$1.2 < \lvert y_{Z/\gamma^*} \rvert < 1.6$	$-0.7 < \cos\theta^*_{CS} < -0.4$	$80 < M_{ee} < 91$ GeV
37	$1.6 < \lvert y_{Z/\gamma^*} \rvert < 2.0$	$-0.7 < \cos\theta^*_{CS} < -0.4$	$80 < M_{ee} < 91$ GeV
38	$2.0 < \lvert y_{Z/\gamma^*} \rvert < 2.4$	$-0.7 < \cos\theta^*_{CS} < -0.4$	$80 < M_{ee} < 91$ GeV
39	$2.4 < \lvert y_{Z/\gamma^*} \rvert < 2.8$	$-0.7 < \cos\theta^*_{CS} < -0.4$	$80 < M_{ee} < 91$ GeV
40	$2.8 < \lvert y_{Z/\gamma^*} \rvert < 3.6$	$-0.7 < \cos\theta^*_{CS} < -0.4$	$80 < M_{ee} < 91$ GeV
41[1]	$1.2 < \lvert y_{Z/\gamma^*} \rvert < 1.6$	$-0.4 < \cos\theta^*_{CS} < 0.0$	$80 < M_{ee} < 91$ GeV
42[1]	$1.6 < \lvert y_{Z/\gamma^*} \rvert < 2.0$	$-0.4 < \cos\theta^*_{CS} < 0.0$	$80 < M_{ee} < 91$ GeV
43	$2.0 < \lvert y_{Z/\gamma^*} \rvert < 2.4$	$-0.4 < \cos\theta^*_{CS} < 0.0$	$80 < M_{ee} < 91$ GeV
44	$2.4 < \lvert y_{Z/\gamma^*} \rvert < 2.8$	$-0.4 < \cos\theta^*_{CS} < 0.0$	$80 < M_{ee} < 91$ GeV
45	$2.8 < \lvert y_{Z/\gamma^*} \rvert < 3.6$	$-0.4 < \cos\theta^*_{CS} < 0.0$	$80 < M_{ee} < 91$ GeV
46[1]	$1.2 < \lvert y_{Z/\gamma^*} \rvert < 1.6$	$0.0 < \cos\theta^*_{CS} < 0.4$	$80 < M_{ee} < 91$ GeV
47[1]	$1.6 < \lvert y_{Z/\gamma^*} \rvert < 2.0$	$0.0 < \cos\theta^*_{CS} < 0.4$	$80 < M_{ee} < 91$ GeV
48	$2.0 < \lvert y_{Z/\gamma^*} \rvert < 2.4$	$0.0 < \cos\theta^*_{CS} < 0.4$	$80 < M_{ee} < 91$ GeV
49	$2.4 < \lvert y_{Z/\gamma^*} \rvert < 2.8$	$0.0 < \cos\theta^*_{CS} < 0.4$	$80 < M_{ee} < 91$ GeV
50	$2.8 < \lvert y_{Z/\gamma^*} \rvert < 3.6$	$0.0 < \cos\theta^*_{CS} < 0.4$	$80 < M_{ee} < 91$ GeV
51	$1.2 < \lvert y_{Z/\gamma^*} \rvert < 1.6$	$0.4 < \cos\theta^*_{CS} < 0.7$	$80 < M_{ee} < 91$ GeV
52	$1.6 < \lvert y_{Z/\gamma^*} \rvert < 2.0$	$0.4 < \cos\theta^*_{CS} < 0.7$	$80 < M_{ee} < 91$ GeV
53	$2.0 < \lvert y_{Z/\gamma^*} \rvert < 2.4$	$0.4 < \cos\theta^*_{CS} < 0.7$	$80 < M_{ee} < 91$ GeV
54	$2.4 < \lvert y_{Z/\gamma^*} \rvert < 2.8$	$0.4 < \cos\theta^*_{CS} < 0.7$	$80 < M_{ee} < 91$ GeV
55	$2.8 < \lvert y_{Z/\gamma^*} \rvert < 3.6$	$0.4 < \cos\theta^*_{CS} < 0.7$	$80 < M_{ee} < 91$ GeV
56	$1.2 < \lvert y_{Z/\gamma^*} \rvert < 1.6$	$0.7 < \cos\theta^*_{CS} < 1.0$	$80 < M_{ee} < 91$ GeV
57	$1.6 < \lvert y_{Z/\gamma^*} \rvert < 2.0$	$0.7 < \cos\theta^*_{CS} < 1.0$	$80 < M_{ee} < 91$ GeV
58	$2.0 < \lvert y_{Z/\gamma^*} \rvert < 2.4$	$0.7 < \cos\theta^*_{CS} < 1.0$	$80 < M_{ee} < 91$ GeV
59	$2.4 < \lvert y_{Z/\gamma^*} \rvert < 2.8$	$0.7 < \cos\theta^*_{CS} < 1.0$	$80 < M_{ee} < 91$ GeV

$3d \to 1d$ Bin number	Bin boundaries		
60	$2.8 < \lvert y_{Z/\gamma^*} \rvert < 3.6$	$0.7 < \cos\theta^*_{CS} < 1.0$	$80 < M_{ee} < 91$ GeV
61	$1.2 < \lvert y_{Z/\gamma^*} \rvert < 1.6$	$-1.0 < \cos\theta^*_{CS} < -0.7$	$91 < M_{ee} < 102$ GeV
62	$1.6 < \lvert y_{Z/\gamma^*} \rvert < 2.0$	$-1.0 < \cos\theta^*_{CS} < -0.7$	$91 < M_{ee} < 102$ GeV
63	$2.0 < \lvert y_{Z/\gamma^*} \rvert < 2.4$	$-1.0 < \cos\theta^*_{CS} < -0.7$	$91 < M_{ee} < 102$ GeV
64	$2.4 < \lvert y_{Z/\gamma^*} \rvert < 2.8$	$-1.0 < \cos\theta^*_{CS} < -0.7$	$91 < M_{ee} < 102$ GeV
65	$2.8 < \lvert y_{Z/\gamma^*} \rvert < 3.6$	$-1.0 < \cos\theta^*_{CS} < -0.7$	$91 < M_{ee} < 102$ GeV
66	$1.2 < \lvert y_{Z/\gamma^*} \rvert < 1.6$	$-0.7 < \cos\theta^*_{CS} < -0.4$	$91 < M_{ee} < 102$ GeV
67	$1.6 < \lvert y_{Z/\gamma^*} \rvert < 2.0$	$-0.7 < \cos\theta^*_{CS} < -0.4$	$91 < M_{ee} < 102$ GeV
68	$2.0 < \lvert y_{Z/\gamma^*} \rvert < 2.4$	$-0.7 < \cos\theta^*_{CS} < -0.4$	$91 < M_{ee} < 102$ GeV
69	$2.4 < \lvert y_{Z/\gamma^*} \rvert < 2.8$	$-0.7 < \cos\theta^*_{CS} < -0.4$	$91 < M_{ee} < 102$ GeV
70	$2.8 < \lvert y_{Z/\gamma^*} \rvert < 3.6$	$-0.7 < \cos\theta^*_{CS} < -0.4$	$91 < M_{ee} < 102$ GeV
71[1]	$1.2 < \lvert y_{Z/\gamma^*} \rvert < 1.6$	$-0.4 < \cos\theta^*_{CS} < 0.0$	$91 < M_{ee} < 102$ GeV
72[1]	$1.6 < \lvert y_{Z/\gamma^*} \rvert < 2.0$	$-0.4 < \cos\theta^*_{CS} < 0.0$	$91 < M_{ee} < 102$ GeV
73	$2.0 < \lvert y_{Z/\gamma^*} \rvert < 2.4$	$-0.4 < \cos\theta^*_{CS} < 0.0$	$91 < M_{ee} < 102$ GeV
74	$2.4 < \lvert y_{Z/\gamma^*} \rvert < 2.8$	$-0.4 < \cos\theta^*_{CS} < 0.0$	$91 < M_{ee} < 102$ GeV
75	$2.8 < \lvert y_{Z/\gamma^*} \rvert < 3.6$	$-0.4 < \cos\theta^*_{CS} < 0.0$	$91 < M_{ee} < 102$ GeV
76[1]	$1.2 < \lvert y_{Z/\gamma^*} \rvert < 1.6$	$0.0 < \cos\theta^*_{CS} < 0.4$	$91 < M_{ee} < 102$ GeV
77[1]	$1.6 < \lvert y_{Z/\gamma^*} \rvert < 2.0$	$0.0 < \cos\theta^*_{CS} < 0.4$	$91 < M_{ee} < 102$ GeV
78	$2.0 < \lvert y_{Z/\gamma^*} \rvert < 2.4$	$0.0 < \cos\theta^*_{CS} < 0.4$	$91 < M_{ee} < 102$ GeV
79	$2.4 < \lvert y_{Z/\gamma^*} \rvert < 2.8$	$0.0 < \cos\theta^*_{CS} < 0.4$	$91 < M_{ee} < 102$ GeV
80	$2.8 < \lvert y_{Z/\gamma^*} \rvert < 3.6$	$0.0 < \cos\theta^*_{CS} < 0.4$	$91 < M_{ee} < 102$ GeV
81	$1.2 < \lvert y_{Z/\gamma^*} \rvert < 1.6$	$0.4 < \cos\theta^*_{CS} < 0.7$	$91 < M_{ee} < 102$ GeV
82	$1.6 < \lvert y_{Z/\gamma^*} \rvert < 2.0$	$0.4 < \cos\theta^*_{CS} < 0.7$	$91 < M_{ee} < 102$ GeV
83	$2.0 < \lvert y_{Z/\gamma^*} \rvert < 2.4$	$0.4 < \cos\theta^*_{CS} < 0.7$	$91 < M_{ee} < 102$ GeV
84	$2.4 < \lvert y_{Z/\gamma^*} \rvert < 2.8$	$0.4 < \cos\theta^*_{CS} < 0.7$	$91 < M_{ee} < 102$ GeV
85	$2.8 < \lvert y_{Z/\gamma^*} \rvert < 3.6$	$0.4 < \cos\theta^*_{CS} < 0.7$	$91 < M_{ee} < 102$ GeV
86	$1.2 < \lvert y_{Z/\gamma^*} \rvert < 1.6$	$0.7 < \cos\theta^*_{CS} < 1.0$	$91 < M_{ee} < 102$ GeV
87	$1.6 < \lvert y_{Z/\gamma^*} \rvert < 2.0$	$0.7 < \cos\theta^*_{CS} < 1.0$	$91 < M_{ee} < 102$ GeV
88	$2.0 < \lvert y_{Z/\gamma^*} \rvert < 2.4$	$0.7 < \cos\theta^*_{CS} < 1.0$	$91 < M_{ee} < 102$ GeV
89	$2.4 < \lvert y_{Z/\gamma^*} \rvert < 2.8$	$0.7 < \cos\theta^*_{CS} < 1.0$	$91 < M_{ee} < 102$ GeV
90	$2.8 < \lvert y_{Z/\gamma^*} \rvert < 3.6$	$0.7 < \cos\theta^*_{CS} < 1.0$	$91 < M_{ee} < 102$ GeV
91	$1.2 < \lvert y_{Z/\gamma^*} \rvert < 1.6$	$-1.0 < \cos\theta^*_{CS} < -0.7$	$102 < M_{ee} < 116$ GeV
92	$1.6 < \lvert y_{Z/\gamma^*} \rvert < 2.0$	$-1.0 < \cos\theta^*_{CS} < -0.7$	$102 < M_{ee} < 116$ GeV
93	$2.0 < \lvert y_{Z/\gamma^*} \rvert < 2.4$	$-1.0 < \cos\theta^*_{CS} < -0.7$	$102 < M_{ee} < 116$ GeV
94	$2.4 < \lvert y_{Z/\gamma^*} \rvert < 2.8$	$-1.0 < \cos\theta^*_{CS} < -0.7$	$102 < M_{ee} < 116$ GeV
95	$2.8 < \lvert y_{Z/\gamma^*} \rvert < 3.6$	$-1.0 < \cos\theta^*_{CS} < -0.7$	$102 < M_{ee} < 116$ GeV
96[1]	$1.2 < \lvert y_{Z/\gamma^*} \rvert < 1.6$	$-0.7 < \cos\theta^*_{CS} < -0.4$	$102 < M_{ee} < 116$ GeV
97	$1.6 < \lvert y_{Z/\gamma^*} \rvert < 2.0$	$-0.7 < \cos\theta^*_{CS} < -0.4$	$102 < M_{ee} < 116$ GeV

$3d \rightarrow 1d$ Bin number	Bin boundaries		
98	$2.0 < \lvert y_{Z/\gamma^*} \rvert < 2.4$	$-0.7 < \cos\theta^*_{CS} < -0.4$	$102 < M_{ee} < 116$ GeV
99	$2.4 < \lvert y_{Z/\gamma^*} \rvert < 2.8$	$-0.7 < \cos\theta^*_{CS} < -0.4$	$102 < M_{ee} < 116$ GeV
100	$2.8 < \lvert y_{Z/\gamma^*} \rvert < 3.6$	$-0.7 < \cos\theta^*_{CS} < -0.4$	$102 < M_{ee} < 116$ GeV
101[1]	$1.2 < \lvert y_{Z/\gamma^*} \rvert < 1.6$	$-0.4 < \cos\theta^*_{CS} < 0.0$	$102 < M_{ee} < 116$ GeV
102[1]	$1.6 < \lvert y_{Z/\gamma^*} \rvert < 2.0$	$-0.4 < \cos\theta^*_{CS} < 0.0$	$102 < M_{ee} < 116$ GeV
103	$2.0 < \lvert y_{Z/\gamma^*} \rvert < 2.4$	$-0.4 < \cos\theta^*_{CS} < 0.0$	$102 < M_{ee} < 116$ GeV
104	$2.4 < \lvert y_{Z/\gamma^*} \rvert < 2.8$	$-0.4 < \cos\theta^*_{CS} < 0.0$	$102 < M_{ee} < 116$ GeV
105[1]	$2.8 < \lvert y_{Z/\gamma^*} \rvert < 3.6$	$-0.4 < \cos\theta^*_{CS} < 0.0$	$102 < M_{ee} < 116$ GeV
106[1]	$1.2 < \lvert y_{Z/\gamma^*} \rvert < 1.6$	$0.0 < \cos\theta^*_{CS} < 0.4$	$102 < M_{ee} < 116$ GeV
107[1]	$1.6 < \lvert y_{Z/\gamma^*} \rvert < 2.0$	$0.0 < \cos\theta^*_{CS} < 0.4$	$102 < M_{ee} < 116$ GeV
108	$2.0 < \lvert y_{Z/\gamma^*} \rvert < 2.4$	$0.0 < \cos\theta^*_{CS} < 0.4$	$102 < M_{ee} < 116$ GeV
109	$2.4 < \lvert y_{Z/\gamma^*} \rvert < 2.8$	$0.0 < \cos\theta^*_{CS} < 0.4$	$102 < M_{ee} < 116$ GeV
110[1]	$2.8 < \lvert y_{Z/\gamma^*} \rvert < 3.6$	$0.0 < \cos\theta^*_{CS} < 0.4$	$102 < M_{ee} < 116$ GeV
111[1]	$1.2 < \lvert y_{Z/\gamma^*} \rvert < 1.6$	$0.4 < \cos\theta^*_{CS} < 0.7$	$102 < M_{ee} < 116$ GeV
112	$1.6 < \lvert y_{Z/\gamma^*} \rvert < 2.0$	$0.4 < \cos\theta^*_{CS} < 0.7$	$102 < M_{ee} < 116$ GeV
113	$2.0 < \lvert y_{Z/\gamma^*} \rvert < 2.4$	$0.4 < \cos\theta^*_{CS} < 0.7$	$102 < M_{ee} < 116$ GeV
114	$2.4 < \lvert y_{Z/\gamma^*} \rvert < 2.8$	$0.4 < \cos\theta^*_{CS} < 0.7$	$102 < M_{ee} < 116$ GeV
115	$2.8 < \lvert y_{Z/\gamma^*} \rvert < 3.6$	$0.4 < \cos\theta^*_{CS} < 0.7$	$102 < M_{ee} < 116$ GeV
116	$1.2 < \lvert y_{Z/\gamma^*} \rvert < 1.6$	$0.7 < \cos\theta^*_{CS} < 1.0$	$102 < M_{ee} < 116$ GeV
117	$1.6 < \lvert y_{Z/\gamma^*} \rvert < 2.0$	$0.7 < \cos\theta^*_{CS} < 1.0$	$102 < M_{ee} < 116$ GeV
118	$2.0 < \lvert y_{Z/\gamma^*} \rvert < 2.4$	$0.7 < \cos\theta^*_{CS} < 1.0$	$102 < M_{ee} < 116$ GeV
119	$2.4 < \lvert y_{Z/\gamma^*} \rvert < 2.8$	$0.7 < \cos\theta^*_{CS} < 1.0$	$102 < M_{ee} < 116$ GeV
120	$2.8 < \lvert y_{Z/\gamma^*} \rvert < 3.6$	$0.7 < \cos\theta^*_{CS} < 1.0$	$102 < M_{ee} < 116$ GeV
121	$1.2 < \lvert y_{Z/\gamma^*} \rvert < 1.6$	$-1.0 < \cos\theta^*_{CS} < -0.7$	$116 < M_{ee} < 150$ GeV
122	$1.6 < \lvert y_{Z/\gamma^*} \rvert < 2.0$	$-1.0 < \cos\theta^*_{CS} < -0.7$	$116 < M_{ee} < 150$ GeV
123	$2.0 < \lvert y_{Z/\gamma^*} \rvert < 2.4$	$-1.0 < \cos\theta^*_{CS} < -0.7$	$116 < M_{ee} < 150$ GeV
124	$2.4 < \lvert y_{Z/\gamma^*} \rvert < 2.8$	$-1.0 < \cos\theta^*_{CS} < -0.7$	$116 < M_{ee} < 150$ GeV
125	$2.8 < \lvert y_{Z/\gamma^*} \rvert < 3.6$	$-1.0 < \cos\theta^*_{CS} < -0.7$	$116 < M_{ee} < 150$ GeV
126[1]	$1.2 < \lvert y_{Z/\gamma^*} \rvert < 1.6$	$-0.7 < \cos\theta^*_{CS} < -0.4$	$116 < M_{ee} < 150$ GeV
127	$1.6 < \lvert y_{Z/\gamma^*} \rvert < 2.0$	$-0.7 < \cos\theta^*_{CS} < -0.4$	$116 < M_{ee} < 150$ GeV
128	$2.0 < \lvert y_{Z/\gamma^*} \rvert < 2.4$	$-0.7 < \cos\theta^*_{CS} < -0.4$	$116 < M_{ee} < 150$ GeV
129	$2.4 < \lvert y_{Z/\gamma^*} \rvert < 2.8$	$-0.7 < \cos\theta^*_{CS} < -0.4$	$116 < M_{ee} < 150$ GeV
130	$2.8 < \lvert y_{Z/\gamma^*} \rvert < 3.6$	$-0.7 < \cos\theta^*_{CS} < -0.4$	$116 < M_{ee} < 150$ GeV
131[1]	$1.2 < \lvert y_{Z/\gamma^*} \rvert < 1.6$	$-0.4 < \cos\theta^*_{CS} < 0.0$	$116 < M_{ee} < 150$ GeV
132[1]	$1.6 < \lvert y_{Z/\gamma^*} \rvert < 2.0$	$-0.4 < \cos\theta^*_{CS} < 0.0$	$116 < M_{ee} < 150$ GeV
133	$2.0 < \lvert y_{Z/\gamma^*} \rvert < 2.4$	$-0.4 < \cos\theta^*_{CS} < 0.0$	$116 < M_{ee} < 150$ GeV
134	$2.4 < \lvert y_{Z/\gamma^*} \rvert < 2.8$	$-0.4 < \cos\theta^*_{CS} < 0.0$	$116 < M_{ee} < 150$ GeV
135[1]	$2.8 < \lvert y_{Z/\gamma^*} \rvert < 3.6$	$-0.4 < \cos\theta^*_{CS} < 0.0$	$116 < M_{ee} < 150$ GeV

$3d \rightarrow 1d$ Bin number	Bin boundaries		
136[1]	$1.2 < \lvert y_{Z/\gamma^*} \rvert < 1.6$	$0.0 < \cos\theta^*_{CS} < 0.4$	$116 < M_{ee} < 150$ GeV
137[1]	$1.6 < \lvert y_{Z/\gamma^*} \rvert < 2.0$	$0.0 < \cos\theta^*_{CS} < 0.4$	$116 < M_{ee} < 150$ GeV
138	$2.0 < \lvert y_{Z/\gamma^*} \rvert < 2.4$	$0.0 < \cos\theta^*_{CS} < 0.4$	$116 < M_{ee} < 150$ GeV
139	$2.4 < \lvert y_{Z/\gamma^*} \rvert < 2.8$	$0.0 < \cos\theta^*_{CS} < 0.4$	$116 < M_{ee} < 150$ GeV
140[1]	$2.8 < \lvert y_{Z/\gamma^*} \rvert < 3.6$	$0.0 < \cos\theta^*_{CS} < 0.4$	$116 < M_{ee} < 150$ GeV
141[1]	$1.2 < \lvert y_{Z/\gamma^*} \rvert < 1.6$	$0.4 < \cos\theta^*_{CS} < 0.7$	$116 < M_{ee} < 150$ GeV
142	$1.6 < \lvert y_{Z/\gamma^*} \rvert < 2.0$	$0.4 < \cos\theta^*_{CS} < 0.7$	$116 < M_{ee} < 150$ GeV
143	$2.0 < \lvert y_{Z/\gamma^*} \rvert < 2.4$	$0.4 < \cos\theta^*_{CS} < 0.7$	$116 < M_{ee} < 150$ GeV
144	$2.4 < \lvert y_{Z/\gamma^*} \rvert < 2.8$	$0.4 < \cos\theta^*_{CS} < 0.7$	$116 < M_{ee} < 150$ GeV
145	$2.8 < \lvert y_{Z/\gamma^*} \rvert < 3.6$	$0.4 < \cos\theta^*_{CS} < 0.7$	$116 < M_{ee} < 150$ GeV
146	$1.2 < \lvert y_{Z/\gamma^*} \rvert < 1.6$	$0.7 < \cos\theta^*_{CS} < 1.0$	$116 < M_{ee} < 150$ GeV
147	$1.6 < \lvert y_{Z/\gamma^*} \rvert < 2.0$	$0.7 < \cos\theta^*_{CS} < 1.0$	$116 < M_{ee} < 150$ GeV
148	$2.0 < \lvert y_{Z/\gamma^*} \rvert < 2.4$	$0.7 < \cos\theta^*_{CS} < 1.0$	$116 < M_{ee} < 150$ GeV
149	$2.4 < \lvert y_{Z/\gamma^*} \rvert < 2.8$	$0.7 < \cos\theta^*_{CS} < 1.0$	$116 < M_{ee} < 150$ GeV
150	$2.8 < \lvert y_{Z/\gamma^*} \rvert < 3.6$	$0.7 < \cos\theta^*_{CS} < 1.0$	$116 < M_{ee} < 150$ GeV

APPENDIX C

Background estimation

The estimation of the multi-jets background follows the data-driven template method described in chapter 10. The triple-differential binning is challenging for the background estimation with data-driven techniques due to the limited statistics. However the number of events can be increased by a factor of two in each bin by taking the absolute value of the $\cos\theta^*_{CS}$ distribution, following the fact that no asymmetry with respect to zero is expected for the background. The results of the multi-jets background estimation for the single-differential measurements as a function of $|\cos\theta^*_{CS}|$ and $|y_{Z/\gamma*}|$ and the estimation of the systematic uncertainties related to the choice of the normalization region are shown in figures C.1-C.4. The results for the triple-differential measurement are shown in figures C.5-C.10. Each set of figures corresponds to a certain dilepton invariant mass region, and within each set of figures the plots are structured to the show $\cos\theta^*_{CS}$ evolution horizontally, from left to right, and the rapidity evolution vertically, from top to bottom. An empty space in place of some bins indicates the exclusion of those bins from the measurement due to low statistics, as discussed in chapter 9.

The triple-differential measurement uses estimation of the number of multi-jet events with both, isolation and $p_T^{\text{elec. fwd}}$, discriminating variables, and the estimate is taken as an average from the two methods. The uncertainty on the multi-jets background estimation in the triple-differential case is calculated following the procedure applied to the single-differential distributions as described in section 10.2, except for the estimation of the systematic uncertainty related to the choice of the normalization region. The bins with low statistics do not allow to perform a scan as described in the chapter 10 without double-counting the statistical uncertainties. Due to that the uncertainty is estimate from the choice of the discriminating variable. More precisely the uncertainty is estimated by the difference of the background estimates derived from the isolation and $p_T^{\text{elec. fwd}}$ distributions.

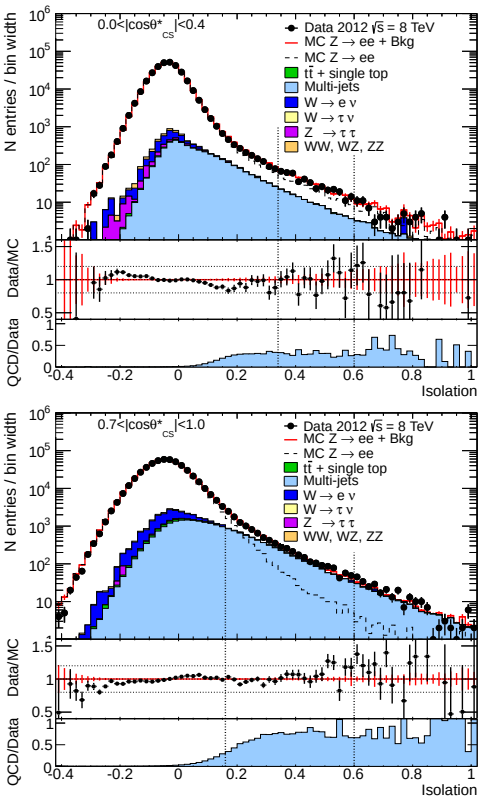

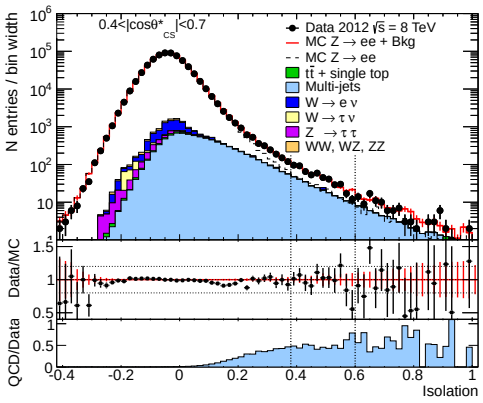

Figure C.1: The multi-jets background estimation in different $|\cos\theta^*_{CS}|$ regions integrated over M_{ee} and $|y_{Z/\gamma^*}|$.

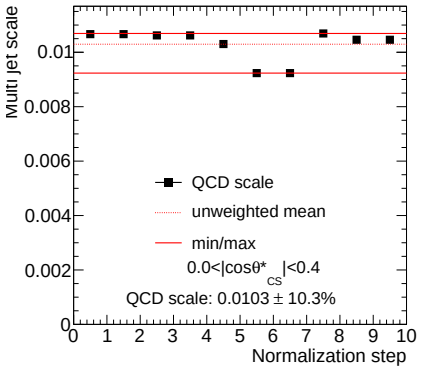

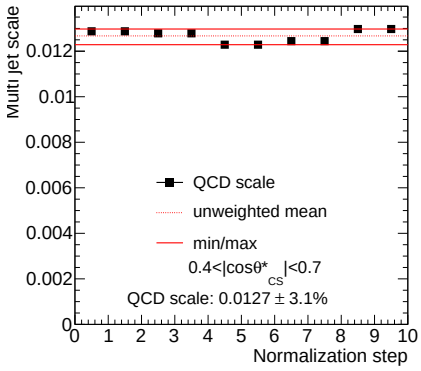

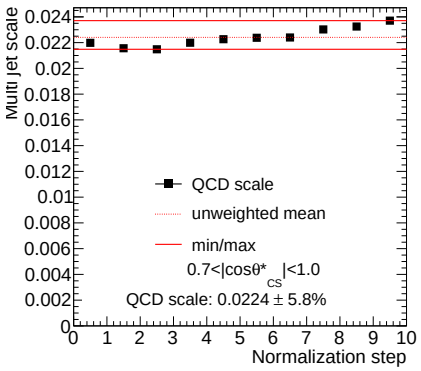

Figure C.2: Scan of normalization regions for the multi-jets background estimation. The scan is performed in bins of $|\cos\theta^*_{CS}|$ integrated over rapidity and dielectron invariant mass regions.

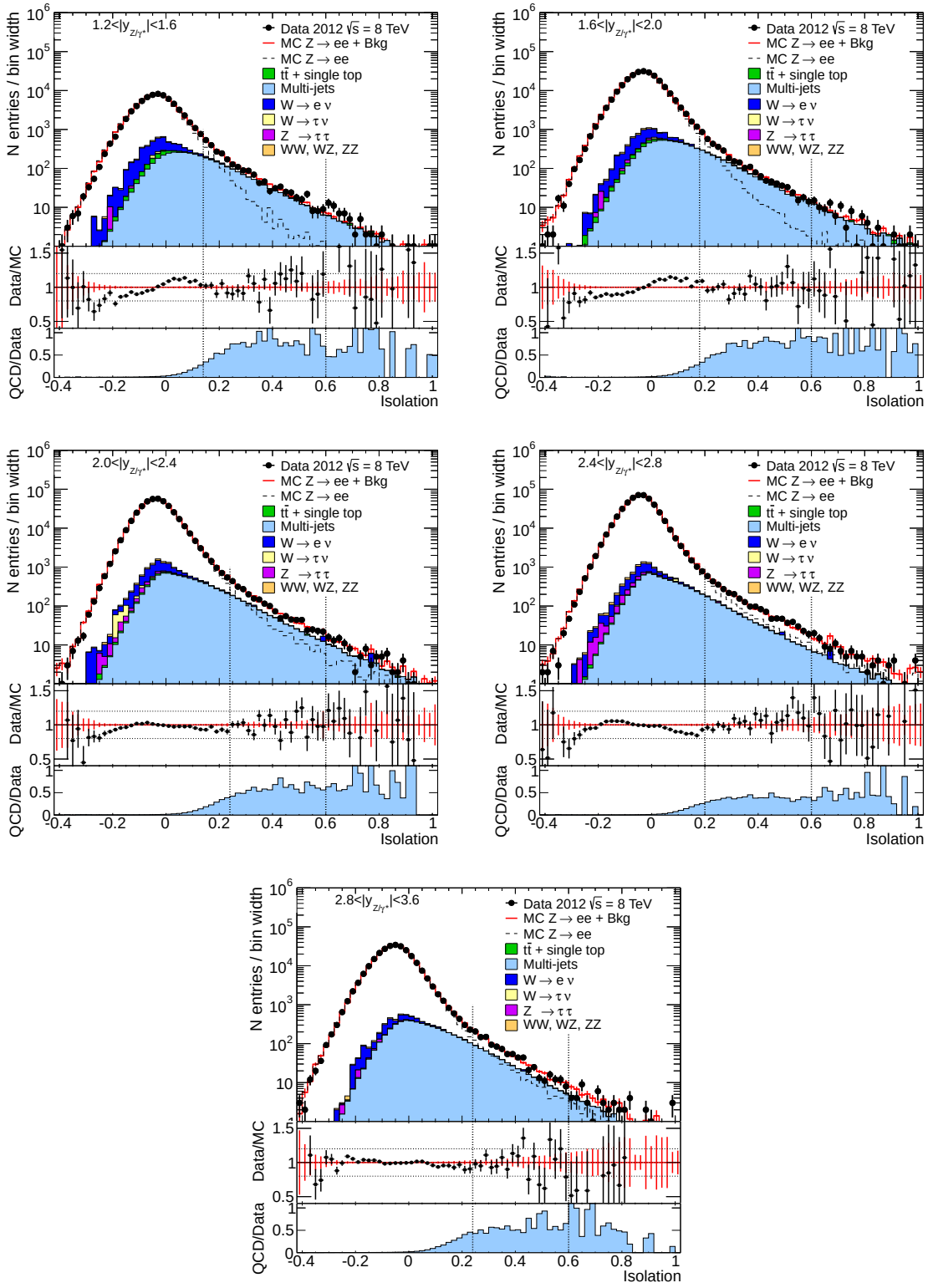

Figure C.3: The background is estimated in different rapidity regions integrated over M_{ee} and $\cos\theta^*_{CS}$.

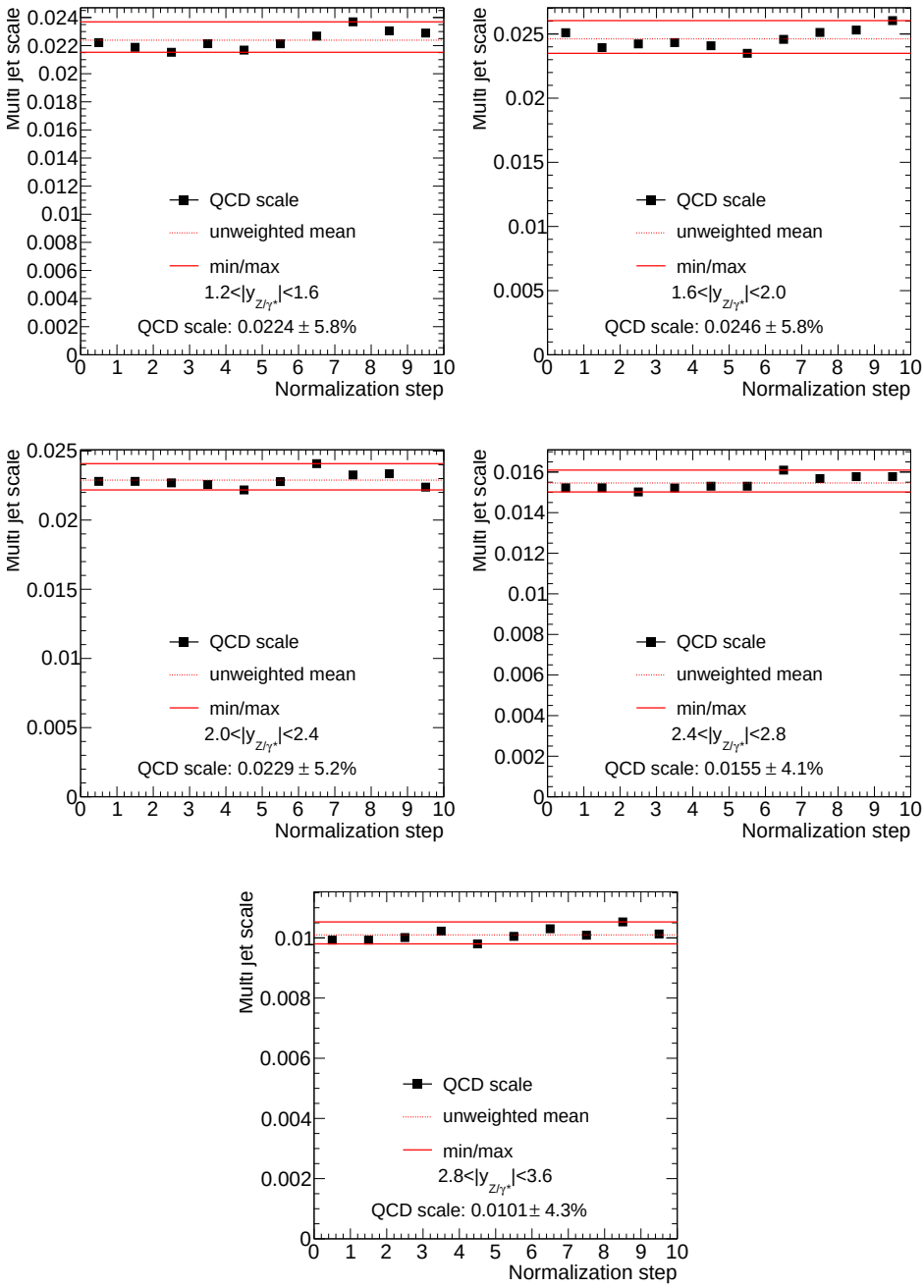

Figure C.4: The correlated systematic uncertainty of the multi-jet background estimation is defined with respect to the rapidity regions integrated over mass and $\cos\theta^*_{CS}$.

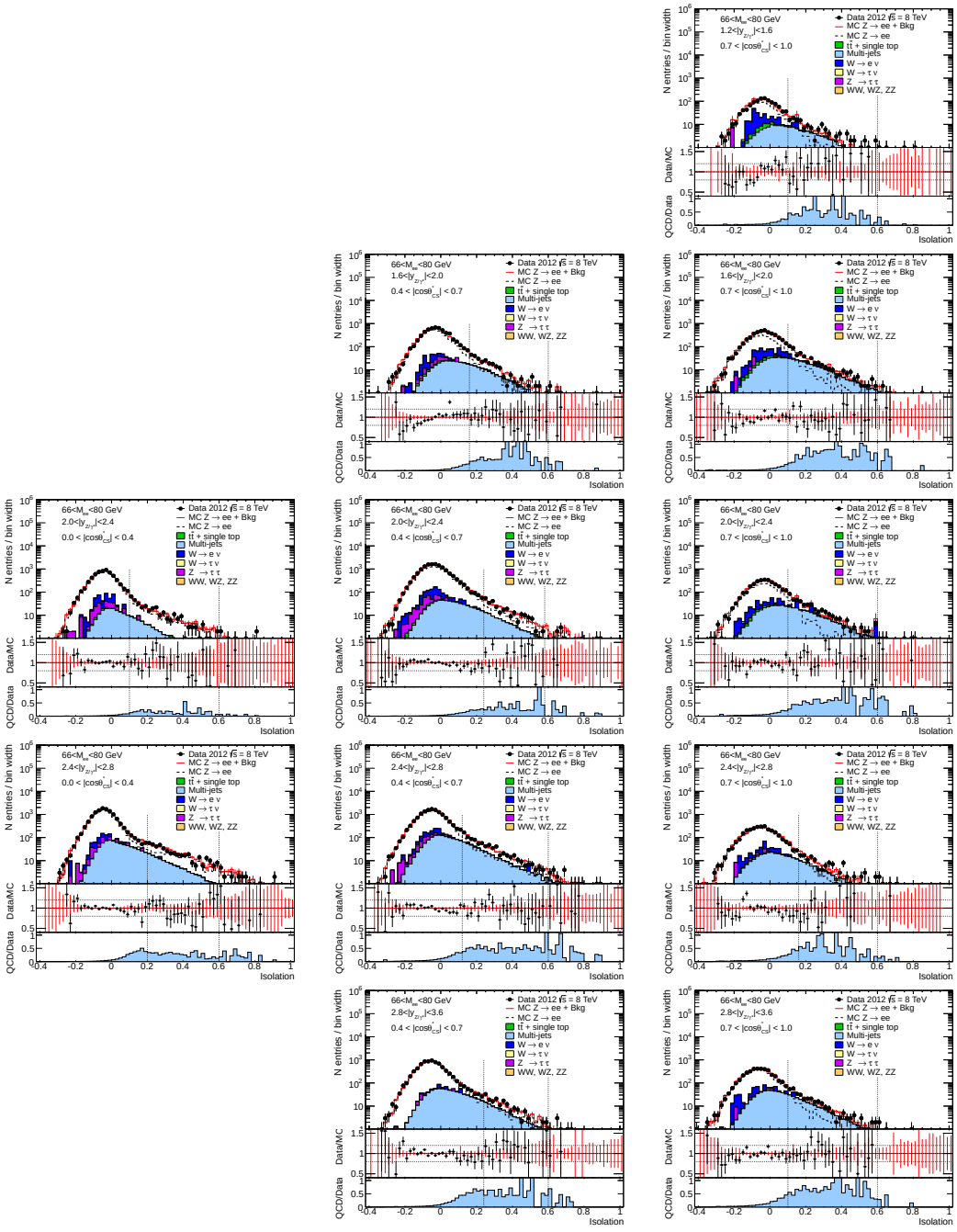

Figure C.5: The background is estimated for the dilepton invariant mass region $66 < M_{ee} < 80$ GeV. The plots are placed to increase rapidity bins from top to bottom, and to increase $|\cos\theta^*_{CS}|$ bins from left to right. The absence of the plots denotes the bins excluded from the measurement due to low statistics and kinematic constrains.

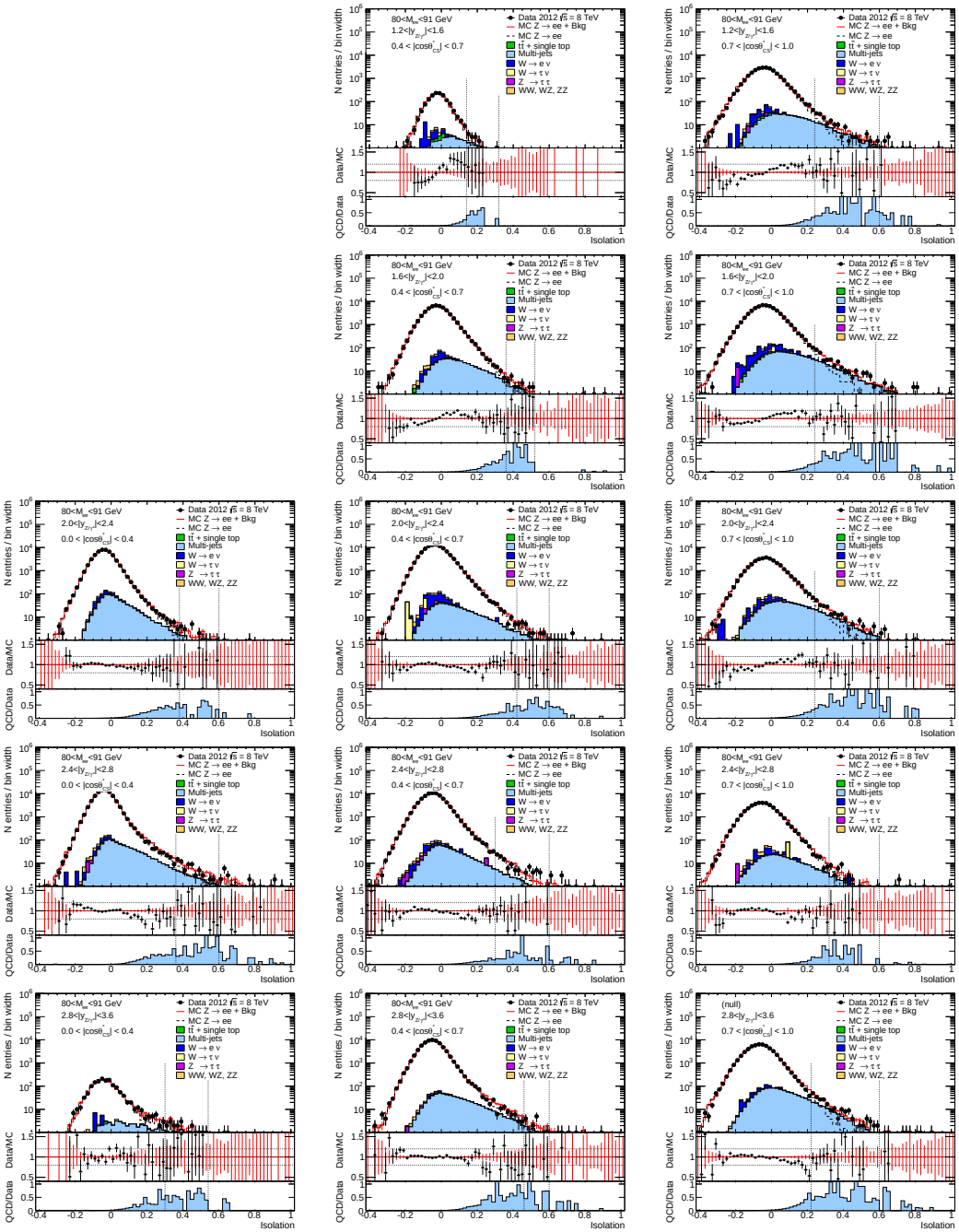

Figure C.6: The background is estimated for the dilepton invariant mass region $80 < M_{ee} < 91$ GeV. The plots are placed to increase rapidity bins from top to bottom, and to increase $|\cos\theta^*_{CS}|$ bins from left to right. The absence of the plots denotes the bins excluded from the measurement due to low statistics and kinematic constrains.

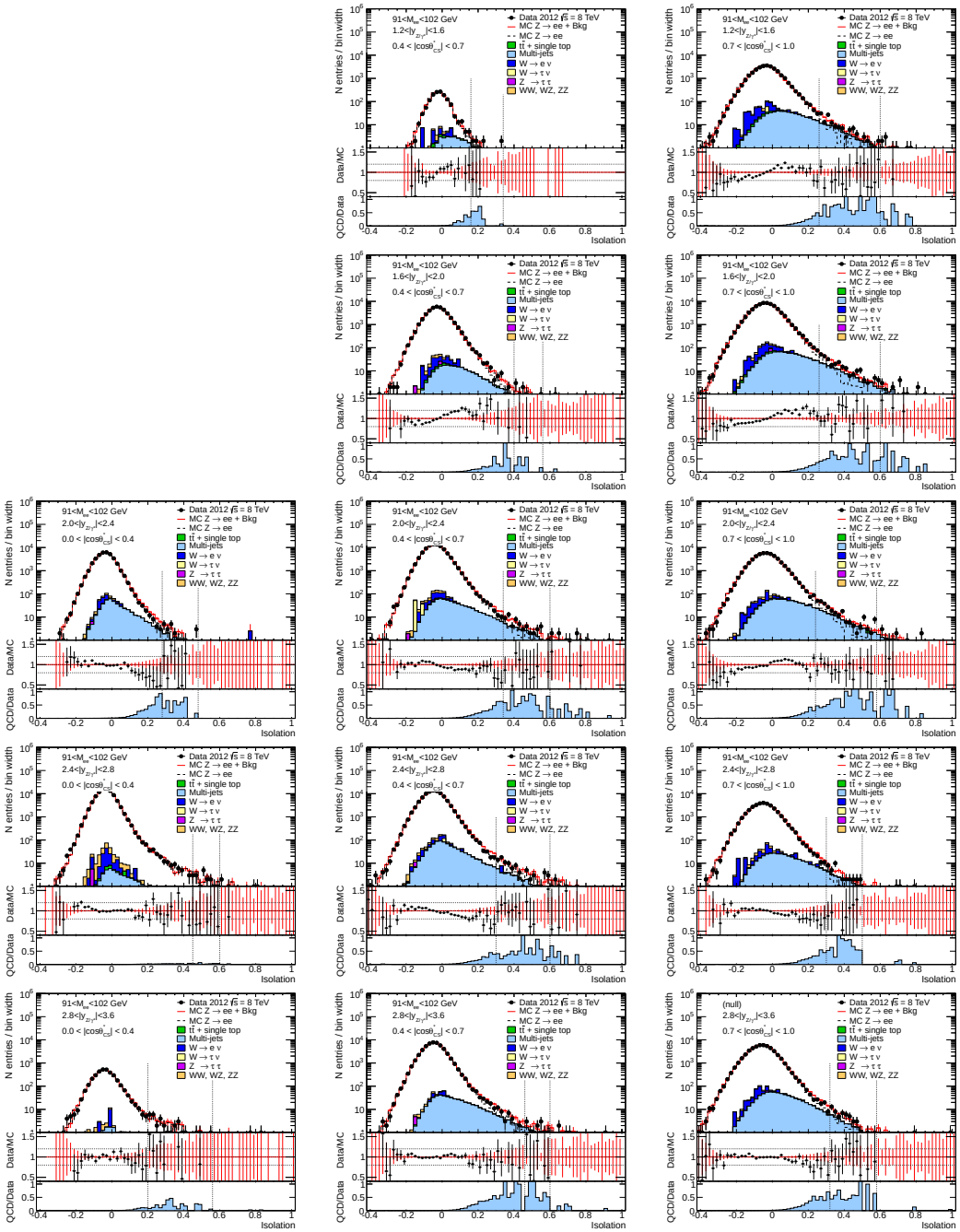

Figure C.7: The background is estimated for the dilepton invariant mass region $91 < M_{ee} < 102$ GeV. The plots are placed to increase rapidity bins from top to bottom, and to increase $|\cos\theta^*_{CS}|$ bins from left to right. The absence of the plots denotes the bins excluded from the measurement due to low statistics and kinematic constrains.

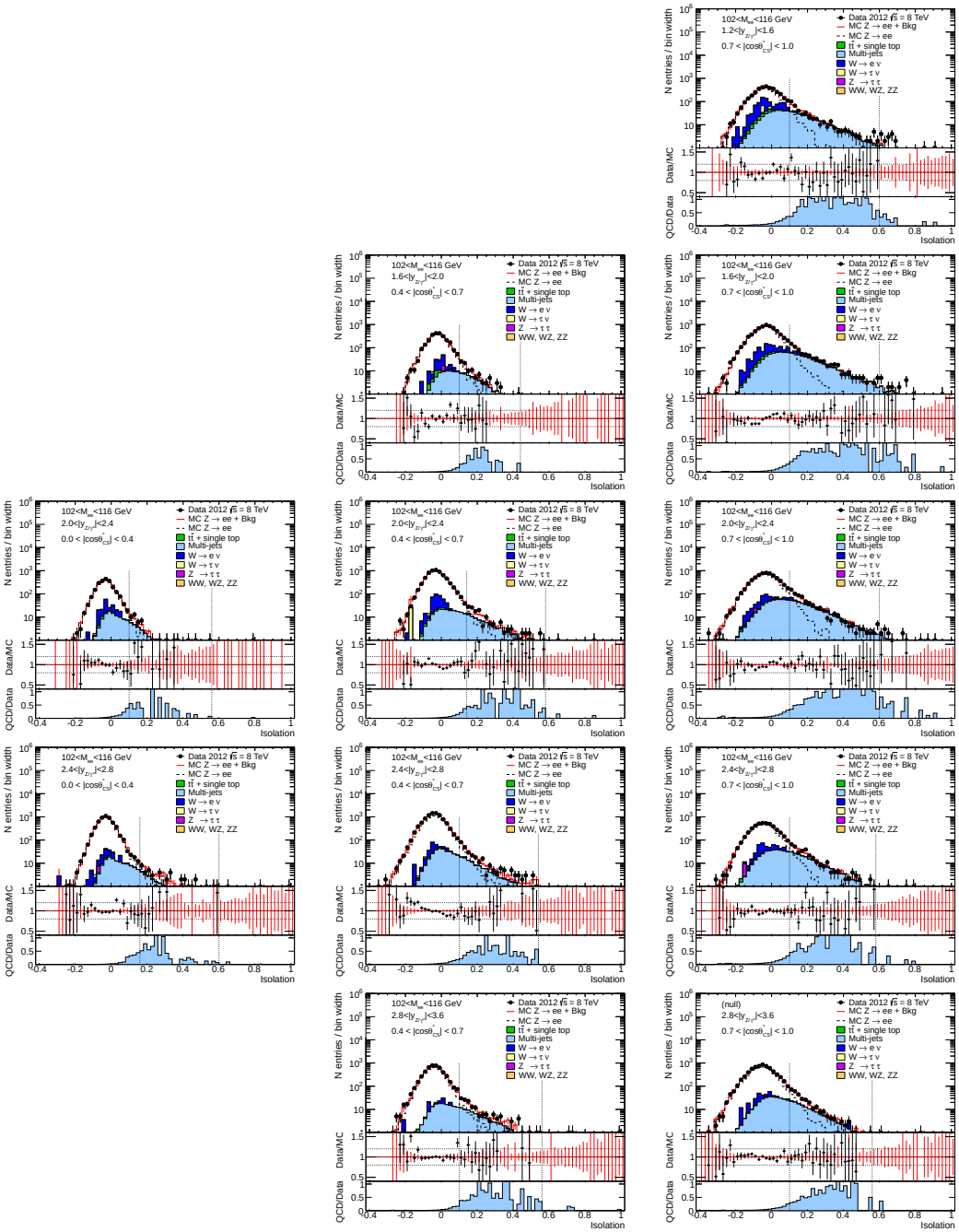

Figure C.8: The background is estimated for the dilepton invariant mass region $102 < M_{ee} < 116$ GeV. The plots are placed to increase rapidity bins from top to bottom, and to increase $|\cos\theta^*_{CS}|$ bins from left to right. The absence of the plots denotes the bins excluded from the measurement due to low statistics and kinematic constrains.

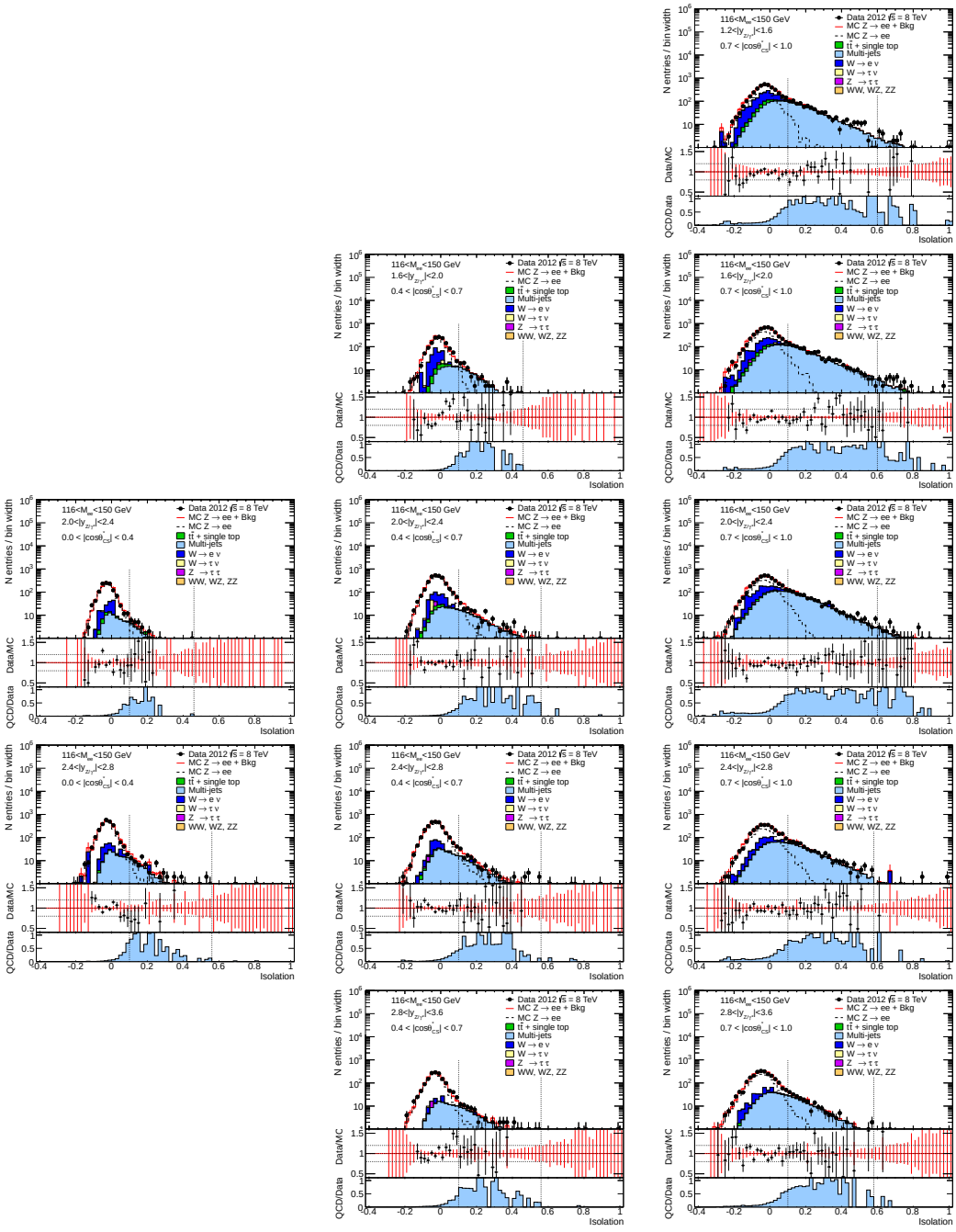

Figure C.9: The background is estimated for the dilepton invariant mass region $116 < M_{ee} < 150$ GeV. The plots are placed to increase rapidity bins from top to bottom, and to increase $|\cos\theta^*_{CS}|$ bins from left to right. The absence of the plots denotes the bins excluded from the measurement due to low statistics and kinematic constrains.

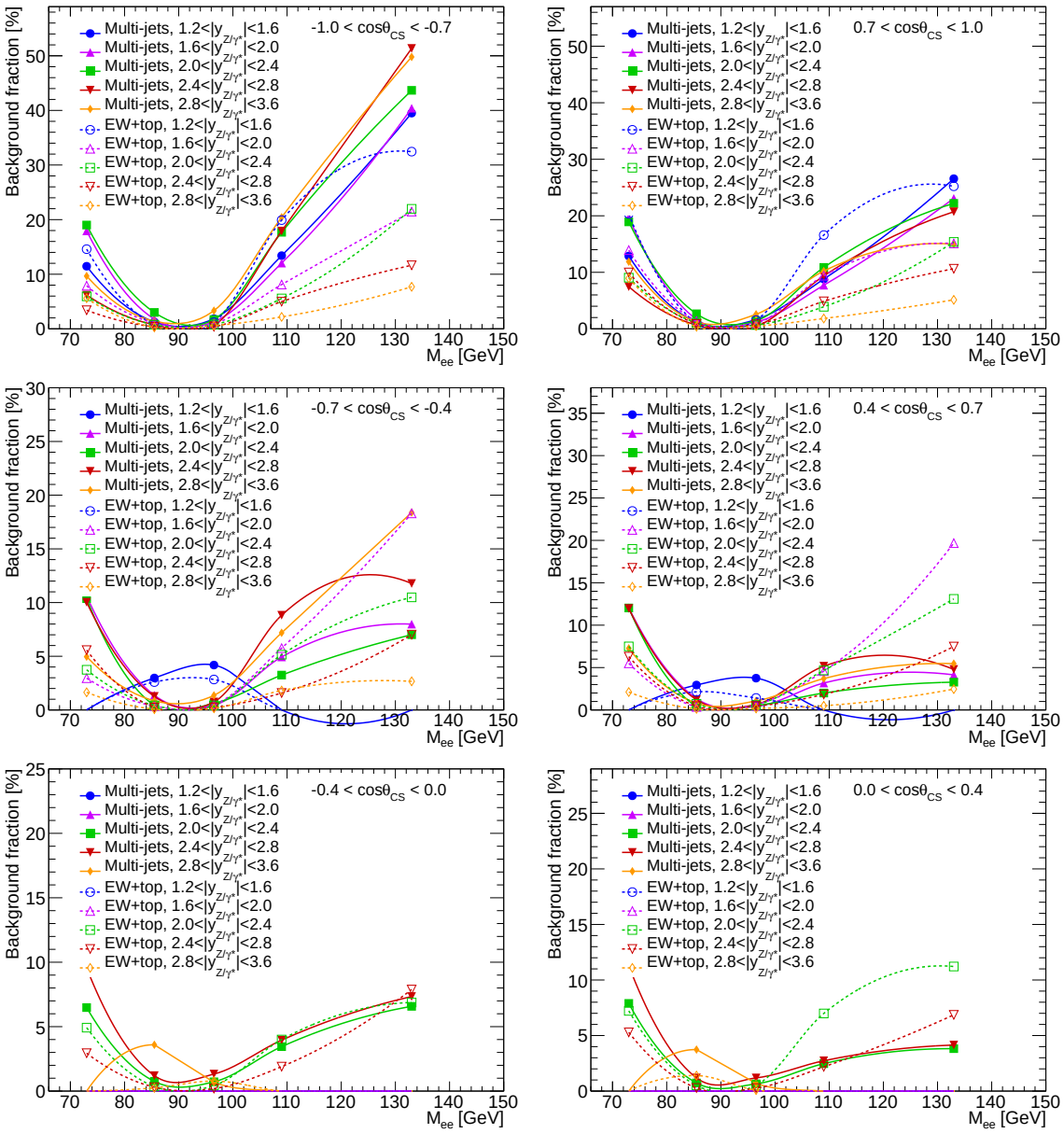

Figure C.10: Fraction of multi-jets and electroweak, including top, background to the selected data sample as a function of M_{ee}, $|y_{Z/\gamma^*}|$ and $\cos\theta^*_{CS}$.

APPENDIX D

Unfolding

The unfolding of the triple-differential distributions is affected by both large bin-to-bin event migrations and big statistical uncertainty. The figures D.1, D.2, D.3 compare the unfolded distributions using Bayesian unfolding with a number of iterations between 1 and 6 to the distribution obtained by bin-by-bin unfolding and the corresponding statistical uncertainties. The description of the unfolding methods and the theoretical and experimental input used for the studies are discussed in chapter 12.

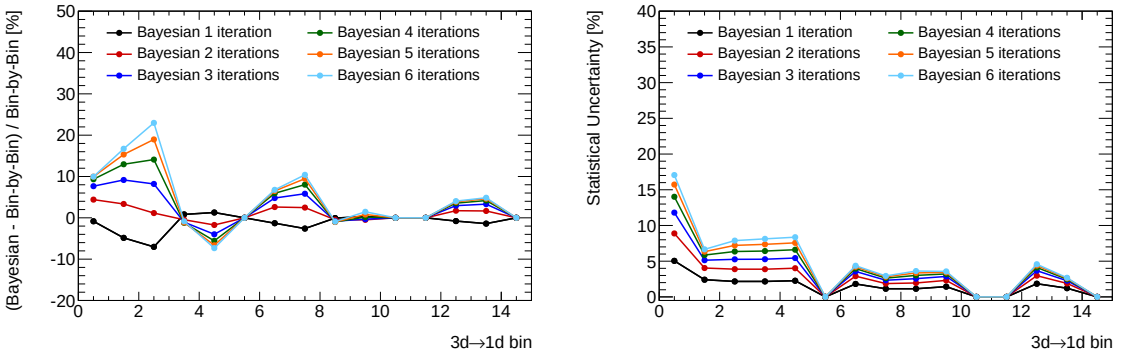

(a) $66 < M_{ee} < 80$ GeV, $\cos\theta^*_{CS} < 0$.

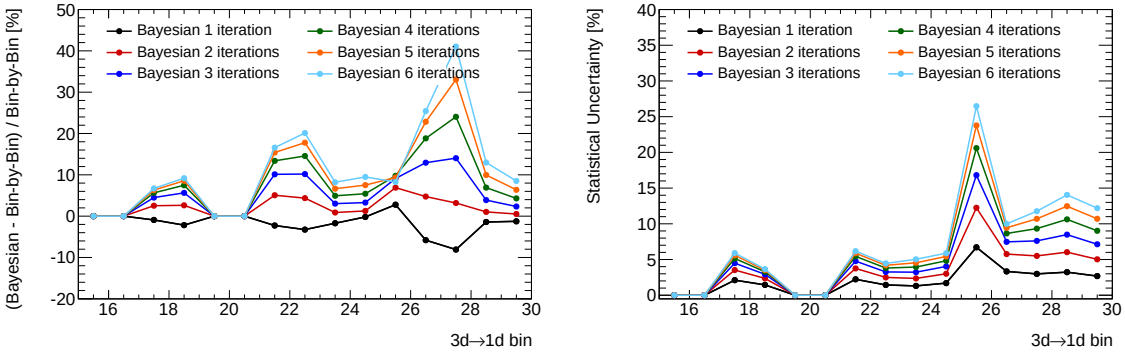

(b) $66 < M_{ee} < 80$ GeV, $\cos\theta^*_{CS} > 0$.

Figure D.1: Deviation of unfolded result using Bayesian unfolding with different number of iterations from bin-by-bin unfolding (left) and the variation of statistical uncertainty (right).

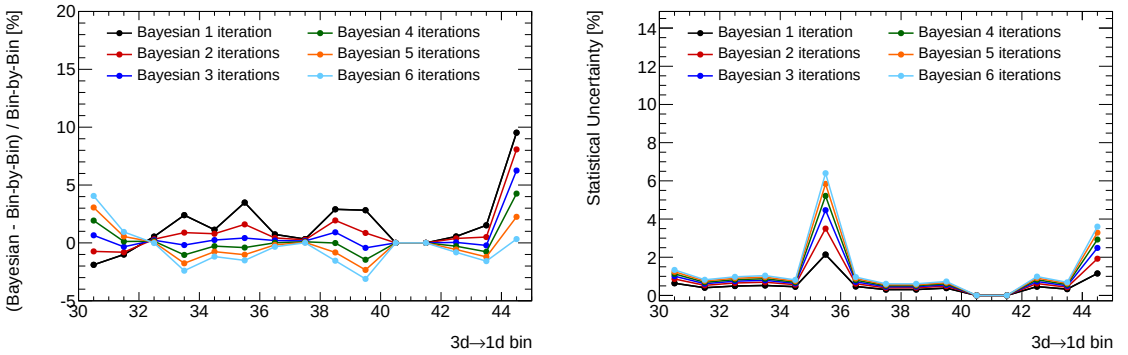

(a) $80 < M_{ee} < 91$ GeV, $\cos\theta^*_{CS} < 0$.

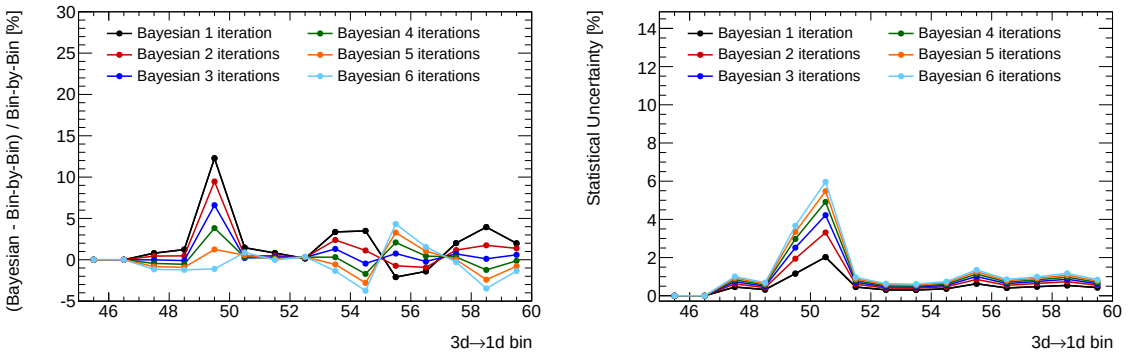

(b) $80 < M_{ee} < 91$ GeV, $\cos\theta^*_{CS} > 0$.

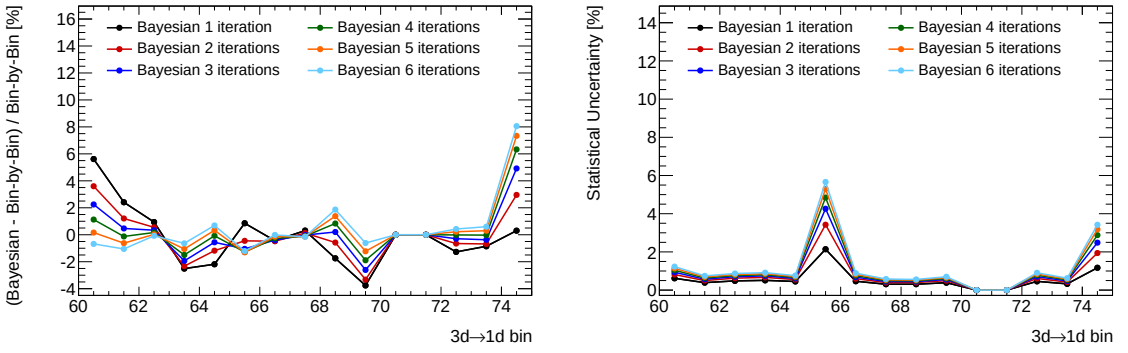

(c) $91 < M_{ee} < 102$ GeV, $\cos\theta^*_{CS} < 0$.

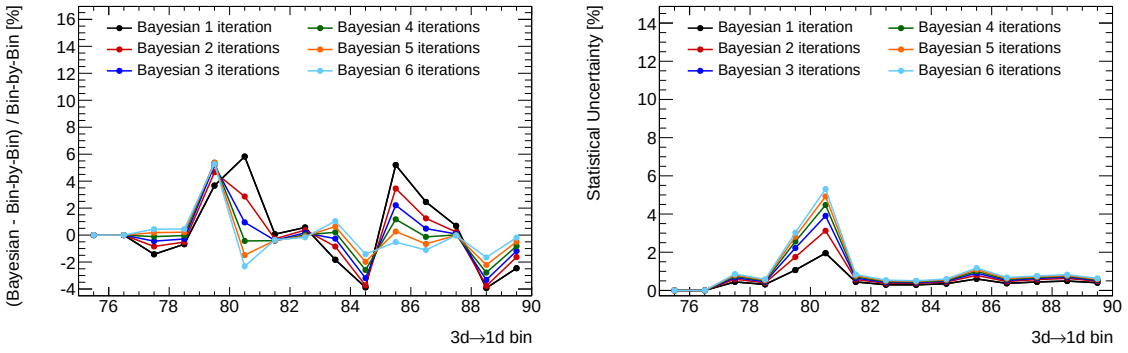

(d) $91 < M_{ee} < 102$ GeV, $\cos\theta^*_{CS} > 0$.

Figure D.2: Deviation of unfolded result using Bayesian unfolding with different number of iterations from bin-by-bin unfolding (left) and the variation of statistical uncertainty (right).

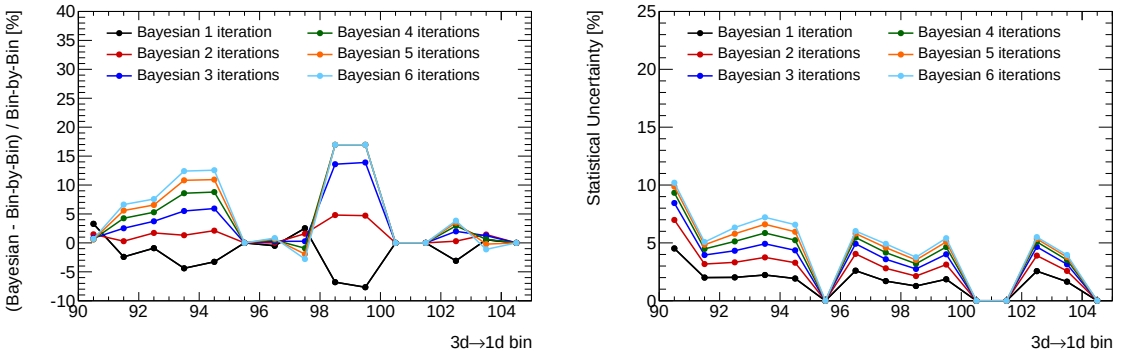

(a) $102 < M_{ee} < 116$ GeV, $\cos\theta^*_{CS} < 0$.

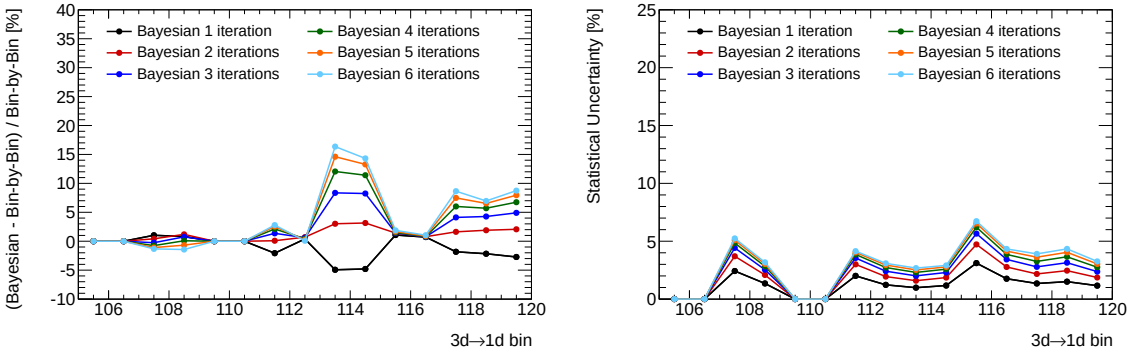

(b) $102 < M_{ee} < 116$ GeV, $\cos\theta^*_{CS} > 0$.

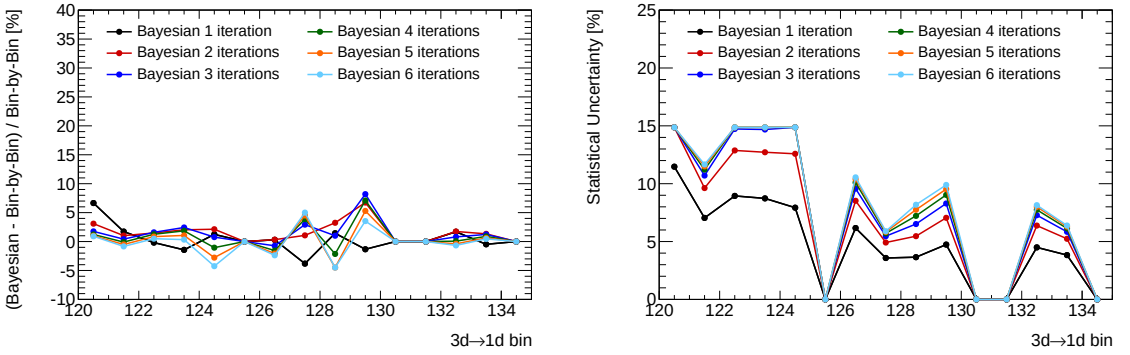

(c) $116 < M_{ee} < 150$ GeV, $\cos\theta^*_{CS} < 0$.

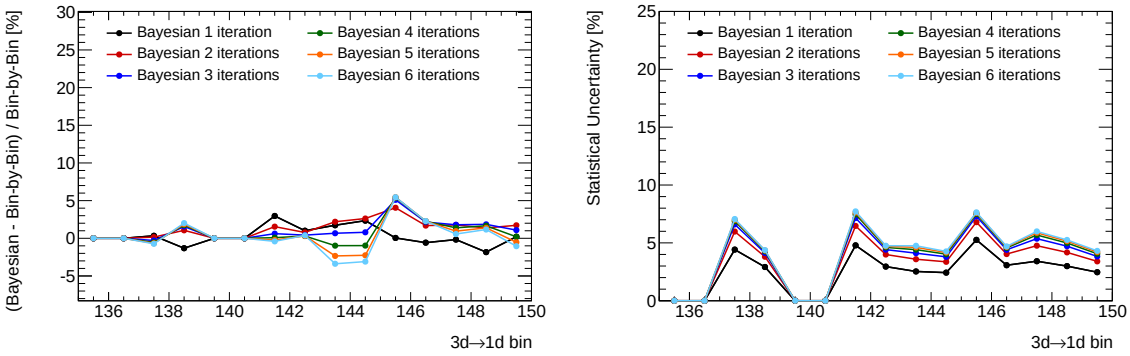

(d) $116 < M_{ee} < 150$ GeV, $\cos\theta^*_{CS} > 0$.

Figure D.3: Deviation of unfolded result using Bayesian unfolding with different number of iterations from bin-by-bin unfolding (left) and the variation of statistical uncertainty (right).

APPENDIX E

Theoretical uncertainties for the triple-differential cross-section measurement

The uncertainties on the theoretical predictions for the triple-differential[1] cross-section measurement are summarized in tables E.1, E.2, E.3. The statistical uncertainty is typically less than 0.5%. The scale and PDF uncertainties are calculated using MSTW2008nlo PDF at 68% confidence level, following the procedures described in section 14.2. As expected the bins which demonstrate an unstable behaviour in the scale scan performed in section 14.1 test have a larger theoretical uncertainty.

[1] Bins are excluded from the analysis as explained in chapter 9.

$3d \to 1d$	Uncertainty [%]					$3d \to 1d$	Uncertainty [%]				
bin	Stat.	Scale_{Up}	$\text{Scale}_{\text{Down}}$	PDF_{Up}	PDF_{Down}	bin	Stat.	Scale_{Up}	$\text{Scale}_{\text{Down}}$	PDF_{Up}	PDF_{Down}
	$66 < M_{ee} < 80$ GeV						$80 < M_{ee} < 91$ GeV				
1	0.549	9.16	7.94	1.81	1.36	31	0.43	3.260	4.540	2.028	1.507
2	0.300	3.28	4.83	2.28	1.68	32	0.20	2.958	3.295	2.312	1.694
3	0.296	3.24	4.71	2.41	1.83	33	0.16	2.578	3.363	2.391	1.825
4	0.717	3.20	4.57	2.60	2.03	34	0.19	2.620	3.415	2.523	1.968
5	0.437	3.33	4.47	2.74	2.23	35	0.17	2.927	3.523	2.626	2.134
6	-	-	-	-	-	36	0.06	12.01	9.641	1.229	0.934
7	0.218	3.28	4.04	2.46	1.86	37	0.35	2.625	3.814	2.236	1.652
8	0.079	3.27	4.02	2.56	2.01	38	0.07	2.611	3.721	2.355	1.798
9	0.079	3.20	4.07	2.70	2.19	39	0.06	2.733	3.723	2.480	1.931
10	0.203	3.79	4.01	2.82	2.34	40	0.25	2.854	3.673	2.591	2.066
11[1]	-	-	-	-	-	41[1]	-	-	-	-	-
12[1]	-	-	-	-	-	42[1]	-	-	-	-	-
13	0.154	3.02	4.57	2.45	1.94	43	0.14	2.700	3.811	2.344	1.791
14	0.088	3.03	4.49	2.55	2.07	44	0.09	2.732	3.752	2.455	1.901
15[1]	-	-	-	-	-	45	1.27	3.051	3.773	2.454	1.903
16[1]	-	-	-	-	-	46[1]	-	-	-	-	-
17[1]	-	-	-	-	-	47[1]	-	-	-	-	-
18	0.133	3.16	4.67	2.17	1.80	48	0.13	2.689	3.795	2.407	1.83
19	0.082	3.14	4.56	2.25	1.93	49	0.08	2.726	3.742	2.511	1.941
20[1]	-	-	-	-	-	50	0.71	3.027	3.729	2.523	1.960
21[1]	-	-	-	-	-	51	0.06	12.00	9.639	1.294	0.969
22	0.245	3.23	4.26	2.22	1.77	52	0.18	2.623	3.806	2.317	1.693
23	0.077	3.20	4.19	2.23	1.86	53	0.08	2.596	3.700	2.453	1.854
24	0.075	2.99	4.25	2.21	1.97	54	0.07	2.732	3.713	2.580	2.002
25	0.122	3.59	4.15	2.30	2.03	55	0.12	2.835	3.640	2.674	2.138
26	0.680	9.20	7.99	1.56	1.31	56	0.49	3.232	4.506	2.093	1.532
27	0.312	3.24	4.77	2.01	1.58	57	0.16	2.945	3.272	2.399	1.737
28	0.308	3.14	4.55	1.97	1.63	58	0.25	2.580	3.339	2.511	1.893
29	0.368	3.13	4.42	2.03	1.76	59	0.17	2.624	3.404	2.649	2.055
30	0.450	3.27	4.32	2.22	1.89	60	0.19	2.911	3.504	2.717	2.212

Table E.1: Uncertainties associated with the theoretical predictions of the Drell-Yan production cross-section in dilepton invariant mass regions $66 < M_{ee} < 80$ and $80 < M_{ee} < 91$ GeV. The calculations are performed with MCFM and APPLGRID at NLO and are convolved with MSTW2008nlo PDF.

$3d \to 1d$	Uncertainty [%]					$3d \to 1d$	Uncertainty [%]				
bin	Stat.	Scale_{Up}	$\text{Scale}_{\text{Down}}$	PDF_{Up}	PDF_{Down}	bin	Stat.	Scale_{Up}	$\text{Scale}_{\text{Down}}$	PDF_{Up}	PDF_{Down}
	$91 < M_{ee} < 102$ GeV						$102 < M_{ee} < 116$ GeV				
61	0.236	2.856	4.035	2.032	1.524	91	0.223	2.357	2.993	1.979	1.557
62	0.122	2.852	3.228	2.247	1.654	92	0.099	2.372	2.942	2.015	1.534
63	0.150	2.494	3.270	2.308	1.769	93	0.103	2.276	2.942	2.049	1.583
64	0.136	2.495	3.327	2.425	1.889	94	0.129	2.409	2.954	2.183	1.650
65	0.104	2.823	3.410	2.532	2.045	95	0.091	2.628	2.969	2.366	1.777
66	0.056	11.92	9.583	1.136	0.867	96[1]	-	-	-	-	-
67	0.135	2.591	3.689	2.163	1.601	97	0.143	2.358	3.175	1.937	1.458
68	0.064	2.574	3.590	2.277	1.740	98	0.075	2.362	3.097	2.043	1.554
69	0.058	2.676	3.572	2.391	1.854	99	0.060	2.412	3.043	2.147	1.625
70	0.110	2.776	3.506	2.503	1.979	100	0.100	2.505	2.973	2.290	1.733
71[1]	-	-	-	-	-	101[1]	-	-	-	-	-
72[1]	-	-	-	-	-	102[1]	-	-	-	-	-
73	0.124	2.605	3.628	2.304	1.750	103	0.140	2.284	3.044	2.174	1.606
74	0.070	2.654	3.587	2.414	1.853	104	0.085	2.363	3.042	2.300	1.712
75	0.523	3.107	3.557	2.382	1.836	105[1]	-	-	-	-	-
76[1]	-	-	-	-	-	106[1]	-	-	-	-	-
77[1]	-	-	-	-	-	107[1]	-	-	-	-	-
78	0.104	2.586	3.615	2.475	1.846	108	0.705	2.275	3.054	2.638	1.869
79	0.077	2.642	3.580	2.572	1.948	109	0.361	2.368	3.067	2.721	1.954
80	0.564	3.079	3.485	2.597	1.971	110[1]	-	-	-	-	-
81	0.052	11.91	9.582	1.328	0.969	111[1]	-	-	-	-	-
82	0.116	2.541	3.647	2.369	1.711	112	0.118	2.283	3.145	2.522	1.765
83	0.074	2.536	3.567	2.529	1.873	113	0.066	2.296	3.088	2.717	1.910
84	0.062	2.652	3.562	2.668	2.021	114	0.053	2.391	3.070	2.860	2.045
85	0.097	2.754	3.491	2.768	2.158	115	0.090	2.467	2.975	2.950	2.168
86	0.228	2.806	3.986	2.184	1.581	116	0.311	2.315	2.897	2.368	1.719
87	0.106	2.816	3.193	2.445	1.755	117	0.085	2.337	2.875	2.578	1.808
88	0.118	2.487	3.246	2.595	1.919	118	0.108	2.159	2.912	2.793	1.963
89	0.300	2.540	3.302	2.744	2.079	119	0.138	2.340	2.970	2.942	2.104
90	0.128	2.802	3.394	2.805	2.236	120	0.119	2.608	2.990	2.969	2.241

Table E.2: Uncertainties associated with the theoretical predictions of the Drell-Yan production cross-section in dilepton invariant mass regions $91 < M_{ee} < 102$ and $102 < M_{ee} < 116$ GeV. The calculations are performed with MCFM and APPLGRID at NLO and are convolved with MSTW2008nlo PDF.

$3d \to 1d$	Uncertainty [%]				
bin	Stat.	Scale_{Up}	$\text{Scale}_{\text{Down}}$	PDF_{Up}	PDF_{Down}
	$116 < M_{ee} < 150$ GeV				
121	0.406	2.068	2.453	1.852	1.494
122	0.058	2.029	2.478	1.884	1.431
123	0.063	2.070	2.450	2.069	1.503
124	0.085	2.131	2.409	2.534	1.743
125	0.182	2.225	2.368	3.116	2.149
126[1]	-	-	-	-	-
127	0.114	1.981	2.509	1.808	1.338
128	0.059	2.027	2.484	1.956	1.420
129	0.055	2.008	2.377	2.147	1.529
130	0.105	2.118	2.359	2.418	1.710
131[1]	-	-	-	-	-
132[1]	-	-	-	-	-
133	0.090	2.165	2.383	2.107	1.492
134	0.069	1.992	2.409	2.273	1.618
135[1]	-	-	-	-	-
136[1]	-	-	-	-	-
137[1]	-	-	-	-	-
138	0.179	2.022	2.532	2.752	1.867
139	0.074	2.023	2.453	2.830	1.938
140[1]	-	-	-	-	-
141[1]	-	-	-	-	-
142	0.123	1.988	2.578	2.648	1.814
143	0.062	2.028	2.550	2.836	1.915
144	0.057	2.079	2.494	2.971	2.028
145	0.095	2.135	2.398	3.015	2.123
146	0.161	2.034	2.406	2.441	1.785
147	0.087	1.895	2.447	2.686	1.859
148	0.064	1.990	2.477	2.908	1.964
149	0.090	2.117	2.490	3.046	2.079
150	0.086	2.283	2.456	3.025	2.186

Table E.3: Uncertainties associated with the theoretical predictions of the Drell-Yan production cross-section in dilepton invariant mass region $116 < M_{ee} < 150$ GeV. The calculations are performed with MCFM and APPLGRID at NLO and are convolved with MSTW2008nlo PDF.

APPENDIX F

Results

Table F.1: Results on the triple-defferential cross-section measurements unfolded to the fiducial phase-space at Born level. The uncertainty due to limunosity is not added.

$3d \rightarrow 1d$ bin	$\frac{d\sigma}{d\lvert y_{Z/\gamma^*}\rvert dM_{ee} d\cos\theta^*_{CS}}$ [nb/GeV]	δ^{stat} [nb/GeV]	δ^{syst} [nb/GeV]	δ^{tot} [nb/GeV]
1	0.0099	0.0003	0.0007	0.0008
2	0.0383	0.0008	0.0047	0.0047
3	0.0431	0.0008	0.0056	0.0056
4	0.0378	0.0007	0.0047	0.0047
5	0.0225	0.0004	0.0032	0.0033
7	0.0685	0.0012	0.0055	0.0057
8	0.1966	0.0021	0.0183	0.0184
9	0.1892	0.0019	0.0120	0.0122
10	0.0618	0.0008	0.0057	0.0057
13	0.0514	0.0008	0.0031	0.0032
14	0.1095	0.0012	0.0072	0.0073
18	0.0353	0.0006	0.0024	0.0025
19	0.0729	0.0009	0.0056	0.0057
22	0.0437	0.0008	0.0043	0.0044
23	0.1092	0.0013	0.0124	0.0124
24	0.0892	0.0010	0.0077	0.0078
25	0.0229	0.0003	0.0033	0.0033
26	0.0064	0.0003	0.0006	0.0006
27	0.0244	0.0006	0.0037	0.0037
28	0.0227	0.0005	0.0034	0.0034
29	0.0165	0.0003	0.0027	0.0027
30	0.0079	0.0001	0.0015	0.0015
31	0.5048	0.0034	0.0178	0.0181
32	1.2542	0.0064	0.0338	0.0344

$3d \to 1d$ bin	$\frac{d\sigma}{d\lvert y_{Z/\gamma^*}\rvert dM_{ee} d\cos\theta^*_{CS}}$ [pb/GeV]	δ^{stat} [pb/GeV]	δ^{syst} [pb/GeV]	δ^{tot} [pb/GeV]
33	1.2570	0.0074	0.0393	0.0400
34	1.1314	0.0070	0.0532	0.0536
35	0.6907	0.0039	0.0736	0.0737
36	0.0309	0.0006	0.0016	0.0017
37	1.0251	0.0059	0.0313	0.0319
38	2.7119	0.0121	0.0653	0.0664
39	2.5540	0.0115	0.0938	0.0945
40	0.7670	0.0039	0.0373	0.0375
43	0.7122	0.0038	0.0214	0.0217
44	1.4055	0.0064	0.0431	0.0436
45	0.0385	0.0004	0.0036	0.0036
48	0.7048	0.0039	0.0219	0.0222
49	1.4058	0.0065	0.0415	0.0420
50	0.0371	0.0004	0.0043	0.0043
51	0.0311	0.0006	0.0014	0.0016
52	1.0217	0.0057	0.0326	0.0331
53	2.6993	0.0121	0.0689	0.0699
54	2.5204	0.0110	0.1040	0.1046
55	0.7549	0.0038	0.0406	0.0408
56	0.5144	0.0035	0.0189	0.0192
57	1.2698	0.0066	0.0383	0.0389
58	1.2568	0.0071	0.0442	0.0447
59	1.1231	0.0065	0.0620	0.0623
60	0.6867	0.0037	0.0746	0.0746
61	0.6467	0.0043	0.0380	0.0382
62	1.4974	0.0076	0.0513	0.0518
63	1.4794	0.0086	0.0417	0.0426
64	1.2987	0.0081	0.0616	0.0621
65	0.7532	0.0043	0.0829	0.0830
66	0.0378	0.0008	0.0014	0.0016
67	1.1103	0.0063	0.0259	0.0266
68	2.8620	0.0130	0.0674	0.0687
69	2.6777	0.0120	0.0805	0.0814
70	0.7712	0.0040	0.0409	0.0411
73	0.7828	0.0043	0.0213	0.0217
74	1.5306	0.0072	0.0452	0.0458
75	0.0408	0.0005	0.0014	0.0014

$3d \to 1d$ bin	$\frac{d\sigma}{d\lvert y_{Z/\gamma^*}\rvert dM_{ee} d\cos\theta^*_{CS}}$ [pb/GeV]	δ^{stat} [pb/GeV]	δ^{syst} [pb/GeV]	δ^{tot} [pb/GeV]
78	0.8756	0.0049	0.0224	0.0229
79	1.7382	0.0080	0.0473	0.0480
80	0.0489	0.0005	0.0023	0.0023
81	0.0403	0.0008	0.0026	0.0027
82	1.2767	0.0070	0.0267	0.0276
83	3.4250	0.0148	0.0742	0.0757
84	3.3368	0.0145	0.0994	0.1004
85	1.0195	0.0050	0.0539	0.0541
86	0.7442	0.0047	0.0402	0.0405
87	1.7622	0.0088	0.0591	0.0597
88	1.8218	0.0100	0.0515	0.0525
89	1.7022	0.0095	0.0933	0.0938
90	1.0547	0.0054	0.1160	0.1161
91	0.0282	0.0007	0.0028	0.0029
92	0.0529	0.0008	0.0054	0.0054
93	0.0463	0.0008	0.0071	0.0071
94	0.0357	0.0006	0.0056	0.0056
95	0.0162	0.0003	0.0038	0.0038
97	0.0295	0.0007	0.0015	0.0016
98	0.0701	0.0009	0.0056	0.0057
99	0.0669	0.0008	0.0121	0.0122
100	0.0167	0.0003	0.0030	0.0030
103	0.0225	0.0005	0.0012	0.0013
104	0.0426	0.0006	0.0038	0.0038
108	0.0320	0.0006	0.0013	0.0014
109	0.0653	0.0008	0.0048	0.0049
112	0.0533	0.0010	0.0021	0.0023
113	0.1387	0.0015	0.0077	0.0078
114	0.1530	0.0013	0.0189	0.0190
115	0.0480	0.0005	0.0058	0.0058
116	0.0501	0.0010	0.0028	0.0030
117	0.0984	0.0012	0.0062	0.0063
118	0.1075	0.0011	0.0105	0.0106
119	0.1026	0.0012	0.0098	0.0099
120	0.0616	0.0006	0.0096	0.0096
121	0.0063	0.0004	0.0008	0.0009
122	0.0100	0.0004	0.0010	0.0011

$3d \to 1d$ bin	$\frac{d\sigma}{d\lvert y_{Z/\gamma^*}\rvert dM_{ee} d\cos\theta^*_{CS}}$ [pb/GeV]	δ^{stat} [pb/GeV]	δ^{syst} [pb/GeV]	δ^{tot} [pb/GeV]
123	0.0084	0.0005	0.0009	0.0010
124	0.0057	0.0004	0.0012	0.0013
125	0.0017	0.0001	0.0006	0.0006
127	0.0052	0.0003	0.0004	0.0005
128	0.0123	0.0004	0.0010	0.0011
129	0.0089	0.0003	0.0008	0.0008
130	0.0020	0.0001	0.0002	0.0003
133	0.0038	0.0002	0.0002	0.0003
134	0.0076	0.0002	0.0004	0.0005
138	0.0069	0.0002	0.0003	0.0003
139	0.0147	0.0003	0.0006	0.0007
142	0.0110	0.0004	0.0006	0.0007
143	0.0308	0.0006	0.0012	0.0014
144	0.0311	0.0006	0.0015	0.0016
145	0.0091	0.0002	0.0006	0.0006
146	0.0168	0.0005	0.0008	0.0010
147	0.0299	0.0006	0.0012	0.0014
148	0.0307	0.0006	0.0013	0.0014
149	0.0290	0.0007	0.0023	0.0024
150	0.0138	0.0003	0.0019	0.0019

Table F.2: Relative uncertainties in percent on the triple-differential cross-section measurements unfolded to the fiducial phase-space at Born level.

Bin $3d \to 1d$	Total Unc.	Data stat.	ID syst.	ID Fwd syst.	Reco syst.	Trig syst.	Ener. scale	Fwd ener. scale	Ener. res.	Fwd ener. res.	Unfold. stat.	Unfold. method	EW+ top	Multi-jet stat.	Multi-jet syst.	Pile-up	PDF	Lineshape
1	8.16	3.43	0.65	1.11	0.16	0.26	2.88	3.02	1.54	2.34	2.42	0.84	0.64	2.04	3.62	1.00	0.72	1.43
2	12.35	1.99	0.73	0.74	0.20	0.28	1.32	3.39	0.87	2.71	1.36	5.10	0.35	1.50	9.75	0.25	0.66	0.57
3	13.03	1.85	0.85	0.92	0.19	0.20	2.07	2.66	1.26	3.89	1.48	7.54	0.24	1.43	8.11	0.28	0.75	3.02
4	12.52	1.81	1.22	2.29	0.13	0.29	2.80	3.91	1.17	10.49	1.59	0.83	0.12	1.06	2.14	1.10	0.60	1.24
5	14.46	1.67	1.13	9.82	0.14	0.26	2.22	4.14	1.04	7.92	1.39	1.27	0.21	0.88	3.95	1.13	0.54	1.02
7	8.25	1.69	0.51	0.96	0.12	0.11	0.81	3.10	0.81	2.22	1.03	1.32	0.10	1.37	6.56	0.25	0.50	0.40
8	9.38	1.08	0.72	0.74	0.09	0.15	1.07	2.82	0.58	2.75	0.68	2.67	0.14	1.50	7.63	0.27	0.55	0.45
9	6.44	1.00	0.62	0.83	0.07	0.16	1.01	2.69	0.53	5.18	0.67	0.05	0.18	0.84	1.25	0.68	0.60	0.62
10	9.25	1.28	0.82	2.70	0.09	0.28	1.20	2.84	1.06	7.33	0.86	0.29	0.07	0.68	2.94	0.64	0.48	0.93
13	6.27	1.53	0.36	1.07	0.04	0.12	0.84	3.12	0.51	1.02	0.98	0.79	0.17	1.70	4.28	0.54	0.35	0.84
14	6.69	1.13	0.43	0.74	0.05	0.20	0.93	2.28	0.64	1.69	0.66	1.42	0.10	1.21	5.29	0.21	0.33	1.12
18	7.00	1.75	0.35	1.08	0.04	0.13	0.78	2.48	0.45	0.99	1.12	0.92	0.27	2.13	5.39	0.58	0.49	0.61
19	7.77	1.29	0.40	0.74	0.05	0.20	1.02	2.16	0.42	1.59	0.84	2.22	0.20	1.48	6.42	0.42	0.35	0.39
22	10.05	1.94	0.47	0.96	0.11	0.11	1.10	3.84	0.62	2.47	1.20	2.32	0.24	1.63	7.85	0.40	0.78	1.28
23	11.37	1.17	0.69	0.74	0.08	0.15	1.41	2.77	0.49	3.53	0.86	3.36	0.29	1.84	9.38	0.28	0.92	0.36
24	8.70	1.08	0.58	0.83	0.07	0.15	1.43	3.09	0.74	7.23	0.93	1.74	0.23	1.02	1.54	0.54	1.06	0.46
25	14.44	1.48	0.75	2.69	0.09	0.25	1.93	4.33	1.31	12.26	1.33	0.19	0.09	0.98	4.29	1.23	1.10	0.12
26	10.08	4.06	0.66	1.08	0.17	0.25	2.45	3.98	1.24	2.42	2.95	2.70	1.00	2.55	5.19	0.90	1.02	1.35
27	15.26	2.30	0.71	0.75	0.19	0.27	1.93	2.18	1.07	4.67	1.72	6.17	0.68	1.83	12.09	0.06	0.74	1.84
28	15.07	2.08	0.84	0.95	0.19	0.20	2.24	3.16	1.54	6.04	2.01	8.78	0.43	1.56	9.02	0.87	1.12	0.22
29	16.30	2.08	1.22	2.14	0.13	0.31	3.55	4.07	0.99	14.30	2.29	1.43	0.40	1.33	2.78	1.53	1.09	0.26
30	19.48	1.89	1.10	9.82	0.13	0.26	3.60	4.00	1.43	14.44	2.26	1.27	0.39	1.12	4.91	2.01	1.27	0.95
31	3.59	0.67	0.53	0.91	0.12	0.12	0.38	1.52	0.33	0.12	0.38	1.93	0.04	0.24	0.55	0.11	0.11	2.12
32	2.74	0.51	0.56	0.73	0.15	0.24	0.25	1.28	0.24	0.30	0.24	1.01	0.05	0.21	0.41	0.08	0.12	1.77
33	3.18	0.59	0.70	0.80	0.17	0.16	0.28	0.48	0.23	1.10	0.33	0.54	0.04	0.36	1.05	0.11	0.18	2.31
34	4.74	0.62	0.97	2.75	0.11	0.20	0.45	0.87	0.43	1.65	0.34	2.34	0.02	0.33	0.56	0.33	0.15	1.87
35	10.67	0.56	0.96	10.19	0.11	0.22	0.31	0.50	0.37	1.68	0.30	1.13	0.03	0.43	0.81	0.21	0.15	1.75
36	5.65	1.93	0.13	1.32	0.03	0.05	1.08	1.93	0.58	0.18	1.48	3.37	0.09	1.37	1.38	0.57	0.23	1.86
37	3.11	0.57	0.26	0.93	0.05	0.07	0.22	1.93	0.13	0.08	0.27	0.73	0.02	0.49	1.00	0.35	0.09	1.63
38	2.45	0.45	0.42	0.74	0.05	0.10	0.33	1.19	0.07	0.16	0.18	0.33	0.02	0.25	0.51	0.15	0.09	1.73

Bin $3d \to 1d$	Total Unc.	Data stat.	ID syst.	ID Fwd syst.	Reco syst.	Trig syst.	Ener. scale	Fwd ener. scale	Ener. res.	Fwd ener. res.	Unfold. stat.	Unfold. method	EW+ top	Multi-jet stat.	Multi-jet syst.	Pile-up	PDF	Lineshape
39	3.70	0.45	0.40	0.79	0.04	0.13	0.26	0.79	0.12	0.52	0.22	2.82	0.02	0.37	0.43	0.22	0.11	1.82
40	4.89	0.51	0.48	2.77	0.07	0.20	0.35	0.80	0.19	2.08	0.25	2.74	0.01	0.40	0.44	0.27	0.12	1.61
43	3.05	0.54	0.23	1.04	0.03	0.10	0.29	1.91	0.14	0.11	0.26	0.55	0.02	0.39	0.55	0.33	0.07	1.78
44	3.10	0.45	0.25	0.74	0.03	0.15	0.39	1.40	0.13	0.46	0.20	1.50	0.01	0.61	0.84	0.14	0.05	1.74
45	9.35	1.12	0.40	1.18	0.06	0.28	1.68	0.42	0.57	0.78	0.98	8.72	0.02	0.87	1.01	-0.06	0.29	1.35
48	3.15	0.56	0.22	1.04	0.03	0.10	0.30	2.05	0.10	0.05	0.27	0.79	0.03	0.39	0.54	0.34	0.14	1.70
49	2.99	0.46	0.25	0.74	0.03	0.15	0.52	1.55	0.12	0.24	0.20	1.21	0.02	0.59	0.83	0.23	0.05	1.66
50	11.63	1.13	0.39	1.21	0.06	0.28	1.69	0.90	0.36	1.22	0.97	10.95	0.03	0.87	1.01	0.14	0.28	2.06
51	5.05	1.98	0.13	1.34	0.03	0.05	0.74	2.22	0.47	0.22	1.43	1.44	0.07	1.32	1.34	0.57	0.38	2.43
52	3.24	0.56	0.25	0.93	0.05	0.07	0.19	1.98	0.08	0.02	0.28	0.81	0.03	0.49	1.03	0.31	0.13	1.78
53	2.59	0.45	0.41	0.74	0.05	0.10	0.42	1.35	0.09	0.07	0.19	0.16	0.03	0.25	0.54	0.18	0.13	1.82
54	4.15	0.43	0.39	0.78	0.04	0.13	0.28	0.94	0.11	0.39	0.21	3.26	0.03	0.36	0.43	0.22	0.12	2.02
55	5.40	0.50	0.47	2.80	0.06	0.20	0.49	1.08	0.24	1.94	0.26	3.37	0.01	0.37	0.42	0.26	0.09	1.95
56	3.74	0.67	0.53	0.91	0.13	0.12	0.30	1.83	0.25	0.13	0.38	2.14	0.06	0.22	0.49	0.28	0.25	1.93
57	3.06	0.52	0.55	0.73	0.15	0.24	0.18	1.47	0.14	0.11	0.25	1.43	0.06	0.20	0.42	0.15	0.14	1.90
58	3.56	0.56	0.70	0.78	0.16	0.16	0.40	0.70	0.30	1.15	0.31	1.98	0.05	0.32	0.94	0.16	0.17	2.03
59	5.55	0.58	0.96	2.78	0.11	0.20	0.50	1.00	0.44	1.45	0.34	3.80	0.04	0.30	0.52	0.27	0.19	1.78
60	10.87	0.53	0.95	10.23	0.11	0.22	0.51	0.75	0.35	1.57	0.28	1.95	0.04	0.37	0.68	0.27	0.12	2.06
61	5.91	0.66	0.50	0.86	0.12	0.10	0.36	1.36	0.21	0.82	0.33	5.32	0.06	0.29	0.45	-0.19	0.18	1.41
62	3.46	0.51	0.51	0.73	0.14	0.23	0.35	1.28	0.25	1.02	0.22	2.35	0.05	0.19	0.29	-0.15	0.10	1.51
63	2.88	0.58	0.65	0.85	0.16	0.15	0.39	1.30	0.33	1.09	0.28	0.93	0.05	0.32	0.75	-0.08	0.13	1.42
64	4.78	0.62	0.90	2.85	0.11	0.19	0.84	1.18	0.45	0.86	0.32	2.58	0.02	0.31	0.57	0.18	0.16	1.79
65	11.02	0.57	0.93	10.34	0.11	0.21	0.20	1.27	0.30	0.40	0.28	2.24	0.03	0.63	1.81	0.06	0.14	1.63
66	4.25	2.05	0.12	1.26	0.03	0.05	0.99	1.06	0.72	1.04	1.30	0.84	0.11	1.59	1.60	0.15	0.19	1.00
67	2.40	0.57	0.23	0.90	0.04	0.06	0.37	0.93	0.06	0.57	0.26	0.44	0.02	0.40	0.55	0.12	0.13	1.57
68	2.40	0.46	0.38	0.74	0.04	0.09	0.46	1.19	0.11	0.63	0.18	0.31	0.02	0.21	0.27	0.01	0.15	1.59
69	3.04	0.45	0.36	0.87	0.04	0.13	0.24	1.17	0.14	0.86	0.20	1.79	0.01	0.34	0.51	0.06	0.13	1.52
70	5.33	0.51	0.44	2.75	0.06	0.19	0.21	1.35	0.10	0.05	0.25	3.91	0.01	0.46	0.60	0.06	0.12	1.59
73	2.77	0.55	0.22	1.01	0.03	0.10	0.36	1.27	0.08	0.43	0.26	1.29	0.02	0.36	0.50	0.11	0.12	1.49
74	2.99	0.47	0.24	0.74	0.03	0.15	0.38	1.64	0.18	0.69	0.18	0.87	0.01	0.80	0.99	0.03	0.05	1.53
75	3.55	1.16	0.36	1.21	0.06	0.26	0.92	1.99	0.60	0.68	0.92	0.29	0.02	0.73	0.89	-0.02	0.29	1.28
78	2.62	0.56	0.22	1.01	0.03	0.10	0.27	0.99	0.14	0.37	0.23	1.45	0.03	0.35	0.46	0.10	0.07	1.33

Bin $3d \to 1d$	Total Unc.	Data stat.	ID syst.	ID Fwd syst.	Reco syst.	Trig syst.	Ener. scale	Fwd ener. scale	Ener. res.	Fwd ener. res.	Unfold. stat.	Unfold. method	EW+ top	Multi-jet stat.	Multi-jet syst.	Pile-up	PDF	Lineshape
79	2.76	0.46	0.24	0.74	0.03	0.15	0.36	1.52	0.17	0.85	0.17	0.68	0.01	0.74	0.92	0.00	0.07	1.30
80	4.74	1.07	0.35	1.22	0.06	0.26	0.87	1.65	0.38	0.15	0.85	3.54	0.02	0.72	0.91	0.11	0.35	1.12
81	6.74	1.97	0.12	1.27	0.03	0.05	1.29	0.66	0.63	0.53	1.31	5.50	0.08	1.44	1.48	0.07	0.17	0.92
82	2.16	0.55	0.23	0.90	0.04	0.06	0.44	0.82	0.11	0.63	0.24	0.06	0.02	0.38	0.54	0.13	0.10	1.31
83	2.21	0.43	0.38	0.74	0.04	0.09	0.40	0.94	0.08	0.70	0.16	0.56	0.03	0.19	0.27	0.01	0.08	1.41
84	3.01	0.43	0.36	0.86	0.04	0.13	0.18	0.97	0.07	0.99	0.18	1.87	0.03	0.31	0.44	0.02	0.12	1.48
85	5.31	0.49	0.43	2.80	0.06	0.19	0.17	1.03	0.10	0.23	0.22	4.04	0.01	0.39	0.49	0.12	0.11	1.38
86	5.44	0.64	0.50	0.86	0.12	0.11	0.37	0.95	0.30	0.68	0.29	4.94	0.07	0.26	0.39	-0.06	0.07	1.36
87	3.39	0.50	0.51	0.73	0.14	0.22	0.23	1.09	0.23	1.13	0.21	2.40	0.05	0.17	0.25	-0.11	0.09	1.37
88	2.88	0.55	0.65	0.84	0.15	0.15	0.27	1.04	0.23	1.51	0.27	0.68	0.05	0.27	0.62	0.03	0.14	1.52
89	5.51	0.56	0.90	2.86	0.11	0.18	0.65	0.77	0.31	0.95	0.30	4.09	0.04	0.24	0.44	0.02	0.09	1.40
90	11.01	0.52	0.92	10.40	0.11	0.21	0.20	0.98	0.29	0.85	0.24	2.53	0.03	0.49	1.29	0.11	0.11	1.30
91	10.24	2.60	0.39	0.73	0.09	0.08	1.62	3.26	1.40	4.26	1.37	3.19	1.25	1.44	6.88	0.05	0.32	0.95
92	10.30	1.55	0.36	0.84	0.10	0.15	1.18	3.78	1.01	8.13	1.07	2.48	0.52	1.01	3.35	-0.07	0.45	0.19
93	15.33	1.68	0.45	0.88	0.11	0.13	2.00	5.09	1.21	13.51	1.26	0.90	0.45	1.41	3.47	0.12	0.61	0.55
94	15.71	1.77	0.67	3.51	0.10	0.14	2.98	5.25	0.95	10.91	1.48	4.58	0.27	1.81	6.86	0.24	0.87	0.02
95	23.24	1.67	0.78	11.29	0.09	0.19	2.33	5.31	0.99	12.56	1.52	3.36	0.15	2.51	13.96	0.58	1.15	0.63
97	5.58	2.22	0.17	0.86	0.02	0.05	2.44	2.72	0.25	2.58	1.35	0.49	0.24	0.93	0.93	0.03	0.27	1.18
98	8.13	1.34	0.30	0.77	0.03	0.08	1.80	3.42	1.28	6.07	1.00	2.47	0.17	0.60	1.49	0.08	0.47	0.51
99	18.19	1.17	0.29	1.03	0.03	0.11	1.09	4.36	1.30	15.42	1.09	7.26	0.09	1.08	3.56	-0.06	0.59	0.85
100	17.77	1.51	0.32	2.65	0.04	0.17	2.62	4.82	1.73	13.98	1.53	8.29	0.07	1.03	1.84	0.49	0.75	1.29
103	6.00	2.26	0.25	0.97	0.04	0.12	0.77	2.77	1.11	1.69	1.37	3.19	0.13	0.81	2.16	0.15	0.23	0.17
104	9.04	1.44	0.27	0.77	0.05	0.18	1.92	4.05	0.94	7.16	1.01	0.54	0.08	1.06	1.22	0.06	0.21	1.66
108	4.49	1.93	0.24	1.02	0.04	0.12	1.70	2.50	0.19	0.89	1.09	1.02	0.26	0.60	1.59	0.24	0.19	0.21
109	7.49	1.25	0.26	0.78	0.04	0.17	1.77	3.45	1.33	5.83	0.78	0.80	0.11	0.76	0.89	0.06	0.18	0.58
112	4.39	1.80	0.17	0.86	0.02	0.05	1.87	1.77	1.04	0.90	1.04	2.11	0.20	0.61	0.57	-0.02	0.22	0.67
113	5.65	1.07	0.29	0.76	0.03	0.08	1.37	2.59	0.72	4.39	0.72	0.39	0.20	0.36	0.85	-0.16	0.24	0.18
114	12.41	0.87	0.28	0.99	0.03	0.11	1.18	3.73	0.57	10.17	0.72	5.17	0.10	0.61	2.11	-0.03	0.32	0.96
115	12.12	1.07	0.32	2.78	0.04	0.16	1.51	4.15	0.79	9.47	0.89	5.03	0.03	0.55	1.03	0.13	0.25	0.74
116	5.99	2.00	0.39	0.73	0.09	0.08	1.05	2.07	0.83	2.43	1.02	1.06	0.82	0.83	3.95	-0.07	0.12	0.04
117	6.38	1.19	0.33	0.79	0.09	0.14	1.00	2.91	0.68	4.75	0.78	0.72	0.47	0.57	2.03	0.08	0.28	0.45
118	9.87	1.06	0.44	0.80	0.11	0.13	1.00	3.84	0.84	8.41	0.89	1.85	0.26	0.70	1.81	-0.08	0.34	0.04

Bin $3d \to 1d$	Total Unc.	Data stat.	ID syst.	ID Fwd syst.	Reco syst.	Trig syst.	Ener. scale	Fwd ener. scale	Ener. res.	Fwd ener. res.	Unfold. stat.	Unfold. method	EW+ top	Multi-jet stat.	Multi-jet syst.	Pile-up	PDF	Lineshape
119	9.62	1.21	0.65	3.55	0.10	0.13	2.33	3.44	0.34	6.71	0.93	2.21	0.22	0.79	2.99	0.28	0.27	0.16
120	15.65	1.05	0.74	11.23	0.08	0.19	1.26	3.96	0.72	7.26	0.81	2.79	0.10	1.06	6.07	0.46	0.26	0.22
121	14.63	6.57	0.27	0.70	0.06	0.06	1.62	1.80	1.37	0.23	1.84	6.24	4.40	4.75	8.85	0.03	0.27	0.06
122	10.62	4.24	0.20	0.69	0.05	0.06	1.55	1.70	0.53	2.02	1.54	1.70	2.20	3.79	7.71	0.42	0.33	0.67
123	12.17	5.64	0.27	0.81	0.07	0.11	3.02	2.25	3.02	3.23	2.09	0.19	2.36	4.40	7.22	0.05	0.57	0.38
124	22.70	6.20	0.43	4.22	0.07	0.10	3.24	3.43	2.22	4.56	2.73	1.45	1.21	6.34	18.92	0.10	1.00	0.88
125	35.00	6.51	0.51	11.00	0.05	0.15	2.44	5.35	3.40	7.67	3.25	1.23	0.68	7.54	29.45	1.45	1.78	3.75
127	9.77	4.81	0.15	0.88	0.03	0.06	2.06	1.39	1.61	0.19	2.21	0.29	0.91	1.51	7.37	0.30	0.19	0.44
128	9.01	3.06	0.27	0.74	0.05	0.10	2.43	1.50	0.27	1.85	1.59	3.97	0.46	1.01	6.27	0.73	0.41	0.26
129	9.23	3.19	0.27	0.92	0.04	0.12	2.35	2.93	1.57	4.53	1.93	1.41	0.30	1.71	5.03	-0.28	0.69	1.56
130	12.29	4.39	0.29	2.48	0.04	0.19	3.30	5.00	1.20	5.76	2.92	1.36	0.14	2.80	4.12	0.51	0.75	4.35
133	6.89	4.23	0.33	0.99	0.07	0.15	1.22	1.90	0.97	0.86	2.12	1.66	0.28	1.95	3.16	0.49	0.17	0.60
134	6.01	3.13	0.37	0.74	0.09	0.24	1.47	2.00	0.94	0.91	1.57	0.48	0.37	1.39	3.57	-0.07	0.10	0.42
138	5.01	3.27	0.32	1.00	0.06	0.15	1.71	0.88	0.47	0.01	1.53	0.33	0.53	1.24	1.95	0.25	0.14	1.11
139	4.71	2.35	0.36	0.75	0.08	0.21	1.60	1.97	0.41	1.14	1.08	1.34	0.34	0.81	2.05	0.22	0.12	0.07
142	6.77	3.26	0.14	0.87	0.03	0.05	1.71	1.82	1.33	0.19	1.36	2.88	0.98	0.77	3.75	0.04	0.07	0.82
143	4.48	1.96	0.27	0.73	0.04	0.10	0.83	1.57	0.81	0.86	0.96	1.00	0.53	0.48	2.93	0.03	0.12	0.04
144	5.17	1.77	0.26	0.89	0.03	0.12	1.15	2.45	0.64	2.50	1.09	1.70	0.34	0.70	1.94	0.17	0.18	0.49
145	6.79	2.27	0.27	2.74	0.04	0.17	2.26	2.53	0.63	3.44	1.33	2.29	0.09	0.89	1.29	0.19	0.19	0.31
146	6.03	3.27	0.28	0.71	0.06	0.06	1.59	0.57	0.75	0.26	1.27	0.05	2.06	1.89	3.48	0.12	0.09	0.07
147	4.67	2.12	0.19	0.69	0.05	0.06	1.16	1.41	0.38	1.11	0.95	0.58	0.93	1.37	2.75	0.12	0.12	0.70
148	4.66	2.12	0.26	0.85	0.07	0.10	1.50	1.50	0.74	1.75	1.11	0.17	0.94	1.29	2.05	-0.01	0.16	0.55
149	8.17	2.37	0.41	4.48	0.07	0.10	1.33	1.84	0.96	2.25	1.22	1.87	0.62	1.53	4.62	0.57	0.13	0.62
150	13.94	2.12	0.48	11.02	0.05	0.14	1.78	2.75	0.61	3.51	1.18	0.21	0.28	1.57	6.34	0.59	0.25	0.42

Bibliography

[1] S.L. Glashow, "*Partial Symmetries of Weak Interactions*", Nucl. Phys. 22 (1961) 279, cited on page 4

[2] A. Salam, "*Renormalizability of Gauge Theories*", Phys. Rev. 127 (1962) 331, cited on page 4

[3] S. Weinberg, "*A Model of Leptons*", Phys. Rev. Lett. 19 (1967) 1264, cited on page 4

[4] P. Higgs, "*Broken Symmetries, Massless Particles and Gauge Fields*", Phys. Lett. 12 (1964) 132, cited on page 4

[5] F. Englert and R. Brout, "*Broken Symmetries and the Mass of Gauge Vector Mesons*", Phys. Lett. 13 (1964) 321, cited on page 4

[6] P. Higgs, "*Broken Symmetries and the Masses of Gauge Bosons*", Phys. Rev. Lett. 13 (1964) 508, cited on page 4

[7] G.S. Guralnik, C.R. Hagen and T.W.B. Kibble, "*Global Conservation Laws and Massless Particles*", Phys. Rev. Lett 13 (1964) 585, cited on page 4

[8] P. Higgs, "*Spontaneous Symmetry Breakdown without Massless Bosons*", Phys. Rev. 145 (1966) 1156, cited on page 4

[9] UA1 Collaboration, "*Experimental observation of lepton pairs of invariant mass around 95 GeV/c^2 at the CERN SPS collider*", Phys. Lett. 126B (1983) 398, cited on page 4

[10] UA2 Collaboration, "*Evidence for $Z^0 \to e^+e^-$ at the CERN $\bar{p}p$ collider*", Phys. Lett. 129B (1983) 130, cited on page 4

[11] UA1 Collaboration, "*Experimental observation of isolated large transverse energy electrons with associated missing energy at $\sqrt{s} = 540$ GeV*", Phys. Lett. 122B (1983) 103, cited on page 4

[12] UA2 Collaboration, "*Observation of single isolated electrons of high transverse momentum in events with missing transverse energy at the CERN $\bar{p}p$ collider*", Phys. Lett. 122B (1983) 476, cited on page 4

[13] L. Evans and P. Bryant (eds.), "*LHC Machine*", JINST 3 (2008) S08001, cited on page 4

[14] ATLAS Collaboration, "*Observation of a new particle in the search for the Standard Model Higgs boson with the ATLAS detector at the LHC*", Phys. Lett. B716.1 (2012), pp.1-29, cited on page 5

[15] CMS Collaboration, "*Observation of a new boson at a mass of 125 GeV with the CMS experiment at the LHC*", Phys. Lett., B 716.1 (2012), pp.30-61, cited on page 5

[16] M. Gell-Mann, "*A Schematic Model of Baryons and Mesons*", Phys. Lett. 8 (1964) 214, cited on page 5

[17] G. Zweig, "*An SU(3) Model for Strong Interaction Symmetry and its Breaking*", CERN Report No.8182/TH.401, cited on page 5

[18] M.Y. Han and Y. Nambu, "*Three-Triplet Model with Double SU(3) Symmetry*", Phys. Rev. 139 (1965) B1006, cited on page 5

[19] R.F. Schwitters, Proc. 1975 Int Sypmosium on Lepton-Photon Interactions at High Energies, Stanford (1975), p. 5, cited on page 5

[20] M. Peskin, "*Beyond the Standard Model*", SLAC-PUB-7479 (1997), cited on page 6

[21] F. Halzen, A.D. Martin, "*Quarks and Leptons: An Introductary Course in Modern Particle Physics*", (1984), cited on page 7

[22] K.A. Olive et al. (Particle Data Group), "*The Review of Particle Physics*", Chin. Phys. C, 38, 090001 (2014), cited on page 7, 11

[23] A. Glazov, "*Measurement of DIS Cross Section at HERA*", Brazilian Journal of Physics 2007 37(2C), cited on page 9

[24] V. N. Gribov, L. N. Lipatov, Sov. J. Nucl. Phys. 15 (1972) 438, cited on page 10

[25] L. N. Lipatov, Sov. J. Nucl. Phys. 20 (1975) 95, cited on page 10

[26] G. Altarelli, G. Parisi, "*Asymptotic Freedom in Parton Language*", Nucl. Phys. B126 (1977) 298, cited on pages 10

[27] Yu. L. Dokshitzer, Sov. Phys. JETP 46 (1977) 641, cited on page 10

[28] H1, ZEUS Collaborations, "*Combined Measurement and QCD Analysis of the Inclusive ep Scattering Cross Sections at HERA*", JHEP 1001:109 (2010), cited on page 11

[29] S. D. Drell, T.-M. Yan, "*Massive Lepton-Pair Production in Hadron-Hadron Collisions at High Energies*", Phys. Rev. Lett. 25, 5 (1970), cited on page 12

[30] ATLAS Collaboration, "*The ATLAS Experiment at the CERN Large Hadron Collider*", JINST 3 (2008), S08003, cited on pages 12, 24, 31, 32, 33

[31] CMS Collaboration, "*The CMS experiment at the CERN LHC*", JINST 3 (2008), S08004, cited on page 12, 24

[32] ATLAS Collaboration, "*Measurement of the inclusive $W^{\pm}$ and Z/γ^{*} cross sections in the e and μ decay channels in pp collisions at $\sqrt{s} = 7$TeV with the ATLAS detector*", PhysRevD.85.072004, cited on page 12

[33] The ALEPH Collaboration, the DELPHI Collaboration, the L3 Collaboration, the OPAL Collaboration, the SLD Collaboration, the LEP Electroweak Working Group, the SLD electroweak, heavy flavour groups, "*Precision Electroweak Measurements on the Z resonance*", Phys.Rept.427:257-454 (2006), cited on page 12, 20

[34] "*https://atlas.web.cern.ch/Atlas/GROUPS/PHYSICS/CombinedSummaryPlots/SM/*", (visited on 08/11/2014), cited on page 13

[35] J.C. Collins and D.E. Soper, "*Angular distribution of dileptons in high-energy hadron collisions*", Phys. Rev. D 16 (1977) 2219-2225, cited on page 15

[36] J. Rosner, "*Off-peak lepton asymmetries from new Z's*", Phys. Rev. D 35, 2244 (1987), cited on page 15, 20

[37] M. Dittmar, "*Neutral current interference in the TeV region: The experimental sensitivity at the CERN LHC*", Phys. Rev. D 55 (1997) 161, cited on page 15

[38] J. Goddard, "*A Measurement of the Low Mass Drell-Yan Differential Cross Section in the Di-Muon Channel with* $\sqrt{s} = 7$ *TeV Proton-Proton Collisioins at the ATLAS Experiment*", (2014), cited on page 17

[39] CMS Collaboration, "*Forward-backward asymmetry of Drell-Yan lepton pairs in pp collisions at sqrt(s) = 7 TeV*", Phys. Lett. B 718 (2013) 752, cited on page 20

[40] ATLAS Collaboration, "*Measurement of the forward-backward asymmetry of* Z/γ^* *bosons decaying into electron or muon pairs with the ATLAS detector at sqrts* $= 7$TeV", ATLAS-CONF-2013-043, cited on page 20, 21

[41] ALICE Collaboration, "*The ALICE experiment at the CERN LHC*", JINST 3.08 (2008), S08002, cited on page 24

[42] LHCb Collaboration, "*The LHCb Detector at the LHC*", JINST 3.08 (2008), S08005, cited on page 24

[43] The LHCf collaboration, "*The LHCf detector at the CERN Large Hadron Collider.*", JINST 3 (2008) S08006, cited on page 24

[44] J. Haffner, "*The CERN accelerator complex*", OPEN-PHO-ACCEL-2013-056-1, cited on page 25

[45] "*http://lhc-machine-outreach.web.cern.ch/lhc-machine-outreach/images/lhc-schematic.jpg*", (visited on 08/11/2014), cited on page 25

[46] The TOTEM Collaboration, "*The TOTEM Experiment at the CERN Large Hadron Collider*", JINST 3 (2008) S08007, cited on page 26

[47] MoEDAL Collaboration, "*Technical Design Report of the MoEDAL Experiment*", CERN-LHC-2009-006, MoEDAL-TDR-1.1 (2009), cited on page 26

[48] J. Pequenao , "*Computer generated image of the whole ATLAS detector*", CERN-GE-0803012-05 (2008), cited on page 27

[49] J. Pequenao, "*Computer generated image of the ATLAS inner detector*", CERN-GE-0803014-03 (2008), cited on page 29

[50] J. Pequenao, "*Computer Generated image of the ATLAS calorimeter*", CERN-GE-0803015-01 (2008), cited on page 29

[51] Dag Gillberg (On behalf of the ATLAS Liquid Argon Calorimeter Group), "*Performance of the ATLAS Forward Calorimeters in First LHC Data*", 2011 J. Phys.: Conf. Ser. 293 012041, cited on page 31

[52] J. P. Rutherfoord, "*Signal degradation due to charge buildup in nobel liquid ionization calirimeters*", Nucl. Instrum. Meth. A 482 (2002) 156-178, cited on page 32

[53] Armitage, J.C. et al., "*Electron signals in the Forward Calorimeter prototype for ATLAS*", JINST 2 (2007) P11001, cited on page 33

[54] ATLAS Collaboration, "*Improved luminosity determination in pp collisions at* $\sqrt{s} = 7$ *TeV using the ATLAS detector at the LHC*", arXiv:1302.4393v2, cited on page 34

[55] S. van der Meer, "*Calibration of the effective beam height in the ISR*", (1968), CERN-ISR-PO-68-31, cited on page 34

[56] C. Rubbia, "*Measurement of the luminosity of* $p\bar{p}$ *collider with a (generalized) van der Meer method*", (1977), CERN-$p\bar{p}$-Note-38, cited on page 34

[57] ATLAS Collaboration, *https://twiki.cern.ch/twiki/bin/view/AtlasPublic/LuminosityPublicResults*, (visited on 08/11/2014), cited on pages 34, 36

[58] ATLAS Collaboration, "*ATLAS Insertable B-Layer, Technical Design Report*", CERN-LHCC-2010-013 (2010), cited on page 35

[59] GEANT4 Collaboration, S. Agostinelli et al., "*GEANT4: A simulation toolkit*", Nucl. Instrum. Meth. A506 (2003) 250, cited on page 37

[60] S. Alioli, P. Nason, C. Oleari and E. Re, "*Single vector-boson production with decay*", JHEP 0807 (2008) 060, arXiv:0805.4802, cited on page 37

[61] P. Nason, ".", JHEP 0411 (2004) 040, hep-ph/0409146, cited on page 37

[62] S. Frixione, P. Nason and C. Oleari, ".", JHEP 0711 (2007) 070, arXiv:0709.2092, cited on page 37

[63] S. Alioli, P. Nason, C. Oleari and E. Re, ".", JHEP 1006 (2010) 043, arXiv:1002.2581, cited on page 37

[64] T. Sjöstrand, S. Mrenna and P. Skands, "*PYTHIA 6.4 Physics and Manual*", JHEP05 (2006) 026, cited on page 37

[65] T. Sjöstrand, S. Mrenna and P. Skands, "*A Brief Introduction to PYTHIA 8.1*", Comput. Phys. Comm. 178 (2008) 852, arXiv:0710.3820, cited on page 37

[66] B. Andersson, G. Gustafson, G. Ingelman and T. Sjöstrand, "", Phys. Rept. 97 (1983) 31, cited on page 37

[67] T. Sjöstrand, Nucl. Phys. B 248 (1984) 469, cited on page 37

[68] G. Corcella et al., "*HERWIG 6.5: an event generator for Hadron Emission Reactions With Interfering Gluons (including supersymmetric processes)*", JHEP 0101 (2001) 010 [arXiv:hep-ph/0011363] 37

[69] T. Gleisberg, S. Hoche, F. Krauss, M. Schonherr, S. Schumann, F Siegert, J. Winter, "*Event generation with Sherpa 1.1*", JHEP 02 (2009) 007 [arXiv:0811.4622], cited on page 37

[70] E. Barberio et al., "*PHOTOS: A Universal Monte Carlo for QED radiative corrections in decays*", Comput.Phys.Commun. 66 (1991) 115-128 CERN-TH-5857-90, cited on page 37

[71] J. Butterworth et al., "*Single Boson and Diboson Production Cross Sections in pp Collisions at* $\sqrt{s} = 7$ *TeV*", ATL-COM-PHYS-2010-695, cited on page 38

[72] T. Cornelissen, M. Elsing, S. Fleischmann, W. Liebig, E. Moyse, A. Salzburger, "*Concepts, Design and Implementation of the ATLAS New Tracking (NEWT)*", ATL-SOFT-PUB-2007-007, ATL-COM-SOFT-2007-002, cited on page 40

[73] R. Fruhwirth, "*Application of Kalman filtering to track and vertex fitting*", Nucl. Inst. Meth. A 262, (1987), cited on page 40

[74] ATLAS Collaboration, "*Improved electron reconstruction in ATLAS using the Gaussian Sum Filter-based model for bremsstrahlung*", ATLAS-CONF-2012-047, cited on page 40

[75] W. Lampl et al., "*Calorimeter Clustering Algorithms: Description and performance*", ATL-LARG-PUB-2008-002, (2007), cited on page 41

[76] ATLAS Collaboration, "*Electron efficiency measurements with the ATLAS detector using the 2012 LHC proton-proton collision data*", ATLAS-CONF-2014-032, cited on page 42, 43, 45, 46, 47, 86

[77] R.A. Fisher, "*The Use of Multiple Measurements in Taxonomic Problems*", Annals Eugenics 7 no. 2, (1936), cited on page 44

[78] ATLAS Collaboration, "*Electron and photon energy calibration with the ATLAS detector using LHC Run 1 data*", Eur.Phys.J. C74 (2014) 3071, cited on page 44, 87

[79] ATLAS Collaboration, *https://twiki.cern.ch/twiki/bin/view/AtlasPublic/EgammaTriggerPublicResults*", (visited on 08/11/2014), cited on page 50

[80] T. Kittelmann, V. Tsulaia, J. Boudreau and E. Moyse, "*The Virtual Point 1 event display for the ATLAS experiment* ", J. Phys.: Conf. Ser. 219 032012 (2010), cited on page 53

[81] G. D'Agostini, "*A multidimentional unfolding method based on Bayes' theorem*", Nucl. Instr. and Meth. in Phys. Res. A362 (1995) 487, cited on page 79

[82] G. D'Agostini, "*Improved iterative Bayesin unfolding*", arXiv:1010.0632 [physics.data-an], cited on pages 79, 80

[83] T. Adye, "*Unfolding algorithms and tests using RooUnfold*", arXiv:1105.1160v1, cited on page 80

[84] T. Adye, Proceedings of the PHYSTAT 2011 Workshop on Statistical Issues Related to Discovery Claims in Search Experiments and Unfolding, CERN, Geneva, Switzerland, 17-20 January 2011, edited by H.B. Prosper and L. Lyons, CERN-2011-006, 313-318., cited on page 80

[85] T. Kwan, Private Communication, cited on page 80

[86] B. Efron, "*Bootstrap methods: Another look at the Jackknife*", The Annals of Statistics 7 (1979), 1-26, cited on page 85

[87] B. Efron, R. Tibshirani, "*An introduction to the Bootstrap*", CRC Press (1993), cited on page 85

[88] H.-L. Lai, M. Guzzi, J. Huston, Z. Li, P. Nadolsky, and others, "*New parton distributions for collider physics*", Phys.Rev. D82 (2010) 074024, [arXiv:1007.2241], cited on page 88

[89] M.R. Whalley, D. Bourilkov, R.C. Group, "*The Les Houches accord PDFs (LHAPDF) and LHAGLUE* ", hep-ph/0508110 (2008), cited on page 89

[90] ATLAS Collaboration, "*Measurement of the inclusive jet cross section is pp collisions at* $\sqrt{s} =$ 2.76 *TeV and comparison to the inclusive jet cross section at* $\sqrt{s} = 7$ *TeV using the ATLAS detector*", Eur. Phys. J. C73 (2013) 2509, cited on page 89

[91] J.M. Campbell and R.K. Ellis, "*MCFM for the Tevatron and the LHC*", Nucl.Phys.Proc.Suppl. 205-206 (2010) 10-15, arXiv:1007.3492 [hep-ph], cited on page 93

[92] T. Carli, D. Clements, A. Cooper-Sarkar, C. Gwenlan, G.P. Salam, F. Siegert, P. Starovoitov, M. Sutton, "*A posteriori inclusion of parton density functions in NLO QCD final-state calculations at hadron colliders: The APPLGRID Project*", Eur.Phys.J. C66 (2010) [arXiv:0911.2985], cited on page 93

[93] P.M. Nadolsky, H.-L. Lai, Q.-H. Cao, J. Huston, J. Pumplin, D. Stump, W.-K. Tung, C.-P. Yuan, "*Implications of CTEQ global analysis for collider observables*", Phys.Rev.D78 013004 (2008), cited on page 93

[94] ATLAS Collaboration, "*Measurement of the low-mass Drell-Yan differential cross section at* $\sqrt{s} = 7$ *TeV using the ATLASdetector*", JHEP 06 (2014) 112, cited on pages 95, 117, 120

[95] A.D. Martin, W.J. Stirling, R.S. Thorne, G. Watt, "*Parton distributions for the LHC*", Eur.Phys.J. C63 (2009) 189-285, cited on page 96

[96] ATLAS Collaboration, "*Determination of the Strange-Quark Density of the Proton from ATLAS Measurements of the* $W \to \ell\nu$ *and* $Z \to \ell\ell$ *Cross Sections*", Phys. Rev. Lett. 109 (2012), 012001, cited on page 101

[97] S. Alekhin, J. Blumlein, S. Moch, "*Parton Distribution Functions and Benchmark Cross Sections at NNLO*", Phys. Rev. D86 (2012), 054009, cited on page 101

[98] H1 and ZEUS Collaboration, "*Combined Measurement and QCD Analysis of the Inclusive $e^{\pm}p$ Scattering Cross Sections at HERA*", JHEP 01 (2009) 61, cited on page 117, 118

[99] HERAFitter, *http://projects.hepforge.org/herafitter*, cited on page 117

[100] H1 Collaboration, "*A Precision Measurement of the Inclusive ep Scattering Cross Section at HERA*", Eur. Phys. J. C 64 (2009) 561, cited on page 117

[101] M. Botje, "*QCDNUM: Fast QCD Evolution and Convolution*", Comput. Phys. Commun. 182 (2011) 409, cited on page 117

[102] F. James and M. Roos, "*Minuit: A System for Function Minimization and Analysis of the Parameter Errors and Correlations*", Comput. Phys. Commun. 10 (1975) 343-367, cited on page 117

[103] R. Gavin et al., "*FEWZ 2.0: A code for hadronic Z production at next-to-next-to-leading order*", Comput. Phys. Commun. 182 (2011) 2388, cited on page 118

[104] ATLAS Collaboration, "*Determination of the strange quark density of the proton from ATLAS measurements of the $W \to l\nu$ and $Z \to ll$ cross-sections*", Phys.Rev.Lett. 109 (2012) 012001, cited on page 118, 119

[105] J. Pumplin, D. Stump, R. Brock, D. Casey, J. Huston, J. Kalk, H.L. Lai, W.K. Tung, "*Uncertainties of predictions from parton distribution functions II: the Hessian method*", Phys.Rev.D65:014013,2001, cited on page 120

[106] ATLAS Collaboration, "*Measurement of the low mass Drell-Yan differential cross section with the ATLAS detector*", ATL-COM-PHYS-2012-966, cited on page 122

Acknowledgements

The years of my PhD were truly exciting and fruitful, which would never have been possible without the people surrounding me. I would like to thank

- my supervisor, Sasha Glazov, for giving me the chance to get involved in experimental HEP and for his wise supervision during my PhD years.
- my committee members, Johannes Haller, Hannes Jung, Sven-Olaf Moch, Michael Rübhausen and Thomas Schörner-Sadenius for making my defense possible.
- my colleagues who were helping me to become a physicist and for providing useful feedback for my thesis: Voica Radescu, Pavel Starovoitov, Mikhail Karnevskiy, Andrey Sapronov, Renat Sadykov, Chris Hengler, Martin Bessner, James Dassoulas and Misha Lisovyi.
- Eram Rizvi, Tony Kwan and Voica Radescu for a very fruitful and inspiring collaboration.
- my group leader, Mike Medinnis, for his help and support during the whole time of my PhD. Alla Grabowsky, Sabine Krohn and DESY International Office for a million things they helped me to solve.
- Spyros Argyropoulos, for everything.
- my Parents.